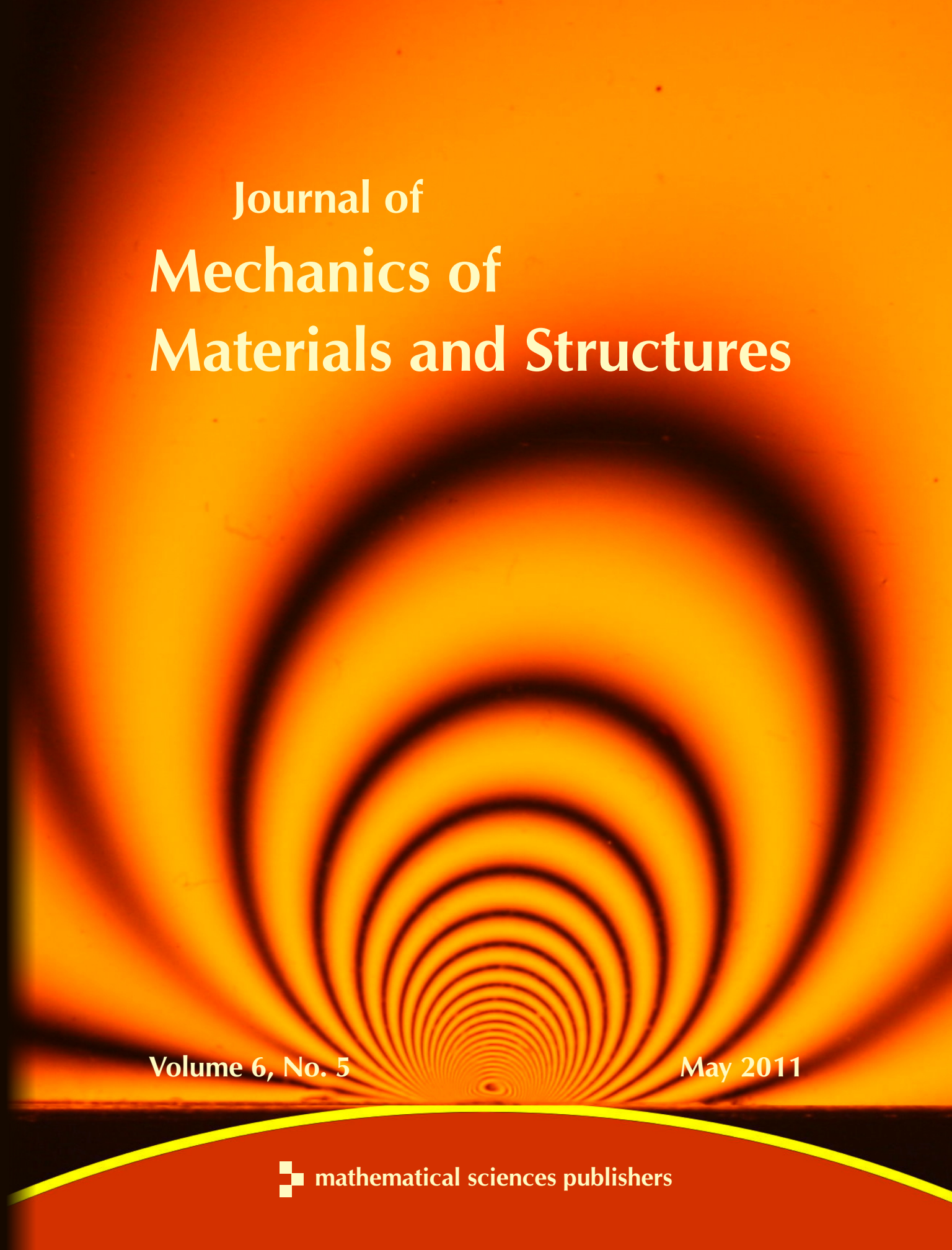
Journal of
Mechanics of
Materials and Structures
Volume 6, No. 5
May 2011
mathematical sciences publishers

JOURNAL OF MECHANICS OF MATERIALS AND STRUCTURES

jomms.org

Founded by Charles R. Steele and Marie-Louise Steele

See http://jomms.org for submission guidelines.

JoMMS (ISSN 1559-3959) is published in 10 issues a year. The subscription price for 2011 is US $520/year for the electronic version, and $690/year (+$60 shipping outside the US) for print and electronic. Subscriptions, requests for back issues, and changes of address should be sent to Mathematical Sciences Publishers, Department of Mathematics, University of California, Berkeley, CA 94720–3840.

JoMMS peer-review and production is managed by EditFLOW™ from Mathematical Sciences Publishers.

PUBLISHED BY
mathematical sciences publishers
http://msp.org/

A NON-PROFIT CORPORATION

Typeset in LaTeX

JOURNAL OF MECHANICS OF MATERIALS AND STRUCTURES
Vol. 6, No. 5, 2011

msp

STUDY OF MULTIPLY-LAYERED CYLINDERS MADE OF FUNCTIONALLY GRADED MATERIALS USING THE TRANSFER MATRIX METHOD

Y. Z. CHEN

This paper provides a general solution for a multiply-layered cylinder made of functionally graded materials. The Young's modulus is assumed to be an arbitrary function of r, and the Poisson's ratio takes a constant value. The first step is to study the single-layer case ($a < r < b$). A transfer matrix is defined, relating the values of radial stress and displacement at the initial point ($r = a$) to those at the end point ($r = b$). The matrix is evaluated on the basis of two fundamental solutions, which are evaluated numerically. The final solution is obtained by using many transfer matrices for layers, continuation conditions between layers, and boundary conditions at inner and outer boundaries. Several numerical examples are provided.

1. Introduction

Functionally graded materials (FGMs) are widely used in industries such as space structures and fusion reactors. Therefore, elastic analysis of structures made of FGMs has attracted many researchers. FGMs are nonhomogeneous elastic mediums. The elastic properties of FGMs are variable with the respect to spatial location. The difficulties of solving elastic FGM problems can be easily seen. Taking the plane elasticity problem of FGMs as an example, the complex variable method is no longer useful in this case. Therefore, it is necessary to develop appropriate methods to solve some problems for FGMs.

Clearly, it is difficult to study the three-dimensional elasticity of FGMs. Researchers have paid attention to some particular problems for FGMs. For example, crack problems for an elastic medium made of FGMs were investigated in [Erdogan and Wu 1997; Jain et al. 2004; Fotuhi and Fariborz 2006].

One topic to investigate regarding FGMs is the stress distribution in a thick cylinder of FGMs. The elasticity problem of a homogeneous hollow circular cylinder has been solved by [Muskhelishvili 1963; Timoshenko and Goodier 1970].

Earlier research for thick cylinder FGMs was proposed [Horgan and Chan 1999a; 1999b]. A solution for the pressurized hollow cylinder or disk problem for functionally graded isotropic linearly elastic materials was achieved. The material and the thermal properties were assumed to vary along the radius r according to a power law function.

Recently, many research works have been devoted to the hollow circular cylinder problem for FGMs [Zhang and Hasebe 1999; Shao 2005; Dryden and Jayaraman 2006; Shi et al. 2007; Tutuncu 2007; Batra and Iaccarino 2008; Chen and Lin 2008; Theotokoglou and Stampouloglou 2008; Li and Peng 2009]. In most of the studies, the Young's modulus is assumed in the form of exponential or power law functions. Thus, the suggested techniques are no longer useful for an arbitrary Young's modulus distribution. In the case of a Young's modulus expression $E(r) = E_0(r/a)^n$, a closed form solution

Keywords: composites, layered structure, nonlinear behavior, transfer matrix method, strength.

for displacement was obtained [Horgan and Chan 1999a; 1999b]. In the case of a Young's modulus expression $E(r) = E_0 \exp \beta r$, an ordinary differential equation for displacement was suggested [Tutuncu 2007]. To obtain the final solution, one needs to complete a detailed derivation.

If the Young's modulus is an arbitrary function, one needs to derive a numerical method to solve the problem. For example, the associated elastic problem is reduced to a Fredholm integral equation. By approximately solving the resulting equation, the distributions of the radial and circumferential stresses can be determined [Li and Peng 2009].

Some papers were devoted to a multiply-layered cylinder [Zhang and Hasebe 1999; Shi et al. 2007]. However, the homogeneous condition was assumed for individual layers. This means that a cylinder of FGMs is approximated by many homogeneous layers, and the nonhomogeneous condition is not considered in individual layers.

In addition, some papers were devoted to the hollow sphere problem for FGMs [Eslami et al. 2005; You et al. 2005; Chen and Lin 2008]. The solution technique is approximately same as in the case of a hollow cylinder.

Axisymmetric displacements and stresses in functionally-graded hollow cylinders, disks, and spheres subjected to uniform internal pressure were determined using plane elasticity theory and the complementary functions method [Tutuncu and Temel 2009].

This paper provides a general solution for a multiply-layered cylinder of FGMs. The Young's modulus is assumed to be an arbitrary function with respect to r, and the Poisson's ratio takes a constant value. The first step is to study the single-layer case. A transfer matrix $\boldsymbol{M}$ is defined for the single-layer case ($a < r < b$). The matrix relates the values of radial stress and displacement at the initial point ($r = a$) to those at the end point ($r = b$). The matrix is evaluated on the basis of two fundamental solutions, which are evaluated numerically. By using many transfer matrices for layers, continuation conditions between layers, and boundary conditions at inner and outer boundaries, the final solution is obtained.

The suggested formulation can be used in the case of an arbitrary Young's modulus. In this paper, the Young's modulus is assumed in the form of an exponential function with respect to r, and Poisson's ratio takes a constant value. Numerical examples for a three-layered cylinder are carried out. It is found that the factor β in the expression of the Young's modulus has significant influence on the distribution of stresses.

2. Boundary value problem for a single-layer cylinder

Since the solution for a multiply-layered cylinder has a close relation to the case of a single-layer cylinder, a formulation for the boundary value problem for a single-layer cylinder is introduced below.

2.1. ***Elastic analysis for a thick cylinder made of FGM.*** A long cylinder with inner radius a and outer radius b is investigated (Figure 1). The cylinder is assumed under some traction or displacement boundary value conditions at the inner boundary ($r = a$) and outer boundary ($r = b$).

The problem can be studied in polar coordinates (r, θ). In the symmetrical deformation case, the displacement in the r-direction is denoted by u. Two strain components can be expressed as follows (see [Muskhelishvili 1963; Timoshenko and Goodier 1970]):

$$\varepsilon_r = \frac{du}{dr}, \quad \varepsilon_\theta = \frac{u}{r} \quad (u = \varepsilon_\theta r). \tag{1}$$

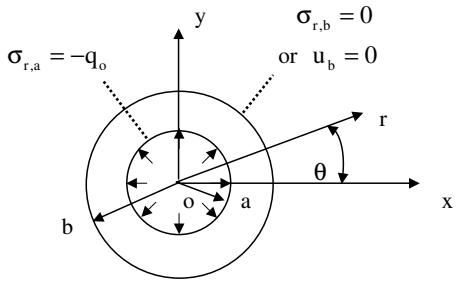

Figure 1. Two typical boundary conditions: (a) $\sigma_{r,a} = -q_0$ at $r = a$, $\sigma_{r,b} = 0$ at $r = b$ and (b) $\sigma_{r,a} = -q_0$ at $r = a$, $u_b = 0$ at $r = b$.

From (1), the compatibility condition of displacement will be

$$\varepsilon_r = \frac{d(r\varepsilon_\theta)}{dr}, \quad \text{or} \quad \varepsilon_r = \varepsilon_\theta + r\frac{d\varepsilon_\theta}{dr}. \tag{2}$$

For the stress components σ_r and σ_θ, the equilibrium equation takes the form

$$\frac{d\sigma_r}{dr} + \frac{\sigma_r - \sigma_\theta}{r} = 0. \tag{3}$$

Equation (3) can be satisfied automatically, if one introduces a function $F(r)$ and lets

$$\sigma_r = \frac{F(r)}{r}, \quad \sigma_\theta = \frac{dF}{dr}. \tag{4}$$

The following derivation is suitable not only for the continuous case of the Young's modulus $E(r)$ and the Poisson's ratio $\nu(r)$ but also for the discontinuous case of $E(r)$ and $\nu(r)$. Therefore, the suggested approach can be used in the general case.

In this paper, it is assumed that the Poisson's ratio ν $(= 0.3)$ takes a constant value. In addition, one type of the Young's modulus takes the following form:

$$E(r) = E_0 \exp[\beta(r-a)/(b-a)], \quad \text{with} \quad E(r)|_{r=a} = E_0, \quad E(r)|_{r=b} = E_0 \exp\beta \quad (a \le r \le b), \tag{5}$$

where E_0 is a constant, and β takes a negative or positive value and represents the property of the FGMs, hereafter called the material parameter. It will be seen later that the suggested technique is valid for an arbitrary function $E(r)$.

In the formulation, the material properties of the FGM are continuous functions of position. Generally, the material coefficients of FGM manufactured in a perfect process are changed in space without acuity. From (5), we can define a ratio by $\gamma = E(r)|_{r=b}/E(r)|_{r=a}$ or $\gamma = \exp(\beta)$. The value γ represents the ratio of the Young's modulus at the outer boundary and at the inner boundary. If $\beta = 0$, $\beta = 0.1$, $\beta = 0.2$, and $\beta = 1$, we have $\gamma = 1$, $\gamma = 1.1052$, $\gamma = 1.2214$, and $\gamma = 2.7183$, respectively. Therefore, (5) can model the material properties of FGM when the properties are not changed significantly along the radial direction.

In the plane strain case, the stress-strain relation will be

$$\varepsilon_r = \frac{1-\nu^2}{E(r)}\Big(\sigma_r - \frac{\nu}{1-\nu}\sigma_\theta\Big), \quad \varepsilon_\theta = \frac{1-\nu^2}{E(r)}\Big(\sigma_\theta - \frac{\nu}{1-\nu}\sigma_r\Big), \tag{6}$$

where the Young's modulus $E(r)$ is an arbitrary function. From (1), (4), and (6), the displacement component u can be expressed as

$$u = \varepsilon_\theta r = \frac{(1-\nu^2)r}{E(r)}\Big(\frac{dF}{dr} - \frac{\nu}{1-\nu}\frac{F}{r}\Big). \tag{7}$$

Substituting (4) into (6) and then (6) into (2) yields

$$\frac{d^2F}{dr^2} + \frac{1}{r}\frac{dF}{dr} - \frac{F}{r^2} - \Big(\frac{dF}{dr} - \frac{\nu}{1-\nu}\frac{F}{r}\Big)p(r) = 0, \quad \text{where } p(r) = \frac{1}{E(r)}\frac{dE(r)}{dr} \quad (\text{or } \Lambda(F(r)) = 0). \tag{8}$$

If the function $E(r)$ is given by (5), we have

$$p(r) = \frac{\beta}{b-a}. \tag{9}$$

Alternatively, if $E(r)$ is defined by

$$E(r) = E_0[1+(\exp\beta - 1)(r-a)/(r-b)], \quad E(r)|_{r=a} = E_0, \quad E(r)|_{r=b} = E_0\exp\beta \quad (a \le r \le b), \tag{10}$$

we have

$$p(r) = \frac{\exp\beta - 1}{b - a + (\exp\beta - 1)(r-a)}. \tag{11}$$

The problem is studied within the range $a \le r \le b$. In the analysis, the following notations are used:

$$\sigma_r|_{r=a} = \sigma_{r,a}, \qquad u|_{r=a} = u_a, \tag{12}$$

$$\sigma_r|_{r=b} = \sigma_{r,b}, \qquad u|_{r=b} = u_b. \tag{13}$$

In (12), $\sigma_{r,a}$ and $\sigma_{r,b}$ denote the stress component σ_r at $r = a$ and $r = b$, and u_a and u_b denote the displacement u at $r = a$ and $r = b$, respectively.

For a single-layer cylinder case, there are four possibilities for formulating the boundary problems. They are as follows:

$$\sigma_{r,a} = f_1, \qquad \sigma_{r,b} = f_2, \tag{14a}$$

$$\sigma_{r,a} = f_1, \qquad u_b = g_2, \tag{14b}$$

$$u_a = g_1, \qquad \sigma_{r,b} = f_2, \tag{14c}$$

$$u_a = g_1, \qquad u_b = g_2, \tag{14d}$$

where f_1, f_2, g_1, and g_2 are values given beforehand.

2.2. ***Formulation of the transfer matrix for the case of a single-layer cylinder.*** Physically, if the two initial values for $\sigma_{r,a}$ and u_a are assumed at $r = a$, we have definite values for $\sigma_{r,b}$ and u_b at $r = b$. This relation can be written in the form

$$\sigma_{r,b} = \boldsymbol{M}_{11}\sigma_{r,a} + \boldsymbol{M}_{12}u_a, \quad u_b = \boldsymbol{M}_{21}\sigma_{r,a} + \boldsymbol{M}_{22}u_a, \tag{15}$$

or in matrix form

$$\{\sigma_{r,b} \;\; u_b\}^T = \boldsymbol{M}\{\sigma_{r,a} \;\; u_a\}^T. \tag{16}$$

The matrix $\boldsymbol{M}$ is called the transfer matrix hereafter.

The introduced matrix $\boldsymbol{M}$ is used not only in the single-layer case but also in the multiply-layered case. In the following analysis, a technique for finding the matrix $\boldsymbol{M}$ will be introduced. In the first step, two fundamental functions $s_1(r)$ and $s_2(r)$ are introduced:

$$\Lambda(s_1(r)) = 0, \qquad s_1|_{r=a} = 1, \qquad \left.\frac{ds_1}{dr}\right|_{r=a} = 0 \qquad \text{(first fundamental function)}, \tag{17}$$

$$\Lambda(s_2(r)) = 0, \qquad s_2|_{r=a} = 0, \qquad \left.\frac{ds_2}{dr}\right|_{r=a} = 1 \qquad \text{(second fundamental function)}, \tag{18}$$

where the operator $\Lambda(F(r))$ has been defined by (8).

From the two fundamental solutions and (4), (7), (17), and (18), we have

$$\sigma_r|_{r=a} = \frac{1}{a} \quad \text{and} \quad u|_{r=a} = -\frac{(1+\nu)\nu}{E(a)} \qquad \text{for the first fundamental solution } s_1(r), \tag{19}$$

$$\sigma_r|_{r=a} = 0 \quad \text{and} \quad u|_{r=a} = \frac{(1-\nu^2)a}{E(a)} \qquad \text{for the first fundamental solution } s_2(r). \tag{20}$$

It is assumed that the studied solution for $F(r)$ is expressed as

$$F(r) = c_1 s_1(r) + c_2 s_2(r). \tag{21}$$

Thus, from (19), (20) and (21), we have

$$\sigma_{r,a} = \frac{1}{a}c_1, \quad u_a = \frac{(1-\nu^2)a}{E(a)}\left(-\frac{\nu}{(1-\nu)a}c_1 + c_2\right). \tag{22}$$

Equation (22) may be rewritten as

$$c_1 = a\sigma_{r,a}, \quad c_2 = \frac{\nu}{1-\nu}\sigma_{r,a} + \frac{E(a)}{(1-\nu^2)a}u_a, \tag{23}$$

or in matrix form

$$\{c_1 \;\; c_2\}^T = \boldsymbol{Q}\{\sigma_{r,a} \;\; u_a\}^T, \tag{24}$$

where

$$Q_{11} = a, \quad Q_{12} = 0, \quad Q_{21} = \frac{\nu}{1-\nu}, \quad Q_{22} = \frac{E(a)}{(1-\nu^2)a}. \tag{25}$$

Now we consider the conditions at $r = b$. After numerical integration, from the two fundamental solutions we obtain

$$\sigma_r^{1*}|_{r=b} = \sigma_{r,b}^{1*}, \qquad u^{1*}|_{r=b} = u_b^{1*} \qquad \text{for the first fundamental solution } s_1(r). \tag{26}$$

$$\sigma_r^{2*}|_{r=b} = \sigma_{r,b}^{2*}, \qquad u^{2*}|_{r=b} = u_b^{2*} \qquad \text{for the second fundamental solution } s_2(r). \tag{27}$$

The values of $\sigma_{r,b}^{1*}$ and u_b^{1*} can be obtained from (4) and (7) by numerically integrating the expression for $s_1(r)$ and taking $r = b$, and similarly for $\sigma_{r,b}^{2*}$ and u_b^{2*}.

From (21), (26) and (27), we have

$$\sigma_{r,b} = \sigma_{r,b}^{1*}c_1 + \sigma_{r,b}^{2*}c_2, \quad u_b = u_b^{1*}c_1 + u_b^{2*}c_2, \tag{28}$$

or in matrix form

$$\{\sigma_{r,b} \;\; u_b\}^T = \boldsymbol{P}\{c_1 \;\; c_2\}^T, \tag{29}$$

where

$$P_{11} = \sigma_{r,b}^{1*}, \quad P_{12} = \sigma_{r,b}^{2*}, \quad P_{21} = u_b^{1*}, \quad P_{22} = u_b^{2*}. \tag{30}$$

Combining (24) with (29), we have

$$\{\sigma_{r.b} \;\; u_b\}^T = \boldsymbol{M}\{\sigma_{r,a} \;\; u_a\}^T, \tag{31}$$

where the matrix $\boldsymbol{M}$ is defined by

$$\boldsymbol{M} = \boldsymbol{P}\,\boldsymbol{Q}. \tag{32}$$

As claimed previously, once the two initial values for $\sigma_{r,a}$ and u_a are assumed at $r = a$, we have definite values for $\sigma_{r,b}$ and u_b at $r = b$. The relation shown by (31) is useful for both the single-layered case and the multiply-layered case.

The evaluation of matrix $\boldsymbol{P}$ depends on the numerical solution of the ordinary differential equation (8). For example, the two components $\boldsymbol{P}_{11} = \sigma_{r,b}^{1*}$ and $\boldsymbol{P}_{12} = u_b^{1*}$ are results of the initial boundary value problem for function $s_1(r)$ defined by (17). In the numerical integration, the Runge–Kutta method is used [Hildebrand 1974]. The components for matrix $\boldsymbol{Q}$ have been defined by (25). Finally, the matrix $\boldsymbol{M}$ can be evaluated from (32) immediately.

Below, we try to solve the boundary value problem

$$\sigma_{r,a} = f_1, \quad \sigma_{r,b} = f_2. \tag{14a}$$

Substituting condition (14a) into (15) or (31) yields

$$f_2 = \boldsymbol{M}_{11} f_1 + \boldsymbol{M}_{12} u_a \quad \text{or} \quad u_a = (f_2 - \boldsymbol{M}_{11} f_1)/\boldsymbol{M}_{12}. \tag{33}$$

Substituting the given $\sigma_{r,a} = f_1$ value and the value u_a from (33) into (24), two values c_1 and c_2 are obtained. Finally, the function $F(r) = c_1 s_1(r) + c_2 s_2(r)$ shown by (21) is obtained. This means that the whole stress field for the single-layer cylinder is obtainable.

2.3. *Numerical solution in single-layer case.*

Example 1. In this example, the Young's modulus is $E(r) = E_0 \exp\{\beta(r-a)/(b-a)\}$, defined by (5). The cylinder is subject to an inner pressure q_0 and the boundary conditions take the following form (Figure 1):

$$\sigma_{r,a} = \sigma_r|_{r=a} = -q_0, \quad \sigma_{r,b} = \sigma_r|_{r=b} = 0. \tag{34}$$

Substituting $f_1 = -q_0$ and $f_2 = 0$ into (33), we have $u_a = \boldsymbol{M}_{11} q_0/\boldsymbol{M}_{12}$. As claimed previously, from two values $\sigma_{r,a}$ $(= -q_0)$ and u_a $(= \boldsymbol{M}_{11} q_0/\boldsymbol{M}_{12})$, and two values c_1 and c_2, the function $F(r) = c_1 s_1(r) + c_2 s_2(r)$ and the whole stress field for the single-layer cylinder are obtainable.

Note that the Young's modulus is expressed by $E(r) = E_0 \exp\{\beta(r-a)/(b-a)\}$, and changes from E_0 at $r = a$ to $E_0 \exp\beta$ at $r = b$. In the solution of the differential equation, $N = 200$ divisions are used in the integration [Hildebrand 1974]. The calculated results for the stresses can be expressed as

$$\sigma_r = f_1(\beta, r)q_0, \quad \sigma_\theta = f_2(\beta, r)q_0, \quad \sigma_e = \sigma_\theta - \sigma_r = f_3(\beta, r)q_0 \quad (f_3 = f_2 - f_1). \tag{35}$$

The calculated results for f_1, f_2, and f_3 under the conditions $a/b = 0.5$ and $\beta \in \{-0.5, 0, 0.5, 1, 1.5\}$ are plotted in Figures 2, 3, and 4. Since $E(a) = E_0$ and $E(b) = E_0 \exp\beta$, we have $E(b)/E(a) =$ 0.6065, 1.0000, 1.6487, 2.7183, and 4.4817 for $\beta = -0.5$, 0, 0.5, 1, and 1.5, respectively.

We see from the general theory of strength of materials that the strength of the cylinder mainly depends on the stress component $\sigma_e = \sigma_\theta - \sigma_r$ (or $f_3(\beta, r)$). From Figure 4 we see that the σ_e distribution along the interval $a \le r \le b$ varies rapidly in the homogeneous material case. For example, at $\beta = 0$, we have $f_3 = 2.6667$, 1.1852, and 0.6667, for $(r-a)/(b-a) = 0$, 0.5, and 1.0, respectively. In addition, a higher β value can considerably improve the σ_e distribution along the interval $(a \le r \le b)$. For example, at $\beta = 1.5$, we have $f_3 = 1.7283$, 1.3428, and 1.5045, for $(r-a)/(b-a) = 0$, 0.5, and 1.0, respectively. This means that if outer portion of the cylinder is more rigid, the safe condition is better. On the contrary,

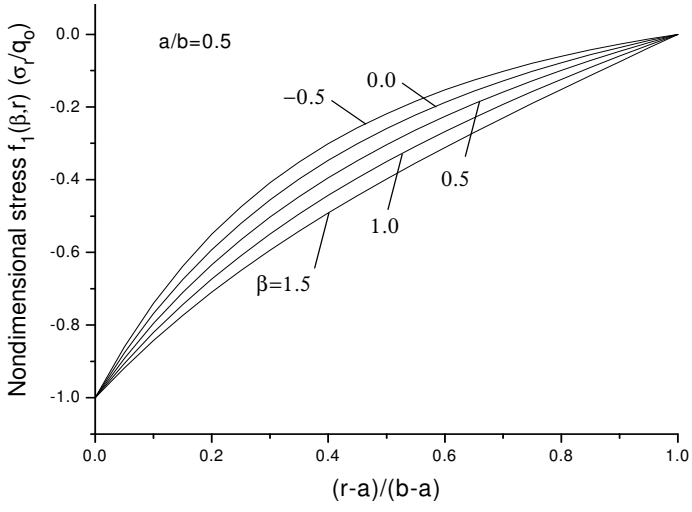

Figure 2. Nondimensional radial stress $f_1(\beta, r)$, for the σ_r component in the cylinder, with $a/b = 0.5$, inner pressure q_0, and $E(r) = E_0 e^{\beta(r-a)/(b-a)}$ (see (35) and Figure 1).

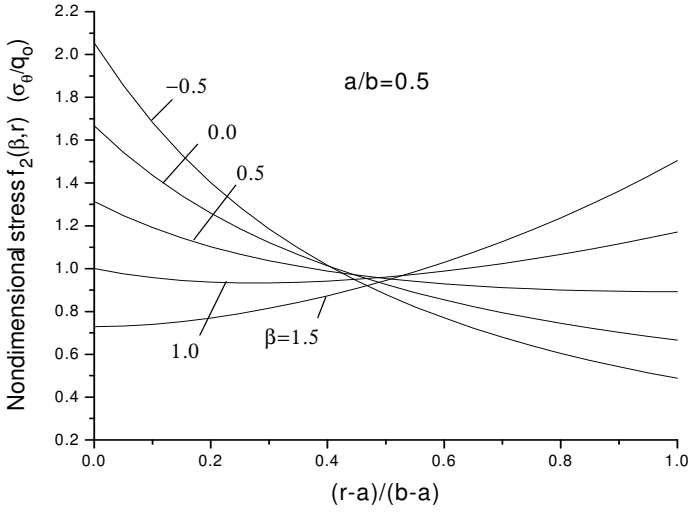

Figure 3. Nondimensional circumferential stress $f_2(\beta, r)$, for the σ_θ component in the cylinder, with $a/b = 0.5$, inner pressure q_0, and $E(r) = E_0 e^{\beta(r-a)/(b-a)}$ (see (35) and Figure 1).

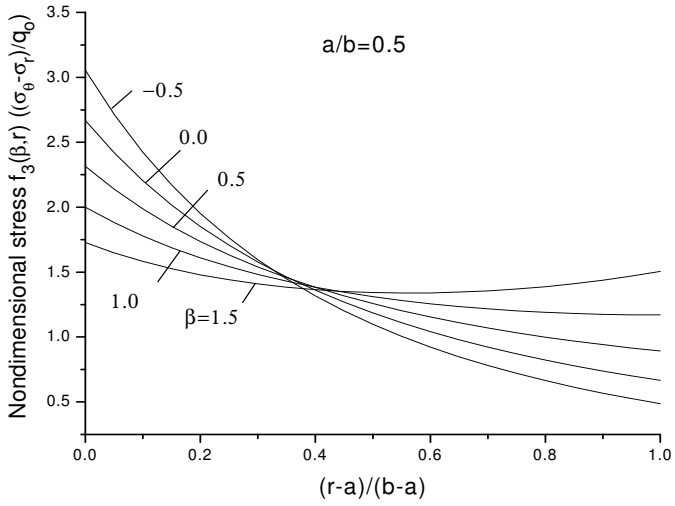

Figure 4. Nondimensional stress $f_3(\beta, r)$, for the $\sigma_e = \sigma_\theta - \sigma_r$ component in the cylinder, with $a/b = 0.5$, inner pressure q_0, and $E(r) = E_0 e^{\beta(r-a)/(b-a)}$ (see (35) and Figure 1).

if the outer portion of the cylinder is less rigid, the safe condition becomes worse (see the curve for $\beta = -0.5$ in Figure 4). It is found that the plotted results coincide with those obtained previously [Chen and Lin 2008].

Example 2. In this example, the Young's modulus is $E(r) = E_0[1 + (\exp\beta - 1)(r-a)/(r-b)]$, defined by (10). The other computed conditions are the same as in Example 1. The computed stresses are still expressed by (35). The calculated results for f_1, f_2, and f_3, under the conditions $a/b = 0.5$ and $\beta \in \{0.5, 0, 0.5, 1, 1.5\}$ are plotted in Figures 5, 6, and 7.

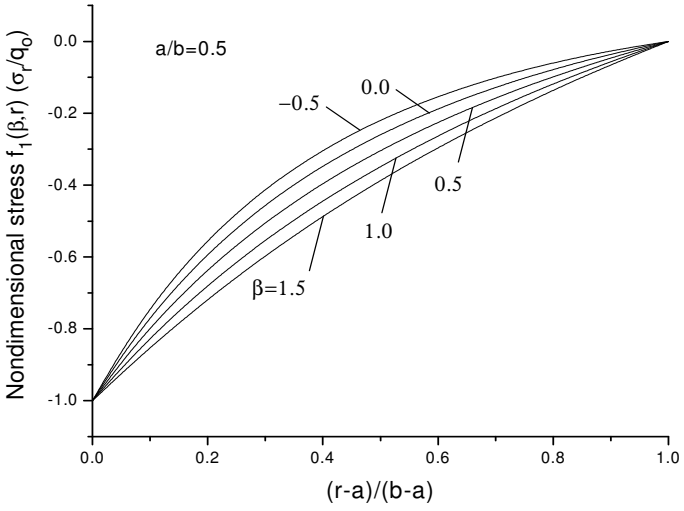

Figure 5. Nondimensional radial stress $f_1(\beta, r)$, for the σ_r component in the cylinder, with $a/b = 0.5$, inner pressure q_0, and $E(r) = E_0[1 + (e^\beta - 1)(r-a)/(b-a)]$ (see (35) and Figure 1).

In Example 1, for $\beta = 1.5$, we have $f_3 = 1.7283$, 1.3428, and 1.5045, for $(r-a)/(b-a) = 0$, 0.5, and 1.0, respectively. However, in the present example, using Young's modulus of linear distribution, we have $f_3 = 1.5398$, 1.4289, and 1.2626, for $(r-a)/(b-a) = 0$, 0.5, and 1.0, respectively (from Figure 7). The stress distribution in the present case is slightly better than that in Example 1.

In both examples $E(r)|_{r=a} = E_0$ and $E(r)|_{r=b} = E_0 \exp\beta$, Figures 2–4 and Figures 5–7 have similar shapes.

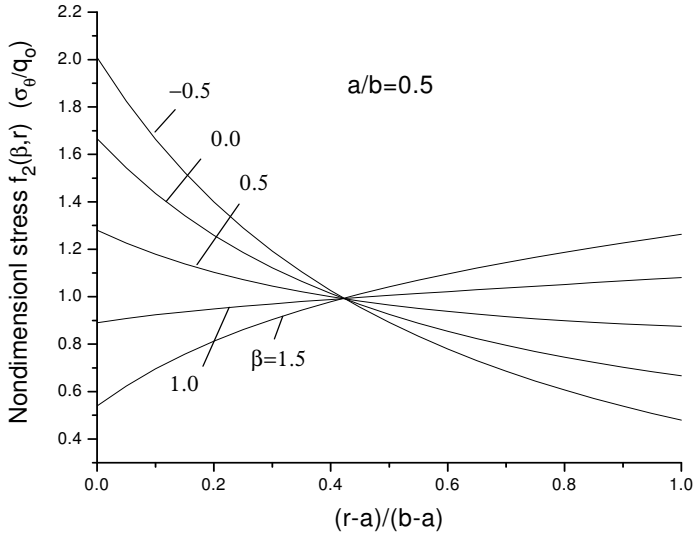

Figure 6. Nondimensional circumferential stress $f_2(\beta, r)$, for the σ_θ component in the cylinder, with $a/b = 0.5$, inner pressure q_0, and $E(r) = E_0[1 + (e^\beta - 1)(r-a)/(b-a)]$ (see (35) and Figure 1).

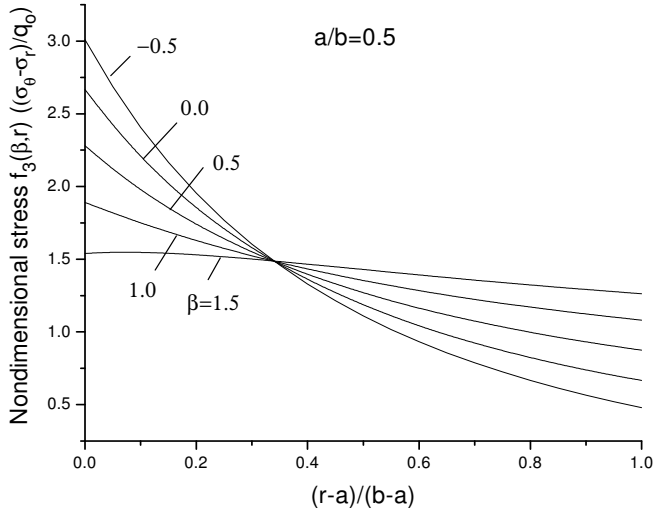

Figure 7. Nondimensional stress $f_3(\beta, r)$, for the $\sigma_e = \sigma_\theta - \sigma_r$ component in the cylinder, with $a/b = 0.5$, inner pressure q_0, and $E(r) = E_0[1 + (e^\beta - 1)(r-a)/(b-a)]$ (see (35) and Figure 1).

3. Solution for multiply-layered cylinder using the transfer matrix method

Based on the concept of the transfer matrix, a solution for multiply-layered cylinder is introduced below.

3.1. ***Procedure for the solution of multiply-layered cylinder using the transfer matrix method.*** The formulation for a cylinder with three layers is introduced below. The cylinder is composed of three layers along the intervals $a_j \le r \le b_j$ $(j = 1, 2, 3)$ (see Figure 8). In each layer, the Young's elastic modulus is assumed as follows:

$$E^{(j)}(r) = E_0^{(j)} \exp[\beta_j (r - a_j)/c], \quad a_j \le r \le b_j \quad (j = 1, 2, 3, \text{ with } c = b - a), \tag{36}$$

where $E_0^{(j)}$ and β_j $(j = 1, 2, 3)$ are given beforehand.

In derivation, the boundary values at the initial point for j-th layer $(j = 1, 2, 3)$ are denoted by $\sigma_{r,\text{in}}^{(j)}, u_{\text{in}}^{(j)}$, and at the end point by $\sigma_{r,\text{end}}^{(j)}, u_{\text{end}}^{(j)}$ $(j = 1, 2, 3)$ (see Figure 5). Clearly, the continuation condition between layers can be expressed in the form

$$\sigma_{r,\text{end}}^{(j)} = \sigma_{r,\text{in}}^{(j+1)}, \quad u_{\text{end}}^{(j)} = u_{\text{in}}^{(j+1)} \quad (j = 1, 2). \tag{37}$$

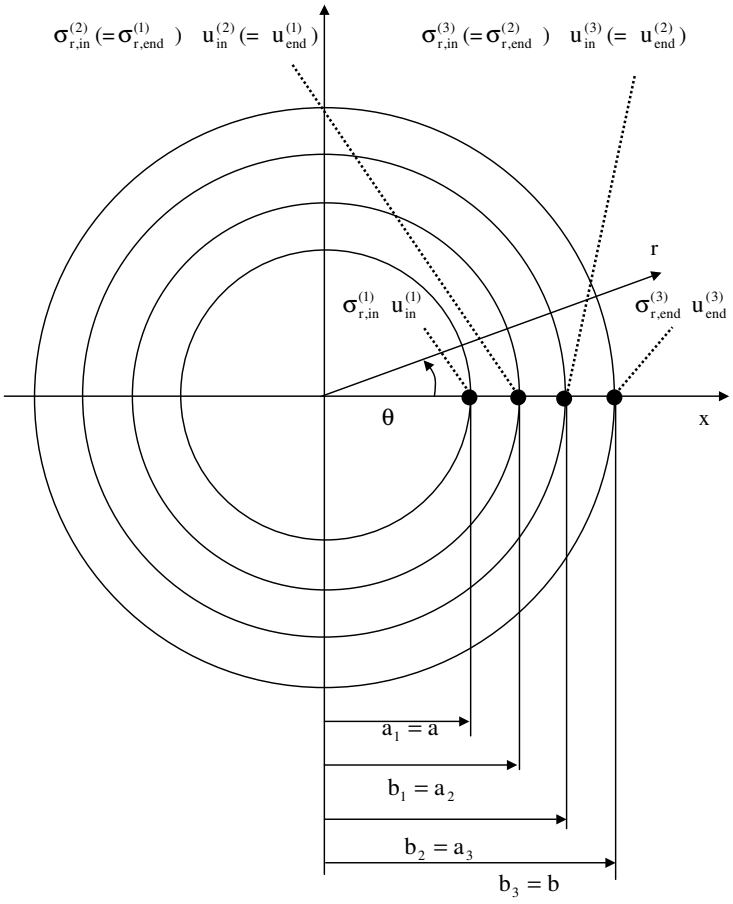

Figure 8. A cylinder with three layers.

In addition, the relevant matrices are denoted by $\boldsymbol{Q}^{(j)}$, $\boldsymbol{P}^{(j)}$, and $\boldsymbol{M}^{(j)}$ $(j = 1, 2, 3)$ — see (24) (29), (31), and (32) — and the coefficients before the fundamental solutions by $c_1^{(j)}$ and $c_2^{(j)}$ — (21).

From the analysis in the single-layer case, or from (31), we have

$$\{\sigma_{r,\text{end}}^{(j)} \;\; u_{\text{end}}^{(j)}\}^T = \boldsymbol{M}^{(j)} \{\sigma_{r,\text{in}}^{(j)} \;\; u_{\text{in}}^{(j)}\}^T \quad (j = 1, 2, 3). \tag{38}$$

It is preferable to write (38) in the form

$$\sigma_{r,\text{end}}^{(1)} = \sigma_{r,\text{in}}^{(2)} = M_{11}^{(1)}\sigma_{r,\text{in}}^{(1)} + M_{12}^{(1)}u_{\text{in}}^{(1)}, \qquad u_{\text{end}}^{(1)} = u_{\text{in}}^{(2)} = M_{21}^{(1)}\sigma_{r,\text{in}}^{(1)} + M_{22}^{(1)}u_{\text{in}}^{(1)}, \tag{39}$$

$$\sigma_{r,\text{end}}^{(2)} = \sigma_{r,\text{in}}^{(3)} = M_{11}^{(2)}\sigma_{r,\text{in}}^{(2)} + M_{12}^{(2)}u_{\text{in}}^{(2)}, \qquad u_{\text{end}}^{(2)} = u_{\text{in}}^{(3)} = M_{21}^{(2)}\sigma_{r,\text{in}}^{(2)} + M_{22}^{(2)}u_{\text{in}}^{(2)}, \tag{40}$$

$$\sigma_{r,\text{end}}^{(3)} = M_{11}^{(3)}\sigma_{r,\text{in}}^{(3)} + M_{12}^{(3)}u_{\text{in}}^{(3)}, \qquad u_{\text{end}}^{(3)} = M_{21}^{(3)}\sigma_{r,\text{in}}^{(3)} + M_{22}^{(3)}u_{\text{in}}^{(3)}. \tag{41}$$

From (39)–(41) we see that there are six equations with eight arguments: $\sigma_{r,\text{in}}^{(1)}$, $u_{\text{in}}^{(1)}$, $\sigma_{r,\text{in}}^{(2)}$, $u_{\text{in}}^{(2)}$, $\sigma_{r,\text{in}}^{(3)}$, $u_{\text{in}}^{(3)}$, $\sigma_{r,\text{end}}^{(3)}$, and $u_{\text{end}}^{(3)}$.

When the three-layered cylinder subjected to an inner pressure with intensity q_0 (at $r = a_1 = a$) and the outer boundary is traction free (at $r = b_3 = b$), the following boundary value problem is formulated:

$$\sigma_{r,\text{in}}^{(1)} = -q_0, \quad \sigma_{r,\text{end}}^{(3)} = 0 \quad (\text{or } \sigma_{r,a} = -q_0, \sigma_{r,b} = 0). \tag{42}$$

Substituting this condition into (39), we will obtain a solution for six unknowns $u_{\text{in}}^{(1)}$, $\sigma_{r,\text{in}}^{(2)}$, $u_{\text{in}}^{(2)}$, $\sigma_{r,\text{in}}^{(3)}$, $u_{\text{in}}^{(3)}$, and $u_{\text{end}}^{(3)}$ from the six algebraic equations (39)–(41). In addition, from (24), we have

$$\{c_1^{(j)} \;\; c_2^{(j)}\}^T = \boldsymbol{Q}^{(j)} \{\sigma_{r,a}^{(j)} \;\; u_a^{(j)}\}^T \quad (j = 1, 2, 3). \tag{43}$$

Finally, the undetermined coefficients $c_1^{(j)}$ and $c_2^{(j)}$ $(j = 1, 2, 3)$ before the fundamental solutions are obtained. This means that the final solution is obtained.

Clearly, if the boundary condition is different from the one in (42), the problem can be solved in a similar manner.

3.2. *Numerical example for three-layered cylinder.*

Example 3. In Example 1, the case of $\beta = 1.5$ can provide a better distribution for the stress component $\sigma_e = \sigma_\theta - \sigma_r$. In the present example, a modification for this case is carried out. For the case of three layers, the Young's elastic modulus is assumed as follows (see Figure 8):

$$E^{(1)}(r) = E_0 \exp \frac{\beta(1-\alpha)(r-a_1)}{c} \qquad (a_1 \le r \le b_1, \text{ with } c = b - a), \tag{44a}$$

$$E^{(2)}(r) = E_0^{(2)} \exp \frac{\beta(r-a_2)}{c} \qquad (a_2 \le r \le b_2), \tag{44b}$$

$$E^{(3)}(r) = E_0^{(3)} \exp \frac{\beta(1+\alpha)(r-a_3)}{c} \qquad (a_3 \le r \le b_3), \tag{44c}$$

where $a_1 = a$, $a_2 = b_1 = (2a + b)/3$, $a_3 = b_2 = (a + 2b)/3$, and $b_3 = b$. In (44), the factor α represents a modification to the case shown by (5).

From the continuation condition for $E^{(j)}(r)$ $(j = 1, 2, 3)$, at $r = a_2$ and $r = a_3$, we find

$$E_0^{(2)} = E_0 \exp \frac{\beta(1-\alpha)}{3}, \quad E_0^{(3)} = E_0 \exp \frac{\beta(2-\alpha)}{3}. \tag{45}$$

When the three-layered cylinder is subjected to an inner pressure with intensity q_0 (at $r = a_1 = a$) and the outer boundary is traction free (at $r = b_3 = b$), the following boundary value problem is formulated:

$$\sigma_{r,\text{in}}^{(1)} = -q_0, \quad \sigma_{r,\text{end}}^{(3)} = 0 \quad (\text{or } \sigma_{r,a} = -q_0 \text{ at } r = a,\ \sigma_{r,b} = 0 \text{ at } r = b). \tag{46}$$

The procedure for the solution has been suggested in the last section. In the computation, we choose $a/b = 0.5$, $\beta = 1.5$, and $\alpha \in \{-0.5, -0.25, 0, 0.25, 0.5\}$. The assumed Young's modulus is denoted by

$$E(r) = h(\beta, \alpha, r)E_0. \tag{47}$$

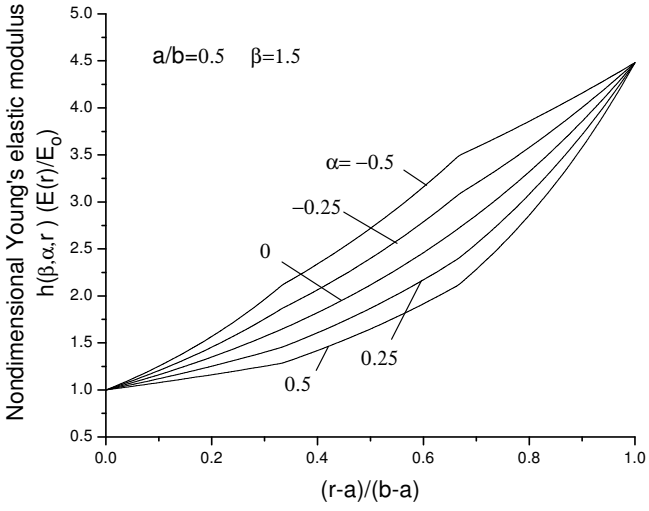

Figure 9. Young's elastic modulus $h(\beta, \alpha, r)$ $(E(r)/E_0)$ (see (44), (45), (47), and Figure 8).

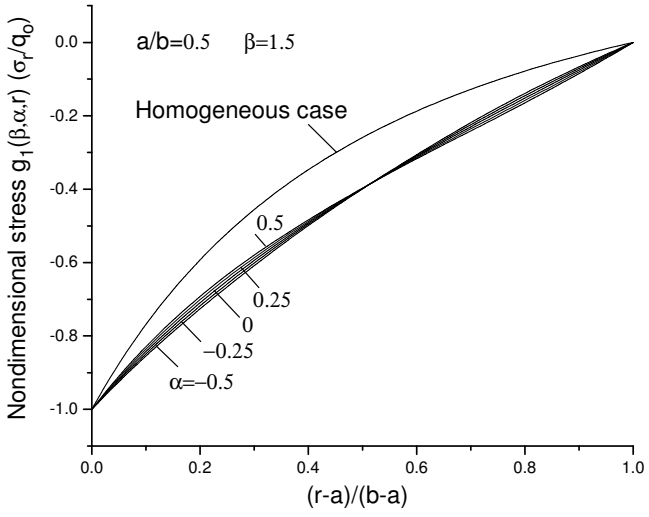

Figure 10. Nondimensional radial stress $g_1(\beta, \alpha, r)$, for the σ_r component in a three-layer cylinder, with $a/b = 0.5$ and $\sigma_{r,a} = -q_0$, $\sigma_{r,b} = 0$ (see (48) and Figure 8).

In addition, the computed stresses are expressed by

$$\sigma_r = g_1(\beta, \alpha, r)q_0, \quad \sigma_\theta = g_2(\beta, \alpha, r)q_0, \quad \sigma_e = \sigma_\theta - \sigma_r = g_3(\beta, \alpha, r)q_0 \quad (g_3 = g_2 - g_1). \tag{48}$$

The function $h(\beta, \alpha, r)$ and the computed $g_1(\beta, \alpha, r)$, $g_2(\beta, \alpha, r)$, and $g_3(\beta, \alpha, r)$ are plotted in Figures 9–12. For the homogeneous case of the Young's modulus or $\beta = 0$, the relevant results are also plotted in those figures.

It is seen from Figure 12 that the condition of $\beta = 1.5$ and $\alpha = -0.5$ can provide a better distribution for the σ_e component. In fact, in the homogeneous case ($\beta = 0$), we have $\sigma_e = 0.6667$ at $r = a$, and

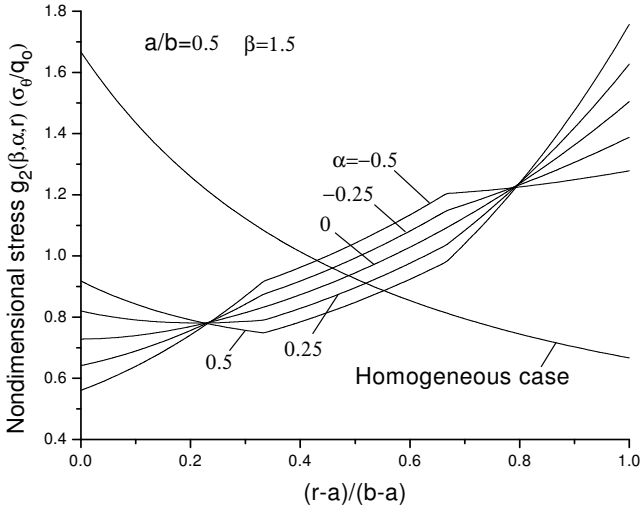

Figure 11. Nondimensional circumferential stress $g_2(\beta, \alpha, r)$, for the σ_θ component in a three-layer cylinder, with $a/b = 0.5$ and $\sigma_{r,a} = -q_0$, $\sigma_{r,b} = 0$ (see (48) and Figure 8).

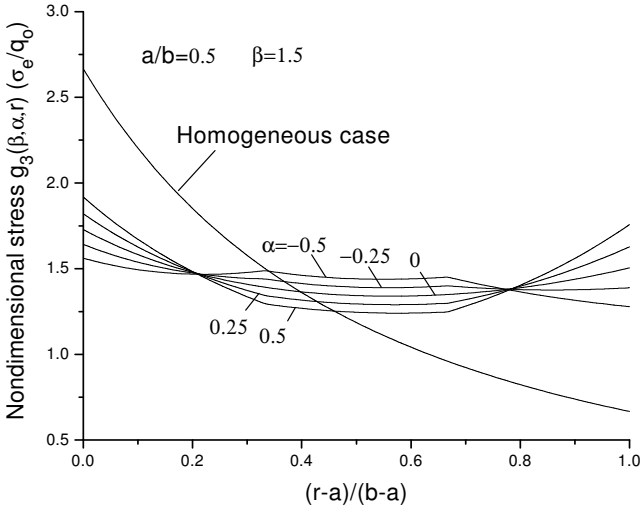

Figure 12. Nondimensional stress $g_3(\beta, \alpha, r)$, for the $\sigma_e = \sigma_\theta - \sigma_r$ component in a cylinder of three layers, with $a/b = 0.5$ and $\sigma_{r,a} = -q_0$, $\sigma_{r,b} = 0$ (see (48) and Figure 8).

$\frac{r-a}{b-a}$	N	$\alpha=-0.5$	$\alpha=-0.25$	$\alpha=0$	$\alpha=0.25$	$\alpha=0.5$
1/6	40	0.7050683358	0.7319400382	0.7577991468	0.7825211369	0.8059881607
1/6	120	0.7050683357	0.7319400381	0.7577991467	0.7825211368	0.8059881604
1/6	200	0.7050683357	0.7319400381	0.7577991467	0.7825211368	0.8059881604
1/2	40	1.0416074339	0.9931088747	0.9446411237	0.8963340949	0.8483207310
1/2	120	1.0416074337	0.9931088746	0.9446411236	0.8963340948	0.8483207308
1/2	200	1.0416074337	0.9931088746	0.9446411236	0.8963340948	0.8483207308
5/6	40	1.2327192411	1.2559360854	1.2771271334	1.2961108296	1.3127162028
5/6	120	1.2327192410	1.2559360853	1.2771271333	1.2961108295	1.3127162025
5/6	200	1.2327192410	1.2559360853	1.2771271333	1.2961108295	1.3127162025

Table 1. Comparison results for nondimensional radial stress $g_2(\beta, \alpha, r)$, for the σ_θ component in a three-layer cylinder, with $a/b = 0.5$, $\beta = 1.5$, and $\sigma_{r,a} = -q_0$, $\sigma_{r.b} = 0$, and various numbers N of intervals used in the integration. See (48) and Figure 8.

$\sigma_e = 2.6667$ at $r = b$. Thus, the ratio $\sigma_e|_{r=b}/\sigma_e|_{r=a} = 0.25$ is achieved. That is to say, the outer boundary has too high a safety factor when σ_e at the inner boundary point reaches its limit value. However, under condition $\beta = 1.5$ and $\alpha = -0.5$, we have $\sigma_e = 1.5609$ at $r = a$, and $\sigma_e = 1.2785$ at $r = b$. In this case, the relative ratio is $\sigma_e|_{r=b}/\sigma_e|_{r=a} = 0.8087$.

To gauge the accuracy of the computations, some results for $g_2(\beta, \alpha, r)$ ($\sigma_e = q_0$) were calculated using $N = 40$, 120, and 200 divisions in the integration. They are listed in Table 1, where we see that even 40 divisions suffice to give an accuracy of nine decimals. The choice $N = 200$ was far beyond the necessary divisions for providing accurate results.

Example 4. In this example, all parameters, E_0, β, α, $a_1 = a$, $a_2 = b_1 = (2a+b)/3$, $a_3 = b_2 = (a+2b)/3$, and $b_3 = b$, are the same as those used in Example 1. However, the following boundary condition is

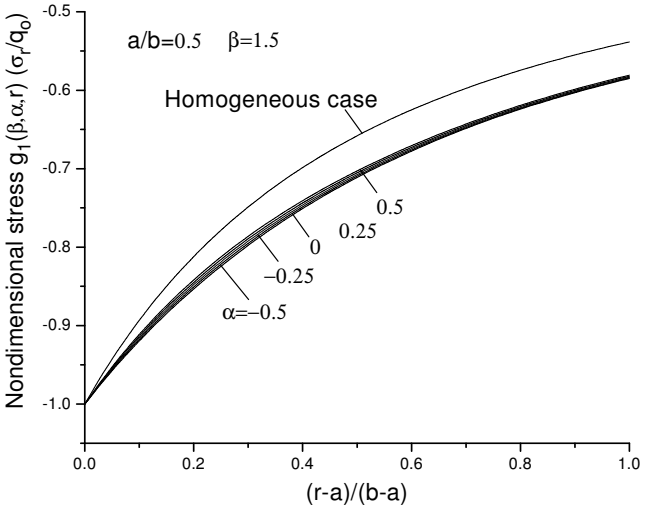

Figure 13. Nondimensional radial stress $g_1(\beta, \alpha, r)$, for the σ_r component in a three-layer cylinder, with $a/b = 0.5$ and $\sigma_{r,a} = -q_0$, $u_b = 0$ (see (48) and Figure 8).

assumed:

$$\sigma_{r,\text{in}}^{(1)} = -q_0, \quad u_{\text{end}}^{(3)} = 0 \quad (\text{or } \sigma_{r,a} = -q_0 \text{ at } r = a, \quad u_b = 0 \text{ at } r = b). \tag{49}$$

In this case, substituting $\sigma_{r,\text{in}}^{(1)} = -q_0$, $u_{\text{end}}^{(3)} = 0$, into (39), we have a solution for $u_{\text{in}}^{(1)}$, $\sigma_{r,\text{in}}^{(2)}$, $u_{\text{in}}^{(2)}$, $\sigma_{r,\text{in}}^{(3)}$, $u_{\text{in}}^{(3)}$, and $\sigma_{r,\text{end}}^{(3)}$. The further steps are the same as in Example 3.

In computation, we choose $a/b = 0.5$, $\beta = 1.5$, $\alpha = -0.50, -0.25, 0, 0.25$ and 0.5. The assumed Young's modulus $E(r) = h(\beta, \alpha, r)E_0$ is same as shown by (47). The computed stresses $\sigma_r = g_1(\beta, \alpha, r)q_0$, $\sigma_\theta = g_2(\beta, \alpha, r)q_0$, $\sigma_e = \sigma_\theta - \sigma_r = g_3(\beta, \alpha, r)q_0$ ($g_3 = g_2 - g_1$), are still expressed by (48).

The function $h(\beta, \alpha, r)$ is the same as plotted in Figure 9. The computed $g_1(\beta, \alpha, r)$, $g_2(\beta, \alpha, r)$, and $g_3(\beta, \alpha, r)$ are plotted in Figures 13–15.

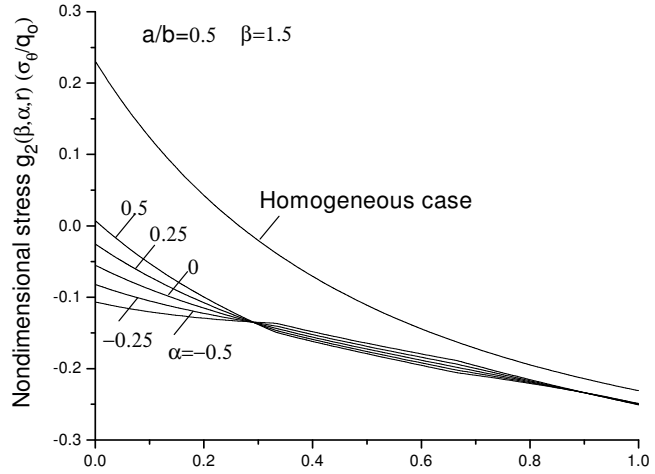

Figure 14. Nondimensional circumferential stress $g_2(\beta, \alpha, r)$, for the σ_θ component in a three-layer cylinder, with $a/b = 0.5$ and $\sigma_{r,a} = -q_0$, $u_b = 0$ (see (48) and Figure 5).

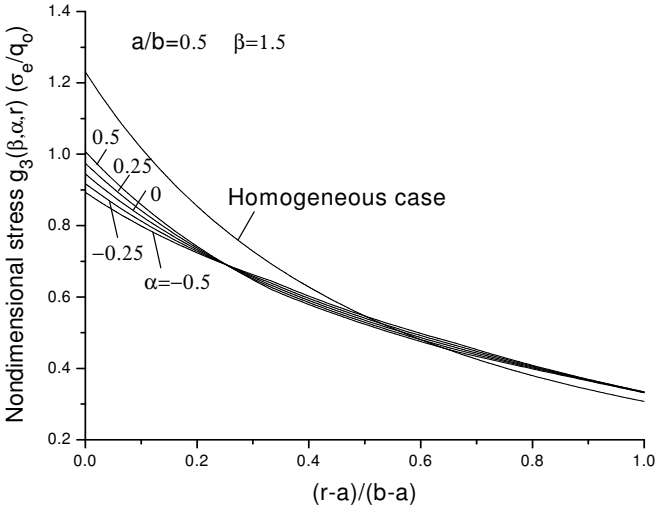

Figure 15. Nondimensional stress $g_3(\beta, \alpha, r)$, for the $\sigma_e = \sigma_\theta - \sigma_r$ component in a cylinder of three layers, with $a/b = 0.5$ and $u_b = 0$, $\sigma_{r,b} = 0$ (see (48) and Figure 5).

It is seen from Figure 15 that the condition $\beta = 1.5$ and $\alpha = -0.5$ can provide a better distribution for the σ_e component. In fact, in the homogeneous case (or $\beta = 0$), we have $\sigma_e = 1.2308$ at $r = a$, and $\sigma_e = 0.3077$ at $r = b$. Thus, the ratio $\sigma_e|_{r=b}/\sigma_e|_{r=a} = 0.25$ is achieved. That is to say, the outer boundary has too much safety factor when σ_e at the inner boundary point reaches its limit value. However, under the condition $\beta = 1.5$ and $\alpha = -0.5$, we have $\sigma_e = 0.8934$ at $r = a$, and $\sigma_e = 0.3343$ at $r = b$. In this case, the relative ratio is $\sigma_e|_{r=b}/\sigma_e|_{r=a} = 0.3742$.

However, in Example 4, the improvement for the σ_e component is not as much as in Example 3. For example, we have $\sigma_e|_{r=b}/\sigma_e|_{r=a} = 0.8087$ and 0.3742 in Examples 3 and 4, respectively, which can be seen from Figures 12 and 15.

4. Conclusion

The transfer matrix method provides an effective way to solve the problem of a multiply-layered cylinder of functionally graded materials (FGMs). In fact, the transfer matrix for the j-th layer links the radial stress and displacement at the initial point to those at the end point of the layer. Those matrices for all layers can be computed and prepared beforehand, and are obtained from two fundamental solutions. After linking all matrices and considering the continuation condition between layers and the boundary conditions, the original problem is solved. In the formulation, the Young's modulus can be arbitrary for the individual layer. In addition, the solution of the mixed boundary value problem is easy to evaluate.

The merit of the suggested method can be expressed alternatively. In fact, the differential operator defined in the left hand of (8) has the following property:

$$\Lambda(cs(r)) = c\Lambda(s(r)) \quad (c \text{ is a constant}). \tag{50}$$

Therefore, if $s_1(r)$ and $s_2(r)$ are two solutions of the ordinary differential equation

$$\Lambda(s(r)) = 0, \tag{51}$$

the function $s(r) = c_1 s_1(r) + c_2 s_2(r)$ must be a solution of (51). Clearly, the suggested solutions $s_1(r)$ and $s_2(r)$ are the solutions from two particular initial conditions. Once the two constants c_1 and c_2 are appropriately assumed, the boundary condition at the end point ($r = b$) will be satisfied. That is to say, the boundary value problem of the ordinary differential equation is changed into the initial boundary value problem.

It is found from the computed results that the influence of the inhomogeneity from FGMs on the stress distribution is significant. From the theory of strength of materials, the stress component $\sigma_e = \sigma_\theta - \sigma_r$ is an appropriate value to predict the component's safety. From Figure 4, we see that a higher value of β, for example $\beta = 1.5$ can provide a better distribution for σ_e. Alternatively speaking, if the outer layer ($r = b$) is more rigid, the safe condition of cylinder is better.

References

[Batra and Iaccarino 2008] R. C. Batra and G. L. Iaccarino, "Exact solutions for radial deformations of a functionally graded isotropic and incompressible second-order elastic cylinder", *Int. J. Non-Linear Mech.* **43**:5 (2008), 383–398.

[Chen and Lin 2008] Y. Z. Chen and X. Y. Lin, "Elastic analysis for thick cylinders and spherical pressure vessels made of functionally graded materials", *Comput. Mater. Sci.* **44**:2 (2008), 581–587.

[Dryden and Jayaraman 2006] J. Dryden and K. Jayaraman, "Effect of inhomogeneity on the stress in pipes", *J. Elasticity* **83**:2 (2006), 179–189.

[Erdogan and Wu 1997] F. Erdogan and B. H. Wu, "The surface crack problem for a plate with functionally graded properties", *J. Appl. Mech.* (*ASME*) **64**:3 (1997), 449–456.

[Eslami et al. 2005] M. R. Eslami, M. H. Babaei, and R. Poultangari, "Thermal and mechanical stresses in a functionally graded thick sphere", *Int. J. Pres. Ves. Pip.* **82**:7 (2005), 522–527.

[Fotuhi and Fariborz 2006] A. R. Fotuhi and S. J. Fariborz, "Anti-plane analysis of a functionally graded strip with multiple cracks", *Int. J. Solids Struct.* **43**:5 (2006), 1239–1252.

[Hildebrand 1974] F. B. Hildebrand, *Introduction to numerical analysis*, 2nd ed., McGraw-Hill, New York, 1974.

[Horgan and Chan 1999a] C. O. Horgan and A. M. Chan, "The pressurized hollow cylinder or disk problem for functionally graded isotropic linearly elastic materials", *J. Elasticity* **55**:1 (1999), 43–59.

[Horgan and Chan 1999b] C. O. Horgan and A. M. Chan, "The stress response of functionally graded isotropic linearly elastic rotating disks", *J. Elasticity* **55**:3 (1999), 219–230.

[Jain et al. 2004] N. Jain, C. E. Rousseau, and A. Shukla, "Crack-tip stress fields in functionally graded materials with linearly varying properties", *Theor. Appl. Fract. Mech.* **42**:2 (2004), 155–170.

[Li and Peng 2009] X.-F. Li and X.-L. Peng, "A pressurized functionally graded hollow cylinder with arbitrarily varying material properties", *J. Elasticity* **96**:1 (2009), 81–95.

[Muskhelishvili 1963] N. I. Muskhelishvili, *Some basic problems of the mathematical theory of elasticity. Fundamental equations, plane theory of elasticity, torsion and bending*, P. Noordhoff, Groningen, 1963.

[Shao 2005] Z. S. Shao, "Mechanical and thermal stresses of a functionally graded circular hollow cylinder with finite length", *Int. J. Pres. Ves. Pip.* **82**:3 (2005), 155–163.

[Shi et al. 2007] Z. Shi, T. Zhang, and H. Xiang, "Exact solutions of heterogeneous elastic hollow cylinders", *Compos. Struct.* **79**:1 (2007), 140–147.

[Theotokoglou and Stampouloglou 2008] E. E. Theotokoglou and I. H. Stampouloglou, "The radially nonhomogeneous elastic axisymmentric problem", *Int. J. Solids Struct.* **45**:25-26 (2008), 6535–6552.

[Timoshenko and Goodier 1970] S. P. Timoshenko and J. N. Goodier, *Theory of elasticity*, McGraw-Hill, New York, 1970.

[Tutuncu 2007] N. Tutuncu, "Stresses in thick-walled FGM cylinders with exponentially-varying properties", *Eng. Struct.* **29**:9 (2007), 2032–2035.

[Tutuncu and Temel 2009] N. Tutuncu and B. Temel, "A novel approach to stress analysis of pressurized FGM cylinders, disks and spheres", *Compos. Struct.* **91**:3 (2009), 385–390.

[You et al. 2005] L. H. You, J. J. Zhang, and X. Y. You, "Elastic analysis of internally pressurized thick-walled spherical pressure vessels of functionally graded materials", *Int. J. Pres. Ves. Pip.* **82**:5 (2005), 347–354.

[Zhang and Hasebe 1999] X. Zhang and N. Hasebe, "Elasticity solution for a radially nonhomogeneous hollow circular cylinder", *J. Appl. Mech.* (*ASME*) **66**:3 (1999), 598–606.

Received 4 Mar 2010. Revised 11 May 2010. Accepted 12 May 2010.

Y. Z. CHEN: chens@ujs.edu.cn
Division of Engineering Mechanics, Jiangsu University, Xue Fu Road 301, Jiangsu, 212013, China

JOURNAL OF MECHANICS OF MATERIALS AND STRUCTURES
Vol. 6, No. 5, 2011

msp

COMPUTATIONAL SHELL MECHANICS BY HELICOIDAL MODELING I: THEORY

TEODORO MERLINI AND MARCO MORANDINI

Starting from recently formulated helicoidal modeling in three-dimensional continua, a low-order kinematical model of a solid shell is established. It relies on both the six degrees of freedom (DOFs) on the reference surface, including the drilling DOF, and a dual director — six additional DOFs — that controls the relative rototranslation of the material particles within the thickness. Since the formulation pertains to the framework of the micropolar mechanics, the solid shell mechanical model includes a workless stress variable — the axial vector of the Biot stress tensor, referred to as the Biot-axial — that allows us to handle nonpolar materials. The local Biot-axial is approximated with a linear field across the thickness and relies on two vector parameters. On the reference surface, the dual director is condensed locally together with one Biot-axial parameter, leaving the surface strains and the other Biot-axial parameter as the basic variables governing the two-dimensional internal work functional.

The continuum-based shell mechanics are cast in weak incremental form from the beginning. They yield the two-dimensional nonlinear constitutive law of the shell in incremental form, built dynamically along the solution process. Poisson thickness locking, related to the low-order kinematical model, is prevented by a dynamical adaptation of the local constitutive law. No hypotheses are introduced that restrict the amplitudes of displacements, rotations, and strains, so the formulation is suitable for computations with strong geometrical and material nonlinearities, as shown in Part II.

1. Introduction

This study belongs to the research field, very prolific in the eighties and nineties, aimed at writing nonlinear shell mechanics with a full and consistent account of the rotation of the material surface particles. In the present decade, however, the scientific community has seemed to desist from seeking a consistent settlement of the drilling rotation and to focus again on more classical approaches to shell mechanics. A recent work by the authors in three-dimensional finite elasticity has motivated a renewed interest in formulations based on an explicit full three-parametric rotation field, which can be addressed now with greater chance of success. Our present contribution to this research field is characterized by, and can be said to be original in, two respects: on the one hand, a total adhesion to a consistent mechanical formulation based on the micropolar description; on the other, the broad usage of an integral kinematic field.

According to the micropolar description, the particle rotations are retained as primary unknowns, even in the case of nonpolar materials. In three-dimensional solid mechanics, variational formulations assuming independent rotation fields were pioneered in [Reissner 1965] and developed in [Fraeijs de

Keywords: nonlinear shell theory, micropolar shell variational mechanics, helicoidal modeling, geometric invariance, shell constitutive equations, finite rotations and rototranslations, dual tensor algebra.

Veubeke 1972; Atluri 1984; Reissner 1984; Bufler 1985; 1995; Atluri and Cazzani 1995]. Then, finite elements were formulated starting, mostly, from the regularized principles proposed in [Hughes and Brezzi 1989] and extended to finite elasticity in [Simo et al. 1992]; see also [Ibrahimbegović and Frey 1995; Sansour et al. 1996]. In such formulations, the rotation is introduced using the polar decomposition theorem of the deformation gradient mostly like an appended constraint equation. Application of these concepts to shell mechanics was pursued by several authors, mainly with the explicit motivation of accommodating the drilling rotation; those principles were applied to either the two-dimensional domain of the shell surface [Gruttmann et al. 1992; Wriggers and Gruttmann 1993; Ibrahimbegović 1994; Zhu and Zacharia 1996], or the three-dimensional domain across the shell thickness [Li and Zhan 2000]. A number of remarkable works were delivered, such as [Chróścielewski et al. 1992; Sansour and Bufler 1992; Sansour and Bednarczyk 1995; Wisniewski 1998]; these works also include important references to the early approaches to finite rotations in shell mechanics. In [Wisniewski and Turska 2000; 2001; 2002] a formulation was proposed with a linear drilling rotation across the thickness to account for in-plane twist. It should be noted that almost all the aforementioned works rely on strain measures of the Biot type instead of the Green type and exploit a full three-parametric rotation tensor, different than the two-parametric one used in the constrained rotation approach [Simo and Fox 1989]. Significant papers on the parameterization of the rotation tensor are [Betsch et al. 1998; Ibrahimbegović et al. 2001; Wang and Thierauf 2001]. Interestingly, in an early paper Badur and Pietraszkiewicz [1986] developed a nonlinear Kirchhoff–Love shell theory from micropolar continuum variational mechanics, which is in spirit similar to our approach, as described next.

Meanwhile, Merlini [1997] proposed a variational formulation for three-dimensional solid mechanics based on a different approach. Starting from micropolar mechanics and invoking a constitutive postulate, three equations governing the mechanics of nonpolar materials, that is, linear balance, angular balance, and internal kinematical constraint, are consistently deduced. Correspondingly, two more variables — the particle rotation and the workless axial vector of the Biot stress tensor, hereafter called the *Biot-axial* — become clearly identified and join the displacement as primary unknown fields. Displacement, rotation, and the Biot-axial are the mixed — and balanced — unknowns of an irreducible variational principle referred to as the internally constrained principle of virtual work of the nonpolar medium. In the continuum-based shell theory proposed in this paper, we adhere to this approach both for the reduction from three-dimensional mechanics and for the subsequent two-dimensional mechanics of the material surface. The local Biot-axial within the shell thickness is retained as a primary unknown, to be solved as a function of an unknown field on the shell surface; then, this Biot-axial parameter surface field is retained as a primary unknown of the material surface mechanics. The drilling DOF, as well as a drilling twist, are implicitly accounted for by this extension to the shell surface of a mechanical formulation consistently based on the micropolar description.

The second important feature that characterizes this work is related to the helicoidal modeling of the continuum. Customarily, the micropolar description relies on two independent and uncoupled fields: the displacements and the rotations. Alternatively, displacements and rotations may be coupled together into a unique comprehensive kinematic field, referred to as the integral field of the rototranslations. This alternative representation of motion is already used nowadays in computational multibody dynamics [Borri et al. 2000], and descends seemingly from the modeling of sections along space-curved beams [Borri and Bottasso 1994]; in either case, however, the rototranslation field is defined over a one-coordinate domain,

the time or a curvilinear abscissa as the case may be. The difficulties inherent in the representation of the rototranslation field over a multicoordinate domain, as in the case of three-dimensional solids, were overcome in [Merlini and Morandini 2004a], who proposed the helicoidal modeling of the continuum as an alternative to the classical Euclidean modeling and provided the relevant variational mechanics. Their work was completed with an original objective interpolation scheme [Merlini and Morandini 2004b] and the formulation of a successful finite element [Merlini and Morandini 2005].

The present shell theory and its numerical implementation resort extensively to helicoidal modeling. First, the three-dimensional solid across the thickness is modeled helicoidally. Though we rely on the simplest scheme, with a constant generalized curvature through the thickness, the resulting low-order solid shell model proves to be quite flexible: the proposed integral kinematic field gives the material particles twelve coupled DOFs, six more than the underlying particle belonging to the shell surface, and this freedom proves advantageous in modeling saddles and buckles. Secondly, the two-dimensional material surface is modeled helicoidally as well — an approach that proves a natural asset with curved shells. Thirdly, the surface elements are interpolated helicoidally, so helping curved and curving low-order elements.

An outline of the proposed formulation follows. In this outline, we sometimes use the words "vector" and "tensor" loosely, to capture the essence of certain objects whose precise nature will become clear when they are introduced rigorously in the body of the paper.

- *Material surface kinematics.* Each material particle of the shell reference surface is identified by an orientation-position tensor $\boldsymbol{A}$ (a total of 6 independent parameters). Deformation of the material surface is described by a kinematical strain field $\boldsymbol{\omega}$ (12 parameters).
- *Solid shell kinematics.* Each material particle of the shell body is identified via a constant-curvature rototranslation along the transverse coordinate from the orientation-position of the parent particle on the material surface. The curvature is related to a 6-parameter vector $\boldsymbol{\theta}$ (referred to as the shell dual director) in such a way that the shell kinematics does not depend on the gradient of $\boldsymbol{\theta}$ on the reference surface; so, the director can be assumed to belong to a piecewise constant field of the material surface. Deformation of the solid shell yields a local kinematical strain depending on the material surface strain field $\boldsymbol{\omega}$ and on the field of the current dual director $\boldsymbol{\theta}'$ (a total of 18 parameters).
- *Solid shell mechanics.* From the internally constrained principle of virtual work [Merlini and Morandini 2005], the term of the internal work is considered; this term, for a hyperelastic nonpolar material, is a function of the local strain and of the local Biot-axial stress. The latter is assumed to be linear across the shell thickness, with the vector $\hat{\boldsymbol{\tau}}$ as the constant part and the vector $\hat{\boldsymbol{\mu}}$ controlling the linear part. So, the internal work virtual functional is finally a function of $\boldsymbol{\omega}$, $\boldsymbol{\theta}'$, $\hat{\boldsymbol{\tau}}$, and $\hat{\boldsymbol{\mu}}$ (a total of 24 parameters on the reference surface domain), and of the relevant virtual variation variables. Linearization of the virtual functional yields the virtual tangent functional, a function of the incremental variation variables, too.
- *Reduction to shell surface mechanics.* The integral, over the shell thickness, of the volume density of the internal work functionals gives the relevant surface densities. In such expressions, some quantities work-conjugate to $\boldsymbol{\omega}$ are found, as well as some quantities work-conjugate to $\boldsymbol{\theta}'$, $\hat{\boldsymbol{\tau}}$, and $\hat{\boldsymbol{\mu}}$; also, the tangent operators mapping the incremental variation variables on the incremental work-conjugate fields are found. All such integral quantities are nonlinear functions of the unknown surface fields,

and are meant to be computed dynamically by numerical quadrature during the whole shell problem solution.

- *Shell constitutive equations.* The shell director $\boldsymbol{\theta}'$ and the Biot-axial parameter $\hat{\boldsymbol{\mu}}$ are recognized to be local surface variables. From the incremental form of the internal work virtual functional, the equations to solve the local incremental variations for the remaining incremental variations can be written. The main surface problem is statically condensed to a form where only the variation variables relevant to $\boldsymbol{\omega}$ and $\hat{\boldsymbol{\tau}}$ appear (a total of 15 parameters). In this form, we may recognize the true stress resultants work-conjugate to the component vectors of the material surface strain $\boldsymbol{\omega}$ and the integrated form of the polar decomposition theorem work-conjugate to the Biot-axial parameter $\hat{\boldsymbol{\tau}}$, as well as the relevant tangent operators. It will be shown that the former integrals represent the shell constitutive equations and the kinematical constraint of the material surface, and the latter integrals the associated tangent map.
- *Shell finite element.* The internally constrained principle of virtual work is finally stated for the material surface in its incremental form, using as internal work contributions the functionals discussed above. Then, this principle is approximated by the finite element method and a four-node quadrilateral shell element is formulated in a similar way to the eight-node hexahedral solid element in [Merlini and Morandini 2005]. The kinematic field is modeled by the helicoidal interpolation between the six-DOF nodes and the Biot-axial parameter is assumed uniform over the element domain.

The whole formulation is computation oriented. A sound variational formulation is applied to the solid shell body and the weak form of the nonlinear governing equations is written in the incremental form from the beginning. The approximation of the solid mechanics is of the finite element type, but is performed in two separate steps: first, a helicoidal model is used through the thickness and a numerical integration reduces the problem to a two-dimensional one; then, a helicoidal nonlinear interpolation is used on the element surface to bring the problem to a discrete form. The numerical integration across the thickness is performed at the quadrature points of the surface element. The surface problem is statically condensed and the local variables $\boldsymbol{\theta}'$ and $\hat{\boldsymbol{\mu}}$ are allocated and updated at the quadrature points themselves. The governing equations of the material surface mechanics are not explicitly written in strong form nor are they necessary to the solution of the shell problem; the stress resultants as well as their derivatives with respect to the material surface strains are computed dynamically during the nonlinear solution process. A vectorial parameterization of the rototranslation and its consistent differentiation allows us to track rotations unrestricted in size.

In the form presented above, however, the solid shell kinematics suffers a serious drawback doomed to impair most shell analyses. The proposed constant-curvature rototranslation model allows for a transverse normal strain that is uniform across the thickness, and is thus inconsistent with the alternate strain induced by the Poisson effect in shell bending; in such circumstances, the so-called Poisson thickness locking manifests, unless the local constitutive law is adjusted for plane-stress; see, for example, [Bischoff and Ramm 2000] for an accurate discussion. In order to allow for unmodified three-dimensional constitutive laws, the method of the enhanced assumed strains has been widely used to build effective solid shell elements based on kinematics of the Reissner–Mindlin kind (see, for example, [Büchter et al. 1994; Sansour and Kollmann 2000; Klinkel et al. 2006], among others). Instead, a different approach is followed here,

which also allows for unmodified three-dimensional nonlinear constitutive laws: the transverse normal strain, say ε_{33}, is regarded as a local, independent variable, disjoint from its kinematical counterpart; from the incremental form of the constitutive equation the increment of ε_{33} is solved for the other strain increments and the constitutive equation is condensed locally; ε_{33} is allocated at each quadrature point across the thickness and updated at each iteration. A similar technique was suggested in [de Borst 1991], whereas in [Klinkel and Govindjee 2002] it was proposed to start a separate iterative process to force plane stress at each quadrature point; see also the implementation in [Campello et al. 2003].

The paper is organized as follows. The present article (Part I) begins with an introduction to helicoidal modeling in three-dimensional solids (Section 2). Then, the material surface kinematics are formulated in Section 3, and used in Section 4 to build the solid shell kinematical model. The solid shell mechanics in the incremental form follow in Section 5, which includes the adaptation of the local constitutive law. In Section 6, the integration across the thickness leads to the shell surface mechanics, and the shell constitutive equations are formulated in incremental form. The companion article (Part II) contains the shell element formulation and a broad selection of nonlinear test cases. Index-free notation is favored throughout, but when necessary, Latin indexes are used for components spanning the range 1 to 3, and Greek indexes for the surface components in the range 1 to 2. The Einsteinian rule of implicit summation over repeated indexes is understood.

2. Overview of three-dimensional modeling

A quick introduction to helicoidal modeling is given in this section; for a more comprehensive discussion refer to [Merlini and Morandini 2004a]. According to the polar description in continuum mechanics, a solid body is regarded as a continuum set of infinitesimal yet three-dimensional material particles. We limit ourselves to a special case of polar description, referred to as micropolar description, where the directors embedded within each particle are not allowed to stretch and rotate relative to each other (see, for example, [Kafadar and Eringen 1971; Eringen and Kafadar 1976] and references therein). In that case, the material particles behave as infinitesimal rigid bodies.

2.1. ***Motion of a particle.*** The configuration of a material particle at point P in space is identified by its position and by its orientation. Let's embed a triad of vectors $\boldsymbol{\alpha}_j$ $(j = 1, 2, 3)$ within the particle. With reference to an absolute frame made of an orthonormal triad of dimensionless unit vectors $\boldsymbol{i}_j \equiv \boldsymbol{i}^j$ and to the associated Cartesian axes x^j departing from the origin O, the particle configuration can be measured by the pair $(\boldsymbol{x}, \boldsymbol{\alpha})$ of the position vector $\boldsymbol{x} = x^j \boldsymbol{i}_j$ and the orientation tensor of the embedded triad, $\boldsymbol{\alpha} = \boldsymbol{\alpha}_j \otimes \boldsymbol{i}^j$. Throughout this work, vectors $\boldsymbol{\alpha}_j$ are assumed to be mutually orthogonal unit vectors, so $\boldsymbol{\alpha}$ is an orthogonal tensor itself, namely a rotation from the identity $\boldsymbol{I} = \boldsymbol{i}_j \otimes \boldsymbol{i}^j$. This assumption is not actually necessary, but it greatly simplifies things without losing generality.

Besides this commonly used way of describing the particle configuration, an alternative exists which relies on the coupled pair $(\boldsymbol{\alpha}, \boldsymbol{x} \times \boldsymbol{\alpha})$, where $\boldsymbol{x} \times \boldsymbol{\alpha}$ is the *moment* of the triad $\boldsymbol{\alpha}$ with respect to the origin O, chosen as the *pole*. That the pole is brought to coincide with the absolute origin is just a matter of convenience. The dual algebra helps managing this kind of geometric pairs of vectors and tensors (see, for example, [Angeles 1998] and references therein, or the recent survey [Pennestrì and Stefanelli 2007]). In fact, the pair $(\boldsymbol{\alpha}, \boldsymbol{x} \times \boldsymbol{\alpha})$ is conveniently represented by the dual tensor $\boldsymbol{A} = \boldsymbol{\alpha} + \varepsilon \boldsymbol{x} \times \boldsymbol{\alpha}$, where ε is the dual unity, a number such that $\varepsilon \neq 0$ and $\varepsilon^2 = \varepsilon^3 = \cdots = 0$. A dual tensor, like a dual

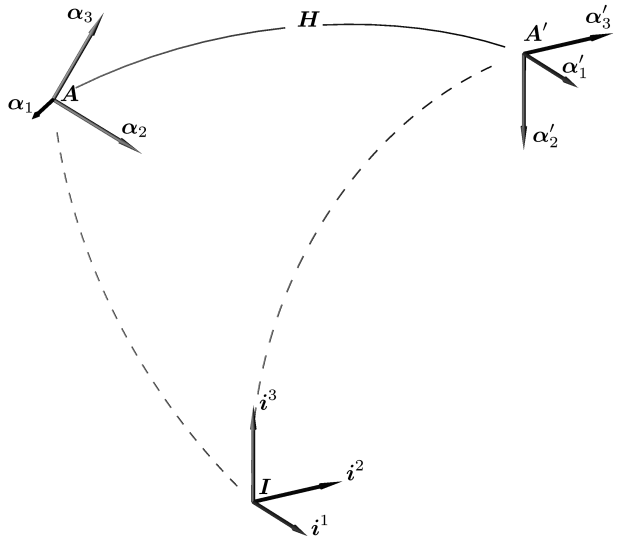

Figure 1. Rototranslation of a particle between the orientopositions in two different configurations.

number, is composed of a primal part plus a dual part multiplied by ε. Note that the dual part is always dimensionally greater than the primal part by a length: within a kinematic context, such parts will be often referred to as the *angular* part and the *linear* part, respectively. The opposite will occur in the cokinematic vector space, where, for example, an applied force-and-couple $(\boldsymbol{f}, \boldsymbol{c})$ shall be represented by a dual vector $\boldsymbol{f} + \varepsilon(\boldsymbol{c} + \boldsymbol{x} \times \boldsymbol{f})$, whose primal part is the linear part (a force) and whose dual part is the angular part (a moment).

The dual tensor

$$\boldsymbol{A} = \boldsymbol{X}\boldsymbol{\alpha} = (\boldsymbol{I} + \varepsilon \boldsymbol{x}\times)\boldsymbol{\alpha} \tag{1}$$

will be called hereafter the *orientoposition* tensor of the material particle. (Here and throughout the paper, the notation $\boldsymbol{v}\times$ denotes a skew-symmetric tensor having $\boldsymbol{v}$ as axial vector. It transforms a vector $\boldsymbol{w}$ into the vector $\boldsymbol{v} \times \boldsymbol{w}$.) In the factorization (1) of $\boldsymbol{A}$, the tensor $\boldsymbol{X}$ is called the dual position tensor and is easily seen to be orthogonal: $\boldsymbol{X}^{-1} = \boldsymbol{I} - \varepsilon \boldsymbol{x}\times = \boldsymbol{X}^{\mathrm{T}}$. Therefore, $\boldsymbol{A}$ is orthogonal too: $\boldsymbol{A} = \boldsymbol{A}^{-\mathrm{T}}$. (Of course, the alternative form $\boldsymbol{A} = \boldsymbol{\alpha}\boldsymbol{X}^{\circ} = \boldsymbol{\alpha}(\boldsymbol{I} + \varepsilon \boldsymbol{x}^{\circ}\times)$ also holds, with $\boldsymbol{x}^{\circ} = \boldsymbol{\alpha}^{\mathrm{T}}\boldsymbol{x}$.)

When the body moves to a new configuration, the particle's orientoposition changes to, say, $\boldsymbol{A}' = \boldsymbol{X}'\boldsymbol{\alpha}'$; see Figure 1. The particle rotates by $\boldsymbol{\Phi} = \boldsymbol{\alpha}'\boldsymbol{\alpha}^{\mathrm{T}}$ and undergoes a *rototranslation*

$$\boldsymbol{H} = \boldsymbol{A}'\boldsymbol{A}^{\mathrm{T}} = \boldsymbol{X}'\boldsymbol{\Phi}\boldsymbol{X}^{\mathrm{T}}. \tag{2}$$

$\boldsymbol{H}$ is an orthogonal dual tensor too and can be factorized into two orthogonal tensors in sequence, specifically the *rotation* $\boldsymbol{\Phi}$ followed by a *translation* dual tensor $\boldsymbol{T}$,

$$\boldsymbol{H} = \boldsymbol{T}\boldsymbol{\Phi} = (\boldsymbol{I} + \varepsilon \boldsymbol{t}\times)\boldsymbol{\Phi}. \tag{3}$$

Here, $\boldsymbol{t} = \boldsymbol{x}' - \boldsymbol{\Phi}\boldsymbol{x}$ is called the *translation vector*. This vector is different from the displacement $\boldsymbol{u} = \boldsymbol{x}' - \boldsymbol{x} = \boldsymbol{t} + (\boldsymbol{\Phi} - \boldsymbol{I})\boldsymbol{x}$, when the particle rotates; the choice of the term *translation* for $\boldsymbol{t}$ is motivated in [Borri et al. 2000; Merlini and Morandini 2004a].

As orthogonal tensors, both the rotation and the rototranslation can be represented as exponential maps of skew-symmetric tensors:

$$\boldsymbol{\Phi} = \exp(\boldsymbol{\varphi}\times) = \sum_{k=0}^{\infty} \frac{\boldsymbol{\varphi}\times^k}{k!}, \tag{4}$$

$$\boldsymbol{H} = \exp(\boldsymbol{\eta}\times) = \sum_{k=0}^{\infty} \frac{\boldsymbol{\eta}\times^k}{k!}, \tag{5}$$

where $\boldsymbol{\varphi}$ is the rotation vector, and $\boldsymbol{\eta} = \boldsymbol{\varphi} + \varepsilon\,\boldsymbol{\rho}$ is called the *helix* of the rototranslation. Also, $\boldsymbol{T} = \exp(\varepsilon \boldsymbol{t}\times)$.

It is worth noting that the rototranslation inherits all the properties of the rotation. As the latter belongs to the special orthogonal Lie group SO(3), so the former can be shown to belong to a six-dimensional extension of such Lie group [Borri et al. 2000]. In particular, an important issue concerning rotations and rototranslations is their differentiation. It is well known that a *differential rotation vector* $\boldsymbol{\varphi}_\mathrm{d}$ characterizes the differentiation of a rotation tensor, that is, $\mathrm{d}\boldsymbol{\Phi}\boldsymbol{\Phi}^\mathrm{T} = \boldsymbol{\varphi}_\mathrm{d}\times$. Analogously, a *differential helix* $\boldsymbol{\eta}_\mathrm{d} = \boldsymbol{\varphi}_\mathrm{d} + \varepsilon\,\boldsymbol{\rho}_\mathrm{d}$ characterizes the differentiation of the rototranslation tensor, $\mathrm{d}\boldsymbol{H}\boldsymbol{H}^\mathrm{T} = \boldsymbol{\eta}_\mathrm{d}\times$. These differential vectors are connected to the differentiations $\mathrm{d}\boldsymbol{\varphi}$ and $\mathrm{d}\boldsymbol{\eta}$ by means of the differential maps associated to the relevant exponential maps (see [Borri et al. 2000]):

$$\boldsymbol{\varphi}_\mathrm{d} = \boldsymbol{\Gamma}\,\mathrm{d}\boldsymbol{\varphi}, \qquad \boldsymbol{\Gamma} = \mathrm{dexp}(\boldsymbol{\varphi}\times) = \sum_{k=0}^{\infty} \frac{\boldsymbol{\varphi}\times^k}{(k+1)!}, \tag{6}$$

$$\boldsymbol{\eta}_\mathrm{d} = \boldsymbol{\Lambda}\,\mathrm{d}\boldsymbol{\eta}, \qquad \boldsymbol{\Lambda} = \mathrm{dexp}(\boldsymbol{\eta}\times) = \sum_{k=0}^{\infty} \frac{\boldsymbol{\eta}\times^k}{(k+1)!}. \tag{7}$$

Incidentally, the differential mapping tensor $\boldsymbol{\Gamma}$ provides a link between the linear part of the helix and the translation vector, $\boldsymbol{t} = \boldsymbol{\Gamma}\boldsymbol{\rho}$ [Merlini and Morandini 2004b].

Now, let's bring the rototranslation to the infinitesimal limit. The differential of the orientation is described by means of a differential rotation vector, that is, $\mathrm{d}\boldsymbol{\alpha} = \boldsymbol{\varphi}_\mathrm{d} \times \boldsymbol{\alpha}$; analogously, the differential of the orientoposition is described by means of a differential helix, $\mathrm{d}\boldsymbol{A} = \boldsymbol{\eta}_\mathrm{d} \times \boldsymbol{A}$. Recalling the factorized form in (1) and resorting to the property $\boldsymbol{B}\boldsymbol{c}\times = (\boldsymbol{B}\boldsymbol{c}) \times \boldsymbol{B}$, which holds true for any orthogonal tensor $\boldsymbol{B}$, it is easily seen that the angular part of $\boldsymbol{\eta}_\mathrm{d}$ is just $\boldsymbol{\varphi}_\mathrm{d}$ whereas the linear part is given by $\boldsymbol{\rho}_\mathrm{d} = \mathrm{d}\boldsymbol{x} + \boldsymbol{x} \times \boldsymbol{\varphi}_\mathrm{d} = \boldsymbol{\alpha}\mathrm{d}(\boldsymbol{\alpha}^\mathrm{T}\boldsymbol{x})$. This is a remarkable issue, that clearly points out that the tangent space of this rototranslatory motion is controlled by a vectorial pair $(\boldsymbol{\varphi}_\mathrm{d}, \boldsymbol{\rho}_\mathrm{d})$ far different from the pair $(\mathrm{d}\boldsymbol{x}, \boldsymbol{\varphi}_\mathrm{d})$ usually considered in classical mechanics. The differential helix $\boldsymbol{\eta}_\mathrm{d}$ couples intimately the infinitesimal rotations and displacements, with a significant effect in a helicoidally modeled variational context [Merlini and Morandini 2004a], where forces and moments will work for $\boldsymbol{\rho}_\delta$ and $\boldsymbol{\varphi}_\delta$, respectively. Conversely, this coupling feature can also be understood by observing that $\mathrm{d}\boldsymbol{x} = \boldsymbol{\rho}_\mathrm{d} - \boldsymbol{x} \times \boldsymbol{\varphi}_\mathrm{d}$, so both the linear and the angular parts of $\boldsymbol{\eta}_\mathrm{d}$ contribute to the differential of the position. In Figure 2, a finite motion of a particle is shown on two different paths, both with a constant tangent space: on path (a), where displacement is uncoupled from rotation, $\mathrm{d}\boldsymbol{x}$ and $\boldsymbol{\varphi}_\mathrm{d}$ are constant, whereas on the seemingly more natural helicoidal path (b), $\boldsymbol{\varphi}_\mathrm{d}$ and $\boldsymbol{\rho}_\mathrm{d}$ are constant. These aspects of the helicoidal parameterization of motion become quite important in computational mechanics, where the choice of an effective discretization of motion may be crucial.

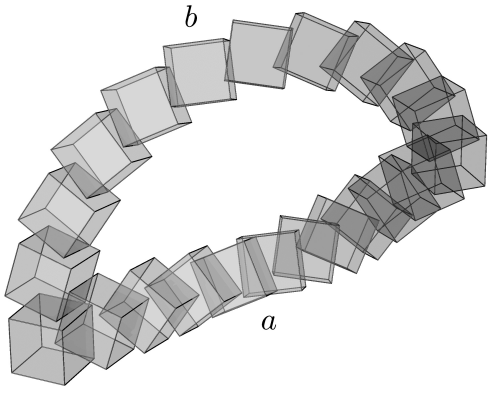

Figure 2. Motion of a particle on two different paths: (a) classical (displacement and rotation are uncoupled); (b) helicoidal.

2.2. ***Helicoidal modeling.*** Helicoidal modeling is the attempt to translate the helicoidal parameterization of motion into the parameterization of the geometry itself of a deformable body at any instant of motion; as a matter of fact, the orientopositions of any two material particles within a body "differ" by a rototranslation. To understand this rewriting, we ought to convert the concept of differentation into the concept of gradient on a three-dimensional field. We shall see that at the limit of an infinitesimal region, the position gradient itself is influenced by the mutual orientations of the neighbor particles. So, the tangent space of the local micropolar geometry can be far different from the classical tangent space proper of a Euclidean modeling.

With reference to a system of convective curvilinear coordinates ξ^j $(j = 1, 2, 3)$ traced within the body, consider the partial derivative $\boldsymbol{A}_{,j} = \partial \boldsymbol{A}/\partial \xi^j$ of the orientoposition field along one coordinate. According to the differentiation formula of orthogonal tensors, $\boldsymbol{A}^{\mathrm{T}}\boldsymbol{A}_{,j} = (\boldsymbol{A}^{\mathrm{T}}\boldsymbol{k}_j)\times$, the derivative $\boldsymbol{A}_{,j}$ is characterized by a dual vector $\boldsymbol{k}_j$ that can be referred to as the (generalized) curvature along that coordinate. The dyadic composition with the metric contravariant base vectors $\boldsymbol{g}^j$ yields the tensorial relation

$$\boldsymbol{A}^{\mathrm{T}}\boldsymbol{A}_{/\otimes} = (\boldsymbol{A}^{\mathrm{T}}\boldsymbol{k})^{\times}, \tag{8}$$

where $(\,)_{/\otimes} = (\,)_{,j} \otimes \boldsymbol{g}^j$ denotes the gradient, $(\,)^{\times} = (\,)_j \times \otimes \boldsymbol{g}^j$ denotes the tensor-cross operator, and $\boldsymbol{k} = \boldsymbol{k}_j \otimes \boldsymbol{g}^j$ is the *curvature* dual tensor. Equation (8) states that the gradient of the orientoposition field, a third-order dual tensor, is characterized by a second-order dual tensor field, the curvature $\boldsymbol{k}$. The tensor-cross operator produces a third-order tensor of skew-symmetric nature; see [Merlini and Morandini 2004a]. Note that, in (8), $\boldsymbol{A}^{\mathrm{T}}\boldsymbol{k}_j$ are the axial vectors of tensors $\boldsymbol{A}^{\mathrm{T}}\boldsymbol{A}_{,j}$, formally $\boldsymbol{A}^{\mathrm{T}}\boldsymbol{k}_j = \mathrm{ax}\,(\boldsymbol{A}^{\mathrm{T}}\boldsymbol{A}_{,j})$, and analogously $\boldsymbol{A}^{\mathrm{T}}\boldsymbol{k}$ is called the axial tensor of third-order tensor $\boldsymbol{A}^{\mathrm{T}}\boldsymbol{A}_{/\otimes}$, formally $\boldsymbol{A}^{\mathrm{T}}\boldsymbol{k} = \mathrm{ax}\,(\boldsymbol{A}^{\mathrm{T}}\boldsymbol{A}_{/\otimes})$.

Using (1) in (8), the dual explicit form of the curvature is easily obtained:

$$\boldsymbol{k} = \boldsymbol{k}_{\mathrm{a}} + \varepsilon\boldsymbol{k}_{\mathrm{l}} = \boldsymbol{\alpha}\,\mathrm{ax}\,(\boldsymbol{\alpha}^{\mathrm{T}}\boldsymbol{\alpha}_{/\otimes}) + \varepsilon\boldsymbol{\alpha}(\boldsymbol{\alpha}^{\mathrm{T}}\boldsymbol{x})_{/\otimes}. \tag{9}$$

The angular part, referred to as the angular curvature, characterizes the gradient of the orientation, $\boldsymbol{\alpha}^{\mathrm{T}}\boldsymbol{\alpha}_{/\otimes} = (\boldsymbol{\alpha}^{\mathrm{T}}\boldsymbol{k}_{\mathrm{a}})^{\times}$, analogously to (8). The linear part is the corotational gradient of the position vector, also given by $\boldsymbol{k}_{\mathrm{l}} = \boldsymbol{x}_{/\otimes} + \boldsymbol{x} \times \boldsymbol{k}_{\mathrm{a}}$. Equation (9) is very important and represents the core of the *helicoidal*

modeling; it allows us to see that $\boldsymbol{k}$, which controls the tangent space of the orientoposition field $\boldsymbol{A}$, couples intimately the spatial derivatives of the orientation with those of the position.

The curvature $\boldsymbol{k}$ is a pole-based dual vector. Changing the pole from O to the point P itself, by means of the arm operator $\boldsymbol{X} = \boldsymbol{I} + \varepsilon \boldsymbol{x}\times$, yields the self-based version of the curvature,

$$\boldsymbol{X}^{\mathrm{T}}\boldsymbol{k} = \boldsymbol{k}_{\mathrm{a}} + \varepsilon\,(\boldsymbol{k}_{\mathrm{l}} - \boldsymbol{x}\times\boldsymbol{k}_{\mathrm{a}}) = \boldsymbol{\alpha}\,\mathrm{ax}\,(\boldsymbol{\alpha}^{\mathrm{T}}\boldsymbol{\alpha}_{/\otimes}) + \varepsilon\boldsymbol{x}_{/\otimes}. \tag{10}$$

Here, the spatial derivatives of orientation and position are disjoint from each other: $\boldsymbol{k}_{\mathrm{a}}$ controls the tangent space of the orientation field whereas $\boldsymbol{x}_{/\otimes}$ represents the tangent space of the classical Euclidean position vector field. It can be seen from (10) that the position vector tangent space is controlled by either part of $\boldsymbol{k}$; in other words, following the concept of a rototranslation-based micropolar description, the orientation field strongly affects the evaluation of neighboring positions.

3. Material surface kinematics

What we mean by *material surface* is a single layer of continuous material particles (infinitesimal yet three-dimensional) lying on a generally curved smooth geometric surface: no particle is allowed to stay out of the surface. Each particle is identified on a two-coordinates domain, spanned by two families of material curvilinear coordinates ξ^α ($\alpha = 1, 2$) traced on the surface. There is no way to define a transversal material coordinate to the surface, nor a material director. The status of the material surface is defined by the two-dimensional field of the positions and orientations of its particles. The particles of a deformable material surface may change their relative distances and orientations, yet they keep on lying on a deformed geometric surface, proper of the current configuration. Since the orientations can change independently from the positions, the mechanism of transverse shear strains is implicitly allowed for. Such an infinitely thin body, also referred to as a Cosserat surface (in [Sansour and Bednarczyk 1995], for example), is the image of a shell-like material solid devoid of thickness.

In this section, we establish the geometry and kinematics of the material surface, using a micropolar description approach in the context of helicoidal modeling (details are found in [Merlini 2008]). In the next section, we will start from the kinematics of the material surface to build the solid shell model, and in Part II we will address the mechanics of the material surface in view of a finite element approximation of the shell.

3.1. ***Reference configuration.*** The reference configuration is identified by the orientoposition dual tensor field $\boldsymbol{A}(\xi^\alpha)$, as defined in (1). Two curvature dual vectors $\boldsymbol{k}_\alpha$ characterize the derivatives of $\boldsymbol{A}$ with respect to the surface coordinates,

$$\boldsymbol{A}^{\mathrm{T}}\boldsymbol{A}_{,\alpha} = (\boldsymbol{A}^{\mathrm{T}}\boldsymbol{k}_\alpha)\times\,. \tag{11}$$

Their explicit dual forms are $\boldsymbol{k}_\alpha = \boldsymbol{k}_{\mathrm{a}\alpha} + \varepsilon\boldsymbol{k}_{\mathrm{l}\alpha} = \boldsymbol{k}_{\mathrm{a}\alpha} + \varepsilon\,(\boldsymbol{x}_{,\alpha} + \boldsymbol{x}\times\boldsymbol{k}_{\mathrm{a}\alpha})$, where vectors $\boldsymbol{k}_{\mathrm{a}\beta}$ characterize the derivatives of the orientation, $\boldsymbol{\alpha}^{\mathrm{T}}\boldsymbol{\alpha}_{,\beta} = (\boldsymbol{\alpha}^{\mathrm{T}}\boldsymbol{k}_{\mathrm{a}\beta})\times$. The relevant self-based versions are $\boldsymbol{X}^{\mathrm{T}}\boldsymbol{k}_\alpha = \boldsymbol{k}_{\mathrm{a}\alpha} + \varepsilon\,(\boldsymbol{k}_{\mathrm{l}\alpha} - \boldsymbol{x}\times\boldsymbol{k}_{\mathrm{a}\alpha}) = \boldsymbol{k}_{\mathrm{a}\alpha} + \varepsilon\boldsymbol{x}_{,\alpha}$.

Two covariant base vectors are obtained as the dual parts of the self-based curvature vectors,

$$\boldsymbol{g}_\alpha = \boldsymbol{x}_{,\alpha} = \mathrm{dual}\,(\boldsymbol{X}^{\mathrm{T}}\boldsymbol{k}_\alpha). \tag{12}$$

We like to think of the coordinates ξ^α as dimensionless measures, so the $\boldsymbol{g}_\alpha$ take physical dimensions of length here. Since we want a solid local triad of base vectors, we conveniently borrow the geometric

unit normal $\boldsymbol{n} = \boldsymbol{g}_1 \times \boldsymbol{g}_2/|\boldsymbol{g}_1 \times \boldsymbol{g}_2|$ to arbitrarily build a third base vector

$$\boldsymbol{g}_3 = h\boldsymbol{n}, \tag{13}$$

where h is an arbitrary length, referred to as the *characteristic length* of the material surface. The dyadic composition of vectors $\boldsymbol{g}_j$ $(j = 1, 2, 3)$ with the absolute unit vectors gives the invertible base frame $\boldsymbol{G} = \boldsymbol{g}_j \otimes \boldsymbol{i}^j$. The reciprocal frame $\boldsymbol{G}^{-\mathrm{T}} = \boldsymbol{g}^j \otimes \boldsymbol{i}_j$ is made of the contravariant base vectors $\boldsymbol{g}^\alpha$ tangent to the surface and of the normal vector $\boldsymbol{g}^3 = h^{-1}\boldsymbol{n}$. Keep in mind, however, that $\boldsymbol{g}_3$ and $\boldsymbol{g}^3$ have nothing to do with material base vectors; they are purely geometric supplementary vectors.

By dyadic composition of (11) with the contravariant base vectors, the definition of the *surface curvature* dual tensor $\boldsymbol{k} = \boldsymbol{k}_\alpha \otimes \boldsymbol{g}^\alpha$ is obtained:

$$\boldsymbol{A}^{\mathrm{T}}\boldsymbol{A}_{/\otimes} = (\boldsymbol{A}^{\mathrm{T}}\boldsymbol{k})^\times, \tag{14}$$

where now $(\,)_{/\otimes} = (\,)_{,\alpha} \otimes \boldsymbol{g}^\alpha$ and $(\,)^\times = (\,)_\alpha \times \otimes \boldsymbol{g}^\alpha$ are the surface gradient and tensor-cross operators. In the explicit dual form of the surface curvature,

$$\boldsymbol{k} = \boldsymbol{\alpha}\,\mathrm{ax}\,(\boldsymbol{\alpha}^{\mathrm{T}}\boldsymbol{\alpha}_{/\otimes}) + \varepsilon\boldsymbol{\alpha}(\boldsymbol{\alpha}^{\mathrm{T}}\boldsymbol{x})_{/\otimes} = \boldsymbol{k}_{\mathrm{a}} + \varepsilon\boldsymbol{k}_{\mathrm{l}} = \boldsymbol{k}_{\mathrm{a}} + \varepsilon(\boldsymbol{x}_{/\otimes} + \boldsymbol{x} \times \boldsymbol{k}_{\mathrm{a}}),$$

it is seen that the angular part is the angular curvature as defined by $\boldsymbol{\alpha}^{\mathrm{T}}\boldsymbol{\alpha}_{/\otimes} = (\boldsymbol{\alpha}^{\mathrm{T}}\boldsymbol{k}_{\mathrm{a}})^\times$, whereas in the linear part there appear the derivatives of both the position and the orientation. Note that, in the self-based version $\boldsymbol{X}^{\mathrm{T}}\boldsymbol{k} = \boldsymbol{k}_{\mathrm{a}} + \varepsilon\boldsymbol{x}_{/\otimes}$, the linear part is the surface position gradient $\boldsymbol{x}_{/\otimes} = \boldsymbol{g}_\alpha \otimes \boldsymbol{g}^\alpha$, which coincides with the projector on the tangent plane, $-\boldsymbol{n} \times \boldsymbol{n} \times = \boldsymbol{I} - \boldsymbol{n} \otimes \boldsymbol{n}$.

3.2. ***Current configuration.*** During the deformation process, the current configuration shall be described in exactly the same way as the reference configuration: the variables pertaining to the current configuration will be denoted by the same symbols as above, followed by an appended prime, $(\,)'$.

So, $\boldsymbol{A}' = \boldsymbol{X}'\boldsymbol{\alpha}' = (\boldsymbol{I} + \varepsilon\boldsymbol{x}' \times)\boldsymbol{\alpha}'$ denotes the current orientoposition; see Figure 3. The derivative relation

$$\boldsymbol{A}'^{\mathrm{T}}\boldsymbol{A}'_{/\otimes} = (\boldsymbol{A}'^{\mathrm{T}}\boldsymbol{k}')^\times \tag{15}$$

defines the *current surface curvature* dual tensor $\boldsymbol{k}' = \boldsymbol{k}'_\alpha \otimes \boldsymbol{g}^\alpha = \boldsymbol{k}'_{\mathrm{a}} + \varepsilon\boldsymbol{k}'_{\mathrm{l}} = \boldsymbol{k}'_{\mathrm{a}} + \varepsilon(\boldsymbol{x}'_{/\otimes} + \boldsymbol{x}' \times \boldsymbol{k}'_{\mathrm{a}})$. Vectors $\boldsymbol{g}'_\alpha = \boldsymbol{x}'_{,\alpha} = \mathrm{dual}\,(\boldsymbol{X}'^{\mathrm{T}}\boldsymbol{k}'_\alpha)$ are the first two current covariant base vectors and $\boldsymbol{g}'_3 = h\boldsymbol{n}'$ (with h the material surface characteristic length) is assumed to be the third one. Vectors $\boldsymbol{g}'_j$ $(j = 1, 2, 3)$ form the current base frame $\boldsymbol{G}' = \boldsymbol{g}'_j \otimes \boldsymbol{i}^j$. In the self-based version of the current curvature, that is, $\boldsymbol{X}'^{\mathrm{T}}\boldsymbol{k}' = \boldsymbol{k}'_{\mathrm{a}} + \varepsilon\boldsymbol{x}'_{/\otimes}$, the linear part is the current surface position gradient $\boldsymbol{x}'_{/\otimes} = \boldsymbol{g}'_\alpha \otimes \boldsymbol{g}^\alpha$. Tensor $\boldsymbol{x}'_{/\otimes}$ differs from the three-dimensional deformation gradient $\boldsymbol{F} = \boldsymbol{g}'_j \otimes \boldsymbol{g}^j$ (the invertible tensor that transforms $\boldsymbol{G}$ to $\boldsymbol{G}' = \boldsymbol{F}\boldsymbol{G}$); in fact, $\boldsymbol{F} = \boldsymbol{x}'_{/\otimes} + \boldsymbol{n}' \otimes \boldsymbol{n}$.

The rototranslation field $\boldsymbol{H}(\xi^\alpha)$ from the reference configuration represents a meaningful alternative choice of the unknowns that define the current configuration,

$$\boldsymbol{A}' = \boldsymbol{H}\boldsymbol{A}. \tag{16}$$

Expressions for the tensor $\boldsymbol{H}$ are found in (2) and (3).

It is known that when a body moves rigidly, all its particles undergo the same rototranslation $\boldsymbol{H}$ [Borri et al. 2000]: this unique rototranslation characterizes the rigid body motion. So, let's examine

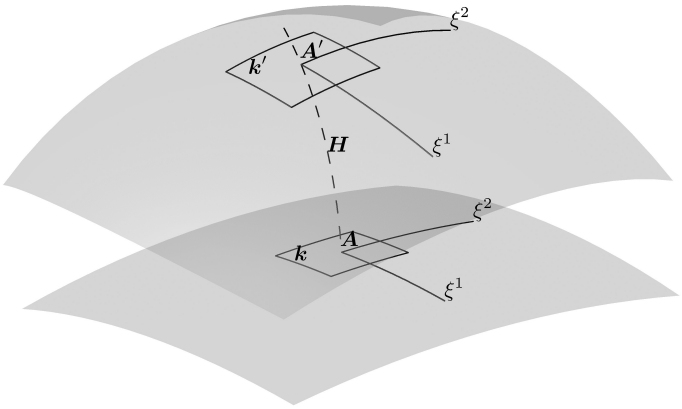

Figure 3. Material surface in the reference configuration and in the current configuration.

the derivatives $\partial \boldsymbol{H}/\partial \xi^\alpha$ within a moving surface. As for the curvatures, two surface strain dual vectors $\boldsymbol{\omega}_\alpha$ characterize such derivatives, $\boldsymbol{H}^{\mathrm{T}}\boldsymbol{H}_{,\alpha} = (\boldsymbol{H}^{\mathrm{T}}\boldsymbol{\omega}_\alpha)\times$. A dyadic composition with the reference contravariant base vectors gives the tensorial relation

$$\boldsymbol{H}^{\mathrm{T}}\boldsymbol{H}_{/\otimes} = (\boldsymbol{H}^{\mathrm{T}}\boldsymbol{\omega})^{\times}, \tag{17}$$

which actually defines the *surface strain* dual tensor $\boldsymbol{\omega} = \boldsymbol{\omega}_\alpha \otimes \boldsymbol{g}^\alpha$. The explicit dual form of the surface strain is

$$\boldsymbol{\omega} = \boldsymbol{\Phi}\ \mathrm{ax}\,(\boldsymbol{\Phi}^{\mathrm{T}}\boldsymbol{\Phi}_{/\otimes}) + \varepsilon\,\boldsymbol{\Phi}(\boldsymbol{\Phi}^{\mathrm{T}}\boldsymbol{t})_{/\otimes} = \boldsymbol{\omega}_{\mathrm{a}} + \varepsilon\,\boldsymbol{\omega}_{\mathrm{l}} = \boldsymbol{\omega}_{\mathrm{a}} + \varepsilon\,(\boldsymbol{t}_{/\otimes} + \boldsymbol{t}\times\boldsymbol{\omega}_{\mathrm{a}}),$$

where $\boldsymbol{t} = \boldsymbol{x}' - \boldsymbol{\Phi}\boldsymbol{x}$ is the translation vector, see (3). The angular part characterizes the surface gradient of the rotation, $\boldsymbol{\Phi}^{\mathrm{T}}\boldsymbol{\Phi}_{/\otimes} = (\boldsymbol{\Phi}^{\mathrm{T}}\boldsymbol{\omega}_{\mathrm{a}})^{\times}$. The self-based version of the surface strain is $\boldsymbol{X}'^{\mathrm{T}}\boldsymbol{\omega} = \boldsymbol{\omega}_{\mathrm{a}} + \varepsilon\,(\boldsymbol{x}'_{/\otimes} - \boldsymbol{\Phi}\boldsymbol{x}_{/\otimes})$.

By taking the gradient of (16) and recalling (15), (17), and (14), a relation between the curvatures in the reference and in the current configuration, involving the surface strain tensor, is easily obtained: $\boldsymbol{k}' = \boldsymbol{\omega} + \boldsymbol{H}\boldsymbol{k}$. When solved for $\boldsymbol{\omega}$, this equation leads to a meaningful expression for the surface strain tensor,

$$\boldsymbol{\omega} = \boldsymbol{k}' - \boldsymbol{H}\boldsymbol{k}, \tag{18}$$

as the difference between the current curvature and the reference curvature rototranslated forward by $\boldsymbol{H}$. In fact, when the motion is rigid, the curvature field $\boldsymbol{k}$ also undergoes the same unique rototranslation and becomes $\boldsymbol{k}' = \boldsymbol{H}\boldsymbol{k}$. Therefore, the difference in (18) is a good strain measure and $\boldsymbol{\omega}$ will be referred to as the *kinematical strain measure* of the material surface. Equation (18) also provides a profitable means to compute $\boldsymbol{\omega}$ in a numerical context, once $\boldsymbol{A}, \boldsymbol{k}$ and $\boldsymbol{A}', \boldsymbol{k}'$ become available, for instance after an interpolation process.

The angular and linear parts of the self-based version of $\boldsymbol{\omega}$ represent the surface angular strain tensor $\boldsymbol{\omega}_{\mathrm{a}} = \boldsymbol{\omega}_{\mathrm{a}\alpha} \otimes \boldsymbol{g}^\alpha = \boldsymbol{k}'_{\mathrm{a}} - \boldsymbol{\Phi}\boldsymbol{k}_{\mathrm{a}}$ and the surface linear strain tensor $\boldsymbol{\chi} = \boldsymbol{\chi}_\alpha \otimes \boldsymbol{g}^\alpha = \boldsymbol{x}'_{/\otimes} - \boldsymbol{\Phi}\boldsymbol{x}_{/\otimes}$, respectively. It is interesting to note that the latter is different from the three-dimensional linear strain tensor $\boldsymbol{F} - \boldsymbol{\Phi}\boldsymbol{I}$ of the Biot kind; in fact, it can be seen that $\boldsymbol{\chi} = \boldsymbol{F} - \boldsymbol{\Phi}\boldsymbol{I} - (\boldsymbol{n}' - \boldsymbol{\Phi}\boldsymbol{n}) \otimes \boldsymbol{n}$. Moreover, the expression $\boldsymbol{\chi} = \boldsymbol{x}'_{/\otimes} - \boldsymbol{\Phi}\boldsymbol{x}_{/\otimes}$ can be used to prove that the present description of the material surface allows for transverse shear strains. For example, consider a change of configuration where a flat surface keeps flat, but the material particles rotate around an in-plane direction; in such a case, $\boldsymbol{x}'_{/\otimes} = \boldsymbol{x}_{/\otimes} = \boldsymbol{g}_\alpha \otimes \boldsymbol{g}^\alpha$, but a

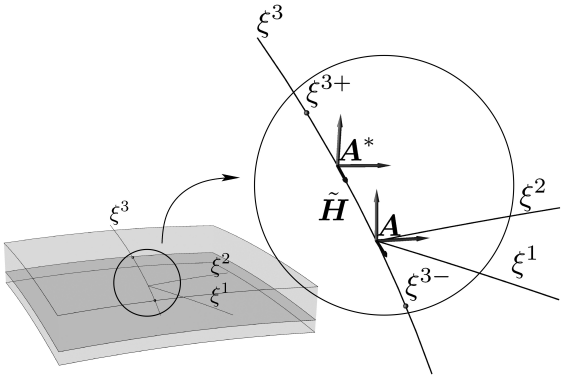

Figure 4. The helicoidal shell model.

nonnull linear strain tensor $\boldsymbol{\chi} = (\boldsymbol{g}_\alpha - \boldsymbol{\Phi}\boldsymbol{g}_\alpha) \otimes \boldsymbol{g}^\alpha$ arises, endowed with out-of-plane component vectors $\boldsymbol{\chi}_\alpha = -(\boldsymbol{\Phi} - \boldsymbol{I})\boldsymbol{g}_\alpha$.

4. Shell kinematical model

A solid shell is a three-dimensional body, lying on a smooth curved surface and thin in the direction locally normal to the surface. For numerical purposes, a solid shell is approximated by a *shell model*; here by shell model we mean a substitute body made of the layers generated by the particles of a material surface that sweep along a transverse curvilinear coordinate ξ^3, from ξ^{3-} to ξ^{3+}. For further details on the shell kinematical model discussed below, refer to [Merlini and Morandini 2008].

4.1. ***The helicoidal shell model.*** The proposed solid shell model is based on the most simple and natural rototranslation of the particles of a reference layer located at $\xi^3 = 0$. This reference layer is understood to coincide with the parent material surface. The above rototranslation is characterized by a curvature dual vector $\boldsymbol{k}_3$ constant along ξ^3 — actually, this is a helicoidal motion, whence the name *helicoidal shell model*. Moreover, a particular dual vector field $\boldsymbol{k}_3(\xi^\alpha)$ is assumed, so that also the curvature dual vectors $\boldsymbol{k}_\alpha$ of each layer hold constant along ξ^3.

The orientoposition $\boldsymbol{A}^*(\xi^\alpha, \xi^3)$ of a material particle of the solid shell model can always be described by a rototranslation $\tilde{\boldsymbol{H}}(\xi^\alpha, \xi^3)$ from the orientoposition $\boldsymbol{A}(\xi^\alpha)$ of the parent particle on the reference material surface (Figure 4),

$$\boldsymbol{A}^* = \tilde{\boldsymbol{H}}\boldsymbol{A}. \tag{19}$$

Equation (19) establishes a multiplicative decomposition of the local orientoposition $\boldsymbol{A}^* = \boldsymbol{X}^*\boldsymbol{\alpha}^* = (\boldsymbol{I} + \varepsilon\boldsymbol{x}^*\times)\boldsymbol{\alpha}^*$. The relative rototranslation can also be expressed as $\tilde{\boldsymbol{H}} = \boldsymbol{X}^*\tilde{\boldsymbol{\Phi}}\boldsymbol{X}^{\mathrm{T}}$, see (2), where $\tilde{\boldsymbol{\Phi}}(\xi^\alpha, \xi^3)$ is the rotation tensor from the orientation $\boldsymbol{\alpha}$ to the orientation $\boldsymbol{\alpha}^* = \tilde{\boldsymbol{\Phi}}\boldsymbol{\alpha}$. Note that we must have $\tilde{\boldsymbol{H}}(\xi^\alpha, 0) = \boldsymbol{I}$ and $\tilde{\boldsymbol{\Phi}}(\xi^\alpha, 0) = \boldsymbol{I}$, in order to have $\boldsymbol{A}^*(\xi^\alpha, 0) \equiv \boldsymbol{A}(\xi^\alpha)$ and $\boldsymbol{\alpha}^*(\xi^\alpha, 0) \equiv \boldsymbol{\alpha}(\xi^\alpha)$.

The helicoidal shell model is characterized as follows. First, $\tilde{\boldsymbol{H}} = \exp(\tilde{\boldsymbol{\eta}}\times)$ is specified as a *constant-curvature* rototranslation across the shell; to this end, the function $\tilde{\boldsymbol{\eta}}(\xi^\alpha, \xi^3)$ is assumed to have the factorized form

$$\tilde{\boldsymbol{\eta}} = \xi^3\boldsymbol{k}_3, \tag{20}$$

with $\boldsymbol{k}_3(\xi^\alpha)$ a dual vector independent of ξ^3. This assumption provides a constant curvature along ξ^3, as shown below. Next, the dual vector field $\boldsymbol{k}_3(\xi^\alpha)$ is specified by connecting it to the material surface orientoposition field $\boldsymbol{A}(\xi^\alpha)$. Formally, it is assumed that

$$\boldsymbol{k}_3 = \boldsymbol{A}\boldsymbol{\theta}, \tag{21}$$

with $\boldsymbol{\theta}$ a unique dual vector independent of ξ^α. We refer to $\boldsymbol{\theta}$ as the *dual director* of the helicoidal shell model. The helicoidal shell model, as described by (19)–(21), is based on the orthogonal dual tensor field $\boldsymbol{A}(\xi^\alpha)$ and on the unique dual parameter $\boldsymbol{\theta}$. The transverse curvature $\boldsymbol{k}_3$ is restricted to rototranslate on the material surface as the orientoposition $\boldsymbol{A}$, hence it is anchored to each material surface particle. It can be claimed that the last assumption, (21), is too strong; indeed, this assumption can be safely relaxed, as it will be shown later on.

Let's examine the curvatures within the helicoidal shell model, both along the layer's coordinates ξ^α and along the transverse coordinate ξ^3. Altogether, the three curvature dual vectors $\boldsymbol{k}_j^*$ ($j = 1, 2, 3$) are defined by $\boldsymbol{A}^{*\mathrm{T}}\boldsymbol{A}^*{}_{,j} = (\boldsymbol{A}^{*\mathrm{T}}\boldsymbol{k}_j^*)\times$. Within this formula, (19)–(21) are exploited in order to derive explicit expressions for $\boldsymbol{k}_j^*$. First it is recognized that $\tilde{\boldsymbol{H}}^{\mathrm{T}}\tilde{\boldsymbol{H}}_{,j} = (\tilde{\boldsymbol{H}}^{\mathrm{T}}\tilde{\boldsymbol{\Lambda}}\tilde{\boldsymbol{\eta}}_{,j})\times$, recall (7); then the derivatives of the transverse curvature are expanded as $\boldsymbol{k}_{3,\alpha} = \boldsymbol{A}_{,\alpha}\boldsymbol{\theta} = \boldsymbol{k}_\alpha \times \boldsymbol{A}\boldsymbol{\theta} = \boldsymbol{k}_\alpha \times \boldsymbol{k}_3$, whence $\tilde{\boldsymbol{\eta}}_{,\alpha} = -\tilde{\boldsymbol{\eta}} \times \boldsymbol{k}_\alpha$; finally the identity $\tilde{\boldsymbol{H}} = \boldsymbol{I} + \tilde{\boldsymbol{\Lambda}}\tilde{\boldsymbol{\eta}}\times$ is recalled, see (5) and (7). Using the property $\tilde{\boldsymbol{\Lambda}}\tilde{\boldsymbol{\eta}} = \tilde{\boldsymbol{\eta}}$ (whence $\tilde{\boldsymbol{\Lambda}}\boldsymbol{k}_3 = \boldsymbol{k}_3$), it is found that $\boldsymbol{k}_3^* = \boldsymbol{k}_3$ and $\boldsymbol{k}_\alpha^* = \boldsymbol{k}_\alpha$, or

$$\boldsymbol{k}_j^* = \boldsymbol{k}_j. \tag{22}$$

Since $\boldsymbol{k}_\alpha$ and $\boldsymbol{k}_3$ are independent of ξ^3, it follows that all three curvature dual vectors $\boldsymbol{k}_j^*$ are *constant* across the shell model thickness.

The explicit dual forms $\boldsymbol{k}_j^* = \boldsymbol{k}_{\mathrm{a}j}^* + \varepsilon\boldsymbol{k}_{1j}^* = \boldsymbol{k}_{\mathrm{a}j}^* + \varepsilon(\boldsymbol{x}^*{}_{,j} + \boldsymbol{x}^* \times \boldsymbol{k}_{\mathrm{a}j}^*)$, and their self-based version $\boldsymbol{X}^{*\mathrm{T}}\boldsymbol{k}_j^* = \boldsymbol{k}_{\mathrm{a}j}^* + \varepsilon\boldsymbol{x}^*{}_{,j}$, allow us to derive the metric of the shell model. The covariant base vectors are obtained from (22) as

$$\boldsymbol{g}_j^* = \boldsymbol{x}^*{}_{,j} = \mathrm{dual}\,(\boldsymbol{X}^{*\mathrm{T}}\boldsymbol{k}_j).$$

They form the base frame $\boldsymbol{G}^* = \boldsymbol{g}_j^* \otimes \boldsymbol{i}^j$. Inversion of tensor $\boldsymbol{G}^*$ yields the reciprocal frame $\boldsymbol{G}^{*-\mathrm{T}} = \boldsymbol{g}^{*j} \otimes \boldsymbol{i}_j$ of the contravariant base vectors such that $\boldsymbol{g}^{*j} \cdot \boldsymbol{g}_k^* = \delta_k^j$, the Kronecker symbol. It is worth comparing the values assumed by $\boldsymbol{g}_j^*(\xi^\alpha, \xi^3)$ at the reference layer with the material surface $\boldsymbol{g}_j(\xi^\alpha)$, (12) and (13): the base vectors tangent to the layers do reduce to the material surface base vectors, $\boldsymbol{g}_\beta^*(\xi^\alpha, 0) \equiv \boldsymbol{g}_\beta(\xi^\alpha)$, whereas the transverse one becomes $\boldsymbol{g}_3^*(\xi^\alpha, 0) = \mathrm{dual}\,(\boldsymbol{A}\boldsymbol{\theta})$ and may differ from $\boldsymbol{g}_3(\xi^\alpha) = h\boldsymbol{n}$, which was introduced by a purely geometric construction. Note that, in the proposed solid shell model, $\boldsymbol{g}_3^*$ is relieved from being normal to the layers and, as a consequence, the contravariant base vectors $\boldsymbol{g}^{*\alpha}$ are no more tangent to the layers. Instead, $\boldsymbol{g}^{*3}$ keeps normal to the layers.

The model base frame $\boldsymbol{G}^*(\xi^\alpha, \xi^3)$ can be related to the material surface base frame $\boldsymbol{G}(\xi^\alpha)$ by means of a sort of modeling gradient $\tilde{\boldsymbol{F}}(\xi^\alpha, \xi^3)$,

$$\boldsymbol{G}^* = \tilde{\boldsymbol{F}}\boldsymbol{G}.$$

An interesting interpretation of the so-called shifter tensor $\tilde{\boldsymbol{F}} = \boldsymbol{g}_j^* \otimes \boldsymbol{g}^j$ as a deformation gradient and its implication in classical shell theories can be found in [Schlebusch and Zastrau 2005]. Note that in the proposed model, it may be $\boldsymbol{G}^*(\xi^\alpha, 0) \neq \boldsymbol{G}(\xi^\alpha)$, whence $\tilde{\boldsymbol{F}}(\xi^\alpha, 0) \neq \boldsymbol{I}$. The base vectors allow writing tensors in dyadic form with reference to the model base frame. Moreover, they provide useful expressions

for the model gradient operator, $(\,)_{/\otimes *} = (\,)_{,j} \otimes \boldsymbol{g}^{*j}$, and for its trace, the model divergence operator, $(\,)_{/\bullet *} = (\,)_{,j} \cdot \boldsymbol{g}^{*j}$. Then, the modeling gradient $\tilde{\boldsymbol{F}}$ allows us to relate dyads in the model base with dyads in the material surface base.

The dyadic composition of the curvature dual vectors with the contravariant base vectors leads to the definition of the *model curvature* dual tensor $\boldsymbol{k}^* = \boldsymbol{k}_j^* \otimes \boldsymbol{g}^{*j}$,

$$\boldsymbol{A}^{*\mathrm{T}} \boldsymbol{A}^*_{/\otimes *} = (\boldsymbol{A}^{*\mathrm{T}} \boldsymbol{k}^*)^{\times}, \tag{23}$$

where in this context $(\,)^{\times} = (\,)_j \times \otimes \boldsymbol{g}^{*j}$. Note that the curvature tensor may be *not* constant across the shell thickness, yet it is made of three constant curvature vectors, $\boldsymbol{k}^* = \boldsymbol{k}_j \otimes \boldsymbol{g}^{*j}$, see (22). We may find it convenient to include the transverse curvature $\boldsymbol{k}_3$ in the dyadic definition of the *surface curvature* dual tensor $\boldsymbol{k} = \boldsymbol{k}_\alpha \otimes \boldsymbol{g}^\alpha$, and bring the latter to the three-dimensional form $\boldsymbol{k} = \boldsymbol{k}_j \otimes \boldsymbol{g}^j$. So, it can be easily seen that

$$\boldsymbol{k}^* = \boldsymbol{k} \tilde{\boldsymbol{F}}^{-1}, \tag{24}$$

and, again, it may be $\boldsymbol{k}^*(\xi^\alpha, 0) \neq \boldsymbol{k}(\xi^\alpha)$.

It is worth pointing out that the rototranslation that generates the solid shell model from a material surface is by no means a rigid motion. In fact, $\tilde{\boldsymbol{H}}$ is a function of the coordinates ξ^α and is not unique for the whole surface; also, each layer has its own curvature dual tensor, which is different from the curvature dual tensor of the parent material surface rototranslated by $\tilde{\boldsymbol{H}}$. Rather, this is like an inflating motion that brings the reference curved layer into a new, and in a sense parallel, curved layer. It is also worth noting that, whereas the tangent coordinate lines ξ^α generated by the shell model reflect those chosen on the parent material surface, the transverse coordinate lines ξ^3 are by construction helices with constant curvature.

4.2. ***Relaxation of a kinematical hypothesis.*** The shell dual director is a kinematical variable of the solid shell model and is extraneous to the material surface kinematics, so it should be advantageous to leave it out of the problem of the material surface mechanics. This observation indicates the opportunity to solve $\boldsymbol{\theta}$ locally. Therefore, we now propose to *relax* the hypothesis of a unique director for the material surface and adopt instead a *piecewise constant director field*; in other words, we assume that $\boldsymbol{\theta}$ is a locally constant function of ξ^α.

This new assumption does not affect the characteristics of the proposed kinematical model: from (21), we still have $\boldsymbol{k}_{3,\alpha} = \boldsymbol{k}_\alpha \times \boldsymbol{k}_3$, so the curvature dual vectors are still constant across the thickness. However, $\boldsymbol{\theta}$ is now allowed to vary from point to point on the material surface and, as a consequence, the transverse curvature $\boldsymbol{k}_3$ becomes unfastened from the orientation of the surface particle. Thus, $\boldsymbol{\theta}$ becomes a true variable field, but its gradient is left out of the variational formulation; the assumption is that a spatial variation of the dual director does not affect the shell mechanical behavior. In the finite element approximation of the material surface mechanics, the dual director shall be understood as an "internal", local variable; typically it shall be confined within the neighborhood of each quadrature point.

4.3. ***Shell model in the current configuration.*** Let the helicoidal shell model so far described refer to the undeformed, or *reference*, configuration. The *current* configuration will be described the same way, with an appended prime to distinguish the variables pertaining to the deformed model. The current orientoposition $\boldsymbol{A}'^* = \boldsymbol{X}'^* \boldsymbol{\alpha}'^* = (\boldsymbol{I} + \varepsilon \boldsymbol{x}'^* \times) \boldsymbol{\alpha}'^*$ of a material particle is decomposed multiplicatively into

the orientoposition $\boldsymbol{A}'$ of the parent material particle followed by a rototranslation,

$$\boldsymbol{A}'^{*} = \tilde{\boldsymbol{H}}'\boldsymbol{A}', \tag{25}$$

with

$$\tilde{\boldsymbol{H}}' = \exp(\tilde{\boldsymbol{\eta}}'\times) = \exp(\xi^3\boldsymbol{k}_3'\times) = \exp\bigl(\xi^3(\boldsymbol{A}'\boldsymbol{\theta}')\times\bigr) \tag{26}$$

and $\boldsymbol{\theta}'$ a piecewise constant dual vector field on the material surface.

With a total-Lagrangian description in mind, the current tensors are based on the reference configuration, that is, their dyadic forms are written with the reference base vectors. So, the current model curvature dual tensor $\boldsymbol{k}'^{*} = \boldsymbol{k}_j'^{*} \otimes \boldsymbol{g}^{*j}$ is defined by

$$\boldsymbol{A}'^{*\mathrm{T}}\boldsymbol{A}'^{*}_{/\otimes *} = (\boldsymbol{A}'^{*\mathrm{T}}\boldsymbol{k}'^{*})^{\times}. \tag{27}$$

Across the shell thickness, $\boldsymbol{k}'^{*}$ will not be constant, though its dual component vectors $\boldsymbol{k}'^{*}\cdot\boldsymbol{g}_j^{*}$ will. In fact, as in (22), $\boldsymbol{k}_j'^{*} = \boldsymbol{k}_j'$. Thus, we can also write $\boldsymbol{k}'^{*} = \boldsymbol{k}_j' \otimes \boldsymbol{g}^{*j}$, and relate $\boldsymbol{k}'^{*}$ to the current surface curvature three-dimensional dual tensor $\boldsymbol{k}' = \boldsymbol{k}_j' \otimes \boldsymbol{g}^{j}$ by

$$\boldsymbol{k}'^{*} = \boldsymbol{k}'\tilde{\boldsymbol{F}}^{-1}. \tag{28}$$

The current covariant base vectors are given by $\boldsymbol{g}_j'^{*} = \boldsymbol{x}'^{*}{}_{,j} = \mathrm{dual}\,(\boldsymbol{X}'^{*\mathrm{T}}\boldsymbol{k}_j')$, and form the current base frame $\boldsymbol{G}'^{*} = \boldsymbol{g}_j'^{*} \otimes \boldsymbol{i}^{j}$. The model deformation gradient $\boldsymbol{F}^{*} = \boldsymbol{x}'^{*}_{/\otimes *} = \boldsymbol{g}_j'^{*} \otimes \boldsymbol{g}^{*j} = \boldsymbol{G}'^{*}\boldsymbol{G}^{*-1}$ can be obtained as $\boldsymbol{F}^{*} = \mathrm{dual}\,(\boldsymbol{X}'^{*\mathrm{T}}\boldsymbol{k}'^{*}) = \mathrm{dual}\,(\boldsymbol{X}'^{*\mathrm{T}}\boldsymbol{k}'\tilde{\boldsymbol{F}}^{-1})$. The modeling gradient $\tilde{\boldsymbol{F}}$ and the model deformation gradient $\boldsymbol{F}^{*}$ allow us to recover the current model base frame from the reference material surface base frame, $\boldsymbol{G}'^{*} = \boldsymbol{F}^{*}\tilde{\boldsymbol{F}}\boldsymbol{G}$.

4.4. ***Model deformation.*** Let's address now the *model rototranslation* that brings the reference orientoposition to the current orientoposition,

$$\boldsymbol{A}'^{*} = \boldsymbol{H}^{*}\boldsymbol{A}^{*}. \tag{29}$$

Useful expressions for $\boldsymbol{H}^{*}$ are obtained from (2) and (3):

$$\boldsymbol{H}^{*} = \boldsymbol{A}'^{*}\boldsymbol{A}^{*\mathrm{T}} = \boldsymbol{X}'^{*}\boldsymbol{\Phi}^{*}\boldsymbol{X}^{*\mathrm{T}} = \bigl(\boldsymbol{I} + \varepsilon\,(\boldsymbol{x}'^{*} - \boldsymbol{\Phi}^{*}\boldsymbol{x}^{*})\times\bigr)\boldsymbol{\Phi}^{*}, \tag{30}$$

where $\boldsymbol{\Phi}^{*}$ is the rotation from the reference to the current orientation, $\boldsymbol{\alpha}'^{*} = \boldsymbol{\Phi}^{*}\boldsymbol{\alpha}^{*}$.

The gradient of the rototranslation $\boldsymbol{H}^{*}$ allows us to define the *model strain* dual tensor $\boldsymbol{\omega}^{*} = \boldsymbol{\omega}_j^{*} \otimes \boldsymbol{g}^{*j}$,

$$\boldsymbol{H}^{*\mathrm{T}}\boldsymbol{H}^{*}_{/\otimes *} = (\boldsymbol{H}^{*\mathrm{T}}\boldsymbol{\omega}^{*})^{\times}. \tag{31}$$

Taking the gradient of (29) and using (27), (31), and (23), a relation between the reference and current model curvatures, involving the model strain, is obtained: $\boldsymbol{k}'^{*} = \boldsymbol{\omega}^{*} + \boldsymbol{H}^{*}\boldsymbol{k}^{*}$. Solving this equation for $\boldsymbol{\omega}^{*}$,

$$\boldsymbol{\omega}^{*} = \boldsymbol{k}'^{*} - \boldsymbol{H}^{*}\boldsymbol{k}^{*}, \tag{32}$$

gives a meaningful expression for the model strain, as the difference between the current curvature and the reference curvature rototranslated forward by $\boldsymbol{H}^{*}$. We shall refer to $\boldsymbol{\omega}^{*}$ as the *kinematical strain measure* of the helicoidal shell model. It can be seen that the angular and linear parts of the self-based version of $\boldsymbol{\omega}^{*}$ represent the model angular-strain tensor $\boldsymbol{\omega}_{\mathrm{a}}^{*} = \boldsymbol{k}_{\mathrm{a}}'^{*} - \boldsymbol{\Phi}^{*}\boldsymbol{k}_{\mathrm{a}}^{*}$ and the model linear-strain tensor $\boldsymbol{\chi}^{*} = \boldsymbol{F}^{*} - \boldsymbol{\Phi}^{*}\boldsymbol{I}$, respectively.

Last, let's investigate the relationship between the model rototranslation and strain tensors, $\boldsymbol{H}^*$ and $\boldsymbol{\omega}^*$ respectively, and the corresponding surface rototranslation and strain tensors, $\boldsymbol{H}$ and $\boldsymbol{\omega}$. Using (19) and (25), the model rototranslation $\boldsymbol{H}^*(\xi^\alpha, \xi^3)$ from (30) can be related to the surface rototranslation $\boldsymbol{H}(\xi^\alpha)$ of (16), by

$$\boldsymbol{H}^* = \tilde{\boldsymbol{H}}' \boldsymbol{H} \tilde{\boldsymbol{H}}^{\mathrm{T}}. \tag{33}$$

Note that, as expected, $\boldsymbol{H}^*(\xi^\alpha, 0) \equiv \boldsymbol{H}(\xi^\alpha)$, whereas, in general, $\boldsymbol{H}^*$ differs from $\boldsymbol{H}$ when $\xi^3 \neq 0$. However, a special case occurs when $\boldsymbol{k}_3' = \boldsymbol{H}\boldsymbol{k}_3$ (that is, when the dual director stays unchanged, $\boldsymbol{\theta}' = \boldsymbol{\theta}$). In this case $\tilde{\boldsymbol{H}}' = \boldsymbol{H}\tilde{\boldsymbol{H}}\boldsymbol{H}^{\mathrm{T}}$ and from (33) it follows that $\boldsymbol{H}^* = \boldsymbol{H}$ independently from ξ^3: the rototranslation is unique for the whole material line lying along ξ^3, that is, that material line rototranslates rigidly.

Therefore, the difference $\boldsymbol{k}_3' - \boldsymbol{H}\boldsymbol{k}_3 = \boldsymbol{A}'(\boldsymbol{\theta}' - \boldsymbol{\theta})$, which is independent of ξ^3, represents a unique strain measure across the thickness. We refer to such strain measure as the *through-the-thickness strain*,

$$\boldsymbol{\omega}_3 = \boldsymbol{k}_3' - \boldsymbol{H}\boldsymbol{k}_3. \tag{34}$$

We may also find it convenient to include $\boldsymbol{\omega}_3(\xi^\alpha)$ in the dyadic definition of the surface strain dual tensor $\boldsymbol{\omega} = \boldsymbol{\omega}_\alpha \otimes \boldsymbol{g}^\alpha$, and bring the latter to the three-dimensional form $\boldsymbol{\omega} = \boldsymbol{\omega}_j \otimes \boldsymbol{g}^j$. Thus, (18) is expanded to the form $\boldsymbol{\omega} = \boldsymbol{k}' - \boldsymbol{H}\boldsymbol{k}$, where $\boldsymbol{k}'$, $\boldsymbol{k}$ and $\boldsymbol{\omega}$ are now full three-dimensional dual tensors on the surface.

Using (28) and (24), the model strain tensor in (32) can be related to the surface strain tensor,

$$\boldsymbol{\omega}^* = (\boldsymbol{k}' - \boldsymbol{H}^*\boldsymbol{k})\tilde{\boldsymbol{F}}^{-1} = \boldsymbol{\omega}\tilde{\boldsymbol{F}}^{-1} - (\boldsymbol{H}^* - \boldsymbol{H})\boldsymbol{k}\tilde{\boldsymbol{F}}^{-1},$$

where $\boldsymbol{\omega}$ is now the full three-dimensional dual tensor. This expression highlights the separate contributions to the local strain, coming from the material surface strains $\boldsymbol{\omega}_\alpha$ and from the through-the-thickness strain $\boldsymbol{\omega}_3$ (in fact, when $\boldsymbol{\omega}_3$ is null, $\boldsymbol{H}^* - \boldsymbol{H}$ is also null).

4.5. ***Geometric invariance.*** The shell model so far described is endowed with a distinctive property that is becoming very important in modern computational mechanics: it is *geometrically invariant*, in the sense pointed out in [Bottasso et al. 2002]. A shell kinematical model can be seen as a mathematical scheme to reduce three-dimensional kinematics to those pertaining to a two-coordinate material surface; being independent of the choice of the reference material surface is a characteristic of the proposed kinematical model. To be more precise, the physical value of the kinematical variables (orientopositions, curvatures, and strains) is not affected by the placement of the reference material surface with respect to the shell thickness. It is only required that the reference surface be identifiable as a layer of the shell model, but which layer is chosen is arbitrary.

The geometric invariance of the proposed shell model is inherent in helicoidal modeling itself across the thickness. To prove the geometric invariance, consider a given solid shell and set up a first kinematical model (A) as follows. Choose the mid surface as the reference surface and trace the coordinate lines ξ^α on it; the orientopositions $\boldsymbol{A}_{\mathrm{A}}$ and the curvatures $\boldsymbol{k}_{\mathrm{A}}$ are known; assume a dual director $\boldsymbol{\theta}_{\mathrm{A}}$ and build the transverse coordinate lines ξ^3 with a linear scale from $\xi^{3-} = -1$ to $\xi^{3+} = +1$. Next, set up a second kinematical model (B) of the same solid shell as follows. Choose the lower surface of model (A) as the reference surface for model (B); hold the coordinate lines ξ^α traced on it, and keep the same coordinate lines ξ^3 across the thickness as model (A), with a linear scale, however, ranging from $\xi^{3-} = 0$ to $\xi^{3+} = +1$; the orientopositions $\boldsymbol{A}_{\mathrm{B}}$, the curvatures $\boldsymbol{k}_{\mathrm{B}}$, and the dual director $\boldsymbol{\theta}_{\mathrm{B}}$ are determined from

$\boldsymbol{A}_\mathrm{A}$, $\boldsymbol{k}_\mathrm{A}$, and $\boldsymbol{\theta}_\mathrm{A}$. Note that $\boldsymbol{\theta}_\mathrm{A}$ and $\boldsymbol{\theta}_\mathrm{B} = 2\boldsymbol{\theta}_\mathrm{A}$ are parallel, however they are scaled due to the different measures of ξ^3 from ξ^{3-} to ξ^{3+}. So far you have built two different helicoidal models for the same shell body. As an exercise, compute the model orientoposition $\boldsymbol{A}^*$ and curvature $\boldsymbol{k}^*$ at a generic placement: you will find values coincident for either model. Now consider a deformed configuration of both models: again, $\boldsymbol{A}'^*$ and $\boldsymbol{k}'^*$ will coincide for either model. So both the rototranslation $\boldsymbol{H}^*$ and the strain $\boldsymbol{\omega}^*$ coincide for either model. This proves the geometric invariance of the helicoidal shell model.

5. Shell model mechanics

The starting point for the present formulation in shell mechanics is the principle of virtual work; this can be stated in the form $\Pi_{\mathrm{int}\delta} + \Pi_{\mathrm{ext}\delta} + \Pi_{\mathrm{bc}\delta} = 0$, where the contributions to the virtual functional Π_δ from the stresses, the external loads and the boundary constraints are kept separate. The terms $\Pi_{\mathrm{ext}\delta}$ and $\Pi_{\mathrm{bc}\delta}$ will be discussed in Part II, when dealing with the material surface mechanics. The internal work contribution, written as

$$\Pi_{\mathrm{int}\delta} = \int_S \pi_{\mathrm{int}\delta}\,\mathrm{d}S, \tag{35}$$

is the integral, over the shell surface S in the reference configuration, of a surface density of the internal work virtual functional of the shell model. The present section concerns the evaluation of $\pi_{\mathrm{int}\delta}$; refer to [Merlini and Morandini 2008] for deeper discussion.

5.1. ***Internal work virtual functional.*** The expression of $\pi_{\mathrm{int}\delta}$ is taken from the internally constrained form of the principle of virtual work [Merlini and Morandini 2005],

$$\pi_{\mathrm{int}\delta} = \int_{\xi^{3-}}^{\xi^{3+}} \delta\big(w^* + \langle \hat{\boldsymbol{\tau}}^*, \mathrm{dual}\,2\,\mathrm{ax}\,(\boldsymbol{\Phi}^{*\mathrm{T}}\boldsymbol{X}'^{*\mathrm{T}}\boldsymbol{\omega}^*)\rangle\big)\,\tilde{f}h\,\mathrm{d}\xi^3, \tag{36}$$

by considering that $\mathrm{d}V^* = g^*\mathrm{d}\xi^1\mathrm{d}\xi^2\mathrm{d}\xi^3$ and $\mathrm{d}S = h^{-1}g\,\mathrm{d}\xi^1\mathrm{d}\xi^2$, with $g = \det\boldsymbol{G}$, $\tilde{f} = \det\tilde{\boldsymbol{F}}$ and $g^* = \det\boldsymbol{G}^* = \tilde{f}g$. Equation (36) is formulated in a micropolar description context and refers to a hyperelastic nonpolar medium: $w^*(\boldsymbol{\varepsilon}^{*\mathrm{S}})$ is the shell model strain-energy density per unit initial volume, a function of the symmetric strain parameter $\boldsymbol{\varepsilon}^{*\mathrm{S}}$, and $\hat{\boldsymbol{\tau}}^*$ is the axial vector of the Biot stress tensor. The angle brackets $\langle\ ,\ \rangle$ denote the scalar product between two vectors (or tensors), one of which belongs to the kinematic vector space and the other to the cokinematic vector space.

The constitutive characterization of the nonpolar medium, see [Merlini and Morandini 2005], passes through the identification of the back rotated kinematical linear-strain tensor

$$\boldsymbol{\Phi}^{*\mathrm{T}}\,\mathrm{dual}\,(\boldsymbol{X}'^{*\mathrm{T}}\boldsymbol{\omega}^*) = \boldsymbol{\Phi}^{*\mathrm{T}}\boldsymbol{\chi}^* = \boldsymbol{\Phi}^{*\mathrm{T}}\boldsymbol{F}^* - \boldsymbol{I}$$

as a strain measure; tensor $\boldsymbol{\Phi}^{*\mathrm{T}}\boldsymbol{F}^*$ is usually referred to as the Cosserat deformation tensor in micropolar elasticity [Ramezani and Naghdabadi 2007]. For a nonpolar medium, the strain energy is restricted to be a function of a symmetric strain parameter $\boldsymbol{\varepsilon}^{*\mathrm{S}}$, which is connected to the symmetric part of the above strain measure by the *strain-displacement relation*

$$\boldsymbol{\varepsilon}^{*\mathrm{S}} = \mathrm{dual}\,(\boldsymbol{\Phi}^{*\mathrm{T}}X'^{*\mathrm{T}}\boldsymbol{\omega}^*)^{\mathrm{S}}. \tag{37}$$

The superscript $(\,)^{\mathrm{S}}$ denotes the symmetric part of a tensor. Correspondingly, the skew-symmetric part of the above strain measure must vanish, whence the *kinematical constraint equation*

$$\operatorname{ax}\operatorname{dual}(\boldsymbol{\Phi}^{*\mathrm{T}}\boldsymbol{X}'^{*\mathrm{T}}\boldsymbol{\omega}^{*}) = \mathbf{0}, \tag{38}$$

which represents a statement of the polar decomposition theorem of the deformation gradient.

The stress parameter work-conjugate to the strain parameter is defined by the *constitutive equation*

$$\hat{\boldsymbol{T}}^{*\mathrm{S}} = w^{*}_{/\boldsymbol{\varepsilon}^{*\mathrm{S}}}, \tag{39}$$

and is itself a function, in general nonlinear, of the strain parameter, that is, $\hat{\boldsymbol{T}}^{*\mathrm{S}}(\boldsymbol{\varepsilon}^{*\mathrm{S}})$. Linearization of (39) gives the incremental *stress-strain elastic law*

$$\partial\hat{\boldsymbol{T}}^{*\mathrm{S}} = \hat{\mathbb{E}}^{*\mathrm{SS}} : \partial\boldsymbol{\varepsilon}^{*\mathrm{S}}, \tag{40}$$

where

$$\hat{\mathbb{E}}^{*\mathrm{SS}} = \hat{\boldsymbol{T}}^{*\mathrm{S}}_{/\boldsymbol{\varepsilon}^{*\mathrm{S}}} = w^{*}_{/\boldsymbol{\varepsilon}^{*\mathrm{S}}\boldsymbol{\varepsilon}^{*\mathrm{S}}} \tag{41}$$

is the fourth-order *elastic tensor* mapping strain-parameter variations onto stress-parameter variations. Of course, the elastic tensor is itself a function of the strain parameter for nonlinear constitutive models.

The internal balance requires the stress parameter to coincide with the symmetric part of the Biot stress tensor $\hat{\boldsymbol{T}}^{*}$, defined as

$$\hat{\boldsymbol{T}}^{*} = \boldsymbol{\Phi}^{*\mathrm{T}}\acute{\boldsymbol{T}}^{*}, \tag{42}$$

with $\acute{\boldsymbol{T}}^{*}$ the first Piola–Kirchhoff stress tensor. Then it clearly appears, from the Euclidean decomposition $\hat{\boldsymbol{T}}^{*} = \hat{\boldsymbol{T}}^{*\mathrm{S}} + \hat{\boldsymbol{\tau}}^{*}\times$, that a workless stress field, the Biot-axial $\hat{\boldsymbol{\tau}}^{*}$, must exist as an independent unknown field. Thus, the mechanics of the nonpolar continuum, when formulated via a micropolar description, rely on the displacement, the rotation *and* the Biot-axial as the three primary unknown fields; the relevant governing equations are the linear and angular balances (where (42) and (39) are understood and (37) is assumed as fulfilled) and the kinematical constraint (38); in weak form, the irreducible variational principle is the internally constrained principle of virtual work, with the internal work virtual functional as in (36), where the kinematical constraint equation and the role of the Biot-axial as a Lagrange multiplier are evident.

Our approach to the three-dimensional finite elasticity belongs to a line of variational formulations developed in the nineties and best represented by [Simo et al. 1992; Bufler 1995]. These works either introduce the polar decomposition of the deformation gradient like an appended constraint requiring a Lagrange multiplier or try to give a constitutive characterization for the full Biot stress tensor to circumvent the introduction of Lagrange multipliers. Our approach, however, distinguishes itself as descending from a sound constitutive characterization of the hyperelastic nonpolar medium as proposed in [Merlini 1997] and later explained in [Merlini and Morandini 2005]. It is based on a strain energy function of a symmetric strain (6 parameters) and leads naturally to a variational principle that holds the definition of the rotation field and allows for a workless stress vector field, which identifies with the axial of the skew-symmetric part of the Biot stress tensor. Note that in all the formulations of this kind the angular balance is forced in a weak sense, hence the symmetry of the second Piola–Kirchhoff stress tensor is relaxed; consistently, in our opinion, the polar decomposition of the deformation gradient (that actually defines the rotation within a nonpolar medium) must be forced in a weak sense as well. That means that

even in the case of isotropic media, for which a symmetrical Biot-stress is expected [Bufler 1985], the symmetry of the Biot stress tensor ought to be relaxed.

5.2. ***The Biot-axial model.*** The approximation of the Biot-axial primary unknown field across the thickness is part of the proposed shell model. On the strength of experience gained with the three-dimensional helicoidal finite elements [Merlini and Morandini 2005], we assume that the Biot-axial covariant components $\hat{\boldsymbol{\tau}}^* \cdot \boldsymbol{g}_j^*$ are linear functions of the transverse coordinate ξ^3. The six coefficients are in turn understood as the covariant components, on the material surface base, of two parameter vectors, $\hat{\boldsymbol{\tau}}$ and $\hat{\boldsymbol{\mu}}$, which are functions only of the coordinates ξ^α. The general expression of the proposed Biot-axial model can then be cast as follows:

$$\hat{\boldsymbol{\tau}}^* = h^{-1}(\hat{\boldsymbol{\tau}} + \xi^3 h^{-1}\hat{\boldsymbol{\mu}}) \cdot \tilde{\boldsymbol{F}}^{-1}, \tag{43}$$

where h is the shell characteristic length. Vectors $\hat{\boldsymbol{\tau}}(\xi^\alpha)$ and $\hat{\boldsymbol{\mu}}(\xi^\alpha)$ have physical dimensions of force per unit length and couple per unit length, respectively; they can also be thought of as the linear and angular parts, respectively, of a dual Biot-axial parameter $\hat{\boldsymbol{\sigma}} = \hat{\boldsymbol{\tau}} + \varepsilon\hat{\boldsymbol{\mu}}$.

5.3. ***Linearization of the internal work virtual functional.*** The variational principle ought to be linearized in view of its use in a numerical context. Linearization of the internal work virtual functional means a truncated Taylor expansion of $\pi_{\text{int}\delta}$ and yields the *incremental form* $\pi_{\text{int}\delta} + \partial\pi_{\text{int}\delta}$. The first term is simply called the virtual functional, the second term the virtual tangent functional: in a Newton–Raphson solution process, they will generate respectively the residual column and the tangent matrix.

The following notes can help developing (36) and its increment $\partial\pi_{\text{int}\delta}$.

(1) In scalar-valued dot products, symmetric and skew-symmetric tensors are uncoupled. This property also holds in a scalar product: $\langle \boldsymbol{A}^{\text{S}} + \boldsymbol{a}\times, \boldsymbol{B}^{\text{S}} + \boldsymbol{b}\times\rangle = \langle \boldsymbol{A}^{\text{S}}, \boldsymbol{B}^{\text{S}}\rangle + \langle \boldsymbol{a}\times, \boldsymbol{b}\times\rangle = \langle \boldsymbol{A}^{\text{S}}, \boldsymbol{B}^{\text{S}}\rangle + 2\langle \boldsymbol{a}, \boldsymbol{b}\rangle$.

(2) Assuming (37) and (39) as fulfilled, the virtual variation of the strain-energy function $w^*(\boldsymbol{\varepsilon}^{*\text{S}})$ in (36) can be written $\delta w^* = \langle \delta\boldsymbol{\varepsilon}^{*\text{S}}, w^*_{/\boldsymbol{\varepsilon}^{*\text{S}}}\rangle = \langle \delta\,\text{dual}\,(\boldsymbol{\Phi}^{*\text{T}} X'^{*\text{T}} \boldsymbol{\omega}^*)^{\text{S}}, \hat{\boldsymbol{T}}^{*\text{S}}\rangle$. Then, recalling (40), the linearized virtual variation becomes

$$\partial\delta w^* = \delta\,\text{dual}\,(\boldsymbol{\Phi}^{*\text{T}} X'^{*\text{T}} \boldsymbol{\omega}^*)^{\text{S}} : \hat{\mathbb{E}}^{*\text{SS}} : \partial\,\text{dual}\,(\boldsymbol{\Phi}^{*\text{T}} X'^{*\text{T}} \boldsymbol{\omega}^*)^{\text{S}} + \langle \partial\delta\,\text{dual}\,(\boldsymbol{\Phi}^{*\text{T}} X'^{*\text{T}} \boldsymbol{\omega}^*)^{\text{S}}, \hat{\boldsymbol{T}}^{*\text{S}}\rangle.$$

(3) The mixed virtual-incremental variation variables are retained here in consideration of a possible nonlinear dependence of the local variables on the ultimate problem unknowns.

(4) The transformations $\boldsymbol{H}^*\boldsymbol{X}^*$ and $\boldsymbol{X}'^*\boldsymbol{\Phi}^*$ are interchangeable, see (30). For convenience, a short notation for such orthogonal transformations is introduced:

$$\boldsymbol{\Psi}^* = \boldsymbol{H}^*\boldsymbol{X}^* = \boldsymbol{X}'^*\boldsymbol{\Phi}^*. \tag{44}$$

The terms of the incremental form of the internal work virtual functional are then obtained:

$$\begin{aligned}
\pi_{\text{int}\delta} &= \int_{\xi^{3-}}^{\xi^{3+}} \big(\text{dual}\,\delta(\boldsymbol{\Psi}^{*\text{T}}\boldsymbol{\omega}^*) : \hat{\boldsymbol{T}}^* + \delta\hat{\boldsymbol{\tau}}^*\times : \text{dual}\,(\boldsymbol{\Psi}^{*\text{T}}\boldsymbol{\omega}^*)\big)\,\tilde{f}h\,\mathrm{d}\xi^3, \\
\partial\pi_{\text{int}\delta} &= \int_{\xi^{3-}}^{\xi^{3+}} \big(\text{dual}\,\delta(\boldsymbol{\Psi}^{*\text{T}}\boldsymbol{\omega}^*) : \hat{\mathbb{E}}^{*\text{SS}} : \text{dual}\,\partial(\boldsymbol{\Psi}^{*\text{T}}\boldsymbol{\omega}^*) + \text{dual}\,\delta(\boldsymbol{\Psi}^{*\text{T}}\boldsymbol{\omega}^*) : \partial\hat{\boldsymbol{\tau}}^*\times \\
&\qquad + \delta\hat{\boldsymbol{\tau}}^*\times : \text{dual}\,\partial(\boldsymbol{\Psi}^{*\text{T}}\boldsymbol{\omega}^*) + \partial\delta\hat{\boldsymbol{\tau}}^*\times : \text{dual}\,(\boldsymbol{\Psi}^{*\text{T}}\boldsymbol{\omega}^*) + \text{dual}\,\partial\delta(\boldsymbol{\Psi}^{*\text{T}}\boldsymbol{\omega}^*) : \hat{\boldsymbol{T}}^*\big)\,\tilde{f}h\,\mathrm{d}\xi^3.
\end{aligned} \tag{45}$$

Here the scalar products have been converted into dot products inside one vector space. The virtual functionals $\pi_{\text{int}\delta}$ and $\partial\pi_{\text{int}\delta}$ are nonlinear functions of the kinematic and cokinematic variables of the shell model and linear functions of the relevant variation variables, specifically the variations of the linear-strain dual $(\boldsymbol{\Psi}^{*\mathrm{T}}\boldsymbol{\omega}^*)$ and of the Biot-axial $\hat{\boldsymbol{\tau}}^*$. Such variations are virtual variations (δ) for the virtual functional $\pi_{\text{int}\delta}$ and virtual (δ), incremental (∂) and mixed virtual-incremental $(\partial\delta)$ variations for the virtual tangent functional $\partial\pi_{\text{int}\delta}$. In $(45)_2$, three distinct contributions to $\partial\pi_{\text{int}\delta}$ can be observed: the *elastic* contribution related to $\hat{\mathbb{E}}^{*\mathrm{SS}}$, the *kinematical constraint* contribution made of three terms involving the variations of $\hat{\boldsymbol{\tau}}^*$, and the *geometric* contribution related to the stress state $\hat{\boldsymbol{T}}^*$.

5.4. ***Adaptation of the local constitutive law.*** It can be shown that evaluating the transverse strain component $\varepsilon^*_{\underline{33}} = \boldsymbol{g}^*_3 \cdot \boldsymbol{\varepsilon}^{*\mathrm{S}} \cdot \boldsymbol{g}^*_3$ according to (37) yields $\varepsilon^*_{\underline{33}} = \boldsymbol{g}^*_3 \cdot \boldsymbol{\alpha}^*$ dual $(\boldsymbol{\theta}' - \boldsymbol{\theta})$. With the most natural choice for the initial value of $\boldsymbol{k}_3$ (that is, a pure dual vector of length h, normal to the surface), it would be $\boldsymbol{g}^*_3 = \boldsymbol{g}_3$ and $\boldsymbol{\alpha}^* = \boldsymbol{\alpha}$, whence $\varepsilon^*_{\underline{33}} = \boldsymbol{g}_3 \cdot \boldsymbol{\alpha}$ dual $(\boldsymbol{\theta}' - \boldsymbol{\theta})$ would be always independent of the transverse coordinate ξ^3. This proves that $\varepsilon^*_{\underline{33}}$ is likely to be anyway uniform across the shell thickness.

This kinematical behavior is inherent in the helicoidal shell model itself (just like a classical 6-parameter model) and is, of course, inconsistent with the change of sign of the transverse normal strain across the shell thickness due to Poisson's effect in shell bending. The strong prevention of a variable transverse strain across the shell thickness induces severe locking in bending problems — a well known phenomenon in shell mechanics, usually referred to as Poisson thickness locking [Bischoff and Ramm 2000]. The classical remedy is to adopt local constitutive laws specifically adjusted for the so-called plane stress state; in nonlinear or complex constitutive models, however, such an adjustment may be quite difficult, so formulations that allow the use of unmodified three-dimensional constitutive laws have been developed. The most popular one is the method of enhanced assumed strains, originated in [Simo and Rifai 1990] and widely exploited since then (for example, in [Brank 2008]): full three-dimensional constitutive laws are allowed at the expense of some more strain variables across the thickness. Alternatively, a plane stress state can be forced dynamically on the three-dimensional constitutive law at the place where the latter is used, that is, at each quadrature point; see the techniques developed in [de Borst 1991; Klinkel and Govindjee 2002].

The method proposed here belongs to the last class of remedies and features a formulation deeply integrated with the incremental variational context. The transverse normal strain is disjoint from the shell model kinematics and allocated at each quadrature point across the thickness as a local scalar variable. The incremental form of the nonlinear constitutive law provides the way to solve locally the increment of the local variable for the increments of the other kinematically related strain variables. The nonlinear constitutive law can then be condensed and a reduced incremental form is obtained. Lastly, the incremental constitutive law is expanded again by means of an artificial transverse stiffness that provides an elastic restraint to the kinematically related transverse normal strain. A full three-dimensional incremental constitutive law, in terms of the whole kinematically related strain of (37), is obtained; this constitutive law is dynamically provided by the shell model routine during the iterative solution of the elastic problem, and the whole process is completely transparent to the user.

First, let's shorten the kinematical-strain notation: denote with $\boldsymbol{\kappa}^{*\mathrm{S}}$ the symmetric tensor in the right-hand side of (37). It is worth stressing that $\boldsymbol{\kappa}^{*\mathrm{S}}$ must be just viewed as a short name for dual $(\boldsymbol{\Phi}^{*\mathrm{T}} X'^{*\mathrm{T}} \boldsymbol{\omega}^*)^{\mathrm{S}}$. Next, introduce the components in the local base frame, $\kappa^*_{\underline{kl}} = \boldsymbol{g}^*_k \cdot \boldsymbol{\kappa}^{*\mathrm{S}} \cdot \boldsymbol{g}^*_l = \boldsymbol{g}^*_k \otimes \boldsymbol{g}^*_l : \boldsymbol{\kappa}^{*\mathrm{S}}$, and analogously

with $\varepsilon^*_{\underline{kl}}$, $\hat{T}^{*\underline{ij}}$, and $\hat{E}^{*\underline{ijkl}}$; here, the underlined couples of indexes reflect the tensor symmetries, and hence are interchangeable. Then, note that the internal *compatibility condition* (37) states that the strain parameter $\boldsymbol{\varepsilon}^{*\mathrm{S}}$ must equal the kinematically related strain $\boldsymbol{\kappa}^{*\mathrm{S}}$. The present formulation is based on the principle of virtual work, and this implies that the internal compatibility is assumed as fulfilled and $\boldsymbol{\varepsilon}^{*\mathrm{S}}$ ought to coincide with $\boldsymbol{\kappa}^{*\mathrm{S}}$. In this adaptation of the local constitutive law, however, we *relax* this assumption and disjoin some components of $\boldsymbol{\varepsilon}^{*\mathrm{S}}$ from the corresponding components of $\boldsymbol{\kappa}^{*\mathrm{S}}$. Specifically, we assume $\varepsilon^*_{\underline{\alpha\beta}} \equiv \kappa^*_{\underline{\alpha\beta}}$ and $\varepsilon^*_{\underline{\alpha 3}} \equiv \kappa^*_{\underline{\alpha 3}}$, but we keep the transverse normal component $\varepsilon^*_{\underline{33}}$ disjoint from $\kappa^*_{\underline{33}}$. That leads us to reason as in a more general three-field context (displacement-stress-strain as unknowns) just for this transverse normal variable; so, disjoining $\varepsilon^*_{\underline{33}}$ from $\kappa^*_{\underline{33}}$ is not, in a sense, an assumption, rather the release of an assumption — the fulfillment of a compatibility condition.

The incremental form of the strain-energy virtual variation, written in terms of components, reads

$$\begin{aligned}\delta w^* + \partial\delta w^* &= \begin{Bmatrix} \delta\kappa^*_{\underline{\alpha\beta}} \\ 2\delta\kappa^*_{\underline{\alpha 3}} \\ \delta\varepsilon^*_{\underline{33}} \end{Bmatrix}^{\mathrm{T}} \left(\begin{Bmatrix} \hat{T}^{*\underline{\alpha\beta}} \\ \hat{T}^{*\underline{\alpha 3}} \\ \hat{T}^{*\underline{33}} \end{Bmatrix} + \begin{bmatrix} \hat{E}^{*\underline{\alpha\beta\gamma\delta}} & \hat{E}^{*\underline{\alpha\beta\gamma 3}} & \hat{E}^{*\underline{\alpha\beta 33}} \\ \hat{E}^{*\underline{\alpha 3\gamma\delta}} & \hat{E}^{*\underline{\alpha 3\gamma 3}} & \hat{E}^{*\underline{\alpha 333}} \\ \hat{E}^{*\underline{33\gamma\delta}} & \hat{E}^{*\underline{33\gamma 3}} & \hat{E}^{*\underline{3333}} \end{bmatrix} \begin{Bmatrix} \partial\kappa^*_{\underline{\gamma\delta}} \\ 2\partial\kappa^*_{\underline{\gamma 3}} \\ \partial\varepsilon^*_{\underline{33}} \end{Bmatrix} \right) + \begin{Bmatrix} \partial\delta\kappa^*_{\underline{\alpha\beta}} \\ 2\partial\delta\kappa^*_{\underline{\alpha 3}} \end{Bmatrix}^{\mathrm{T}} \begin{Bmatrix} \hat{T}^{*\underline{\alpha\beta}} \\ \hat{T}^{*\underline{\alpha 3}} \end{Bmatrix}. \end{aligned} \tag{46}$$

Here, $\kappa^*_{\underline{\alpha\beta}}$ and $\kappa^*_{\underline{\alpha 3}}$ have been substituted for $\varepsilon^*_{\underline{\alpha\beta}}$ and $\varepsilon^*_{\underline{\alpha 3}}$, respectively, but $\varepsilon^*_{\underline{33}}$ has been retained; the term with $\partial\delta\varepsilon^*_{\underline{33}}$ is of course lacking, since $\varepsilon^*_{\underline{33}}$ is now understood as a local, independent variable. Equation (46) contributes to the integrand of $\pi_{\mathrm{int}\delta} + \partial\pi_{\mathrm{int}\delta}$, however the term in $\delta\varepsilon^*_{\underline{33}}$ keeps disjoint from the overall principle and originates the local incremental equation

$$\hat{T}^{*\underline{33}} + \begin{bmatrix} \hat{E}^{*\underline{33\gamma\delta}} & \hat{E}^{*\underline{33\gamma 3}} \end{bmatrix} \begin{Bmatrix} \partial\kappa^*_{\underline{\gamma\delta}} \\ 2\partial\kappa^*_{\underline{\gamma 3}} \end{Bmatrix} + \hat{E}^{*\underline{3333}}\partial\varepsilon^*_{\underline{33}} = 0. \tag{47}$$

It is worth noting that (47) is the incremental form of the nonlinear equation $\hat{T}^{*\underline{33}} = \partial w^*/\partial\varepsilon^*_{\underline{33}} = 0$, stating the independence of the strain-energy function from the transverse normal strain. Note that the condition of transverse normal stress — $\hat{T}^{*\underline{33}}$ in the present Biot-type parameterization of the strain energy w^* — identically zero is the classical assumption introduced to reduce the constitutive law to the so-called plane-stress state in shell analyses; see, for example, [Bischoff et al. 2004] (though the popular notion "plane-stress" is strictly speaking not correct when transverse shear stresses are allowed).

Equation (47) is now solved for $\partial\varepsilon^*_{\underline{33}}$ and the result is substituted within (46), yielding the condensed form

$$\delta w^* + \partial\delta w^* = \begin{Bmatrix} \delta\kappa^*_{\underline{\alpha\beta}} \\ 2\delta\kappa^*_{\underline{\alpha 3}} \end{Bmatrix}^{\mathrm{T}} \left(\begin{Bmatrix} \hat{\bar{T}}^{*\underline{\alpha\beta}} \\ \hat{\bar{T}}^{*\underline{\alpha 3}} \end{Bmatrix} + \begin{bmatrix} \hat{\bar{E}}^{*\underline{\alpha\beta\gamma\delta}} & \hat{\bar{E}}^{*\underline{\alpha\beta\gamma 3}} \\ \hat{\bar{E}}^{*\underline{\alpha 3\gamma\delta}} & \hat{\bar{E}}^{*\underline{\alpha 3\gamma 3}} \end{bmatrix} \begin{Bmatrix} \partial\kappa^*_{\underline{\gamma\delta}} \\ 2\partial\kappa^*_{\underline{\gamma 3}} \end{Bmatrix} \right) + \begin{Bmatrix} \partial\delta\kappa^*_{\underline{\alpha\beta}} \\ 2\partial\delta\kappa^*_{\underline{\alpha 3}} \end{Bmatrix}^{\mathrm{T}} \begin{Bmatrix} \hat{T}^{*\underline{\alpha\beta}} \\ \hat{T}^{*\underline{\alpha 3}} \end{Bmatrix}, \tag{48}$$

where

$$\begin{aligned} \begin{Bmatrix} \hat{\bar{T}}^{*\underline{\alpha\beta}} \\ \hat{\bar{T}}^{*\underline{\alpha 3}} \end{Bmatrix} &= \begin{Bmatrix} \hat{T}^{*\underline{\alpha\beta}} \\ \hat{T}^{*\underline{\alpha 3}} \end{Bmatrix} - \begin{bmatrix} \hat{E}^{*\underline{\alpha\beta 33}} \\ \hat{E}^{*\underline{\alpha 333}} \end{bmatrix} \hat{E}^{*\underline{3333}-1} \hat{T}^{*\underline{33}}, \\ \begin{bmatrix} \hat{\bar{E}}^{*\underline{\alpha\beta\gamma\delta}} & \hat{\bar{E}}^{*\underline{\alpha\beta\gamma 3}} \\ \hat{\bar{E}}^{*\underline{\alpha 3\gamma\delta}} & \hat{\bar{E}}^{*\underline{\alpha 3\gamma 3}} \end{bmatrix} &= \begin{bmatrix} \hat{E}^{*\underline{\alpha\beta\gamma\delta}} & \hat{E}^{*\underline{\alpha\beta\gamma 3}} \\ \hat{E}^{*\underline{\alpha 3\gamma\delta}} & \hat{E}^{*\underline{\alpha 3\gamma 3}} \end{bmatrix} - \begin{bmatrix} \hat{E}^{*\underline{\alpha\beta 33}} \\ \hat{E}^{*\underline{\alpha 333}} \end{bmatrix} \hat{E}^{*\underline{3333}-1} \begin{bmatrix} \hat{E}^{*\underline{33\gamma\delta}} & \hat{E}^{*\underline{33\gamma 3}} \end{bmatrix}, \end{aligned} \tag{49}$$

collect the reduced components of the stress parameter and elastic tensor.

The incremental form (48) deserves further development. It is apparent that, in (48),

$$\delta w^* = \delta\kappa^*_{\underline{\alpha\beta}}\hat{\bar{T}}^{*\underline{\alpha\beta}} + 2\delta\kappa^*_{\underline{\alpha 3}}\hat{\bar{T}}^{*\underline{\alpha 3}},$$

so

$$\partial\delta w^* = \delta\kappa^*_{\underline{\alpha\beta}}\partial\hat{\bar{T}}^{*\underline{\alpha\beta}} + 2\delta\kappa^*_{\underline{\alpha 3}}\partial\hat{\bar{T}}^{*\underline{\alpha 3}} + \partial\delta\kappa^*_{\underline{\alpha\beta}}\hat{\bar{T}}^{*\underline{\alpha\beta}} + 2\partial\delta\kappa^*_{\underline{\alpha 3}}\hat{\bar{T}}^{*\underline{\alpha 3}}$$

is also identified as the remaining part of $\delta w^* + \partial\delta w^*$. Therefore, using $(49)_1$, it follows that

$$\begin{Bmatrix}\delta\kappa^*_{\underline{\alpha\beta}}\\ 2\delta\kappa^*_{\underline{\alpha 3}}\end{Bmatrix}^{\mathrm{T}}\begin{Bmatrix}\partial\hat{\bar{T}}^{*\underline{\alpha\beta}}\\ \partial\hat{\bar{T}}^{*\underline{\alpha 3}}\end{Bmatrix} H = \begin{Bmatrix}\delta\kappa^*_{\underline{\alpha\beta}}\\ 2\delta\kappa^*_{\underline{\alpha 3}}\end{Bmatrix}^{\mathrm{T}}\begin{bmatrix}\hat{\bar{E}}^{*\underline{\alpha\beta\gamma\delta}} & \hat{\bar{E}}^{*\underline{\alpha\beta\gamma 3}}\\ \hat{\bar{E}}^{*\underline{\alpha 3\gamma\delta}} & \hat{\bar{E}}^{*\underline{\alpha 3\gamma 3}}\end{bmatrix}\begin{Bmatrix}\partial\kappa^*_{\gamma\delta}\\ 2\partial\kappa^*_{\gamma 3}\end{Bmatrix} + \begin{Bmatrix}\partial\delta\kappa^*_{\underline{\alpha\beta}}\\ 2\partial\delta\kappa^*_{\underline{\alpha 3}}\end{Bmatrix}^{\mathrm{T}}\begin{bmatrix}\hat{E}^{*\underline{\alpha\beta 33}}\\ \hat{E}^{*\underline{\alpha 333}}\end{bmatrix}\hat{E}^{*\underline{3333}-1}\hat{T}^{*\underline{33}}. \tag{50}$$

Now, in the context of a discrete approximation, $\partial\delta\boldsymbol{\kappa}^{*\mathrm{S}}$ will be always reduced to a linear function of the ultimate virtual variation unknowns (δ) and of the ultimate incremental variation unknowns (∂) of the discrete problem [Merlini and Morandini 2005]; thus, the second term in the right-hand side of (50) is always logically reducible to a form like the first term and thus will add to the first term. When doing so, the matrix elements $\hat{\bar{E}}^*$ of the first term will be corrected by terms proportional to $\hat{T}^{*\underline{33}}$ and dependent on the whole shell model. However, in the present adaptation of a local constitutive law, we find it convenient to miss this correction of the reduced stress-strain tangent map and retain only that part coming from the first term. Note that the term omitted is almost negligible, since $\hat{T}^{*\underline{33}}$ will vanish at convergence, see (47). Moreover, the error is on the problem tangent matrix, but not on the residual, so it will affect only the convergence rate, not the final result.

The foregoing discussion allows us to correct (48) and write the separate terms of the incremental form of the strain-energy virtual variation as

$$\begin{aligned}\delta w^* &= \begin{Bmatrix}\delta\kappa^*_{\underline{\alpha\beta}}\\ 2\delta\kappa^*_{\underline{\alpha 3}}\end{Bmatrix}^{\mathrm{T}}\begin{Bmatrix}\hat{\bar{T}}^{*\underline{\alpha\beta}}\\ \hat{\bar{T}}^{*\underline{\alpha 3}}\end{Bmatrix},\\ \partial\delta w^* &= \begin{Bmatrix}\delta\kappa^*_{\underline{\alpha\beta}}\\ 2\delta\kappa^*_{\underline{\alpha 3}}\end{Bmatrix}^{\mathrm{T}}\begin{bmatrix}\hat{\bar{E}}^{*\underline{\alpha\beta\gamma\delta}} & \hat{\bar{E}}^{*\underline{\alpha\beta\gamma 3}}\\ \hat{\bar{E}}^{*\underline{\alpha 3\gamma\delta}} & \hat{\bar{E}}^{*\underline{\alpha 3\gamma 3}}\end{bmatrix}\begin{Bmatrix}\partial\kappa^*_{\gamma\delta}\\ 2\partial\kappa^*_{\gamma 3}\end{Bmatrix} + \begin{Bmatrix}\partial\delta\kappa^*_{\underline{\alpha\beta}}\\ 2\partial\delta\kappa^*_{\underline{\alpha 3}}\end{Bmatrix}^{\mathrm{T}}\begin{Bmatrix}\hat{\bar{T}}^{*\underline{\alpha\beta}}\\ \hat{\bar{T}}^{*\underline{\alpha 3}}\end{Bmatrix},\end{aligned} \tag{51}$$

where only the reduced components of the stress parameter and elastic tensor appear.

The strain-energy variations in (51) depend implicitly on any strain components $\kappa^*_{\underline{\alpha\beta}}$, $\kappa^*_{\underline{\alpha 3}}$, *and* $\varepsilon^*_{\underline{33}}$, and explicitly on the variations of all the components of the kinematical strain $\boldsymbol{\kappa}^{*\mathrm{S}}$ except $\kappa^*_{\underline{33}}$. It is seen that the component $\kappa^*_{\underline{33}}$ is left elastically unrestrained. The release of the transverse normal strain from the shell model kinematics may overcome the deficiencies of the kinematical model in representing correctly the actual strain state, for example, in shell bending; however this expedient leaves an intrinsic transverse lability. Since no more stiffness is guaranteed against transverse collapse — a deformation consistent with a uniform transverse normal strain $\kappa^*_{\underline{33}}$ — the present constitutive adaptation infers a lability in membrane stretching.

A convenient remedy for this lability is to modify again the constitutive model by introducing an artificial transverse stiffness. This can be accomplished by enhancing the strain energy with a term

quadratic in $\kappa^*_{\underline{33}}$, say

$$w^*_{33} = \tfrac{1}{2}\,\hat{E}^{*\underline{3333}}\kappa^{*2}_{\underline{33}}, \tag{52}$$

where the elastic constant is conveniently borrowed from the proper component of the original elastic tensor in (46). In order not to affect the mechanical response of the overall shell model, this contribution must be independent of the other kinematically related strain components, so the current value of $\hat{E}^{*\underline{3333}}$ must hold constant in (52). Taking the derivatives of $w^*_{33}(\kappa^*_{\underline{33}})$, the expressions of a transverse constitutive equation and the relevant tangent map are obtained:

$$\hat{\bar{T}}^{*\underline{33}} = \hat{E}^{*\underline{3333}}\kappa^*_{\underline{33}}, \qquad \hat{\bar{E}}^{*\underline{3333}} = \hat{E}^{*\underline{3333}}. \tag{53}$$

The virtual variation and the linearized virtual variation of the energy term (52), $\delta w^*_{33} = \delta\kappa^*_{\underline{33}}\hat{\bar{T}}^{*\underline{33}}$ and $\partial\delta w^*_{33} = \delta\kappa^*_{\underline{33}}\hat{\bar{E}}^{*\underline{3333}}\partial\kappa^*_{\underline{33}} + \partial\delta\kappa^*_{\underline{33}}\hat{\bar{T}}^{*\underline{33}}$, are now added to (51). The latter can be finally written in tensor form as

$$\delta w^* = \delta\boldsymbol{\kappa}^{*\mathrm{S}} : \hat{\bar{\boldsymbol{T}}}^{*\mathrm{S}}, \qquad \partial\delta w^* = \delta\boldsymbol{\kappa}^{*\mathrm{S}} : \hat{\bar{\mathbb{E}}}^{*\mathrm{SS}} : \partial\boldsymbol{\kappa}^{*\mathrm{S}} + \partial\delta\boldsymbol{\kappa}^{*\mathrm{S}} : \hat{\bar{\boldsymbol{T}}}^{*\mathrm{S}}, \tag{54}$$

where

$$\hat{\bar{\boldsymbol{T}}}^{*\mathrm{S}} = \hat{\bar{T}}^{*ij}\boldsymbol{g}^*_i \otimes \boldsymbol{g}^*_j, \qquad \hat{\bar{\mathbb{E}}}^{*\mathrm{SS}} = \hat{\bar{E}}^{*ijkl}\boldsymbol{g}^*_i \otimes \boldsymbol{g}^*_j \otimes \boldsymbol{g}^*_k \otimes \boldsymbol{g}^*_l, \tag{55}$$

are referred to as the *full reduced stress parameter* and the *full reduced elastic tensor*, respectively. Equation (54) holds the elements of a full three-dimensional constitutive law, written in incremental form, with $\hat{\bar{\boldsymbol{T}}}^{*\mathrm{S}}$ the stress parameter and $\hat{\bar{\mathbb{E}}}^{*\mathrm{SS}}$ the relevant elastic tensor. $\hat{\bar{\boldsymbol{T}}}^{*\mathrm{S}}$ should replace $\hat{\boldsymbol{T}}^{*\mathrm{S}}$ in the computation of the Biot stress tensor, $\hat{\boldsymbol{T}}^* = \hat{\bar{\boldsymbol{T}}}^{*\mathrm{S}} + \hat{\boldsymbol{\tau}}^*\times$, to be used within (45). In $(45)_2$, $\hat{\bar{\mathbb{E}}}^{*\mathrm{SS}}$ should replace $\hat{\mathbb{E}}^{*\mathrm{SS}}$.

The three-dimensional incremental constitutive law is built dynamically during the solution process. Every component in (55) is computed as in (49) and (53), using the current components of the stress parameter and elastic tensor of the original three-dimensional constitutive law. These computations are performed within the Newton–Raphson iterations themselves of the overall problem solution, as in [de Borst 1991]. At the end of each iteration, once the increments $\partial\boldsymbol{\kappa}^{*\mathrm{S}}$ are known from the overall solution, $\partial\varepsilon^*_{\underline{33}}$ is computed locally from (47) and the locally stored transverse normal strain component is updated additively, $\varepsilon^*_{\underline{33}} \leftarrow \varepsilon^*_{\underline{33}} + \partial\varepsilon^*_{\underline{33}}$. Of course, at that stage the coefficients in (47) must be consistent with those in (49), so they must be saved in the quadrature point storage area.

5.5. ***Case of linear elasticity.*** The purpose of this section is to show how the adaptation discussed above can accommodate the classical plane-stress state in linear elasticity. This section is included for the sake of completeness, and not reading it does not impair understanding of the formulation.

The adaptation of the local constitutive law is somewhat simpler in linear elasticity, when

$$w^*(\boldsymbol{\varepsilon}^{*\mathrm{S}}) = \tfrac{1}{2}\,\boldsymbol{\varepsilon}^{*\mathrm{S}} : \hat{\mathbb{E}}^{*\mathrm{SS}} : \boldsymbol{\varepsilon}^{*\mathrm{S}} \quad \text{and} \quad \hat{\boldsymbol{T}}^{*\mathrm{S}}(\boldsymbol{\varepsilon}^{*\mathrm{S}}) = \hat{\mathbb{E}}^{*\mathrm{SS}} : \boldsymbol{\varepsilon}^{*\mathrm{S}},$$

with $\hat{\mathbb{E}}^{*\mathrm{SS}}$ a constant fourth-order tensor. In this case, study of the simple strain-energy virtual variation $\delta w^* = \delta\boldsymbol{\varepsilon}^{*\mathrm{S}} : \hat{\boldsymbol{T}}^{*\mathrm{S}} = \delta\boldsymbol{\varepsilon}^{*\mathrm{S}} : \hat{\mathbb{E}}^{*\mathrm{SS}} : \boldsymbol{\varepsilon}^{*\mathrm{S}}$ suffices, and study of the incremental form is not required. In

component form, with $\kappa^*_{\underline{\alpha\beta}}$ and $\kappa^*_{\underline{\alpha 3}}$ substituted for $\varepsilon^*_{\underline{\alpha\beta}}$ and $\varepsilon^*_{\underline{\alpha 3}}$, δw^* reads

$$\delta w^* = \begin{Bmatrix} \delta\kappa^*_{\underline{\alpha\beta}} \\ 2\delta\kappa^*_{\underline{\alpha 3}} \\ \delta\varepsilon^*_{\underline{33}} \end{Bmatrix}^{\mathrm{T}} \begin{Bmatrix} \hat{T}^{*\underline{\alpha\beta}} \\ \hat{T}^{*\underline{\alpha 3}} \\ \hat{T}^{*\underline{33}} \end{Bmatrix} = \begin{Bmatrix} \delta\kappa^*_{\underline{\alpha\beta}} \\ 2\delta\kappa^*_{\underline{\alpha 3}} \\ \delta\varepsilon^*_{\underline{33}} \end{Bmatrix}^{\mathrm{T}} \begin{bmatrix} \hat{E}^{*\underline{\alpha\beta\gamma\delta}} & \hat{E}^{*\underline{\alpha\beta\gamma 3}} & \hat{E}^{*\underline{\alpha\beta 33}} \\ \hat{E}^{*\underline{\alpha 3\gamma\delta}} & \hat{E}^{*\underline{\alpha 3\gamma 3}} & \hat{E}^{*\underline{\alpha 333}} \\ \hat{E}^{*\underline{33\gamma\delta}} & \hat{E}^{*\underline{33\gamma 3}} & \hat{E}^{*\underline{3333}} \end{bmatrix} \begin{Bmatrix} \kappa^*_{\underline{\gamma\delta}} \\ 2\kappa^*_{\underline{\gamma 3}} \\ \varepsilon^*_{\underline{33}} \end{Bmatrix}. \tag{56}$$

The term in $\delta\varepsilon^*_{\underline{33}}$ of this contribution to the overall principle yields now the local finite equation

$$\hat{T}^{*\underline{33}} = \begin{bmatrix} \hat{E}^{*\underline{33\gamma\delta}} & \hat{E}^{*\underline{33\gamma 3}} \end{bmatrix} \begin{Bmatrix} \kappa^*_{\underline{\gamma\delta}} \\ 2\kappa^*_{\underline{\gamma 3}} \end{Bmatrix} + \hat{E}^{*\underline{3333}} \varepsilon^*_{\underline{33}} = 0, \tag{57}$$

which again states the independence of the strain-energy function from the transverse normal strain. Solving (57) for $\varepsilon^*_{\underline{33}}$ and substituting the result into (56) yields a condensed form where the reduced components of the elastic tensor are those found in $(49)_2$. Finally, a transverse stiffness is introduced as for (52) and (53), and (56) takes the final tensor form

$$\delta w^* = \delta\boldsymbol{\kappa}^{*\mathrm{S}} : \hat{\bar{\boldsymbol{T}}}^{*\mathrm{S}} = \delta\boldsymbol{\kappa}^{*\mathrm{S}} : \hat{\bar{\mathbb{E}}}^{*\mathrm{SS}} : \boldsymbol{\kappa}^{*\mathrm{S}}, \tag{58}$$

with

$$\hat{\bar{\boldsymbol{T}}}^{*\mathrm{S}} = \hat{\bar{\mathbb{E}}}^{*\mathrm{SS}} : \boldsymbol{\kappa}^{*\mathrm{S}} \tag{59}$$

the full three-dimensional linear constitutive equation. The components of $\hat{\bar{\mathbb{E}}}^{*\mathrm{SS}}$ are found in $(49)_2$ and $(53)_2$. Since such components are constant, they can be computed once and for all, and there is no need to allocate the variable $\varepsilon^*_{\underline{33}}$ in linear elasticity.

6. Reduction to the shell surface mechanics

The next step is to integrate the internal work virtual functional across the shell model thickness and to obtain the shell constitutive equations.

6.1. ***Integration across the thickness.*** The local variation variables in (45) must be solved for the relevant surface variation variables before addressing the integration across the thickness. The kinematical variation variables are quite complicated to develop; they are discussed in the Appendix and yield the final result

$$\begin{aligned}
\delta(\boldsymbol{\Psi}^{*\mathrm{T}}\boldsymbol{\omega}^*) &= \left(\boldsymbol{\Psi}^{*\mathrm{T}} \cdot \boldsymbol{H}\delta(\boldsymbol{H}^{\mathrm{T}}\boldsymbol{\omega}_\alpha) + \xi^3\boldsymbol{\Psi}^{*\mathrm{T}}\boldsymbol{k}'_\alpha \times \tilde{\boldsymbol{\Lambda}}' \cdot \boldsymbol{A}'\delta\boldsymbol{\theta}'\right) \otimes \boldsymbol{g}^{*\alpha} + \boldsymbol{\Psi}^{*\mathrm{T}}\tilde{\boldsymbol{H}}' \cdot \boldsymbol{A}'\delta\boldsymbol{\theta}' \otimes \boldsymbol{g}^{*3}, \\
\partial(\boldsymbol{\Psi}^{*\mathrm{T}}\boldsymbol{\omega}^*) &= \left(\boldsymbol{\Psi}^{*\mathrm{T}} \cdot \boldsymbol{H}\partial(\boldsymbol{H}^{\mathrm{T}}\boldsymbol{\omega}_\alpha) + \xi^3\boldsymbol{\Psi}^{*\mathrm{T}}\boldsymbol{k}'_\alpha \times \tilde{\boldsymbol{\Lambda}}' \cdot \boldsymbol{A}'\partial\boldsymbol{\theta}'\right) \otimes \boldsymbol{g}^{*\alpha} + \boldsymbol{\Psi}^{*\mathrm{T}}\tilde{\boldsymbol{H}}' \cdot \boldsymbol{A}'\partial\boldsymbol{\theta}' \otimes \boldsymbol{g}^{*3}, \\
\partial\delta(\boldsymbol{\Psi}^{*\mathrm{T}}\boldsymbol{\omega}^*) &= \Big(\boldsymbol{\Psi}^{*\mathrm{T}} \cdot \boldsymbol{H}\partial\delta(\boldsymbol{H}^{\mathrm{T}}\boldsymbol{\omega}_\alpha) + \xi^3\boldsymbol{\Psi}^{*\mathrm{T}}\boldsymbol{k}'_\alpha \times \tilde{\boldsymbol{\Lambda}}' \cdot \boldsymbol{A}'\partial\delta\boldsymbol{\theta}' \\
&\qquad - \xi^3\boldsymbol{\Psi}^{*\mathrm{T}}\boldsymbol{I}^{\times}\tilde{\boldsymbol{\Lambda}}' : \left(\boldsymbol{H}\delta(\boldsymbol{H}^{\mathrm{T}}\boldsymbol{\omega}_\alpha) \otimes \boldsymbol{A}'\partial\boldsymbol{\theta}' + \boldsymbol{H}\partial(\boldsymbol{H}^{\mathrm{T}}\boldsymbol{\omega}_\alpha) \otimes \boldsymbol{A}'\delta\boldsymbol{\theta}'\right) \\
&\qquad + (\xi^3)^2\boldsymbol{\Psi}^{*\mathrm{T}} \cdot \left(\boldsymbol{k}'_\alpha \times \tilde{\boldsymbol{\Lambda}}'^{\underline{123}}_{\mathrm{III}} + (\boldsymbol{I}^{\times}\boldsymbol{k}'_\alpha \times \tilde{\boldsymbol{\Lambda}}')^{\mathrm{T}132}\tilde{\boldsymbol{\Lambda}}'\right)^{\mathrm{S}1\underline{23}} : \boldsymbol{A}'\delta\boldsymbol{\theta}' \otimes \boldsymbol{A}'\partial\boldsymbol{\theta}'\Big) \otimes \boldsymbol{g}^{*\alpha} \\
&\quad + \boldsymbol{\Psi}^{*\mathrm{T}}\tilde{\boldsymbol{H}}' \cdot \boldsymbol{A}'\partial\delta\boldsymbol{\theta}' \otimes \boldsymbol{g}^{*3}.
\end{aligned} \tag{60}$$

Obtaining the Biot-axial variation variables from (43), instead, is immediate:

$$\begin{gathered}\delta\hat{\boldsymbol{\tau}}^* = h^{-1}\tilde{\boldsymbol{F}}^{-\mathrm{T}}(\delta\hat{\boldsymbol{\tau}} + \xi^3 h^{-1}\delta\hat{\boldsymbol{\mu}}), \quad \partial\hat{\boldsymbol{\tau}}^* = h^{-1}\tilde{\boldsymbol{F}}^{-\mathrm{T}}(\partial\hat{\boldsymbol{\tau}} + \xi^3 h^{-1}\partial\hat{\boldsymbol{\mu}}),\\ \partial\delta\hat{\boldsymbol{\tau}}^* = h^{-1}\tilde{\boldsymbol{F}}^{-\mathrm{T}}(\partial\delta\hat{\boldsymbol{\tau}} + \xi^3 h^{-1}\partial\delta\hat{\boldsymbol{\mu}}).\end{gathered} \tag{61}$$

Substituting (60) and (61) into (45) yields

$$\begin{aligned}\pi_{\mathrm{int}\delta} &= \begin{Bmatrix}\delta(\boldsymbol{H}^{\mathrm{T}}\boldsymbol{\omega}_\alpha)\\ \delta\boldsymbol{\theta}'\\ \delta\hat{\boldsymbol{\mu}}\\ \delta\hat{\boldsymbol{\tau}}\end{Bmatrix}^{\mathrm{T}} \cdot \begin{Bmatrix}\boldsymbol{H}^{\mathrm{T}}\boldsymbol{R}^\alpha_{\boldsymbol{\omega}}\\ \boldsymbol{A}'^{\mathrm{T}}\boldsymbol{R}_{\boldsymbol{\theta}}\\ \boldsymbol{R}_{\boldsymbol{\mu}}\\ \boldsymbol{R}_{\boldsymbol{\tau}}\end{Bmatrix},\\ \partial\pi_{\mathrm{int}\delta} &= \begin{Bmatrix}\delta(\boldsymbol{H}^{\mathrm{T}}\boldsymbol{\omega}_\alpha)\\ \delta\boldsymbol{\theta}'\\ \delta\hat{\boldsymbol{\mu}}\\ \delta\hat{\boldsymbol{\tau}}\end{Bmatrix}^{\mathrm{T}} \cdot \begin{bmatrix}\boldsymbol{H}^{\mathrm{T}}\boldsymbol{D}^{\alpha\beta}_{\boldsymbol{\omega\omega}}\boldsymbol{H} & \boldsymbol{H}^{\mathrm{T}}\boldsymbol{D}^{\alpha}_{\boldsymbol{\omega\theta}}\boldsymbol{A}' & \boldsymbol{H}^{\mathrm{T}}\boldsymbol{D}^{\alpha}_{\boldsymbol{\omega\mu}} & \boldsymbol{H}^{\mathrm{T}}\boldsymbol{D}^{\alpha}_{\boldsymbol{\omega\tau}}\\ \boldsymbol{A}'^{\mathrm{T}}\boldsymbol{D}^{\beta\mathrm{T}}_{\boldsymbol{\omega\theta}}\boldsymbol{H} & \boldsymbol{A}'^{\mathrm{T}}\boldsymbol{D}_{\boldsymbol{\theta\theta}}\boldsymbol{A}' & \boldsymbol{A}'^{\mathrm{T}}\boldsymbol{D}_{\boldsymbol{\theta\mu}} & \boldsymbol{A}'^{\mathrm{T}}\boldsymbol{D}_{\boldsymbol{\theta\tau}}\\ \boldsymbol{D}^{\beta\mathrm{T}}_{\boldsymbol{\omega\mu}}\boldsymbol{H} & \boldsymbol{D}^{\mathrm{T}}_{\boldsymbol{\theta\mu}}\boldsymbol{A}' & \boldsymbol{0} & \boldsymbol{0}\\ \boldsymbol{D}^{\beta\mathrm{T}}_{\boldsymbol{\omega\tau}}\boldsymbol{H} & \boldsymbol{D}^{\mathrm{T}}_{\boldsymbol{\theta\tau}}\boldsymbol{A}' & \boldsymbol{0} & \boldsymbol{0}\end{bmatrix} \cdot \begin{Bmatrix}\partial(\boldsymbol{H}^{\mathrm{T}}\boldsymbol{\omega}_\beta)\\ \partial\boldsymbol{\theta}'\\ \partial\hat{\boldsymbol{\mu}}\\ \partial\hat{\boldsymbol{\tau}}\end{Bmatrix}\\ &\quad + \begin{Bmatrix}\partial\delta(\boldsymbol{H}^{\mathrm{T}}\boldsymbol{\omega}_\alpha)\\ \partial\delta\boldsymbol{\theta}'\\ \partial\delta\hat{\boldsymbol{\mu}}\\ \partial\delta\hat{\boldsymbol{\tau}}\end{Bmatrix}^{\mathrm{T}} \cdot \begin{Bmatrix}\boldsymbol{H}^{\mathrm{T}}\boldsymbol{R}^\alpha_{\boldsymbol{\omega}}\\ \boldsymbol{A}'^{\mathrm{T}}\boldsymbol{R}_{\boldsymbol{\theta}}\\ \boldsymbol{R}_{\boldsymbol{\mu}}\\ \boldsymbol{R}_{\boldsymbol{\tau}}\end{Bmatrix},\end{aligned} \tag{62}$$

where the sequence angular–linear is understood while writing dual vectors and tensors in matrix notation. After some involved manipulations, detailed in [Merlini and Morandini 2008], the vectors $\boldsymbol{R}$ and tensors $\boldsymbol{D}$ in (62) can be written as the integrals

$$\begin{aligned}\{\boldsymbol{R}^\alpha_{\boldsymbol{\omega}}\} &= \int_{\xi^{3-}}^{\xi^{3+}} \begin{Bmatrix}\text{dual } \acute{\boldsymbol{S}}^{*\alpha}\\ \text{primal } \acute{\boldsymbol{S}}^{*\alpha}\end{Bmatrix} \tilde{f}h\,\mathrm{d}\xi^3,\\ \{\boldsymbol{R}_{\boldsymbol{\theta}}\} &= \int_{\xi^{3-}}^{\xi^{3+}} \begin{Bmatrix}\text{dual } (\xi^3\tilde{\boldsymbol{\Lambda}}'^{\mathrm{T}}\acute{\boldsymbol{S}}^{*\gamma} \times \boldsymbol{k}'_\gamma + \tilde{\boldsymbol{H}}'^{\mathrm{T}}\acute{\boldsymbol{S}}^{*3})\\ \text{primal } (\xi^3\tilde{\boldsymbol{\Lambda}}'^{\mathrm{T}}\acute{\boldsymbol{S}}^{*\gamma} \times \boldsymbol{k}'_\gamma + \tilde{\boldsymbol{H}}'^{\mathrm{T}}\acute{\boldsymbol{S}}^{*3})\end{Bmatrix} \tilde{f}h\,\mathrm{d}\xi^3,\\ \boldsymbol{R}_{\boldsymbol{\mu}} &= \int_{\xi^{3-}}^{\xi^{3+}} \xi^3 h^{-2}\tilde{\boldsymbol{F}}^{-1}\,\text{dual}\,2\,\text{ax}\,(\boldsymbol{\Psi}^{*\mathrm{T}}\boldsymbol{\omega}^*)\,\tilde{f}h\,\mathrm{d}\xi^3,\\ \boldsymbol{R}_{\boldsymbol{\tau}} &= \int_{\xi^{3-}}^{\xi^{3+}} h^{-1}\tilde{\boldsymbol{F}}^{-1}\,\text{dual}\,2\,\text{ax}\,(\boldsymbol{\Psi}^{*\mathrm{T}}\boldsymbol{\omega}^*)\,\tilde{f}h\,\mathrm{d}\xi^3,\end{aligned} \tag{63}$$

and

$$\begin{aligned}[\boldsymbol{D}^{\alpha\beta}_{\boldsymbol{\omega\omega}}] &= \int_{\xi^{3-}}^{\xi^{3+}} \begin{bmatrix}\text{dual } \boldsymbol{\Psi}^*\\ \text{primal } \boldsymbol{\Psi}^*\end{bmatrix} (\boldsymbol{g}^{*\alpha}\hat{\bar{\mathbb{E}}}^{*\mathrm{SS}}\boldsymbol{g}^{*\beta}) \begin{bmatrix}\text{dual } \boldsymbol{\Psi}^{*\mathrm{T}} & \text{primal } \boldsymbol{\Psi}^{*\mathrm{T}}\end{bmatrix} \tilde{f}h\,\mathrm{d}\xi^3,\\ [\boldsymbol{D}^{\alpha}_{\boldsymbol{\omega\theta}}] &= \int_{\xi^{3-}}^{\xi^{3+}} \begin{bmatrix}\text{dual } \boldsymbol{\Psi}^*\\ \text{primal } \boldsymbol{\Psi}^*\end{bmatrix} \begin{bmatrix}\boldsymbol{g}^{*\alpha}\hat{\bar{\mathbb{E}}}^{*\mathrm{SS}}\boldsymbol{g}^{*\delta} & \boldsymbol{g}^{*\alpha}\hat{\bar{\mathbb{E}}}^{*\mathrm{SS}}\boldsymbol{g}^{*3}\end{bmatrix}\\ &\qquad \cdot \begin{bmatrix}\text{dual } (-\xi^3\tilde{\boldsymbol{\Lambda}}'^{\mathrm{T}}\boldsymbol{k}'_\delta \times \boldsymbol{\Psi}^*)^{\mathrm{T}} & \text{primal } (-\xi^3\tilde{\boldsymbol{\Lambda}}'^{\mathrm{T}}\boldsymbol{k}'_\delta \times \boldsymbol{\Psi}^*)^{\mathrm{T}}\\ \text{dual } (\tilde{\boldsymbol{H}}'^{\mathrm{T}}\boldsymbol{\Psi}^*)^{\mathrm{T}} & \text{primal } (\tilde{\boldsymbol{H}}'^{\mathrm{T}}\boldsymbol{\Psi}^*)^{\mathrm{T}}\end{bmatrix} \tilde{f}h\,\mathrm{d}\xi^3\\ &\qquad + \int_{\xi^{3-}}^{\xi^{3+}} \begin{bmatrix}\text{dual } (-\xi^3\acute{\boldsymbol{S}}^{*\alpha} \times \tilde{\boldsymbol{\Lambda}}') & \text{primal } (-\xi^3\acute{\boldsymbol{S}}^{*\alpha} \times \tilde{\boldsymbol{\Lambda}}')\\ \text{primal } (-\xi^3\acute{\boldsymbol{S}}^{*\alpha} \times \tilde{\boldsymbol{\Lambda}}') & \boldsymbol{0}\end{bmatrix} \tilde{f}h\,\mathrm{d}\xi^3,\end{aligned}$$

$$
\begin{aligned}
[\boldsymbol{D}^{\alpha}_{\boldsymbol{\omega\mu}}] &= \int_{\xi^{3-}}^{\xi^{3+}} \begin{bmatrix} \text{dual}\,\boldsymbol{\Psi}^* \\ \text{primal}\,\boldsymbol{\Psi}^* \end{bmatrix} (\xi^3 h^{-2}\tilde{\boldsymbol{F}}^{-1}\boldsymbol{g}^{*\alpha}\times)^{\mathrm{T}}\tilde{f}h\,\mathrm{d}\xi^3,\\
[\boldsymbol{D}^{\alpha}_{\boldsymbol{\omega\tau}}] &= \int_{\xi^{3-}}^{\xi^{3+}} \begin{bmatrix} \text{dual}\,\boldsymbol{\Psi}^* \\ \text{primal}\,\boldsymbol{\Psi}^* \end{bmatrix} (h^{-1}\tilde{\boldsymbol{F}}^{-1}\boldsymbol{g}^{*\alpha}\times)^{\mathrm{T}}\tilde{f}h\,\mathrm{d}\xi^3,\\
[\boldsymbol{D}^{*}_{\boldsymbol{\theta\theta}}] &= \int_{\xi^{3-}}^{\xi^{3+}} \begin{bmatrix} \text{dual}\,(-\xi^3\tilde{\boldsymbol{\Lambda}}'^{\mathrm{T}}\boldsymbol{k}'_{\gamma}\times\boldsymbol{\Psi}^*) & \text{dual}\,(\tilde{\boldsymbol{H}}'^{\mathrm{T}}\boldsymbol{\Psi}^*) \\ \text{primal}\,(-\xi^3\tilde{\boldsymbol{\Lambda}}'^{\mathrm{T}}\boldsymbol{k}'_{\gamma}\times\boldsymbol{\Psi}^*) & \text{primal}\,(\tilde{\boldsymbol{H}}'^{\mathrm{T}}\boldsymbol{\Psi}^*) \end{bmatrix} \begin{bmatrix} \boldsymbol{g}^{*\gamma}\hat{\bar{\mathbb{E}}}^{*\mathrm{SS}}\boldsymbol{g}^{*\delta} & \boldsymbol{g}^{*\gamma}\hat{\bar{\mathbb{E}}}^{*\mathrm{SS}}\boldsymbol{g}^{*3} \\ \boldsymbol{g}^{*3}\hat{\bar{\mathbb{E}}}^{*\mathrm{SS}}\boldsymbol{g}^{*\delta} & \boldsymbol{g}^{*3}\hat{\bar{\mathbb{E}}}^{*\mathrm{SS}}\boldsymbol{g}^{*3} \end{bmatrix}\\
&\quad\cdot \begin{bmatrix} \text{dual}\,(-\xi^3\tilde{\boldsymbol{\Lambda}}'^{\mathrm{T}}\boldsymbol{k}'_{\delta}\times\boldsymbol{\Psi}^*)^{\mathrm{T}} & \text{primal}\,(-\xi^3\tilde{\boldsymbol{\Lambda}}'^{\mathrm{T}}\boldsymbol{k}'_{\delta}\times\boldsymbol{\Psi}^*)^{\mathrm{T}} \\ \text{dual}\,(\tilde{\boldsymbol{H}}'^{\mathrm{T}}\boldsymbol{\Psi}^*)^{\mathrm{T}} & \text{primal}\,(\tilde{\boldsymbol{H}}'^{\mathrm{T}}\boldsymbol{\Psi}^*)^{\mathrm{T}} \end{bmatrix} f h\,\mathrm{d}\xi^3\\
&\quad+\int_{\xi^{3-}}^{\xi^{3+}} \begin{bmatrix} \text{dual}\left((\xi^3)^2\big(\acute{\boldsymbol{S}}^{*\gamma}\times\boldsymbol{k}'_{\gamma}\cdot\tilde{\boldsymbol{\Lambda}}'^{\underline{123}}_{\mathrm{III}}+\tilde{\boldsymbol{\Lambda}}'^{\mathrm{T}}(\acute{\boldsymbol{S}}^{*\gamma}\times\boldsymbol{k}'_{\gamma}\times)^{\mathrm{S}}\tilde{\boldsymbol{\Lambda}}'\big)\right) \\ \text{primal}\left((\xi^3)^2\big(\acute{\boldsymbol{S}}^{*\gamma}\times\boldsymbol{k}'_{\gamma}\cdot\tilde{\boldsymbol{\Lambda}}'^{\underline{123}}_{\mathrm{III}}+\tilde{\boldsymbol{\Lambda}}'^{\mathrm{T}}(\acute{\boldsymbol{S}}^{*\gamma}\times\boldsymbol{k}'_{\gamma}\times)^{\mathrm{S}}\tilde{\boldsymbol{\Lambda}}'\big)\right) \\ \text{primal}\left((\xi^3)^2\big(\acute{\boldsymbol{S}}^{*\gamma}\times\boldsymbol{k}'_{\gamma}\cdot\tilde{\boldsymbol{\Lambda}}'^{\underline{123}}_{\mathrm{III}}+\tilde{\boldsymbol{\Lambda}}'^{\mathrm{T}}(\acute{\boldsymbol{S}}^{*\gamma}\times\boldsymbol{k}'_{\gamma}\times)^{\mathrm{S}}\tilde{\boldsymbol{\Lambda}}'\big)\right) \\ \boldsymbol{0} \end{bmatrix} \tilde{f}h\,\mathrm{d}\xi^3,\\
[\boldsymbol{D}_{\boldsymbol{\theta\mu}}] &= \int_{\xi^{3-}}^{\xi^{3+}} \begin{bmatrix} \text{dual}\,(-\xi^3\tilde{\boldsymbol{\Lambda}}'^{\mathrm{T}}\boldsymbol{k}'_{\gamma}\times\boldsymbol{\Psi}^*) & \text{dual}\,(\tilde{\boldsymbol{H}}'^{\mathrm{T}}\boldsymbol{\Psi}^*) \\ \text{primal}\,(-\xi^3\tilde{\boldsymbol{\Lambda}}'^{\mathrm{T}}\boldsymbol{k}'_{\gamma}\times\boldsymbol{\Psi}^*) & \text{primal}\,(\tilde{\boldsymbol{H}}'^{\mathrm{T}}\boldsymbol{\Psi}^*) \end{bmatrix} \begin{bmatrix} (\xi^3 h^{-2}\tilde{\boldsymbol{F}}^{-1}\boldsymbol{g}^{*\gamma}\times)^{\mathrm{T}} \\ (\xi^3 h^{-2}\tilde{\boldsymbol{F}}^{-1}\boldsymbol{g}^{*3}\times)^{\mathrm{T}} \end{bmatrix} \tilde{f}h\,\mathrm{d}\xi^3,\\
[\boldsymbol{D}_{\boldsymbol{\theta\tau}}] &= \int_{\xi^{3-}}^{\xi^{3+}} \begin{bmatrix} \text{dual}\,(-\xi^3\tilde{\boldsymbol{\Lambda}}'^{\mathrm{T}}\boldsymbol{k}'_{\gamma}\times\boldsymbol{\Psi}^*) & \text{dual}\,(\tilde{\boldsymbol{H}}'^{\mathrm{T}}\boldsymbol{\Psi}^*) \\ \text{primal}\,(-\xi^3\tilde{\boldsymbol{\Lambda}}'^{\mathrm{T}}\boldsymbol{k}'_{\gamma}\times\boldsymbol{\Psi}^*) & \text{primal}\,(\tilde{\boldsymbol{H}}'^{\mathrm{T}}\boldsymbol{\Psi}^*) \end{bmatrix} \begin{bmatrix} (h^{-1}\tilde{\boldsymbol{F}}^{-1}\boldsymbol{g}^{*\gamma}\times)^{\mathrm{T}} \\ (h^{-1}\tilde{\boldsymbol{F}}^{-1}\boldsymbol{g}^{*3}\times)^{\mathrm{T}} \end{bmatrix} \tilde{f}h\,\mathrm{d}\xi^3,
\end{aligned}
\tag{64}
$$

where $\acute{\boldsymbol{S}}^*$ must be understood as a short notation for $\boldsymbol{X}'^*\acute{\boldsymbol{T}}^* = \acute{\boldsymbol{T}}^* + \varepsilon\boldsymbol{x}'^*\times\acute{\boldsymbol{T}}^*$, the pole-based dual version of the first Piola–Kirchhoff stress tensor.

Equation (63) collects the vectors work-conjugate to the material surface variation variables in the virtual functional $\pi_{\mathrm{int}\delta}$, whereas (64) gives the tensors of the relevant tangent map in $\partial\pi_{\mathrm{int}\delta}$. Note that the tangent map is symmetrical, see $(62)_2$. Vectors and tensors in (63) and (64) are integrals along ξ^3 of quantities depending ultimately on the current values of the kinematical variables and Biot-axial parameters of the material surface. Thus, the internal-work incremental virtual functional $\pi_{\mathrm{int}\delta} + \partial\pi_{\mathrm{int}\delta}$ becomes two-dimensional: it depends linearly on the virtual, incremental, and mixed virtual-incremental variations of the surface strain component vectors $\boldsymbol{H}^{\mathrm{T}}\boldsymbol{\omega}_{\alpha}$, the dual director $\boldsymbol{\theta}'$, and the Biot-axial parameters $\hat{\boldsymbol{\tau}}$ and $\hat{\boldsymbol{\mu}}$. Note that the back-rototranslated dual strains $\boldsymbol{H}^{\mathrm{T}}\boldsymbol{\omega}_{\alpha}$ are the pole-based version of the back-rotated self-based dual strains $\boldsymbol{\Phi}^{\mathrm{T}}\boldsymbol{X}'^{\mathrm{T}}\boldsymbol{\omega}_{\alpha}$.

6.2. ***Shell constitutive equations.*** As stated in Section 4.2, the dual director kinematic field is a gradientless, piecewise constant field on the shell surface. In a finite element context, $\boldsymbol{\theta}$ should be understood as a local variable, and as such, it would be profitably considered for a local condensation process. However, it can be observed that $\boldsymbol{\theta}$ alone cannot be condensed. In fact, the rototranslation generating the shell model, $\tilde{\boldsymbol{H}} = \exp(\xi^3(\boldsymbol{A}\boldsymbol{\theta})\times)$, is endowed ultimately with the contribution of three linear and three angular components. When the shell deforms, the change of the linear part produces strains, which

are withstood elastically; the change of the angular part, instead, is a rotation that must fulfill the kinematical constraint (38) and entails a workless Biot-axial field as a multiplier. So, $\boldsymbol{\theta}$ alone is three times indeterminate, and needs three further parameters to be condensed with: the Biot-axial parameter vector $\hat{\boldsymbol{\mu}}$, which controls that part of $\hat{\boldsymbol{\tau}}^*$ variable across the shell thickness, appears a likely candidate to make $\boldsymbol{\theta}$ determinate. As a matter of fact, after a systematic series of numerical tests with several combinations of the components of $\hat{\boldsymbol{\tau}}$ and $\hat{\boldsymbol{\mu}}$, it was confirmed that the set composed of $\boldsymbol{\theta}'$ and the vector $\hat{\boldsymbol{\mu}}$ could be safely solved locally. This choice leaves $\boldsymbol{\omega}_\alpha$ and $\hat{\boldsymbol{\tau}}$ as the *basic parameters* governing the internal work virtual functional of the material surface — a picture consistent with the case of three-dimensional elasticity outlined in Section 5.1.

The condensation process traces the steps carried out in Section 5.4 for the local constitutive law (refer to [Merlini and Morandini 2008] for further details). Starting from (62), the internal-work incremental virtual functional $\pi_{\mathrm{int}\delta} + \partial\pi_{\mathrm{int}\delta}$ is written; since $\boldsymbol{\theta}'$ and $\hat{\boldsymbol{\mu}}$ are local, independent variables, the terms with $\partial\delta\boldsymbol{\theta}'$ and $\partial\delta\hat{\boldsymbol{\mu}}$ are of course omitted, whereas the terms in $\delta\boldsymbol{\theta}'$ and $\delta\hat{\boldsymbol{\mu}}$ keep disjoint from the overall principle and originate the local incremental equation

$$\begin{Bmatrix} \boldsymbol{A}'^{\mathrm{T}}\boldsymbol{R}_\theta \\ \boldsymbol{R}_\mu \end{Bmatrix} + \begin{bmatrix} \boldsymbol{A}'^{\mathrm{T}}\boldsymbol{D}^{\beta\mathrm{T}}_{\omega\theta}\boldsymbol{H} & \boldsymbol{A}'^{\mathrm{T}}\boldsymbol{D}_{\theta\tau} \\ \boldsymbol{D}^{\beta\mathrm{T}}_{\omega\mu}\boldsymbol{H} & \boldsymbol{0} \end{bmatrix} \cdot \begin{Bmatrix} \partial(\boldsymbol{H}^{\mathrm{T}}\boldsymbol{\omega}_\beta) \\ \partial\hat{\boldsymbol{\tau}} \end{Bmatrix} + \begin{bmatrix} \boldsymbol{A}'^{\mathrm{T}}\boldsymbol{D}_{\theta\theta}\boldsymbol{A}' & \boldsymbol{A}'^{\mathrm{T}}\boldsymbol{D}_{\theta\mu} \\ \boldsymbol{D}^{\mathrm{T}}_{\theta\mu}\boldsymbol{A}' & \boldsymbol{0} \end{bmatrix} \cdot \begin{Bmatrix} \partial\boldsymbol{\theta}' \\ \partial\hat{\boldsymbol{\mu}} \end{Bmatrix} = \begin{Bmatrix} \boldsymbol{0} \\ \boldsymbol{0} \end{Bmatrix}. \tag{65}$$

Solving (65) for $\partial\boldsymbol{\theta}'$ and $\partial\hat{\boldsymbol{\mu}}$ and substituting the result in the expression of $\pi_{\mathrm{int}\delta} + \partial\pi_{\mathrm{int}\delta}$ yields the condensed form

$$\pi_{\mathrm{int}\delta} + \partial\pi_{\mathrm{int}\delta} = \begin{Bmatrix} \delta(\boldsymbol{H}^{\mathrm{T}}\boldsymbol{\omega}_\alpha) \\ \delta\hat{\boldsymbol{\tau}} \end{Bmatrix}^{\mathrm{T}} \cdot \left(\begin{Bmatrix} \boldsymbol{H}^{\mathrm{T}}\bar{\boldsymbol{R}}^\alpha_\omega \\ \bar{\boldsymbol{R}}_\tau \end{Bmatrix} + \begin{bmatrix} \boldsymbol{H}^{\mathrm{T}}\bar{\boldsymbol{D}}^{\alpha\beta}_{\omega\omega}\boldsymbol{H} & \boldsymbol{H}^{\mathrm{T}}\bar{\boldsymbol{D}}^\alpha_{\omega\tau} \\ \bar{\boldsymbol{D}}^{\beta\mathrm{T}}_{\omega\tau}\boldsymbol{H} & \bar{\boldsymbol{D}}_{\tau\tau} \end{bmatrix} \cdot \begin{Bmatrix} \partial(\boldsymbol{H}^{\mathrm{T}}\boldsymbol{\omega}_\beta) \\ \partial\hat{\boldsymbol{\tau}} \end{Bmatrix} \right) + \begin{Bmatrix} \partial\delta(\boldsymbol{H}^{\mathrm{T}}\boldsymbol{\omega}_\alpha) \\ \partial\delta\hat{\boldsymbol{\tau}} \end{Bmatrix}^{\mathrm{T}} \cdot \begin{Bmatrix} \boldsymbol{H}^{\mathrm{T}}\boldsymbol{R}^\alpha_\omega \\ \boldsymbol{R}_\tau \end{Bmatrix},$$

where

$$\begin{aligned} \begin{Bmatrix} \bar{\boldsymbol{R}}^\alpha_\omega \\ \bar{\boldsymbol{R}}_\tau \end{Bmatrix} &= \begin{Bmatrix} \boldsymbol{R}^\alpha_\omega \\ \boldsymbol{R}_\tau \end{Bmatrix} - \begin{bmatrix} \boldsymbol{D}^\alpha_{\omega\theta} & \boldsymbol{D}^\alpha_{\omega\mu} \\ \boldsymbol{D}^{\mathrm{T}}_{\theta\tau} & \boldsymbol{0} \end{bmatrix} \begin{bmatrix} \boldsymbol{D}_{\theta\theta} & \boldsymbol{D}_{\theta\mu} \\ \boldsymbol{D}^{\mathrm{T}}_{\theta\mu} & \boldsymbol{0} \end{bmatrix}^{-1} \begin{Bmatrix} \boldsymbol{R}_\theta \\ \boldsymbol{R}_\mu \end{Bmatrix}, \\ \begin{bmatrix} \bar{\boldsymbol{D}}^{\alpha\beta}_{\omega\omega} & \bar{\boldsymbol{D}}^\alpha_{\omega\tau} \\ \bar{\boldsymbol{D}}^{\beta\mathrm{T}}_{\omega\tau} & \bar{\boldsymbol{D}}_{\tau\tau} \end{bmatrix} &= \begin{bmatrix} \boldsymbol{D}^{\alpha\beta}_{\omega\omega} & \boldsymbol{D}^\alpha_{\omega\tau} \\ \boldsymbol{D}^{\beta\mathrm{T}}_{\omega\tau} & \boldsymbol{0} \end{bmatrix} - \begin{bmatrix} \boldsymbol{D}^\alpha_{\omega\theta} & \boldsymbol{D}^\alpha_{\omega\mu} \\ \boldsymbol{D}^{\mathrm{T}}_{\theta\tau} & \boldsymbol{0} \end{bmatrix} \begin{bmatrix} \boldsymbol{D}_{\theta\theta} & \boldsymbol{D}_{\theta\mu} \\ \boldsymbol{D}^{\mathrm{T}}_{\theta\mu} & \boldsymbol{0} \end{bmatrix}^{-1} \begin{bmatrix} \boldsymbol{D}^{\beta\mathrm{T}}_{\omega\theta} & \boldsymbol{D}_{\theta\tau} \\ \boldsymbol{D}^{\beta\mathrm{T}}_{\omega\mu} & \boldsymbol{0} \end{bmatrix}, \end{aligned} \tag{66}$$

are the *reduced* work-conjugate parameters and tangent map. Resorting to the same arguments as in Section 5.4, the terms $\boldsymbol{R}^\alpha_\omega$ and $\boldsymbol{R}_\tau$ in the expression of $\pi_{\mathrm{int}\delta} + \partial\pi_{\mathrm{int}\delta}$ are corrected for $\bar{\boldsymbol{R}}^\alpha_\omega$ and $\bar{\boldsymbol{R}}_\tau$ and the internal work virtual functional and virtual tangent functional are finally written as

$$\begin{aligned} \pi_{\mathrm{int}\delta} &= \begin{Bmatrix} \delta(\boldsymbol{H}^{\mathrm{T}}\boldsymbol{\omega}_\alpha) \\ \delta\hat{\boldsymbol{\tau}} \end{Bmatrix}^{\mathrm{T}} \cdot \begin{Bmatrix} \boldsymbol{H}^{\mathrm{T}}\bar{\boldsymbol{R}}^\alpha_\omega \\ \bar{\boldsymbol{R}}_\tau \end{Bmatrix}, \\ \partial\pi_{\mathrm{int}\delta} &= \begin{Bmatrix} \delta(\boldsymbol{H}^{\mathrm{T}}\boldsymbol{\omega}_\alpha) \\ \delta\hat{\boldsymbol{\tau}} \end{Bmatrix}^{\mathrm{T}} \cdot \begin{bmatrix} \boldsymbol{H}^{\mathrm{T}}\bar{\boldsymbol{D}}^{\alpha\beta}_{\omega\omega}\boldsymbol{H} & \boldsymbol{H}^{\mathrm{T}}\bar{\boldsymbol{D}}^\alpha_{\omega\tau} \\ \bar{\boldsymbol{D}}^{\beta\mathrm{T}}_{\omega\tau}\boldsymbol{H} & \bar{\boldsymbol{D}}_{\tau\tau} \end{bmatrix} \cdot \begin{Bmatrix} \partial(\boldsymbol{H}^{\mathrm{T}}\boldsymbol{\omega}_\beta) \\ \partial\hat{\boldsymbol{\tau}} \end{Bmatrix} + \begin{Bmatrix} \partial\delta(\boldsymbol{H}^{\mathrm{T}}\boldsymbol{\omega}_\alpha) \\ \partial\delta\hat{\boldsymbol{\tau}} \end{Bmatrix}^{\mathrm{T}} \cdot \begin{Bmatrix} \boldsymbol{H}^{\mathrm{T}}\bar{\boldsymbol{R}}^\alpha_\omega \\ \bar{\boldsymbol{R}}_\tau \end{Bmatrix}. \end{aligned} \tag{67}$$

In (67), the elements of the incremental form of a nonlinear constitutive law of the shell material surface are recognized. $\boldsymbol{H}^{\mathrm{T}}\bar{\boldsymbol{R}}^\alpha_\omega$ are the (generalized) *stress resultants* work-conjugate to the dual strains

$\boldsymbol{H}^{\mathrm{T}}\boldsymbol{\omega}_\alpha$, and $\bar{\boldsymbol{R}}_{\boldsymbol{\tau}}$ is the *integral kinematical constraint* work-conjugate to the Biot-axial parameter $\hat{\boldsymbol{\tau}}$. So, $(66)_1$ represents the *shell constitutive equations*. Linearization of the shell constitutive equations yields the *tangent map*

$$\begin{Bmatrix} \partial(\boldsymbol{H}^{\mathrm{T}}\bar{\boldsymbol{R}}^{\alpha}_{\boldsymbol{\omega}}) \\ \partial\bar{\boldsymbol{R}}_{\boldsymbol{\tau}} \end{Bmatrix} = \begin{bmatrix} \boldsymbol{H}^{\mathrm{T}}\bar{\boldsymbol{D}}^{\alpha\beta}_{\boldsymbol{\omega}\boldsymbol{\omega}}\boldsymbol{H} & \boldsymbol{H}^{\mathrm{T}}\bar{\boldsymbol{D}}^{\alpha}_{\boldsymbol{\omega}\boldsymbol{\tau}} \\ \bar{\boldsymbol{D}}^{\beta\mathrm{T}}_{\boldsymbol{\omega}\boldsymbol{\tau}}\boldsymbol{H} & \bar{\boldsymbol{D}}_{\boldsymbol{\tau}\boldsymbol{\tau}} \end{bmatrix} \cdot \begin{Bmatrix} \partial(\boldsymbol{H}^{\mathrm{T}}\boldsymbol{\omega}_\beta) \\ \partial\hat{\boldsymbol{\tau}} \end{Bmatrix}, \tag{68}$$

giving the appropriate increments of the resultant vectors from the relevant increments of the surface parameters. The *mapping tensors* $\bar{\boldsymbol{D}}$, which represent the derivatives of the resultant vectors with respect to the surface parameters, are given in $(66)_2$: they comprise altogether every kind of contribution, specifically the elastic contribution, the kinematical constraint contribution, and the geometric contribution due to the stress state.

It is worth comparing (67) with the parent (45), where the interrelation among the primary mechanical variables in three-dimensional elasticity is clear. In order to highlight a particular difference, suppose that $\hat{\boldsymbol{\tau}}$ is a linear function of the free unknowns, so that the terms with $\partial\delta\hat{\boldsymbol{\tau}}^*$ and $\partial\delta\hat{\boldsymbol{\tau}}$ disappear. Equation $(45)_2$ clearly shows that the virtual and the incremental variations of $\hat{\boldsymbol{\tau}}^*$ are locally uncoupled and work directly for the opposite variations of dual $(\boldsymbol{\Psi}^{*\mathrm{T}}\boldsymbol{\omega}^*)$ (that is, the incremental and the virtual variations, respectively). In contrast, in $(67)_2$ the variations of $\hat{\boldsymbol{\tau}}$ are coupled together and with the variations of $\boldsymbol{H}^{\mathrm{T}}\boldsymbol{\omega}_\alpha$ through tensors $\bar{\boldsymbol{D}}_{\boldsymbol{\tau}\boldsymbol{\tau}}$ and $\bar{\boldsymbol{D}}^{\alpha}_{\boldsymbol{\omega}\boldsymbol{\tau}}$. Therefore, the term $\delta\hat{\boldsymbol{\tau}}\cdot\bar{\boldsymbol{R}}_{\boldsymbol{\tau}}$ in $(67)_1$ cannot correspond to a scalar product like $\langle\delta\hat{\boldsymbol{\tau}}\times, \mathrm{dual}\,(\boldsymbol{X}^{\mathrm{T}}\boldsymbol{H}^{\mathrm{T}}\boldsymbol{\omega})\rangle$, as in $(45)_1$, and the virtual functional $\pi_{\mathrm{int}\delta}$ can be hardly given a constrained form as in (36). Rather, the incremental form of the nonlinear shell constitutive law in (67) couples together the surface mechanical variables $\boldsymbol{\omega}_\alpha$ and $\hat{\boldsymbol{\tau}}$, and their respective roles become confused. This fact makes it hard to derive the two-dimensional equations governing the material surface mechanics — should this be necessary — from the three-dimensional continuum, with distinct expressions for the balance conditions and for the kinematical constraint. However, though $\hat{\boldsymbol{\tau}}$ cannot be identified as the axial vector of a stress resultant, we keep on referring to $\hat{\boldsymbol{\tau}}$ as the surface Biot-axial stress parameter.

The shell incremental constitutive law is built dynamically during the solution process of the whole shell problem. Vectors and tensors $\bar{\boldsymbol{R}}$ and $\bar{\boldsymbol{D}}$ in (66) are computed from the integrals $\boldsymbol{R}$ and $\boldsymbol{D}$ in (63) and (64); the latter are nonlinear functions of both the surface fields $(\boldsymbol{\omega}_\alpha, \hat{\boldsymbol{\tau}})$ and the local variables $(\boldsymbol{\theta}', \hat{\boldsymbol{\mu}})$, and can be computed by a numerical integration across the shell thickness. At the end of each Newton–Raphson iteration, once the increments $\partial(\boldsymbol{H}^{\mathrm{T}}\boldsymbol{\omega}_\beta)$ and $\partial\hat{\boldsymbol{\tau}}$ are known from the overall solution, the local increments $\partial\boldsymbol{\theta}'$ and $\partial\hat{\boldsymbol{\mu}}$ are recovered from (65), and the locally stored variables, which pertain to a Euclidean vector space, are updated additively, $\boldsymbol{\theta}' \leftarrow \boldsymbol{\theta}' + \partial\boldsymbol{\theta}'$ and $\hat{\boldsymbol{\mu}} \leftarrow \hat{\boldsymbol{\mu}} + \partial\hat{\boldsymbol{\mu}}$. At this stage, the coefficients in (65) must be consistent with those used early in (66), so they must be saved for the subsequent recovery. In a finite-element context, the local condensation would be carried out at each quadrature point of a shell element, where the shell director $\boldsymbol{\theta}'$ and the angular Biot-axial parameter $\hat{\boldsymbol{\mu}}$ can be stored as internal variables.

Though the proposed formulation may seem quite unusual in shell mechanics, some similarity with [Wisniewski and Turska 2000] can be observed, however. These authors too aim to release the rotation within the thickness from the reference surface rotation, in particular the drilling rotation, so to account for the in-plane twist. They use the skew-symmetric part of the Biot stress to force the constraint that defines such rotations, both within the thickness (in-plane twist) and on the reference surface (drilling

rotation), and arrive at a two-dimensional formulation endowed with a surface Biot-axial stress parameter. The main difference with our formulation lies in the modeling of the continuum: the classical, uncoupled modeling adopted in [Wisniewski and Turska 2000] allows us to examine the physical meaning of every variable component, but it also induces several simplifying hypotheses; instead, the coupled helicoidal modeling used here is concise and stands on only few hypotheses.

7. Conclusion

Let's summarize some noteworthy features of the proposed shell theory.

Micropolar mechanics of the shell material surface. The mechanics of the material surface are based on a thorough micropolar description over a two-coordinate domain; the surface particles have full three-dimensional freedom, including the drilling rotation. The material surface, however, is like a nonpolar medium in its tangent plane, so the drilling rotation is actually a further DOF whose definition entails an extra stress field. In the present formulation, the surface density of the internal work functional comes as a function of the kinematical strain component vectors and a Biot-axial parameter vector. The role of the latter is evident, and this stress parameter must be retained, in our opinion, as a primary unknown field of the material surface mechanics, even in a displacement-based formulation. This strategy could be the answer to the issue raised by [Yu and Hodges 2004] in the closure, and should finally shed full light on the nature of drilling DOFs.

Hypotheses of the solid shell model. The solid shell model is based on the orientoposition of the parent material surface (six DOFs, five of which correspond to those of the so-called 5-parameter shell theory, while the last is the drilling DOF), on an orientoposition field across the thickness, and on a Biot-axial field across the thickness. The inherent approximation of this shell model is related to the hypotheses on which the last two fields are built. Only three hypotheses have been made. (1) The orientoposition field is determined by a *constant-curvature* rototranslation across the thickness; the curvature is governed by the shell director, a dual vector field on the surface (another six DOFs, out of which one corresponds to the sixth DOF of the so-called 6-parameter shell theory, while the others are five additional freedoms of the present theory). (2) The shell director is assumed to belong to a *piecewise constant*, gradientless field on the surface. (3) The Biot-axial field is assumed to be *linear* across the thickness, and is governed by two vector fields on the surface. No more assumptions are made. The helicoidal modeling and its consistent linearization allow us to deal with finite displacements, rotations, and strains of any magnitude, in an easy and natural way.

Computational approach to nonlinear shell mechanics. The proposed formulation is computation oriented in several respects. The mechanics of the solid shell are formulated in weak form, the appropriate variational principle is linearized from the beginning, and the relevant incremental form is made discrete across the thickness by means of an approximation of the finite-element kind. The integrals in the transverse direction are computed numerically at each point of interest on the reference surface. The ensuing two-dimensional problem is stated in a weak incremental form that inherits and exploits the property of geometric invariance of the helicoidal model. The extra parameters of the solid shell model (the shell director and the second Biot-axial parameter) are regarded as local variables and condensed statically. The surface strains and the first Biot-axial parameter are left as the vectorial entities work-conjugate to the stress resultants and the surface kinematical constraint. The latter entities are coupled together in

an incremental form, which represents the dynamically built nonlinear constitutive law of the shell. A similar dynamical adaptation of the incremental form of the local constitutive law allows us to prevent Poisson locking related to the low-order kinematical model.

In shell mechanics, a very attractive and often-pursued approach is the so-called direct approach whose object body is the Cosserat surface. From the wide literature on this subject, we quote the early paper [Zhilin 1976], which is still modern in concepts and notation on rotational kinematics; the successful finite-element formulation [Sansour and Bednarczyk 1995]; and the comprehensive survey and deep study [Valid 1995]. When addressing direct approaches, it is worth focusing on the point that, contrary to beams, shells are hybrid structured solids: in fact, as remarked above, a shell can bend and torque but behaves in an essentially nonpolar way in its tangent plane. This particular feature must be carefully accounted for in the formulation of consistent material surface mechanics. Our line, in this respect, is as follows. As in three-dimensional solid mechanics a micropolar rotation unknown is allowed for even in nonpolar media by formulations based on strain and stress parameters of the Biot type and on the Biot-axial as a workless stress unknown, so in the material surface mechanics a full three-parametric rotation unknown can be allowed for by a consistent formulation that retains a surface Biot-axial parameter as a primary unknown. However, though the extension of the direct approach to encompass a surface Biot-axial unknown is feasible [Merlini 2008], its usefulness is questionable: in fact, the interpretation of the surface Biot-axial vector and its relation with the Biot-axial field within the solid give rise to new difficulties that add to the lack of constitutive laws, which is characteristic of direct approaches. In this paper we showed that a sound variational approach to the solid shell leads to the appropriate ingredients to set up the consistent nonlinear two-dimensional mechanics of the material surface. The methodology proposed in this paper is, in our opinion, the right way to tie a reasonably approximate model across the thickness with a full micropolar approach to the material surface mechanics in geometrically nonlinear problems. So, the proposed formulation overcomes the seemingly inconsistent feature of shells of being nonpolar in their tangent plane.

Appendix: Kinematical strain variations

In the development of the simple and mixed variations $\delta(\boldsymbol{\Psi}^{*\mathrm{T}}\boldsymbol{\omega}^*)$ and $\partial\delta(\boldsymbol{\Psi}^{*\mathrm{T}}\boldsymbol{\omega}^*)$ in (45), it is helpful to focus on the corototranslational variations $\boldsymbol{H}^*\delta(\boldsymbol{H}^{*\mathrm{T}}\boldsymbol{\omega}^*)$ and $\boldsymbol{H}^*\partial\delta(\boldsymbol{H}^{*\mathrm{T}}\boldsymbol{\omega}^*)$ of the model strain. In fact, the former variations can be always recovered from the latter ones, since for (44) $\boldsymbol{\Psi}^*\delta(\boldsymbol{\Psi}^{*\mathrm{T}}\boldsymbol{\omega}^*) = \boldsymbol{H}^*\delta(\boldsymbol{H}^{*\mathrm{T}}\boldsymbol{\omega}^*)$ and $\boldsymbol{\Psi}^*\partial\delta(\boldsymbol{\Psi}^{*\mathrm{T}}\boldsymbol{\omega}^*) = \boldsymbol{H}^*\partial\delta(\boldsymbol{H}^{*\mathrm{T}}\boldsymbol{\omega}^*)$. Using (32), (28), and (24), the following dyadic forms are written:

$$\boldsymbol{H}^*\delta(\boldsymbol{H}^{*\mathrm{T}}\boldsymbol{\omega}^*) = \boldsymbol{H}^*\delta(\boldsymbol{H}^{*\mathrm{T}}\boldsymbol{k}'_\alpha)\otimes\boldsymbol{g}^{*\alpha} + \boldsymbol{H}^*\delta(\boldsymbol{H}^{*\mathrm{T}}\boldsymbol{k}'_3)\otimes\boldsymbol{g}^{*3},$$
$$\boldsymbol{H}^*\partial\delta(\boldsymbol{H}^{*\mathrm{T}}\boldsymbol{\omega}^*) = \boldsymbol{H}^*\partial\delta(\boldsymbol{H}^{*\mathrm{T}}\boldsymbol{k}'_\alpha)\otimes\boldsymbol{g}^{*\alpha} + \boldsymbol{H}^*\partial\delta(\boldsymbol{H}^{*\mathrm{T}}\boldsymbol{k}'_3)\otimes\boldsymbol{g}^{*3}.$$

Recalling (33) and (18), and exploiting the rototranslation differentiation formulae [Merlini and Morandini 2004a]

$$\delta\boldsymbol{H}\boldsymbol{H}^{\mathrm{T}} = \boldsymbol{\eta}_\delta\times, \quad \partial\delta\boldsymbol{H}\boldsymbol{H}^{\mathrm{T}} = \boldsymbol{\eta}_{\partial\delta}\times + \tfrac{1}{2}(\boldsymbol{\eta}_\partial\times\boldsymbol{\eta}_\delta\times + \boldsymbol{\eta}_\delta\times\boldsymbol{\eta}_\partial\times),$$

and

$$\delta\tilde{\boldsymbol{H}}'\tilde{\boldsymbol{H}}'^{\mathrm{T}} = \tilde{\boldsymbol{\eta}}'_\delta\times, \quad \partial\delta\tilde{\boldsymbol{H}}'\tilde{\boldsymbol{H}}'^{\mathrm{T}} = \tilde{\boldsymbol{\eta}}'_{\partial\delta}\times + \tfrac{1}{2}(\tilde{\boldsymbol{\eta}}'_\partial\times\tilde{\boldsymbol{\eta}}'_\delta\times + \tilde{\boldsymbol{\eta}}'_\delta\times\tilde{\boldsymbol{\eta}}'_\partial\times),$$

the surface component vectors can be transformed to

$$\begin{aligned}
&\boldsymbol{H}^*\delta(\boldsymbol{H}^{*\mathrm{T}}\boldsymbol{k}'_\alpha) = \boldsymbol{H}\delta(\boldsymbol{H}^{\mathrm{T}}\boldsymbol{\omega}_\alpha) - (\tilde{\boldsymbol{\eta}}'_\delta + (\tilde{\boldsymbol{H}}' - \boldsymbol{I})\boldsymbol{\eta}_\delta)\times\boldsymbol{k}'_\alpha,\\
&\boldsymbol{H}^*\partial\delta(\boldsymbol{H}^{*\mathrm{T}}\boldsymbol{k}'_\alpha) = \boldsymbol{H}\partial\delta(\boldsymbol{H}^{\mathrm{T}}\boldsymbol{\omega}_\alpha) - (\tilde{\boldsymbol{\eta}}'_\partial + (\tilde{\boldsymbol{H}}' - \boldsymbol{I})\boldsymbol{\eta}_\partial)\times\boldsymbol{H}\delta(\boldsymbol{H}^{\mathrm{T}}\boldsymbol{\omega}_\alpha) - (\tilde{\boldsymbol{\eta}}'_\delta + (\tilde{\boldsymbol{H}}' - \boldsymbol{I})\boldsymbol{\eta}_\delta)\times\boldsymbol{H}\partial(\boldsymbol{H}^{\mathrm{T}}\boldsymbol{\omega}_\alpha)\\
&\qquad -\Big(\tilde{\boldsymbol{\eta}}'_{\partial\delta} + (\tilde{\boldsymbol{H}}' - \boldsymbol{I})\boldsymbol{\eta}_{\partial\delta} + \tfrac{1}{2}\big((\tilde{\boldsymbol{\eta}}'_\partial + (\tilde{\boldsymbol{H}}' - \boldsymbol{I})\boldsymbol{\eta}_\partial)\times(\tilde{\boldsymbol{H}}' + \boldsymbol{I})\boldsymbol{\eta}_\delta + \boldsymbol{\eta}_\partial\times(\tilde{\boldsymbol{H}}' + \boldsymbol{I})\boldsymbol{\eta}_\delta\\
&\qquad\qquad +(\tilde{\boldsymbol{\eta}}'_\delta + (\tilde{\boldsymbol{H}}' - \boldsymbol{I})\boldsymbol{\eta}_\delta)\times(\tilde{\boldsymbol{H}}' + \boldsymbol{I})\boldsymbol{\eta}_\partial + \boldsymbol{\eta}_\delta\times(\tilde{\boldsymbol{H}}' + \boldsymbol{I})\boldsymbol{\eta}_\partial\big)\Big)\times\boldsymbol{k}'_\alpha\\
&\qquad +\tfrac{1}{2}\big((\tilde{\boldsymbol{\eta}}'_\partial + (\tilde{\boldsymbol{H}}' - \boldsymbol{I})\boldsymbol{\eta}_\partial)\times(\tilde{\boldsymbol{\eta}}'_\delta + (\tilde{\boldsymbol{H}}' - \boldsymbol{I})\boldsymbol{\eta}_\delta)\times + (\tilde{\boldsymbol{\eta}}'_\delta + (\tilde{\boldsymbol{H}}' - \boldsymbol{I})\boldsymbol{\eta}_\delta)\times(\tilde{\boldsymbol{\eta}}'_\partial + (\tilde{\boldsymbol{H}}' - \boldsymbol{I})\boldsymbol{\eta}_\partial)\times\big)\boldsymbol{k}'_\alpha.
\end{aligned}$$

The differential maps of the rototranslation $\tilde{\boldsymbol{H}}'$ through the thickness,

$$\tilde{\boldsymbol{\eta}}'_\delta = \tilde{\boldsymbol{\Lambda}}'\delta\tilde{\boldsymbol{\eta}}', \quad \tilde{\boldsymbol{\eta}}'_{\partial\delta} = \tilde{\boldsymbol{\Lambda}}'\partial\delta\tilde{\boldsymbol{\eta}}' + \tilde{\boldsymbol{\Lambda}}'^{\underline{123}}_{\mathrm{III}} : \delta\tilde{\boldsymbol{\eta}}'\otimes\partial\tilde{\boldsymbol{\eta}}',$$

are now used to solve the differential helices $\tilde{\boldsymbol{\eta}}'_\delta$ and $\tilde{\boldsymbol{\eta}}'_{\partial\delta}$ for the variations of the helix $\tilde{\boldsymbol{\eta}}'$. The expressions of the mapping tensors $\tilde{\boldsymbol{\Lambda}}'(\tilde{\boldsymbol{\eta}}')$ and $\tilde{\boldsymbol{\Lambda}}'^{\underline{123}}_{\mathrm{III}}(\tilde{\boldsymbol{\eta}}')$ can be found in [Merlini and Morandini 2004b, Appendix B]. Using (26) and (34), the variations $\delta\tilde{\boldsymbol{\eta}}'$ and $\partial\delta\tilde{\boldsymbol{\eta}}'$ are in turn related to the differential helices $\boldsymbol{\eta}_\delta$ and $\boldsymbol{\eta}_{\partial\delta}$ of the surface rototranslation $\boldsymbol{H}$ and to the corototranslational variations of the strain $\boldsymbol{\omega}_3$,

$$\begin{aligned}
&\delta\tilde{\boldsymbol{\eta}}' = \xi^3\boldsymbol{H}\delta(\boldsymbol{H}^{\mathrm{T}}\boldsymbol{\omega}_3) - \tilde{\boldsymbol{\eta}}'\times\boldsymbol{\eta}_\delta,\\
&\partial\delta\tilde{\boldsymbol{\eta}}' = \xi^3\boldsymbol{H}\partial\delta(\boldsymbol{H}^{\mathrm{T}}\boldsymbol{\omega}_3) - \tilde{\boldsymbol{\eta}}'\times\boldsymbol{\eta}_{\partial\delta} + \xi^3\boldsymbol{\eta}_\partial\times\boldsymbol{H}\delta(\boldsymbol{H}^{\mathrm{T}}\boldsymbol{\omega}_3) + \xi^3\boldsymbol{\eta}_\delta\times\boldsymbol{H}\partial(\boldsymbol{H}^{\mathrm{T}}\boldsymbol{\omega}_3) + \tfrac{1}{2}(\boldsymbol{\eta}_\partial\times\boldsymbol{\eta}_\delta\times + \boldsymbol{\eta}_\delta\times\boldsymbol{\eta}_\partial\times)\tilde{\boldsymbol{\eta}}'.
\end{aligned}$$

Putting all together and using the identity $(\tilde{\boldsymbol{\Lambda}}'^{\underline{123}}_{\mathrm{III}}\tilde{\boldsymbol{\eta}}'\times)^{\mathrm{T}132} + \tilde{\boldsymbol{\Lambda}}'\boldsymbol{I}^\times - \boldsymbol{I}^\times\tilde{\boldsymbol{\Lambda}}' + \frac{1}{2}(\boldsymbol{I}^\times\tilde{\boldsymbol{\Lambda}}'\tilde{\boldsymbol{\eta}}'\times)^{\mathrm{T}132}\tilde{\boldsymbol{\Lambda}}' = \boldsymbol{0}$, where $\boldsymbol{I}^\times = \boldsymbol{g}_j\times\otimes\boldsymbol{g}^j$ is the third-order Ricci tensor, after several algebraic manipulations detailed in [Merlini and Morandini 2008], one obtains

$$\begin{aligned}
&\tilde{\boldsymbol{\eta}}'_\delta + (\tilde{\boldsymbol{H}}' - \boldsymbol{I})\boldsymbol{\eta}_\delta = \xi^3\tilde{\boldsymbol{\Lambda}}'\cdot\boldsymbol{H}\delta(\boldsymbol{H}^{\mathrm{T}}\boldsymbol{\omega}_3),\\
&\tilde{\boldsymbol{\eta}}'_{\partial\delta} + (\tilde{\boldsymbol{H}}' - \boldsymbol{I})\boldsymbol{\eta}_{\partial\delta} = \xi^3\tilde{\boldsymbol{\Lambda}}'\cdot\boldsymbol{H}\partial\delta(\boldsymbol{H}^{\mathrm{T}}\boldsymbol{\omega}_3) + (\xi^3)^2\tilde{\boldsymbol{\Lambda}}'^{\underline{123}}_{\mathrm{III}} : \boldsymbol{H}\delta(\boldsymbol{H}^{\mathrm{T}}\boldsymbol{\omega}_3)\otimes\boldsymbol{H}\partial(\boldsymbol{H}^{\mathrm{T}}\boldsymbol{\omega}_3)\\
&\qquad\qquad -\tfrac{1}{2}\big((\tilde{\boldsymbol{\eta}}'_\partial + (\tilde{\boldsymbol{H}}' - \boldsymbol{I})\boldsymbol{\eta}_\partial)\times(\tilde{\boldsymbol{H}}' + \boldsymbol{I})\boldsymbol{\eta}_\delta + \boldsymbol{\eta}_\partial\times(\tilde{\boldsymbol{H}}' + \boldsymbol{I})\boldsymbol{\eta}_\delta\\
&\qquad\qquad\qquad + (\tilde{\boldsymbol{\eta}}'_\delta + (\tilde{\boldsymbol{H}}' - \boldsymbol{I})\boldsymbol{\eta}_\delta)\times(\tilde{\boldsymbol{H}}' + \boldsymbol{I})\boldsymbol{\eta}_\partial + \boldsymbol{\eta}_\delta\times(\tilde{\boldsymbol{H}}' + \boldsymbol{I})\boldsymbol{\eta}_\partial\big).
\end{aligned}$$

Therefore, the surface component vectors are finally brought to the form

$$\begin{aligned}
&\boldsymbol{H}^*\delta(\boldsymbol{H}^{*\mathrm{T}}\boldsymbol{k}'_\alpha) = \boldsymbol{H}\delta(\boldsymbol{H}^{\mathrm{T}}\boldsymbol{\omega}_\alpha) + \xi^3\boldsymbol{k}'_\alpha\times\tilde{\boldsymbol{\Lambda}}'\cdot\boldsymbol{H}\delta(\boldsymbol{H}^{\mathrm{T}}\boldsymbol{\omega}_3),\\
&\boldsymbol{H}^*\partial\delta(\boldsymbol{H}^{*\mathrm{T}}\boldsymbol{k}'_\alpha) = \boldsymbol{H}\partial\delta(\boldsymbol{H}^{\mathrm{T}}\boldsymbol{\omega}_\alpha) + \xi^3\boldsymbol{k}'_\alpha\times\tilde{\boldsymbol{\Lambda}}'\cdot\boldsymbol{H}\partial\delta(\boldsymbol{H}^{\mathrm{T}}\boldsymbol{\omega}_3)\\
&\qquad\qquad -\xi^3\boldsymbol{I}^\times\tilde{\boldsymbol{\Lambda}}' : \big(\boldsymbol{H}\delta(\boldsymbol{H}^{\mathrm{T}}\boldsymbol{\omega}_\alpha)\otimes\boldsymbol{H}\partial(\boldsymbol{H}^{\mathrm{T}}\boldsymbol{\omega}_3) + \boldsymbol{H}\partial(\boldsymbol{H}^{\mathrm{T}}\boldsymbol{\omega}_\alpha)\otimes\boldsymbol{H}\delta(\boldsymbol{H}^{\mathrm{T}}\boldsymbol{\omega}_3)\big)\\
&\qquad\qquad +(\xi^3)^2(\boldsymbol{k}'_\alpha\times\tilde{\boldsymbol{\Lambda}}'^{\underline{123}}_{\mathrm{III}} + (\boldsymbol{I}^\times\boldsymbol{k}'_\alpha\times\tilde{\boldsymbol{\Lambda}}')^{\mathrm{T}132}\tilde{\boldsymbol{\Lambda}}')^{\mathrm{S}1\underline{23}} : \boldsymbol{H}\delta(\boldsymbol{H}^{\mathrm{T}}\boldsymbol{\omega}_3)\otimes\boldsymbol{H}\partial(\boldsymbol{H}^{\mathrm{T}}\boldsymbol{\omega}_3).
\end{aligned}$$

The development of the transverse component vectors is straightforward:

$$\boldsymbol{H}^*\delta(\boldsymbol{H}^{*\mathrm{T}}\boldsymbol{k}'_3) = \tilde{\boldsymbol{H}}'\cdot\boldsymbol{H}\delta(\boldsymbol{H}^{\mathrm{T}}\boldsymbol{\omega}_3), \quad \boldsymbol{H}^*\partial\delta(\boldsymbol{H}^{*\mathrm{T}}\boldsymbol{k}'_3) = \tilde{\boldsymbol{H}}'\cdot\boldsymbol{H}\partial\delta(\boldsymbol{H}^{\mathrm{T}}\boldsymbol{\omega}_3).$$

At last, recalling (34), (16), and (26), it is seen that $\boldsymbol{H}\delta(\boldsymbol{H}^{\mathrm{T}}\boldsymbol{\omega}_3) = \boldsymbol{A}'\delta\boldsymbol{\theta}'$ and $\boldsymbol{H}\partial\delta(\boldsymbol{H}^{\mathrm{T}}\boldsymbol{\omega}_3) = \boldsymbol{A}'\partial\delta\boldsymbol{\theta}'$, and recalling again (44), (60) is obtained.

References

[Angeles 1998] J. Angeles, "The application of dual algebra to kinematic analysis", pp. 1–32 in *Computational methods in mechanical systems: mechanism analysis, synthesis, and optimization* (Varna, 1997), edited by J. Angeles and E. Zakhariev, NATO ASI Series, Series F: Computer and systems sciences **161**, Springer, Heidelberg, 1998.

[Atluri 1984] S. N. Atluri, "Alternate stress and conjugate strain measures, and mixed variational formulations involving rigid rotations, for computational analyses of finitely deformed solids, with application to plates and shells, I: Theory", *Comput. Struct.* **18**:1 (1984), 93–116.

[Atluri and Cazzani 1995] S. N. Atluri and A. Cazzani, "Rotations in computational solid mechanics", *Arch. Comput. Methods Eng.* **2**:1 (1995), 49–138.

[Badur and Pietraszkiewicz 1986] J. Badur and W. Pietraszkiewicz, "On geometrically non-linear theory of elastic shells derived from pseudo-Cosserat continuum with constrained micro-rotations", pp. 19–32 in *Finite rotations in structural mechanics*, edited by W. Pietraszkiewicz, Springer, Berlin, 1986.

[Betsch et al. 1998] P. Betsch, A. Menzel, and E. Stein, "On the parametrization of finite rotations in computational mechanics: a classification of concepts with application to smooth shells", *Comput. Methods Appl. Mech. Eng.* **155**:3-4 (1998), 273–305.

[Bischoff and Ramm 2000] M. Bischoff and E. Ramm, "On the physical significance of higher order kinematic and static variables in a three-dimensional shell formulation", *Int. J. Solids Struct.* **37**:46–47 (2000), 6933–6960.

[Bischoff et al. 2004] M. Bischoff, W. A. Wall, K.-U. Bletzinger, and E. Ramm, "Models and finite elements for thin-walled structures", Chapter 3, pp. 59–137 in *Encyclopedia of computational mechanics, 2: Solids and structures*, edited by E. Stein et al., Wiley, Chichester, 2004.

[Borri and Bottasso 1994] M. Borri and C. Bottasso, "An intrinsic beam model based on a helicoidal approximation, I: Formulation", *Int. J. Numer. Methods Eng.* **37**:13 (1994), 2267–2289.

[Borri et al. 2000] M. Borri, L. Trainelli, and C. L. Bottasso, "On representations and parameterizations of motion", *Multibody Syst. Dyn.* **4**:2-3 (2000), 129–193.

[de Borst 1991] R. de Borst, "The zero-normal-stress condition in plane-stress and shell elastoplasticity", *Commun. Appl. Numer. Methods* **7**:1 (1991), 29–33.

[Bottasso et al. 2002] C. L. Bottasso, M. Borri, and L. Trainelli, "Geometric invariance", *Comput. Mech.* **29**:2 (2002), 163–169.

[Brank 2008] B. Brank, "Assessment of 4-node EAS-ANS shell elements for large deformation analysis", *Comput. Mech.* **42**:1 (2008), 39–51.

[Büchter et al. 1994] N. Büchter, E. Ramm, and D. Roehl, "Three-dimensional extension of non-linear shell formulation based on the enhanced assumed strain concept", *Int. J. Numer. Methods Eng.* **37**:15 (1994), 2551–2568.

[Bufler 1985] H. Bufler, "The Biot stresses in nonlinear elasticity and the associated generalized variational principles", *Arch. Appl. Mech.* **55**:6 (1985), 450–462.

[Bufler 1995] H. Bufler, "On drilling degrees of freedom in nonlinear elasticity and a hyperelastic material description in terms of the stretch tensor, I: Theory", *Acta Mech.* **113**:1-4 (1995), 21–35.

[Campello et al. 2003] E. M. B. Campello, P. M. Pimenta, and P. Wriggers, "A triangular finite shell element based on a fully nonlinear shell formulation", *Comput. Mech.* **31**:6 (2003), 505–518.

[Chróścielewski et al. 1992] J. Chróścielewski, J. Makowski, and H. Stumpf, "Genuinely resultant shell finite elements accounting for geometric and material non-linearity", *Int. J. Numer. Methods Eng.* **35**:1 (1992), 63–94.

[Eringen and Kafadar 1976] A. C. Eringen and C. B. Kafadar, "Polar field theories", pp. 1–73 in *Continuum physics*, vol. 4, edited by A. C. Eringen, Academic Press, New York, 1976.

[Fraeijs de Veubeke 1972] B. M. Fraeijs de Veubeke, "A new variational principle for finite elastic displacements", *Int. J. Eng. Sci.* **10**:9 (1972), 745–763.

[Gruttmann et al. 1992] F. Gruttmann, W. Wagner, and P. Wriggers, "A nonlinear quadrilateral shell element with drilling degrees of freedom", *Arch. Appl. Mech.* **62**:7 (1992), 474–486.

[Hughes and Brezzi 1989] T. J. R. Hughes and F. Brezzi, "On drilling degrees of freedom", *Comput. Methods Appl. Mech. Eng.* **72**:1 (1989), 105–121.

[Ibrahimbegović 1994] A. Ibrahimbegović, "Stress resultant geometrically nonlinear shell theory with drilling rotations, I: A consistent formulation", *Comput. Methods Appl. Mech. Eng.* **118**:3–4 (1994), 265–284.

[Ibrahimbegović and Frey 1995] A. Ibrahimbegović and F. Frey, "Variational principles and membrane finite elements with drilling rotations for geometrically non-linear elasticity", *Int. J. Numer. Methods Eng.* **38**:11 (1995), 1885–1900.

[Ibrahimbegović et al. 2001] A. Ibrahimbegović, B. Brank, and P. Courtois, "Stress resultant geometrically exact form of classical shell model and vector-like parameterization of constrained finite rotations", *Int. J. Numer. Methods Eng.* **52**:11 (2001), 1235–1252.

[Kafadar and Eringen 1971] C. B. Kafadar and A. C. Eringen, "Micropolar media, I: The classical theory", *Int. J. Eng. Sci.* **9**:3 (1971), 271–305.

[Klinkel and Govindjee 2002] S. Klinkel and S. Govindjee, "Using finite strain 3D-material models in beam and shell elements", *Eng. Computation.* **19**:8 (2002), 902–921.

[Klinkel et al. 2006] S. Klinkel, F. Gruttmann, and W. Wagner, "A robust non-linear solid shell element based on a mixed variational formulation", *Comput. Methods Appl. Mech. Eng.* **195**:1–3 (2006), 179–201.

[Li and Zhan 2000] M. Li and F. Zhan, "The finite deformation theory for beam, plate and shell, V: The shell element with drilling degree of freedom based on Biot strain", *Comput. Methods Appl. Mech. Eng.* **189**:3 (2000), 743–759.

[Merlini 1997] T. Merlini, "A variational formulation for finite elasticity with independent rotation and Biot-axial fields", *Comput. Mech.* **19**:3 (1997), 153–168.

[Merlini 2008] T. Merlini, *Variational formulations for the helicoidal modeling of the shell material surface*, Aracne, Rome, 2008. Scientific report DIA-SR 08-06.

[Merlini and Morandini 2004a] T. Merlini and M. Morandini, "The helicoidal modeling in computational finite elasticity, I: Variational formulation", *Int. J. Solids Struct.* **41**:18–19 (2004), 5351–5381.

[Merlini and Morandini 2004b] T. Merlini and M. Morandini, "The helicoidal modeling in computational finite elasticity, II: Multiplicative interpolation", *Int. J. Solids Struct.* **41**:18–19 (2004), 5383–5409. Erratum on *Int. J. Solids Struct.* **42**:3–4 (2005), 1269.

[Merlini and Morandini 2005] T. Merlini and M. Morandini, "The helicoidal modeling in computational finite elasticity, III: Finite element approximation for non-polar media", *Int. J. Solids Struct.* **42**:24–25 (2005), 6475–6513.

[Merlini and Morandini 2008] T. Merlini and M. Morandini, *Helicoidal shell theory*, Aracne, Rome, 2008. Scientific report DIA-SR 08-07.

[Pennestrì and Stefanelli 2007] E. Pennestrì and R. Stefanelli, "Linear algebra and numerical algorithms using dual numbers", *Multibody Syst. Dyn.* **18**:3 (2007), 323–344.

[Ramezani and Naghdabadi 2007] S. Ramezani and R. Naghdabadi, "Energy pairs in the micropolar continuum", *Int. J. Solids Struct.* **44**:14–15 (2007), 4810–4818.

[Reissner 1965] E. Reissner, "A note on variational principles in elasticity", *Int. J. Solids Struct.* **1**:1 (1965), 93–95.

[Reissner 1984] E. Reissner, "Formulation of variational theorems in geometrically nonlinear elasticity", *J. Eng. Mech.* (*ASCE*) **110**:9 (1984), 1377–1390.

[Sansour and Bednarczyk 1995] C. Sansour and H. Bednarczyk, "The Cosserat surface as a shell model: theory and finite-element formulation", *Comput. Methods Appl. Mech. Eng.* **120**:1–2 (1995), 1–32.

[Sansour and Bufler 1992] C. Sansour and H. Bufler, "An exact finite rotation shell theory, its mixed variational formulation and its finite element implementation", *Int. J. Numer. Methods Eng.* **34**:1 (1992), 73–115.

[Sansour and Kollmann 2000] C. Sansour and F. G. Kollmann, "Families of 4-node and 9-node finite elements for a finite deformation shell theory: an assessment of hybrid stress, hybrid strain and enhanced strain elements", *Comput. Mech.* **24**:6 (2000), 435–447.

[Sansour et al. 1996] C. Sansour, H. Bufler, and H. Müllerschön, "On drilling degrees of freedom in nonlinear elasticity and a hyperelastic material description in terms of the stretch tensor, II: Application to membranes", *Acta Mech.* **115**:1-4 (1996), 103–117.

[Schlebusch and Zastrau 2005] R. Schlebusch and B. W. Zastrau, "On an analogy between the deformation gradient and a generalized shell shifter tensor", *Arch. Appl. Mech.* **74**:11-12 (2005), 853–862.

[Simo and Fox 1989] J. C. Simo and D. D. Fox, "On a stress resultant geometrically exact shell model, I: Formulation and optimal parametrization", *Comput. Methods Appl. Mech. Eng.* **72**:3 (1989), 267–304.

[Simo and Rifai 1990] J. C. Simo and M. S. Rifai, "A class of mixed assumed strain methods and the method of incompatible modes", *Int. J. Numer. Methods Eng.* **29**:8 (1990), 1595–1638.

[Simo et al. 1992] J. C. Simo, D. D. Fox, and T. J. R. Hughes, "Formulations of finite elasticity with independent rotations", *Comput. Methods Appl. Mech. Eng.* **95**:2 (1992), 277–288.

[Valid 1995] R. Valid, *The nonlinear theory of shells through variational principles: from elementary algebra to differential geometry*, Wiley, Chichester, 1995.

[Wang and Thierauf 2001] L. Wang and G. Thierauf, "Finite rotations in non-linear analysis of elastic shells", *Comput. Struct.* **79**:26–28 (2001), 2357–2367.

[Wisniewski 1998] K. Wisniewski, "A shell theory with independent rotations for relaxed Biot stress and right stretch strain", *Comput. Mech.* **21**:2 (1998), 101–122.

[Wisniewski and Turska 2000] K. Wisniewski and E. Turska, "Kinematics of finite rotation shells with in-plane twist parameter", *Comput. Methods Appl. Mech. Eng.* **190**:8–10 (2000), 1117–1135.

[Wisniewski and Turska 2001] K. Wisniewski and E. Turska, "Warping and in-plane twist parameters in kinematics of finite rotation shells", *Comput. Methods Appl. Mech. Eng.* **190**:43–44 (2001), 5739–5758.

[Wisniewski and Turska 2002] K. Wisniewski and E. Turska, "Second-order shell kinematics implied by rotation constraint-equation", *J. Elasticity* **67**:3 (2002), 229–246.

[Wriggers and Gruttmann 1993] P. Wriggers and F. Gruttmann, "Thin shells with finite rotations formulated in Biot stresses: theory and finite element formulation", *Int. J. Numer. Methods Eng.* **36**:12 (1993), 2049–2071.

[Yu and Hodges 2004] W. Yu and D. H. Hodges, "A geometrically nonlinear shear deformation theory for composite shells", *J. Appl. Mech.* (*ASME*) **71**:1 (2004), 1–9. Erratum on *J. Appl. Mech.* (*ASME*) **74**:3 (2007), 599.

[Zhilin 1976] P. A. Zhilin, "Mechanics of deformable directed surfaces", *Int. J. Solids Struct.* **12**:9–10 (1976), 635–648.

[Zhu and Zacharia 1996] Y. Zhu and T. Zacharia, "A new one-point quadrature, quadrilateral shell element with drilling degrees of freedom", *Comput. Methods Appl. Mech. Eng.* **136**:1–2 (1996), 165–203.

Received 8 Mar 2010. Revised 27 Sep 2010. Accepted 2 Oct 2010.

TEODORO MERLINI: teodoro.merlini@polimi.it
Politecnico di Milano, Dipartimento di Ingegneria Aerospaziale, via La Masa 34, 20156 Milano, Italy
http://www.aero.polimi.it/merlini

MARCO MORANDINI: marco.morandini@polimi.it
Politecnico di Milano, Dipartimento di Ingegneria Aerospaziale, via La Masa 34, 20156 Milano, Italy
http://www.aero.polimi.it/morandini/Home

JOURNAL OF MECHANICS OF MATERIALS AND STRUCTURES
Vol. 6, No. 5, 2011

msp

COMPUTATIONAL SHELL MECHANICS BY HELICOIDAL MODELING II: SHELL ELEMENT

TEODORO MERLINI AND MARCO MORANDINI

The virtual work of stresses developed in Part I for the helicoidal shell model and then reduced to the material surface is taken as one term of a variational principle stated on a two-dimensional domain. The other terms related to the external loads and to the boundary constraints are added here and include a weak-form treatment of the constraints, which becomes necessary in the context of helicoidal modeling. All terms are cast in incremental form and yield a linearized variational principle of the virtual work type for two-dimensional continua, endowed with an internal constraint conjugate to an extra stress field that is able to control the drilling degree of freedom.

The virtual functional and the virtual tangent functional are approximated by the finite element method, using helicoidal interpolation for the kinematic field (which ensures objectivity and path independence) and a uniform representation for the extra stress field. A low-order four-node shell element is obtained, with 6 degrees of freedom per node and a unique stress-vector discrete unknown per element. Several test cases demonstrate the performance of the element and its outstanding locking-free behavior.

1. Introduction

This second part of the paper deals with the finite element approximation of the mechanics of the shell material surface, whose kinematical description was introduced in Part I. The formulation, which is briefly outlined here, follows a straightforward course. The intrinsic mechanics of the material surface are stated directly from a variational approach. The virtual work of stresses was developed in Part I for the helicoidal shell model and then reduced to the material surface; here, the external loads and the boundary constraints are introduced, and the proposed variational principle is stated on a two-dimensional domain. This principle is of the virtual work type for nonpolar continua and is endowed with an internal constraint related to an extra stress field; it also includes a weak-form treatment of the boundary constraints. The variational principle is given an incremental form from the beginning and exploits the shell linearized constitutive law obtained in Part I; then, the virtual functional and the virtual tangent functional are approximated by the finite element method.

Within the formulation outlined above, the two characteristic features of the present contribution, already introduced in Part I, are still in evidence. As with the three-dimensional mechanics, the material surface mechanics are based on a micropolar description. Since the shell is essentially nonpolar in its tangent plane, this description entails a workless stress parameter whose role is to force the definition of the drilling degree of freedom. Even if this workless stress parameter cannot be identified as the axial vector of a stress tensor, nevertheless an extra stress exists and is rightly introduced as one of the

Keywords: nonlinear shell elements, helicoidal multiplicative interpolation, micropolar shell mechanics and drilling degrees of freedom, constraints in weak form, finite rotations and rototranslations, dual tensor algebra.

parameters that control the Biot-axial distribution within the shell model thickness. This vector parameter is an irreducible primary unknown of the intrinsic shell mechanics: in the proposed finite element scheme (4 nodes by 6 DOFs), a unique extra stress vector per element (3 stress components) is sufficient to control the drilling rotation ensuing from a three-parametric representation of the nodal rotations.

The second characteristic feature is of great importance in Part II as well. As explained in Part I, Section 3, an integral kinematic field that couples displacements and rotations is adopted for the material surface. In this paper, helicoidal modeling is fully exploited to define the approximate kinematic field within the shell element. The local orientoposition and curvatures are computed from the nodal orientopositions by means of a new kind of multiplicative interpolation proposed by [Merlini and Morandini 2004b]. This methodology is endowed with the important properties of objectivity and path independence and allows us to build curved and curving elements based on nodal frames and capable of large displacements and rotations. In such elements, the nodal orientations control both the orientation and the position of the material surface at any internal point. This is clearly evident from Figure 1, where the striking difference between two interpolation schemes — the classical and the helicoidal — is shown on a quadrilateral element.

In the last two decades a considerable number of high-performing shell elements have been developed. Some elements are built on mixed or full three-field variational formulations [Sansour and Bufler 1992; Wagner and Gruttmann 2005; Klinkel et al. 2008]. Other elements (for example, [Chróścielewski et al. 1992; Arciniega and Reddy 2007]) rely on high-order interpolants in order to avoid, or mitigate, shear and membrane locking. Others are based on particular techniques, such as reduced integration [Wriggers and Gruttmann 1993; Hauptmann et al. 2000; Cardoso and Yoon 2005], discrete Kirchhoff–Love constraints [Areias et al. 2005], or incompatible modes [Ibrahimbegović and Frey 1994]. Most of the elements proposed in the literature, however, use the assumed natural strain or enhanced assumed strain concepts, such as those developed by [Büchter et al. 1994; Bischoff and Ramm 1997; Sansour and Kollmann 2000; Fontes Valente et al. 2003; Chróścielewski and Witkowski 2006; Brank 2008], to mention just a few. Few are the successful low-order displacement-based elements free of any of the above techniques; see, for example, [Campello et al. 2003; Pimenta et al. 2004]. The element proposed in the present paper is based on an alternative modeling of the continuum and does not rely on any of the above-mentioned techniques. Here, the intrinsic coupling between positions and orientations proves to be the key for the successful development of a low-order four-node element that is essentially free from membrane and shear locking.

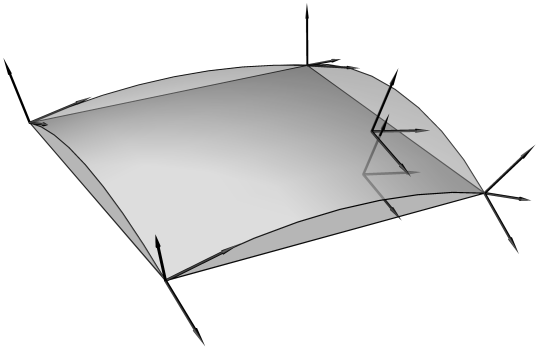

Figure 1. A curved helicoidal shell element over a classical flat element.

In a sense, the present element can be thought of as a high-order element, because helicoidal modeling allows us to describe curved and curving surfaces in a natural way despite low-order interpolants. The locking-free behavior of the element has to be likely ascribed to a fair approximate representation of the orientoposition field, faithful to the helicoidal modeling of the surface: the proposed coupling of positions and orientations of the interpolated field strictly reflects the coupling inherent in helicoidal modeling (Part I, Section 2.2).

This paper also has to tackle another problem that arises when the evolution of the discrete model along the solution process (that is, the rototranslation of the nodal frames) is described through incremental helicoidal motions. The problem is that of selective external constraints, that is, when nodes — or, in general, structure boundaries — are constrained along some degrees while the remaining degrees keep free. Selective constraints are hardly consistent with helicoidal motion: partial constraints on some components of incremental helices are unlikely in common practice. In our past computations, we could fulfill selective constraints by grounding appropriate incremental unknowns along a self-based solution process [Merlini and Morandini 2005]. This expedient, however, cannot be used with every problem: the hemispherical shell test case, for instance, when modeled as a quarter of the dome, requires selective symmetry constraints that cannot be handled by simply grounding appropriate incremental unknowns. Therefore, a nonlinear constraint element, capable of dealing with external constraints in weak form, has been developed.

The paper is organized as follows. The formulation of the variational principle, including the treatment of external loads and selective constraints, is discussed and linearized in Section 2. In Section 3, the interpolations are introduced and the linearized variational principle is approximated by the finite element method. In Section 4, several numerical examples are presented to demonstrate the performance of the proposed element. Section 5 concludes the paper.

2. Material surface variational mechanics

As stated in Part I, the starting point for the present formulation in shell mechanics is the principle of virtual work. It can be written in the form $\Pi_{\mathrm{int}\delta} + \Pi_{\mathrm{ext}\delta} + \Pi_{\mathrm{bc}\delta} = 0$, where the contributions to the virtual functional from the stresses, the external loads and the boundary constraints are kept separate. The term $\Pi_{\mathrm{int}\delta}$ was introduced in Part I, Equation (35) and developed and linearized therein assuming the helicoidal shell model for the reduction from three dimensions. In this section, the terms $\Pi_{\mathrm{ext}\delta}$ and $\Pi_{\mathrm{bc}\delta}$ are discussed directly for the two-dimensional material surface, and are consistently linearized.

2.1. ***Virtual functionals.*** The contributions from the external loads and boundary constraints are taken from the analogous terms written for the three-dimensional formulation based on helicoidal modeling [Merlini and Morandini 2004a]. For the shell material surface, they can be cast in the form (see details in [Merlini 2008b])

$$\Pi_{\mathrm{ext}\delta} = -\int_S \langle \boldsymbol{\eta}_\delta, \boldsymbol{b} \rangle \, \mathrm{d}S - \int_{L_\mathrm{f}} \langle \boldsymbol{\eta}_\delta, \boldsymbol{s} \rangle \, \mathrm{d}L_\mathrm{f}, \quad \Pi_{\mathrm{bc}\delta} = -\int_{L_\mathrm{c}} \delta\langle \boldsymbol{\Lambda}^\mathrm{T} \boldsymbol{s}_\mathrm{c}, \boldsymbol{\eta} - \boldsymbol{\eta}_\mathrm{c} \rangle \, \mathrm{d}L_\mathrm{c}. \tag{1}$$

Here, S is the shell surface in the reference configuration and $L = L_\mathrm{f} \cup L_\mathrm{c}$ its boundary line, split into free portion L_f and constrained portion L_c. The dual vectors $\boldsymbol{b} = \boldsymbol{X}'(\boldsymbol{f} + \varepsilon \boldsymbol{c}) = \boldsymbol{f} + \varepsilon(\boldsymbol{c} + \boldsymbol{x}' \times \boldsymbol{f})$ and $\boldsymbol{s} = \boldsymbol{X}'(\boldsymbol{t} + \varepsilon \boldsymbol{m}) = \boldsymbol{t} + \varepsilon(\boldsymbol{m} + \boldsymbol{x}' \times \boldsymbol{t})$ are the pole-based external load dual densities per unit reference

surface and boundary line, respectively ($\boldsymbol{X}' = \boldsymbol{I} + \varepsilon \boldsymbol{x}'\times$ is the current position dual tensor and $\boldsymbol{x}'$ the current position vector); the relevant self-based densities, $\boldsymbol{X}'^{\mathrm{T}}\boldsymbol{b} = \boldsymbol{f} + \varepsilon \boldsymbol{c}$ and $\boldsymbol{X}'^{\mathrm{T}}\boldsymbol{s} = \boldsymbol{t} + \varepsilon \boldsymbol{m}$, are composed of the forces $\boldsymbol{f}$ and $\boldsymbol{t}$ and the couples $\boldsymbol{c}$ and $\boldsymbol{m}$; all such load densities are valued in the current configuration; the multiplier $\boldsymbol{\eta}_\delta$ is a virtual helix. The boundary constraint equation to fulfill in weak form is $\boldsymbol{\eta} = \boldsymbol{\eta}_\mathrm{c}$, with $\boldsymbol{\eta}$ the helix of the unknown rototranslation $\boldsymbol{H} = \boldsymbol{A}'\boldsymbol{A}^{\mathrm{T}}$ and $\boldsymbol{\eta}_\mathrm{c}$ a known dual vector; $\boldsymbol{s}_\mathrm{c} = \boldsymbol{X}'(\boldsymbol{t}_\mathrm{c} + \varepsilon \boldsymbol{m}_\mathrm{c}) = \boldsymbol{t}_\mathrm{c} + \varepsilon(\boldsymbol{m}_\mathrm{c} + \boldsymbol{x}' \times \boldsymbol{t}_\mathrm{c})$ is the pole-based unknown reaction dual density on L_c, and $\boldsymbol{t}_\mathrm{c} + \varepsilon \boldsymbol{m}_\mathrm{c}$ is the relevant self-based version, with $\boldsymbol{t}_\mathrm{c}$ the traction and $\boldsymbol{m}_\mathrm{c}$ the couple.

Equation $(1)_2$ shows that the constraint virtual functional $\Pi_{\mathrm{bc}\delta}$ is actually the virtual variation of a finite functional. Recalling the differential map of the rototranslation, $\boldsymbol{\eta}_\delta = \boldsymbol{\Lambda}\delta\boldsymbol{\eta}$ (Part I, Equation (7)), the constraint virtual functional can be developed as $\Pi_{\mathrm{bc}\delta} = -\int_{L_\mathrm{c}} \langle \boldsymbol{\eta}_\delta, \boldsymbol{s}_\mathrm{c}\rangle \,\mathrm{d}L_\mathrm{c} - \int_{L_\mathrm{c}} \langle \delta(\boldsymbol{\Lambda}^{\mathrm{T}}\boldsymbol{s}_\mathrm{c}), \boldsymbol{\eta} - \boldsymbol{\eta}_\mathrm{c}\rangle \,\mathrm{d}L_\mathrm{c}$. The first term is the virtual work of the constraint reactions, and the second term represents the weak form of the constraint condition. The account of the virtual multiplier in the second term was given in [Merlini and Morandini 2004a] for three-dimensional elasticity, and rewritten for material surface mechanics in [Merlini 2008b].

So far, the constraint condition of a boundary particle is cast in terms of rototranslation. However, such kinds of constraints (say, helicoidal constraints) are hardly of interest in common practice, since the single six components of a dual helix $\boldsymbol{\eta} = \boldsymbol{\varphi} + \varepsilon\boldsymbol{\rho}$, and in particular the components of its linear part $\boldsymbol{\rho}$, lose in general physical significance in real applications. In fact, it is difficult just to devise the assignment of a nonnull constraint $\boldsymbol{\eta}_\mathrm{c}$. Furthermore, difficulties arise in the case of *selective constraints*, when a boundary particle has some directions constrained and others free [Merlini and Morandini 2004a]. A convenient way of tackling the issue of selective constraints is to write them with a variational formulation based on classical Euclidean-rotational modeling, then to rephrase them in the context of helicoidal modeling. A constraint variational formulation of this kind was developed, linearized, and applied to helicoidal modeling by [Merlini 2008a], with reference to three-dimensional elasticity. The same formulation can be rewritten for the material surface starting from the constraint virtual functional

$$\Pi_{\mathrm{bc}\delta} = -\int_{L_\mathrm{c}} \delta(\langle \boldsymbol{t}_\mathrm{c}, \boldsymbol{u} - \boldsymbol{u}_\mathrm{c}\rangle + \langle \boldsymbol{\Gamma}^{\mathrm{T}}\boldsymbol{m}_\mathrm{c}, \boldsymbol{\varphi} - \boldsymbol{\varphi}_\mathrm{c}\rangle)\,\mathrm{d}L_\mathrm{c}, \tag{2}$$

where $\boldsymbol{u}$ are displacements and $\boldsymbol{\varphi}$ rotation vectors; $\boldsymbol{\Gamma}$ is the mapping tensor of the differential map of the rotation $\boldsymbol{\Phi}$, such that $\boldsymbol{\varphi}_\delta = \boldsymbol{\Gamma}\delta\boldsymbol{\varphi}$ (Part I, Equation (6)). The uncoupled structure of the linear and angular constraint conditions in (2) is straightforward. Using this expression of the constraint virtual functional instead of $(1)_2$ makes the treatment of selective constraints affordable.

A further improvement for the treatment of selective constraints is the introduction of local constraint frames. A *constraint frame* is made of three orthonormal vectors $\boldsymbol{n}_j \equiv \boldsymbol{n}^j$ that compose the orientation tensor $\boldsymbol{N} = \boldsymbol{N}^{-\mathrm{T}} = \boldsymbol{n}_j \otimes \boldsymbol{i}^j = \boldsymbol{n}^j \otimes \boldsymbol{i}_j$; this is a given tensor and is used to define the service vectors

$$\breve{\boldsymbol{u}}_\mathrm{c} = \boldsymbol{N}^{\mathrm{T}}\boldsymbol{u}_\mathrm{c}, \quad \breve{\boldsymbol{\varphi}}_\mathrm{c} = \boldsymbol{N}^{\mathrm{T}}\boldsymbol{\varphi}_\mathrm{c}, \tag{3}$$

and

$$\breve{\boldsymbol{t}}_\mathrm{c} = \boldsymbol{N}^{\mathrm{T}}\boldsymbol{t}_\mathrm{c}, \quad \breve{\boldsymbol{m}}_\mathrm{c} = \boldsymbol{N}^{\mathrm{T}}\boldsymbol{m}_\mathrm{c}. \tag{4}$$

Vectors $\breve{\boldsymbol{u}}_\mathrm{c}$ and $\breve{\boldsymbol{\varphi}}_\mathrm{c}$ are the known constraint displacement and rotation vector back-rotated by $\boldsymbol{N}^{\mathrm{T}}$, whereas $\breve{\boldsymbol{t}}_\mathrm{c}$ and $\breve{\boldsymbol{m}}_\mathrm{c}$ are the unknown constraint reaction and reaction couple back-rotated by $\boldsymbol{N}^{\mathrm{T}}$. So, the absolute components of such service vectors are just the components of the true vectors in the local constraint

frame. This fact makes it easy to apply the constraints along a subset of the boundary particle degrees of freedom, without depriving the formulation of its clean vectorial notation: in practice, it corresponds to referring the constraint to a local reference frame. Using (3) and (4), (2) is rewritten as

$$\Pi_{\mathrm{bc}\delta} = -\int_{L_\mathrm{c}} \delta(\langle \check{\boldsymbol{t}}_\mathrm{c}, \boldsymbol{N}^\mathrm{T}\boldsymbol{u} - \check{\boldsymbol{u}}_\mathrm{c}\rangle + \langle \boldsymbol{N}^\mathrm{T}\boldsymbol{\Gamma}^\mathrm{T}\boldsymbol{N}\check{\boldsymbol{m}}_\mathrm{c}, \boldsymbol{N}^\mathrm{T}\boldsymbol{\varphi} - \check{\boldsymbol{\varphi}}_\mathrm{c}\rangle)\,\mathrm{d}L_\mathrm{c}. \tag{5}$$

2.2. ***Linearization.*** Linearization of functional $\Pi_{\mathrm{ext}\delta}$ is accomplished under the hypothesis of only two kinds of external loads: *dead-loads* $\boldsymbol{f}_\mathrm{D} + \varepsilon\boldsymbol{c}_\mathrm{D}$ and $\boldsymbol{t}_\mathrm{D} + \varepsilon\boldsymbol{m}_\mathrm{D}$ and *follower-loads* $\boldsymbol{\Phi}(\boldsymbol{f}_\mathrm{F} + \varepsilon\boldsymbol{c}_\mathrm{F})$ and $\boldsymbol{\Phi}(\boldsymbol{t}_\mathrm{F} + \varepsilon\boldsymbol{m}_\mathrm{F})$, with $\boldsymbol{f}_\mathrm{D}$, $\boldsymbol{c}_\mathrm{D}$, $\boldsymbol{t}_\mathrm{D}$, $\boldsymbol{m}_\mathrm{D}$ and $\boldsymbol{f}_\mathrm{F}$, $\boldsymbol{c}_\mathrm{F}$, $\boldsymbol{t}_\mathrm{F}$, $\boldsymbol{m}_\mathrm{F}$ assigned densities. So, the expressions of the pole-based loads in $(1)_1$ become

$$\boldsymbol{b} = \boldsymbol{X}'\big((\boldsymbol{f}_\mathrm{D} + \boldsymbol{\Phi}\boldsymbol{f}_\mathrm{F}) + \varepsilon(\boldsymbol{c}_\mathrm{D} + \boldsymbol{\Phi}\boldsymbol{c}_\mathrm{F})\big), \quad \boldsymbol{s} = \boldsymbol{X}'\big((\boldsymbol{t}_\mathrm{D} + \boldsymbol{\Phi}\boldsymbol{t}_\mathrm{F}) + \varepsilon(\boldsymbol{m}_\mathrm{D} + \boldsymbol{\Phi}\boldsymbol{m}_\mathrm{F})\big).$$

After realizing that $\partial(\boldsymbol{X}'^\mathrm{T}\boldsymbol{\eta}_\delta) = \boldsymbol{X}'^\mathrm{T}\boldsymbol{\eta}_{\partial\delta} + \frac{1}{2}\boldsymbol{\varphi}_\partial \times \boldsymbol{\varphi}_\delta + \frac{1}{2}\boldsymbol{\varphi}_\partial \times \boldsymbol{X}'^\mathrm{T}\boldsymbol{\eta}_\delta + \frac{1}{2}\boldsymbol{\varphi}_\delta \times \boldsymbol{X}'^\mathrm{T}\boldsymbol{\eta}_\partial$, linearization of $(1)_1$ involves simple algebraic manipulations (see [Merlini 2008b]) and yields

$$\begin{aligned}
\Pi_{\mathrm{ext}\delta} &= -\int_S \{\boldsymbol{\eta}_\delta\}^\mathrm{T} \cdot \{\boldsymbol{R}^S_{\mathrm{f}\eta}\}\,\mathrm{d}S - \int_{L_\mathrm{f}} \{\boldsymbol{\eta}_\delta\}^\mathrm{T} \cdot \{\boldsymbol{R}^L_{\mathrm{f}\eta}\}\,\mathrm{d}L_\mathrm{f},\\
\partial\Pi_{\mathrm{ext}\delta} &= -\int_S (\{\boldsymbol{\eta}_\delta\}^\mathrm{T} \cdot [\boldsymbol{D}^S_{\mathrm{f}\eta\eta}] \cdot \{\boldsymbol{\eta}_\partial\} + \{\boldsymbol{\eta}_{\partial\delta}\}^\mathrm{T} \cdot \{\boldsymbol{R}^S_{\mathrm{f}\eta}\})\,\mathrm{d}S - \int_{L_\mathrm{f}} (\{\boldsymbol{\eta}_\delta\}^\mathrm{T} \cdot [\boldsymbol{D}^L_{\mathrm{f}\eta\eta}] \cdot \{\boldsymbol{\eta}_\partial\} + \{\boldsymbol{\eta}_{\partial\delta}\}^\mathrm{T} \cdot \{\boldsymbol{R}^L_{\mathrm{f}\eta}\})\,\mathrm{d}L_\mathrm{f},
\end{aligned} \tag{6}$$

where

$$\{\boldsymbol{R}^S_{\mathrm{f}\eta}\} = \begin{Bmatrix} (\boldsymbol{c}_\mathrm{D} + \boldsymbol{\Phi}\boldsymbol{c}_\mathrm{F}) + \boldsymbol{x}' \times (\boldsymbol{f}_\mathrm{D} + \boldsymbol{\Phi}\boldsymbol{f}_\mathrm{F}) \\ \boldsymbol{f}_\mathrm{D} + \boldsymbol{\Phi}\boldsymbol{f}_\mathrm{F} \end{Bmatrix},$$

$$[\boldsymbol{D}^S_{\mathrm{f}\eta\eta}] = \begin{bmatrix} \frac{1}{2}(\boldsymbol{c}_\mathrm{D} + \boldsymbol{\Phi}\boldsymbol{c}_\mathrm{F})\times + \frac{1}{2}\big(\boldsymbol{x}' \times (\boldsymbol{f}_\mathrm{D} + \boldsymbol{\Phi}\boldsymbol{f}_\mathrm{F})\times + (\boldsymbol{f}_\mathrm{D} + \boldsymbol{\Phi}\boldsymbol{f}_\mathrm{F}) \times \boldsymbol{x}'\times\big) & \frac{1}{2}(\boldsymbol{f}_\mathrm{D} + \boldsymbol{\Phi}\boldsymbol{f}_\mathrm{F})\times^\mathrm{T} \\ \frac{1}{2}(\boldsymbol{f}_\mathrm{D} + \boldsymbol{\Phi}\boldsymbol{f}_\mathrm{F})\times & \boldsymbol{0} \end{bmatrix}$$
$$- \begin{bmatrix} (\boldsymbol{\Phi}\boldsymbol{c}_\mathrm{F}) \times + \boldsymbol{x}' \times (\boldsymbol{\Phi}\boldsymbol{f}_\mathrm{F})\times & \boldsymbol{0} \\ (\boldsymbol{\Phi}\boldsymbol{f}_\mathrm{F})\times & \boldsymbol{0} \end{bmatrix},$$

and

$$\{\boldsymbol{R}^L_{\mathrm{f}\eta}\} = \begin{Bmatrix} (\boldsymbol{m}_\mathrm{D} + \boldsymbol{\Phi}\boldsymbol{m}_\mathrm{F}) + \boldsymbol{x}' \times (\boldsymbol{t}_\mathrm{D} + \boldsymbol{\Phi}\boldsymbol{t}_\mathrm{F}) \\ \boldsymbol{t}_\mathrm{D} + \boldsymbol{\Phi}\boldsymbol{t}_\mathrm{F} \end{Bmatrix},$$

$$[\boldsymbol{D}^L_{\mathrm{f}\eta\eta}] = \begin{bmatrix} \frac{1}{2}(\boldsymbol{m}_\mathrm{D} + \boldsymbol{\Phi}\boldsymbol{m}_\mathrm{F})\times + \frac{1}{2}\big(\boldsymbol{x}' \times (\boldsymbol{t}_\mathrm{D} + \boldsymbol{\Phi}\boldsymbol{t}_\mathrm{F})\times + (\boldsymbol{t}_\mathrm{D} + \boldsymbol{\Phi}\boldsymbol{t}_\mathrm{F}) \times \boldsymbol{x}'\times\big) & \frac{1}{2}(\boldsymbol{t}_\mathrm{D} + \boldsymbol{\Phi}\boldsymbol{t}_\mathrm{F})\times^\mathrm{T} \\ \frac{1}{2}(\boldsymbol{t}_\mathrm{D} + \boldsymbol{\Phi}\boldsymbol{t}_\mathrm{F})\times & \boldsymbol{0} \end{bmatrix}$$
$$- \begin{bmatrix} (\boldsymbol{\Phi}\boldsymbol{m}_\mathrm{F}) \times + \boldsymbol{x}' \times (\boldsymbol{\Phi}\boldsymbol{t}_\mathrm{F})\times & \boldsymbol{0} \\ (\boldsymbol{\Phi}\boldsymbol{t}_\mathrm{F})\times & \boldsymbol{0} \end{bmatrix}.$$

As assumed in Part I, here and in the following the sequence angular–linear is understood while writing dual vectors and tensors in matrix notation. So, for example, in column $\{\boldsymbol{\eta}_\delta\}$ vector $\boldsymbol{\varphi}_\delta$ is the first element and vector $\boldsymbol{\rho}_\delta$ the second.

Linearization of the functional $\Pi_{\mathrm{bc}\delta}$ needs more skills about the successive differentiations of the rotation tensor [Merlini 2002; 2003]. Here, it suffices to recall that $\partial\boldsymbol{\varphi}_\delta = \boldsymbol{\varphi}_{\partial\delta} + \frac{1}{2}\boldsymbol{\varphi}_\partial \times \boldsymbol{\varphi}_\delta$, $\boldsymbol{\varphi}_\delta = \boldsymbol{\Gamma}\delta\boldsymbol{\varphi}$, $\delta\boldsymbol{\Gamma} = \boldsymbol{\Gamma}_/ : \delta\boldsymbol{\varphi} \otimes \boldsymbol{I}$, $\partial\boldsymbol{\Gamma}_/ = \boldsymbol{\Gamma}^{1234}_{//} : \partial\boldsymbol{\varphi} \otimes \boldsymbol{I}$; the expressions for tensors $\boldsymbol{\Gamma}$, $\boldsymbol{\Gamma}_/$ and $\boldsymbol{\Gamma}^{1234}_{//}$ can be found

in [Merlini and Morandini 2004b, Appendix A]. After some algebraic manipulation [Merlini 2008b], linearization of (5) yields

$$
\begin{aligned}
\Pi_{\mathrm{bc}\delta} &= -\int_{L_\mathrm{c}} \left(\begin{Bmatrix} \boldsymbol{\varphi}_\delta \\ \delta \boldsymbol{u} \end{Bmatrix}^{\mathrm{T}} \cdot \begin{Bmatrix} \boldsymbol{Q}_{\mathrm{IIc}} \check{\boldsymbol{m}}_\mathrm{c} \\ \boldsymbol{N} \check{\boldsymbol{t}}_\mathrm{c} \end{Bmatrix} + \begin{Bmatrix} \delta \check{\boldsymbol{m}}_\mathrm{c} \\ \delta \check{\boldsymbol{t}}_\mathrm{c} \end{Bmatrix}^{\mathrm{T}} \cdot \begin{Bmatrix} \boldsymbol{Q}_{\mathrm{Ic}} \\ \boldsymbol{Q}_{\mathrm{Lc}} \end{Bmatrix} \right) \mathrm{d}L_\mathrm{c}, \\
\partial \Pi_{\mathrm{bc}\delta} &= -\int_{L_\mathrm{c}} \left(\boldsymbol{\varphi}_\delta \cdot \left[\boldsymbol{\Gamma}^{-\mathrm{T}} (\check{\boldsymbol{m}}_\mathrm{c} \cdot \boldsymbol{Q}_{\mathrm{IIIc}}) \boldsymbol{\Gamma}^{-1} + \tfrac{1}{2} (\boldsymbol{Q}_{\mathrm{IIc}} \check{\boldsymbol{m}}_\mathrm{c}) \times \right] \cdot \boldsymbol{\varphi}_\partial + \begin{Bmatrix} \boldsymbol{\varphi}_\delta \\ \delta \boldsymbol{u} \end{Bmatrix}^{\mathrm{T}} \cdot \begin{bmatrix} \boldsymbol{Q}_{\mathrm{IIc}} & \boldsymbol{0} \\ \boldsymbol{0} & \boldsymbol{N} \end{bmatrix} \cdot \begin{Bmatrix} \partial \check{\boldsymbol{m}}_\mathrm{c} \\ \partial \check{\boldsymbol{t}}_\mathrm{c} \end{Bmatrix} \right. \\
&\qquad \left. + \begin{Bmatrix} \delta \check{\boldsymbol{m}}_\mathrm{c} \\ \delta \check{\boldsymbol{t}}_\mathrm{c} \end{Bmatrix}^{\mathrm{T}} \cdot \begin{bmatrix} \boldsymbol{Q}_{\mathrm{IIc}}^{\mathrm{T}} & \boldsymbol{0} \\ \boldsymbol{0} & \boldsymbol{N}^{\mathrm{T}} \end{bmatrix} \cdot \begin{Bmatrix} \boldsymbol{\varphi}_\partial \\ \partial \boldsymbol{u} \end{Bmatrix} + \begin{Bmatrix} \boldsymbol{\varphi}_{\partial\delta} \\ \partial \delta \boldsymbol{u} \end{Bmatrix}^{\mathrm{T}} \cdot \begin{Bmatrix} \boldsymbol{Q}_{\mathrm{IIc}} \check{\boldsymbol{m}}_\mathrm{c} \\ \boldsymbol{N} \check{\boldsymbol{t}}_\mathrm{c} \end{Bmatrix} + \begin{Bmatrix} \partial \delta \check{\boldsymbol{m}}_\mathrm{c} \\ \partial \delta \check{\boldsymbol{t}}_\mathrm{c} \end{Bmatrix}^{\mathrm{T}} \cdot \begin{Bmatrix} \boldsymbol{Q}_{\mathrm{Ic}} \\ \boldsymbol{Q}_{\mathrm{Lc}} \end{Bmatrix} \right) \mathrm{d}L_\mathrm{c},
\end{aligned}
\tag{7}
$$

where convenient tensors have been introduced as

$$
\begin{aligned}
\boldsymbol{Q}_{\mathrm{Lc}} &= \boldsymbol{N}^{\mathrm{T}} \boldsymbol{u} - \check{\boldsymbol{u}}_\mathrm{c}, \\
\boldsymbol{Q}_{\mathrm{Ic}} &= \boldsymbol{N}^{\mathrm{T}} \boldsymbol{\Gamma} \boldsymbol{N} (\boldsymbol{N}^{\mathrm{T}} \boldsymbol{\varphi} - \check{\boldsymbol{\varphi}}_\mathrm{c}), \\
\boldsymbol{Q}_{\mathrm{IIc}} &= \boldsymbol{N} + \boldsymbol{\Gamma}^{-\mathrm{T}} \big(\boldsymbol{N}^{\mathrm{T}} \boldsymbol{\Gamma}_{/} \boldsymbol{N} (\boldsymbol{N}^{\mathrm{T}} \boldsymbol{\varphi} - \check{\boldsymbol{\varphi}}_\mathrm{c}) \big)^{\mathrm{T}}, \\
\boldsymbol{Q}_{\mathrm{IIIc}} &= \boldsymbol{N}^{\mathrm{T}} \boldsymbol{\Gamma}_{/} + \boldsymbol{N}^{\mathrm{T}} \big(\boldsymbol{\Gamma}_{//}^{1\underline{23}4} - (\boldsymbol{\Gamma}_{/}^{\mathrm{T}132} \boldsymbol{\Gamma}^{-1} \boldsymbol{\Gamma}_{/}^{\mathrm{T}132})^{\mathrm{T}1342} \big) \boldsymbol{N} (\boldsymbol{N}^{\mathrm{T}} \boldsymbol{\varphi} - \check{\boldsymbol{\varphi}}_\mathrm{c}).
\end{aligned}
$$

In order to use the constraint virtual functionals $\Pi_{\mathrm{bc}\delta}$ and $\partial \Pi_{\mathrm{bc}\delta}$ in the context of helicoidal modeling, it remains to pass from Euclidean-rotational kinematics to helicoidal kinematics. The constraint reactions are conveniently grouped into the dual reaction $\check{\boldsymbol{r}}_\mathrm{c} = \check{\boldsymbol{t}}_\mathrm{c} + \varepsilon \check{\boldsymbol{m}}_\mathrm{c}$ and the kinematical variables into the dual vector $\boldsymbol{e} = \boldsymbol{\varphi} + \varepsilon \boldsymbol{u}$. Consistently, the dual kinematical variation variables $\boldsymbol{e}_\delta = \boldsymbol{\varphi}_\delta + \varepsilon \delta \boldsymbol{u}$, $\boldsymbol{e}_\partial = \boldsymbol{\varphi}_\partial + \varepsilon \partial \boldsymbol{u}$, and $\boldsymbol{e}_{\partial\delta} = \boldsymbol{\varphi}_{\partial\delta} + \varepsilon \partial \delta \boldsymbol{u}$ are introduced. It can be shown that the dual vector $\boldsymbol{e}$ and the helix $\boldsymbol{\eta}$ are related by $\boldsymbol{e} = \boldsymbol{\Gamma}^{\mathrm{T}} \boldsymbol{X}'^{\mathrm{T}} \boldsymbol{\eta}$, and the relevant variation variables by

$$
\boldsymbol{e}_\delta = \boldsymbol{X}'^{\mathrm{T}} \boldsymbol{\eta}_\delta, \quad \boldsymbol{e}_\partial = \boldsymbol{X}'^{\mathrm{T}} \boldsymbol{\eta}_\partial, \quad \boldsymbol{e}_{\partial\delta} = \boldsymbol{X}'^{\mathrm{T}} \boldsymbol{\eta}_{\partial\delta} + \tfrac{1}{2} (\boldsymbol{\varphi}_\partial \times \boldsymbol{X}'^{\mathrm{T}} \boldsymbol{\eta}_\delta + \boldsymbol{\varphi}_\delta \times \boldsymbol{X}'^{\mathrm{T}} \boldsymbol{\eta}_\partial),
$$

see [Merlini 2008a]. Thus, (7) are finally brought to the form

$$
\begin{aligned}
\Pi_{\mathrm{bc}\delta} &= -\int_{L_\mathrm{c}} \begin{Bmatrix} \boldsymbol{\eta}_\delta \\ \delta \check{\boldsymbol{r}}_\mathrm{c} \end{Bmatrix}^{\mathrm{T}} \cdot \begin{Bmatrix} \boldsymbol{R}_{\mathrm{c}\eta}^L \\ \boldsymbol{R}_{\mathrm{c}r}^L \end{Bmatrix} \mathrm{d}L_\mathrm{c}, \\
\partial \Pi_{\mathrm{bc}\delta} &= -\int_{L_\mathrm{c}} \left(\begin{Bmatrix} \boldsymbol{\eta}_\delta \\ \delta \check{\boldsymbol{r}}_\mathrm{c} \end{Bmatrix}^{\mathrm{T}} \cdot \begin{bmatrix} \boldsymbol{D}_{\mathrm{c}\eta\eta}^L & \boldsymbol{D}_{\mathrm{c}\eta r}^L \\ \boldsymbol{D}_{\mathrm{c}\eta r}^{L\,\mathrm{T}} & \boldsymbol{0} \end{bmatrix} \cdot \begin{Bmatrix} \boldsymbol{\eta}_\partial \\ \partial \check{\boldsymbol{r}}_\mathrm{c} \end{Bmatrix} + \begin{Bmatrix} \boldsymbol{\eta}_{\partial\delta} \\ \partial \delta \check{\boldsymbol{r}}_\mathrm{c} \end{Bmatrix}^{\mathrm{T}} \cdot \begin{Bmatrix} \boldsymbol{R}_{\mathrm{c}\eta}^L \\ \boldsymbol{R}_{\mathrm{c}r}^L \end{Bmatrix} \right) \mathrm{d}L_\mathrm{c},
\end{aligned}
\tag{8}
$$

where

$$
\begin{aligned}
\{\boldsymbol{R}_{\mathrm{c}\eta}^L\} &= \begin{Bmatrix} \boldsymbol{Q}_{\mathrm{IIc}} \check{\boldsymbol{m}}_\mathrm{c} + \boldsymbol{x}' \times \boldsymbol{N} \check{\boldsymbol{t}}_\mathrm{c} \\ \boldsymbol{N} \check{\boldsymbol{t}}_\mathrm{c} \end{Bmatrix}, \\
\{\boldsymbol{R}_{\mathrm{c}r}^L\} &= \begin{Bmatrix} \boldsymbol{Q}_{\mathrm{Ic}} \\ \boldsymbol{Q}_{\mathrm{Lc}} \end{Bmatrix}, \\
[\boldsymbol{D}_{\mathrm{c}\eta\eta}^L] &= \begin{bmatrix} \boldsymbol{\Gamma}^{-\mathrm{T}} (\check{\boldsymbol{m}}_\mathrm{c} \cdot \boldsymbol{Q}_{\mathrm{IIIc}}) \boldsymbol{\Gamma}^{-1} + \frac{1}{2} (\boldsymbol{Q}_{\mathrm{IIc}} \check{\boldsymbol{m}}_\mathrm{c}) \times + \frac{1}{2} \big(\boldsymbol{x}' \times (\boldsymbol{N} \check{\boldsymbol{t}}_\mathrm{c}) \times + (\boldsymbol{N} \check{\boldsymbol{t}}_\mathrm{c}) \times \boldsymbol{x}' \times \big) & \frac{1}{2} (\boldsymbol{N} \check{\boldsymbol{t}}_\mathrm{c}) \times^{\mathrm{T}} \\ \frac{1}{2} (\boldsymbol{N} \check{\boldsymbol{t}}_\mathrm{c}) \times & \boldsymbol{0} \end{bmatrix}, \\
[\boldsymbol{D}_{\mathrm{c}\eta r}^L] &= \begin{bmatrix} \boldsymbol{Q}_{\mathrm{IIc}} & \boldsymbol{x}' \times \boldsymbol{N} \\ \boldsymbol{0} & \boldsymbol{N} \end{bmatrix}.
\end{aligned}
\tag{9}
$$

Note that the mixed virtual-incremental variation variables are retained in the tangent functionals $\partial\Pi_{\mathrm{ext}\delta}$ and $\partial\Pi_{\mathrm{bc}\delta}$, in consideration of a possible nonlinear dependence of the local variables on the ultimate problem unknowns.

3. Finite elements

3.1. ***Linearized discrete variational principle.*** The virtual functionals discussed above are assembled as a sum of contributions from the appropriate elements according to the finite element method. Three kinds of element contributions are considered.

First, the material surface *shell element* itself: the integrals $\Pi_{\mathrm{int}\delta} = \int_S \pi_{\mathrm{int}\delta}\,\mathrm{d}S$ and $\partial\Pi_{\mathrm{int}\delta} = \int_S \partial\pi_{\mathrm{int}\delta}\,\mathrm{d}S$, relevant to the internal work as discussed in Part I, and part of the integrals $\Pi_{\mathrm{ext}\delta}$ and $\partial\Pi_{\mathrm{ext}\delta}$ from (6), relevant to the external loads, pertain to this element. So, recalling Part I, Equation (67), the virtual functional and the virtual tangent functional of the shell element, which spans over the surface S^e, are written

$$\begin{aligned}
\Pi_\delta^{S^e} &= \int_{S^e} \left(\begin{Bmatrix} \delta(\boldsymbol{H}^{\mathrm{T}}\boldsymbol{\omega}_\alpha) \\ \delta\hat{\boldsymbol{\tau}} \end{Bmatrix}^{\mathrm{T}} \cdot \begin{Bmatrix} \boldsymbol{H}^{\mathrm{T}}\bar{\boldsymbol{R}}_{\boldsymbol{\omega}}^{\alpha} \\ \bar{\boldsymbol{R}}_{\boldsymbol{\tau}} \end{Bmatrix} - \{\boldsymbol{\eta}_\delta\}^{\mathrm{T}} \cdot \{\boldsymbol{R}_{\mathrm{f}\eta}^S\} \right) \mathrm{d}S^e, \\
\partial\Pi_\delta^{S^e} &= \int_{S^e} \left(\begin{Bmatrix} \delta(\boldsymbol{H}^{\mathrm{T}}\boldsymbol{\omega}_\alpha) \\ \delta\hat{\boldsymbol{\tau}} \end{Bmatrix}^{\mathrm{T}} \cdot \begin{bmatrix} \boldsymbol{H}^{\mathrm{T}}\bar{\boldsymbol{D}}_{\boldsymbol{\omega}\boldsymbol{\omega}}^{\alpha\beta}\boldsymbol{H} & \boldsymbol{H}^{\mathrm{T}}\bar{\boldsymbol{D}}_{\boldsymbol{\omega}\boldsymbol{\tau}}^{\alpha} \\ \bar{\boldsymbol{D}}_{\boldsymbol{\omega}\boldsymbol{\tau}}^{\beta\mathrm{T}}\boldsymbol{H} & \bar{\boldsymbol{D}}_{\boldsymbol{\tau}\boldsymbol{\tau}} \end{bmatrix} \cdot \begin{Bmatrix} \partial(\boldsymbol{H}^{\mathrm{T}}\boldsymbol{\omega}_\beta) \\ \partial\hat{\boldsymbol{\tau}} \end{Bmatrix} - \{\boldsymbol{\eta}_\delta\}^{\mathrm{T}} \cdot [\boldsymbol{D}_{\mathrm{f}\eta\eta}^S] \cdot \{\boldsymbol{\eta}_\partial\} \right. \\
&\qquad \left. + \begin{Bmatrix} \partial\delta(\boldsymbol{H}^{\mathrm{T}}\boldsymbol{\omega}_\alpha) \\ \partial\delta\hat{\boldsymbol{\tau}} \end{Bmatrix}^{\mathrm{T}} \cdot \begin{Bmatrix} \boldsymbol{H}^{\mathrm{T}}\bar{\boldsymbol{R}}_{\boldsymbol{\omega}}^{\alpha} \\ \bar{\boldsymbol{R}}_{\boldsymbol{\tau}} \end{Bmatrix} - \{\boldsymbol{\eta}_{\partial\delta}\}^{\mathrm{T}} \cdot \{\boldsymbol{R}_{\mathrm{f}\eta}^S\} \right) \mathrm{d}S^e,
\end{aligned} \tag{10}$$

where tensors $\bar{\boldsymbol{R}}$ and $\bar{\boldsymbol{D}}$ are given in Part I, Equation (66).

Second, the *border load element*, to which the other terms in (6) relevant to the external loads pertain. It lies on the line L_{f}^e, and the relevant functionals are written

$$\Pi_\delta^{L_{\mathrm{f}}^e} = -\int_{L_{\mathrm{f}}^e} \{\boldsymbol{\eta}_\delta\}^{\mathrm{T}} \cdot \{\boldsymbol{R}_{\mathrm{f}\eta}^L\}\,\mathrm{d}L_{\mathrm{f}}^e, \quad \partial\Pi_\delta^{L_{\mathrm{f}}^e} = -\int_{L_{\mathrm{f}}^e} (\{\boldsymbol{\eta}_\delta\}^{\mathrm{T}} \cdot [\boldsymbol{D}_{\mathrm{f}\eta\eta}^L] \cdot \{\boldsymbol{\eta}_\partial\} + \{\boldsymbol{\eta}_{\partial\delta}\}^{\mathrm{T}} \cdot \{\boldsymbol{R}_{\mathrm{f}\eta}^L\})\,\mathrm{d}L_{\mathrm{f}}^e. \tag{11}$$

This element is a useful means to introduce external loads distributed along the shell boundary.

Third, an element to implement the boundary constraints as for (8). However, in the present version of the finite element code, this element is not integrated over a line L_{c}^e, but instead is attached to a single node N_{c}^e; hence, it is referred to as the *node constraint element*. The relevant functionals are written

$$\begin{aligned}
\Pi_\delta^{N_{\mathrm{c}}^e} &= -\begin{Bmatrix} \boldsymbol{\eta}_{\delta J} \\ \delta\check{\boldsymbol{r}}_{\mathrm{c}J} \end{Bmatrix}^{\mathrm{T}} \cdot \begin{Bmatrix} \boldsymbol{R}_{\mathrm{c}\eta}^N \\ \boldsymbol{R}_{\mathrm{c}\boldsymbol{r}}^N \end{Bmatrix}, \\
\partial\Pi_\delta^{N_{\mathrm{c}}^e} &= -\left(\begin{Bmatrix} \boldsymbol{\eta}_{\delta J} \\ \delta\check{\boldsymbol{r}}_{\mathrm{c}J} \end{Bmatrix}^{\mathrm{T}} \cdot \begin{bmatrix} \boldsymbol{D}_{\mathrm{c}\eta\eta}^N & \boldsymbol{D}_{\mathrm{c}\eta\boldsymbol{r}}^N \\ \boldsymbol{D}_{\mathrm{c}\eta\boldsymbol{r}}^{N\mathrm{T}} & \boldsymbol{0} \end{bmatrix} \cdot \begin{Bmatrix} \boldsymbol{\eta}_{\partial J} \\ \partial\check{\boldsymbol{r}}_{\mathrm{c}J} \end{Bmatrix} + \{\boldsymbol{\eta}_{\partial\delta J}\}^{\mathrm{T}} \cdot \{\boldsymbol{R}_{\mathrm{c}\eta}^N\} \right),
\end{aligned} \tag{12}$$

where $\boldsymbol{\eta}_J$ and $\check{\boldsymbol{r}}_{\mathrm{c}J}$ refer to the helix and the dual reaction at the constrained node J, and the dual vectors $\boldsymbol{R}_{\mathrm{c}}^N$ and tensors $\boldsymbol{D}_{\mathrm{c}}^N$ are evaluated from (9) at that node. Note that the mixed virtual-incremental variation $\partial\delta\check{\boldsymbol{r}}_{\mathrm{c}}$ has been discarded while passing from (8) to (12); in fact $\check{\boldsymbol{r}}_{\mathrm{c}J}$ is now an ultimate free unknown of

the discrete problem. This is not the case for $\boldsymbol{\eta}_{\partial\delta}$. The node constraint element is not specific to the shell modeling and can be used in any finite element analysis.

The linearized variational principle is therefore cast in the form $\Pi_\delta + \partial\Pi_\delta = 0$, where the discrete virtual functional and virtual tangent functional of the whole problem are built with the contribution from all the elements:

$$\Pi_\delta = \sum_{S^e} \Pi_\delta^{S^e} + \sum_{L_\mathrm{f}^e} \Pi_\delta^{L_\mathrm{f}^e} + \sum_{N_\mathrm{c}^e} \Pi_\delta^{N_\mathrm{c}^e}, \quad \partial\Pi_\delta = \sum_{S^e} \partial\Pi_\delta^{S^e} + \sum_{L_\mathrm{f}^e} \partial\Pi_\delta^{L_\mathrm{f}^e} + \sum_{N_\mathrm{c}^e} \partial\Pi_\delta^{N_\mathrm{c}^e}.$$

Note that the external loads and possibly the reaction constraints will contribute to the tangent stiffness.

3.2. ***Element kinematic field.*** As discussed in Part I, Section 3, the formulation of the material surface kinematics is based on the integral field of the rototranslations. Rototranslations are orthogonal dual tensors, and as such they compose multiplicatively and do not commute. These distinctive properties of the kinematic field should be preserved in the approximate, substitute field on which a surface element is built. The *helicoidal interpolation* developed in [Merlini and Morandini 2004b] fulfills this requirement and is adopted here for both the shell and the border load elements.

Given N nodal frames in space, with orientoposition tensors $\boldsymbol{A}_J$ ($J = 1, 2, \ldots, N$), the interpolated orientoposition $\boldsymbol{A}$ is determined by the equation

$$\sum_{J=1}^{N} W_J \log(\boldsymbol{A}\boldsymbol{A}_J^{\mathrm{T}}) = \boldsymbol{0}, \tag{13}$$

where W_J are N given weights that measure the influence of each frame J on the sought one. Solution of (13) yields the *weighted average orientoposition* $\boldsymbol{A}$, that is, an orientoposition with a null weighted average of the logarithms of the relative rototranslations $\tilde{\boldsymbol{H}}_J = \boldsymbol{A}\boldsymbol{A}_J^{\mathrm{T}}$ from the nodal frames, hence with a null weighted average of the relative helices $\tilde{\boldsymbol{\eta}}_J$ from $\boldsymbol{A}_J$ to $\boldsymbol{A}$ (see Figure 2). In the present application, as in the solid elements [Merlini and Morandini 2005], Lagrange polynomial interpolants on rectangular domains are assumed; so, the proposed corner-node elements (4-node shell element and 2-node border load element) are built with standard multilinear weight functions W_J. It is worth noting, in Figure 2, that the nodal orientations control the orientation as well as the position of the interpolated point.

Equation (13) is an implicit nonlinear equation. In general, it cannot give the interpolated orientoposition $\boldsymbol{A}$ in closed form, however it can be solved numerically by a refined Newton–Raphson procedure that proves very efficient. Then, the spatial derivatives of the weight functions W_J with respect to the local curvilinear coordinates ξ^α allow us to compute the curvature dual vectors in closed form as

$$\boldsymbol{k}_\alpha = -(\boldsymbol{\Lambda}_{\mathrm{II}}^-)^{-1} \sum_{J=1}^{N} W_{J,\alpha}\tilde{\boldsymbol{\eta}}_J, \tag{14}$$

where

$$\boldsymbol{\Lambda}_{\mathrm{II}}^- = \sum_{J=1}^{N} W_J \tilde{\boldsymbol{\Lambda}}_J^{-1}, \quad \tilde{\boldsymbol{\Lambda}}_J = \operatorname{dexp}(\tilde{\boldsymbol{\eta}}_J \times).$$

The helicoidal interpolation, (13) and (14), is first performed in the reference, undeformed configuration (this operation also allows an accurate setting of elements with possibly curved geometry). Then,

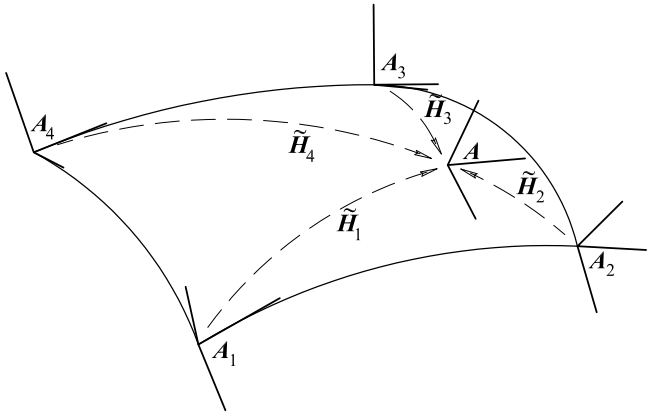

Figure 2. Helicoidal interpolation on a quadrilateral shell element.

the same interpolation scheme is applied to any current, deformed configuration; the comparison of the interpolated quantities between the current and the reference configurations allows us to recover (according to a total-Lagrangian approach) the local rototranslation $\boldsymbol{H} = \boldsymbol{A}'\boldsymbol{A}^{\mathrm{T}}$ and the kinematical dual strains $\boldsymbol{\omega}_\alpha = \boldsymbol{k}'_\alpha - \boldsymbol{H}\boldsymbol{k}_\alpha$ at the shell element quadrature points. It is worth stressing that this way of building the local kinematics is manifestly far from the customary standpoint of interpolating the rototranslations (or the rotations) of the nodal frames — a concept, in our opinion, devoid of consistency [Merlini and Morandini 2004b]. Note that operating on the orientopositions instead of the rototranslations makes this interpolation scheme path independent, as the local orientoposition and curvatures are computed independently from the past history of the nodal orientopositions. The proposed interpolation scheme is objective as well: the frame indifference and the invariance against rigid motions has been proved in [Merlini and Morandini 2004b], and is strictly connected to the concept of averaging the relative rototranslations from the nodal frames.

Evaluation of the integrals in (10) and (11) requires expressions for the virtual, incremental, and mixed virtual-incremental local variation variables. These are the outcome of the linearization of the helicoidal interpolation (13), a complicated process discussed in [Merlini and Morandini 2004b], that yields the local variation variables as linear functions of the relevant nodal variation variables. In the following, just the resulting interpolation formulae are written for the specific case of shell elements (see [Merlini and Morandini 2008]):

$$
\begin{aligned}
\{\boldsymbol{\eta}_\delta\} &= \sum_{J=1}^{N} [\boldsymbol{N}_{\mathrm{A}J}] \cdot \{\boldsymbol{\eta}_{\delta J}\}, \\
\{\boldsymbol{\eta}_\partial\} &= \sum_{K=1}^{N} [\boldsymbol{N}_{\mathrm{A}K}] \cdot \{\boldsymbol{\eta}_{\partial K}\}, \\
\{\boldsymbol{\eta}_{\partial\delta}\} &= \sum_{J=1}^{N} [\boldsymbol{N}_{\mathrm{A}J}] \cdot \{\boldsymbol{\eta}_{\partial\delta J}\} + \sum_{J=1}^{N}\sum_{K=1}^{N} \begin{Bmatrix} \{\boldsymbol{\eta}_{\delta J}\} \cdot [\mathcal{N}^{\mathrm{T213}}_{\mathrm{Aa}JK}] \cdot \{\boldsymbol{\eta}_{\partial K}\} \\ \{\boldsymbol{\eta}_{\delta J}\} \cdot [\mathcal{N}^{\mathrm{T213}}_{\mathrm{Al}JK}] \cdot \{\boldsymbol{\eta}_{\partial K}\} \end{Bmatrix},
\end{aligned}
\tag{15}
$$

and

$$\begin{aligned}
\{\boldsymbol{H}\delta(\boldsymbol{H}^{\mathrm{T}}\boldsymbol{\omega}_\alpha)\} &= \sum_{J=1}^{N}[\mathcal{N}_{\mathrm{K}J\alpha}]\cdot\{\boldsymbol{\eta}_{\delta J}\},\\
\{\boldsymbol{H}\partial(\boldsymbol{H}^{\mathrm{T}}\boldsymbol{\omega}_\beta)\} &= \sum_{K=1}^{N}[\mathcal{N}_{\mathrm{K}K\beta}]\cdot\{\boldsymbol{\eta}_{\partial K}\},\\
\{\boldsymbol{H}\partial\delta(\boldsymbol{H}^{\mathrm{T}}\boldsymbol{\omega}_\alpha)\} &= \sum_{J=1}^{N}[\mathcal{N}_{\mathrm{K}J\alpha}]\cdot\{\boldsymbol{\eta}_{\partial\delta J}\} + \sum_{J=1}^{N}\sum_{K=1}^{N}\left\{\begin{matrix}\{\boldsymbol{\eta}_{\delta J}\}\cdot[\mathbb{N}^{\mathrm{T213}}_{\mathrm{Ka}JK\alpha}]\cdot\{\boldsymbol{\eta}_{\partial K}\}\\ \{\boldsymbol{\eta}_{\delta J}\}\cdot[\mathbb{N}^{\mathrm{T213}}_{\mathrm{Kl}JK\alpha}]\cdot\{\boldsymbol{\eta}_{\partial K}\}\end{matrix}\right\}.
\end{aligned}\tag{16}$$

It is worth noting that the linearization of the helicoidal interpolation supplies interpolation formulae capable of relating the mixed virtual-incremental local variation variables to the virtual, incremental, and mixed virtual-incremental nodal variation variables. The tensor matrices in (15) and (16) are defined as

$$[\boldsymbol{N}_{\mathrm{A}J}] = \begin{bmatrix}\text{primal } \boldsymbol{V}_J & \boldsymbol{0}\\ \text{dual } \boldsymbol{V}_J & \text{primal } \boldsymbol{V}_J\end{bmatrix},$$

$$[\mathcal{N}_{\mathrm{Aa}JK}] = \begin{bmatrix}\text{primal } \mathcal{V}_{JK} & \boldsymbol{0}\\ \boldsymbol{0} & \boldsymbol{0}\end{bmatrix},$$

$$[\mathcal{N}_{\mathrm{Al}JK}] = \begin{bmatrix}\text{dual } \mathcal{V}_{JK} & \text{primal } \mathcal{V}_{JK}\\ \text{primal } \mathcal{V}_{JK} & \boldsymbol{0}\end{bmatrix},$$

and

$$[\mathcal{N}_{\mathrm{K}J\alpha}] = \begin{bmatrix}\text{primal } \breve{\mathcal{W}}_{J\alpha} & \boldsymbol{0}\\ \text{dual } \breve{\mathcal{W}}_{J\alpha} & \text{primal } \breve{\mathcal{W}}_{J\alpha}\end{bmatrix},$$

$$[\mathbb{N}_{\mathrm{Ka}JK\alpha}] = \begin{bmatrix}\text{primal } \breve{\mathbb{W}}_{JK\alpha} & \boldsymbol{0}\\ \boldsymbol{0} & \boldsymbol{0}\end{bmatrix},$$

$$[\mathbb{N}_{\mathrm{Kl}JK\alpha}] = \begin{bmatrix}\text{dual } \breve{\mathbb{W}}_{JK\alpha} & \text{primal } \breve{\mathbb{W}}_{JK\alpha}\\ \text{primal } \breve{\mathbb{W}}_{JK\alpha} & \boldsymbol{0}\end{bmatrix},$$

where

$$\breve{\mathcal{W}}_{J\alpha} = \mathcal{W}_{J\alpha} + \tfrac{1}{2}\boldsymbol{k}'_\alpha \times \boldsymbol{V}_J,$$

$$\breve{\mathbb{W}}_{JK\alpha} = \mathbb{W}_{JK\alpha} + \tfrac{1}{2}\boldsymbol{k}'_\alpha \times \mathcal{V}_{JK} + \tfrac{1}{2}(\boldsymbol{I}\times\mathcal{W}_{J\alpha})^{\mathrm{T132}}\boldsymbol{V}_K + \tfrac{1}{2}((\boldsymbol{I}\times\mathcal{W}_{K\alpha})^{\mathrm{T132}}\boldsymbol{V}_J)^{\mathrm{T132}} + ((\boldsymbol{I}\otimes\boldsymbol{k}'_\alpha)^{\mathrm{S}\underline{123}}\boldsymbol{V}_J)^{\mathrm{T132}}\boldsymbol{V}_K,$$

and tensors $\boldsymbol{V}_J$, $\mathcal{V}_{JK}$, $\mathcal{W}_{J\alpha}$, and $\mathbb{W}_{JK\alpha}$ are defined in [Merlini and Morandini 2004b].

3.3. ***Element Biot-axial field.*** The so-called surface Biot-axial stress parameter $\hat{\boldsymbol{\tau}}$, which pertains to the Euclidean vector space, is approximated in a much simpler way: it is assumed *uniform* over the shell element domain, say

$$\hat{\boldsymbol{\tau}} = \hat{\boldsymbol{\tau}}_E,$$

with $\hat{\boldsymbol{\tau}}_E$ a discrete variable of the global problem, unique for the each single element. Linearization of $\hat{\boldsymbol{\tau}}$ is straightforward, $\delta\hat{\boldsymbol{\tau}} = \delta\hat{\boldsymbol{\tau}}_E$ and $\partial\hat{\boldsymbol{\tau}} = \partial\hat{\boldsymbol{\tau}}_E$, whereas of course $\partial\delta\hat{\boldsymbol{\tau}} = \boldsymbol{0}$, since $\hat{\boldsymbol{\tau}}_E$ is an ultimate free unknown of the discrete problem.

The choice of a uniform Biot-axial parameter is consistent with the interpolation of $\hat{\boldsymbol{\tau}}$ discussed in [Merlini and Morandini 2005] for the solid element, see the particular case of planar elements. Other interpolation schemes have been investigated [Merlini and Morandini 2008] and tested, however with less success.

3.4. ***Element matrices.*** Using the variation variables obtained in Sections 3.2 and 3.3 within (10)–(12), the element contributions to the virtual functional and virtual tangent functional are brought to the following form (details in [Merlini and Morandini 2008]).

- Shell element:

$$\begin{aligned}
\Pi_\delta^{S^e} &= \sum_{J=1}^{4} \{\boldsymbol{\eta}_{\delta J}\}^{\mathrm{T}} \cdot \{\boldsymbol{F}^S_{\boldsymbol{\eta} J}\} + \delta\hat{\boldsymbol{\tau}}_E \cdot \boldsymbol{F}^S_{\boldsymbol{\tau} E},\\
\partial\Pi_\delta^{S^e} &= \sum_{J=1}^{4}\sum_{K=1}^{4} \{\boldsymbol{\eta}_{\delta J}\}^{\mathrm{T}} \cdot [\boldsymbol{K}^S_{\boldsymbol{\eta}\eta JK}] \cdot \{\boldsymbol{\eta}_{\partial K}\} + \sum_{J=1}^{4} \{\boldsymbol{\eta}_{\delta J}\}^{\mathrm{T}} \cdot [\boldsymbol{K}^S_{\boldsymbol{\eta}\tau JE}] \cdot \partial\hat{\boldsymbol{\tau}}_E \\
&\qquad + \delta\hat{\boldsymbol{\tau}}_E \cdot \sum_{K=1}^{4} [\boldsymbol{K}^S_{\boldsymbol{\eta}\tau KE}]^{\mathrm{T}} \cdot \{\boldsymbol{\eta}_{\partial K}\} + \delta\hat{\boldsymbol{\tau}}_E \cdot \boldsymbol{K}^S_{\boldsymbol{\tau}\tau EE} \cdot \partial\hat{\boldsymbol{\tau}}_E + \sum_{J=1}^{4} \{\boldsymbol{\eta}_{\partial\delta J}\}^{\mathrm{T}} \cdot \{\boldsymbol{F}^S_{\boldsymbol{\eta} J}\}.
\end{aligned} \tag{17}$$

- Border load element:

$$\begin{aligned}
\Pi_\delta^{L^e_{\mathrm{f}}} &= \sum_{J=1}^{2} \{\boldsymbol{\eta}_{\delta J}\}^{\mathrm{T}} \cdot \{\boldsymbol{F}^L_{\boldsymbol{\eta} J}\},\\
\partial\Pi_\delta^{L^e_{\mathrm{f}}} &= \sum_{J=1}^{2}\sum_{K=1}^{2} \{\boldsymbol{\eta}_{\delta J}\}^{\mathrm{T}} \cdot [\boldsymbol{K}^L_{\boldsymbol{\eta}\eta JK}] \cdot \{\boldsymbol{\eta}_{\partial K}\} + \sum_{J=1}^{2} \{\boldsymbol{\eta}_{\partial\delta J}\}^{\mathrm{T}} \cdot \{\boldsymbol{F}^L_{\boldsymbol{\eta} J}\}.
\end{aligned} \tag{18}$$

- Node constraint element:

$$\begin{aligned}
\Pi_\delta^{N^e_{\mathrm{c}}} &= \{\boldsymbol{\eta}_{\delta J}\}^{\mathrm{T}} \cdot \{\boldsymbol{F}^N_{\boldsymbol{\eta} J}\} + \{\delta\check{\boldsymbol{r}}_{\mathrm{c}J}\}^{\mathrm{T}} \cdot \{\boldsymbol{F}^N_{\boldsymbol{r} J}\},\\
\partial\Pi_\delta^{N^e_{\mathrm{c}}} &= \{\boldsymbol{\eta}_{\delta J}\}^{\mathrm{T}} \cdot [\boldsymbol{K}^N_{\boldsymbol{\eta}\eta JJ}] \cdot \{\boldsymbol{\eta}_{\partial J}\} + \{\boldsymbol{\eta}_{\delta J}\}^{\mathrm{T}} \cdot [\boldsymbol{K}^N_{\boldsymbol{\eta}\boldsymbol{r} JJ}] \cdot \{\partial\check{\boldsymbol{r}}_{\mathrm{c}J}\} \\
&\qquad + \{\delta\check{\boldsymbol{r}}_{\mathrm{c}J}\}^{\mathrm{T}} \cdot [\boldsymbol{K}^N_{\boldsymbol{\eta}\boldsymbol{r} JJ}]^{\mathrm{T}} \cdot \{\boldsymbol{\eta}_{\partial J}\} + \{\boldsymbol{\eta}_{\partial\delta J}\}^{\mathrm{T}} \cdot \{\boldsymbol{F}^N_{\boldsymbol{\eta} J}\}.
\end{aligned} \tag{19}$$

Equations (17)–(19) can be directly assembled within the global variational functionals of the whole discrete problem. The element contributions to the problem residual and tangent matrix are as follows.

- Shell element:

$$\begin{aligned}
\{\boldsymbol{F}^S_{\boldsymbol{\eta} J}\} &= \int_{S^e} (\{\bar{\boldsymbol{R}}^\alpha_{\boldsymbol{\omega}}\}^{\mathrm{T}} \cdot [\mathcal{N}_{\mathrm{K}J\alpha}] - \{\boldsymbol{R}^S_{\mathrm{f}\boldsymbol{\eta}}\}^{\mathrm{T}} \cdot [\boldsymbol{N}_{\mathrm{A}J}])\,\mathrm{d}S^e,\\
\boldsymbol{F}^S_{\boldsymbol{\tau} E} &= \int_{S^e} \bar{\boldsymbol{R}}_{\boldsymbol{\tau}}\,\mathrm{d}S^e,\\
[\boldsymbol{K}^S_{\boldsymbol{\eta}\eta JK}] &= \int_{S^e} ([\mathcal{N}_{\mathrm{K}J\alpha}]^{\mathrm{T}} \cdot [\bar{\boldsymbol{D}}^{\alpha\beta}_{\boldsymbol{\omega}\boldsymbol{\omega}}] \cdot [\mathcal{N}_{\mathrm{K}K\beta}] + [\mathrm{dual}\ \bar{\boldsymbol{R}}^\alpha_{\boldsymbol{\omega}} \cdot \mathbb{N}_{\mathrm{Ka}JK\alpha}] + [\mathrm{primal}\ \bar{\boldsymbol{R}}^\alpha_{\boldsymbol{\omega}} \cdot \mathbb{N}_{\mathrm{Kl}JK\alpha}] \\
&\qquad - [\boldsymbol{N}_{\mathrm{A}J}]^{\mathrm{T}} \cdot [\boldsymbol{D}^S_{\mathrm{f}\boldsymbol{\eta}\eta}] \cdot [\boldsymbol{N}_{\mathrm{A}K}] - [\mathrm{dual}\ \boldsymbol{R}^S_{\mathrm{f}\boldsymbol{\eta}} \cdot \mathcal{N}_{\mathrm{Aa}JK}] - [\mathrm{primal}\ \boldsymbol{R}^S_{\mathrm{f}\boldsymbol{\eta}} \cdot \mathcal{N}_{\mathrm{Al}JK}])\,\mathrm{d}S^e,
\end{aligned}$$

$$[\boldsymbol{K}^S_{\boldsymbol{\eta\tau}JE}] = \int_{S^e} [\mathcal{N}_{\mathrm{K}J\alpha}]^{\mathrm{T}} \cdot [\overline{\boldsymbol{D}}^{\alpha}_{\boldsymbol{\omega\tau}}] \,\mathrm{d}S^e,$$

$$\boldsymbol{K}^S_{\boldsymbol{\tau\tau}EE} = \int_{S^e} \overline{\boldsymbol{D}}_{\boldsymbol{\tau\tau}} \,\mathrm{d}S^e.$$

- Border load element:

$$\{\boldsymbol{F}^L_{\boldsymbol{\eta}J}\} = \int_{L^e_{\mathrm{f}}} (-\{\boldsymbol{R}^L_{\mathrm{f}\boldsymbol{\eta}}\}^{\mathrm{T}} \cdot [\boldsymbol{N}_{\mathrm{A}J}]) \,\mathrm{d}L^e_{\mathrm{f}},$$

$$[\boldsymbol{K}^L_{\boldsymbol{\eta\eta}JK}] = \int_{L^e_{\mathrm{f}}} (-[\boldsymbol{N}_{\mathrm{A}J}]^{\mathrm{T}} \cdot [\boldsymbol{D}^L_{\mathrm{f}\boldsymbol{\eta\eta}}] \cdot [\boldsymbol{N}_{\mathrm{A}K}] - [\text{dual } \boldsymbol{R}^L_{\mathrm{f}\boldsymbol{\eta}} \cdot \mathcal{N}_{\mathrm{Aa}JK}] - [\text{primal } \boldsymbol{R}^L_{\mathrm{f}\boldsymbol{\eta}} \cdot \mathcal{N}_{\mathrm{Al}JK}]) \,\mathrm{d}L^e_{\mathrm{f}}.$$

- Node constraint element:

$$\{\boldsymbol{F}^N_{\boldsymbol{\eta}J}\} = -\{\boldsymbol{R}^N_{\mathrm{c}\boldsymbol{\eta}}\}, \quad \{\boldsymbol{F}^N_{\boldsymbol{r}J}\} = -\{\boldsymbol{R}^N_{\mathrm{c}\boldsymbol{r}}\}, \quad [\boldsymbol{K}^N_{\boldsymbol{\eta\eta}JJ}] = -[\boldsymbol{D}^N_{\mathrm{c}\boldsymbol{\eta\eta}}], \quad [\boldsymbol{K}^N_{\boldsymbol{\eta r}JJ}] = -[\boldsymbol{D}^N_{\mathrm{c}\boldsymbol{\eta r}}].$$

3.5. ***Nodal mixed variation variables.*** It is noted that $(17)_2$, $(18)_2$, and $(19)_2$ contain terms in the mixed virtual-incremental variation variables $\boldsymbol{\eta}_{\partial\delta J}$ relevant to the nodal helices. Before assembling the problem matrix, these mixed variation variables must be solved for the simple variation variables $\boldsymbol{\eta}_{\delta J}$ and $\boldsymbol{\eta}_{\partial J}$. The resolution of $\boldsymbol{\eta}_{\partial\delta J}$ is now possible at the nodes, since there the nodal helices are actually free variables. As explained in [Merlini and Morandini 2004b; 2005], using the differential map of the rototranslation and discarding, of course, the term $\partial\delta\boldsymbol{\eta}_J$, the resolution formula is easily obtained:

$$\boldsymbol{\eta}_{\partial\delta J} = \boldsymbol{\Lambda}_J \boldsymbol{\Lambda}^{-\underline{123}}_{\mathrm{III}J} : \boldsymbol{\eta}_{\delta J} \otimes \boldsymbol{\eta}_{\partial J}. \tag{20}$$

Here, $\boldsymbol{\Lambda}_J$ and $\boldsymbol{\Lambda}^{-\underline{123}}_{\mathrm{III}J}$ are the first and second differential mapping tensors associated with the exponential map of the nodal rototranslation $\boldsymbol{H}_J$; they are built with the current value of the nodal helix $\boldsymbol{\eta}_J$.

Using (20), terms of the type $\{\boldsymbol{\eta}_{\partial\delta J}\}^{\mathrm{T}} \cdot \{\boldsymbol{F}_J\}$ in (17)–(19) are transformed to $\{\boldsymbol{\eta}_{\delta J}\}^{\mathrm{T}} \cdot [\boldsymbol{K}_{JJ}] \cdot \{\boldsymbol{\eta}_{\partial J}\}$, where

$$[\boldsymbol{K}_{JJ}] = \begin{bmatrix} \text{dual } \boldsymbol{F}_J \cdot \text{primal}(\boldsymbol{\Lambda}_J \boldsymbol{\Lambda}^{-\underline{123}}_{\mathrm{III}J}) + \text{primal } \boldsymbol{F}_J \cdot \text{dual}(\boldsymbol{\Lambda}_J \boldsymbol{\Lambda}^{-\underline{123}}_{\mathrm{III}J}) & \text{primal } \boldsymbol{F}_J \cdot \text{primal}(\boldsymbol{\Lambda}_J \boldsymbol{\Lambda}^{-\underline{123}}_{\mathrm{III}J}) \\ \text{primal } \boldsymbol{F}_J \cdot \text{primal}(\boldsymbol{\Lambda}_J \boldsymbol{\Lambda}^{-\underline{123}}_{\mathrm{III}J}) & \boldsymbol{0} \end{bmatrix}. \tag{21}$$

4. Numerical tests

The elements so far described have been implemented in the authors' own finite-element code, already used in the past computations with solid elements. The code, written in C++ language, is object-oriented and is equipped with an original geometrical library to help in manipulating high-order tensors. The surface elements exploit the Gauss quadrature rule with three integration points per local coordinate. At each surface quadrature point, the shell model is integrated across the thickness by the Gauss rule with two integration points along ξ^3 over the domain $[-1, +1]$. This choice of the through-the-thickness domain implies that in the present element version, the material surface lies on the mid shell surface. The characteristic length h is chosen as half the shell thickness, so the third base vector $\boldsymbol{g}_3$ (Part I, Equation (13)) is the normal segment from the mid surface to the outer surface at $\xi^3 = +1$ in the reference

configuration. The reference director is chosen as a pure dual vector $\boldsymbol{\theta} = \varepsilon h \boldsymbol{\alpha}^{\mathrm{T}} \boldsymbol{n}$, so that $\boldsymbol{k}_3 = \varepsilon h \boldsymbol{n}$ and $\boldsymbol{g}^{*3} = \boldsymbol{g}^3 = h\boldsymbol{n}$ is constant across the thickness. The target loads on the shell element and on the border load element are assigned by the user as density properties pertaining to each surface quadrature point.

Most test cases concern linear elastic isotropic materials. Since in the present variational formulation the strain-energy density w^* is by assumption a function of the Biot strain $\boldsymbol{\varepsilon}^{*\mathrm{S}}$ instead of the classical Green strain (see Part I, Section 5.1), the linear constitutive law analogous to the Saint Venant–Kirchhoff law descends from the hyperelastic strain-energy function

$$w^*(\boldsymbol{\varepsilon}^{*\mathrm{S}}) = \tfrac{1}{2}\hat{\lambda}(\operatorname{tr}\boldsymbol{\varepsilon}^{*\mathrm{S}})^2 + \hat{\mu}\operatorname{tr}(\boldsymbol{\varepsilon}^{*\mathrm{S}})^2,$$

where $\hat{\lambda}$ and $\hat{\mu}$ are Lamé moduli proper of the Biot-type parameterization. Using such a linear constitutive law instead of adapting the original Saint Venant–Kirchhoff law induces an error that is negligible as long as the strains remain small. This is the case of all the linear-material examples presented below; in the examples, the material data are given as an elastic modulus E and a Poisson ratio ν, from which the Lamé moduli are computed as usual as $\hat{\lambda} = E\nu/(1+\nu)(1-2\nu)$ and $\hat{\mu} = E/2(1+\nu)$. Besides the linear constitutive law, a classical neo-Hookean constitutive law is available; it descends, for the Biot-type parameterization, from the strain-energy function [Merlini and Morandini 2005]

$$w^*(\boldsymbol{U}^*) = \tfrac{1}{2}\lambda(\ln\det\boldsymbol{U}^*)^2 - \mu\ln\det\boldsymbol{U}^* + \tfrac{1}{2}\mu\operatorname{tr}(\boldsymbol{U}^{*2} - \boldsymbol{I}), \tag{22}$$

with $\boldsymbol{U}^* = \boldsymbol{I} + \boldsymbol{\varepsilon}^{*\mathrm{S}}$ the Cosserat deformation tensor.

The standard nonlinear solution is achieved by subsequent load steps. At each step, an iterative procedure of the Newton–Raphson kind is started. At each iteration, the nodal orientopositions are updated multiplicatively, $\boldsymbol{A}'_J \leftarrow \exp(\boldsymbol{\eta}_{\partial J}\times)\boldsymbol{A}'_J$, whereas the Biot-axial and reaction unknowns are updated additively. At the time of solving the linearized equations, the kinematical unknowns are transformed to become self-based, as described in [Merlini and Morandini 2005]. The solution of snapping and buckling problems is achieved by an arc-length procedure based on a modified Riks algorithm of the spherical type; implementation details and relevant references are given in [Merlini and Morandini 2008]. Both the monotone procedure and the arc-length procedure are equipped with an automatic step control, which makes the load-step size (respectively, the arc-step size) shrink or stretch dynamically.

Different convergence criteria are applied to the different subsets of the residual, work-conjugate respectively to the angular and linear parts of the kinematical variables, the constraint reactions, and the Biot-axial parameters. For each subset relevant to a single kind of kinematical variable, the maximum absolute value is first normalized with respect to the average of all the absolute contributions to that subset in the assembling process, then is requested to lower below 5×10^{-3}. For the other subsets, the maximum absolute value must vanish with a tolerance of 10^{-5}. Finally, the Euclidean norm of the whole computed solution must be less that 10^{-3}.

In the following examples, the helicoidal shell element is referred to as the HSE. It is worth emphasizing that in the pictures of the finite element models, the element geometry is built from the corner orientopositions by the helicoidal interpolation itself. This means that in the problem analysis, the quadrature points are located exactly where they can be actually imagined to stay, in local curvilinear coordinates, on the images (for example, observe Figure 3). No units are explicitly used in the examples, so it is understood that all measures in each test are associated with a coherent system of units, for example, SI.

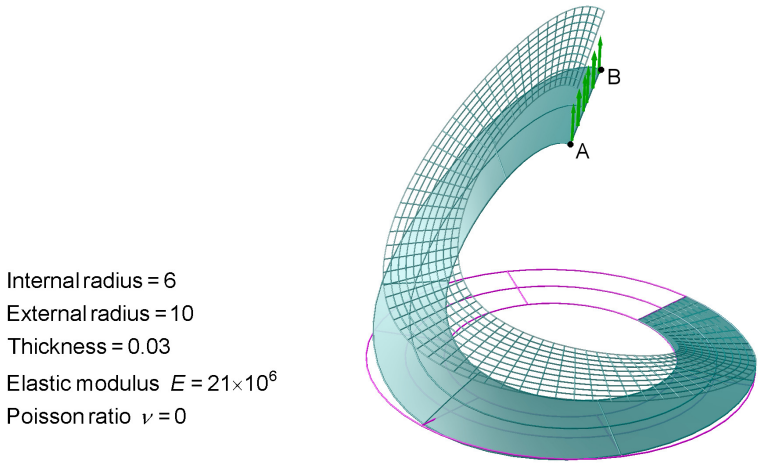

Figure 3. Slit annular plate: meshes of 2×6 and 10×70 at the final load (force/length $= 1$).

4.1. ***Slit annular plate.*** The slit annular plate was introduced in [Başar et al. 1992] as a benchmark problem for finite rotation formulations in geometrically nonlinear shell problems. Since then, most investigators have used this example to test the performance of shell elements, in [Wriggers and Gruttmann 1993; Ibrahimbegović and Frey 1994; Sansour and Kollmann 2000; Sze et al. 2002; Fontes Valente et al. 2003; Campello et al. 2003; Cardoso and Yoon 2005; Areias et al. 2005; Arciniega and Reddy 2007], among others. One edge of a slit ring plate is clamped, while the other edge is subjected to a transverse line load, which induces strong distortions in the originally plane elements. The problem data and the notable deformation of a coarse mesh of twelve HSE curved elements are shown in Figure 3. The distributed force is applied by a string of border load elements.

The free edge displacements with increasing load are plotted in Figure 4 for three different meshes and compared with the best results reported by [Sze et al. 2004]. The results from [Li and Zhan 2000], obtained with a shell element endowed with the drilling degree of freedom and based on Biot strain, are included in Figure 4. The convergence of the HSE and a very good agreement with the computations found in the literature are observed. Displacements every 0.2 force/length are reported in Table 1. Using such refined meshes, a high number of steps (130–140, with an average of 5–6 iterations per step) is necessary to reach the final solution (force/length $= 1$) by the monotone loading procedure.

	w_A			w_B		
Force/length	6×30	8×48	10×70	6×30	8×48	10×70
0.2	7.576	7.584	7.586	10.258	10.267	10.270
0.4	10.391	10.422	10.433	13.691	13.722	13.733
0.6	12.147	12.224	12.250	15.680	15.756	15.782
0.8	13.653	13.772	13.811	17.290	17.410	17.449
1.0	14.972	15.128	15.175	18.663	18.820	18.867

Table 1. Slit annular plate: displacements of points A and B with three different meshes.

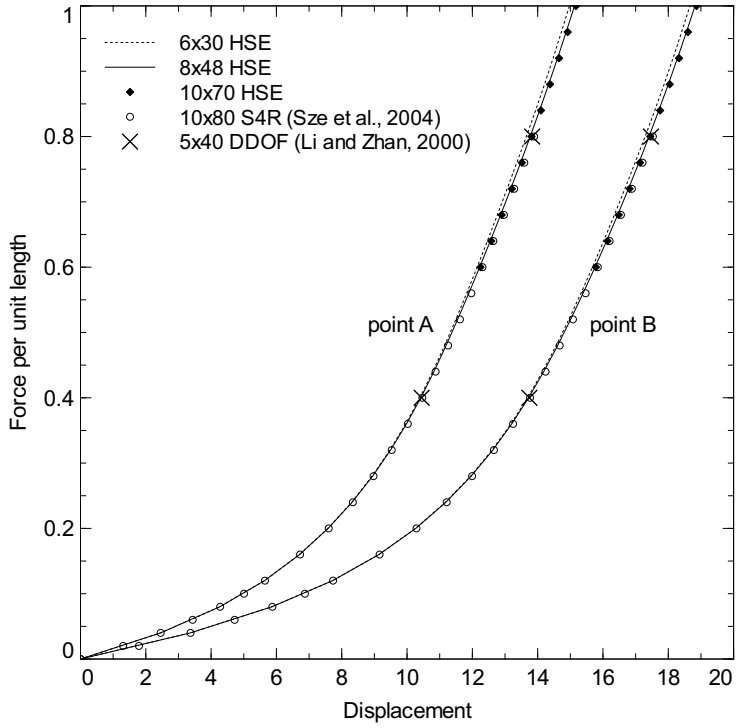

Figure 4. Slit annular plate: load-displacement curves.

4.2. ***Twisted beam.*** The example of a straight twisted strip, clamped at one end and loaded at the other end by a transverse force, was studied in the nonlinear regime by [Sansour and Kollmann 2000; Chróścielewski and Witkowski 2006]. The problem data are given in Figure 5. The analysis is performed on two meshes: 2×24 and 4×48 warped HSEs. The load is assigned as a distributed force along the tip edge in its own plane, by means of border load elements. The total load versus the tip deflections is plotted

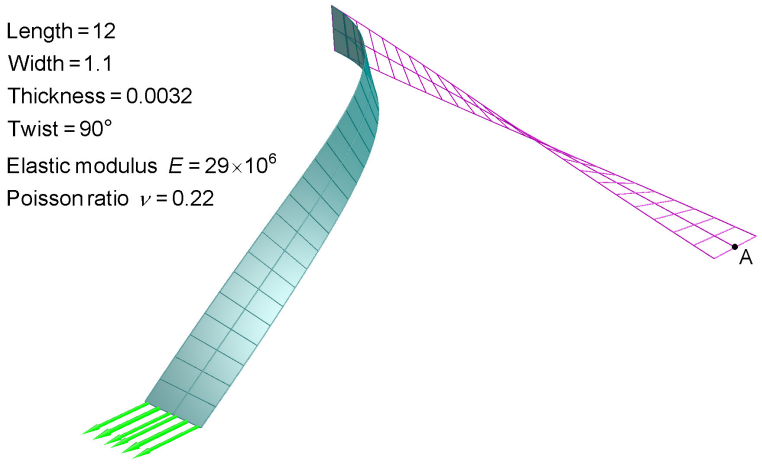

Figure 5. Twisted beam: 2×24 mesh in the reference configuration and at load of 0.007.

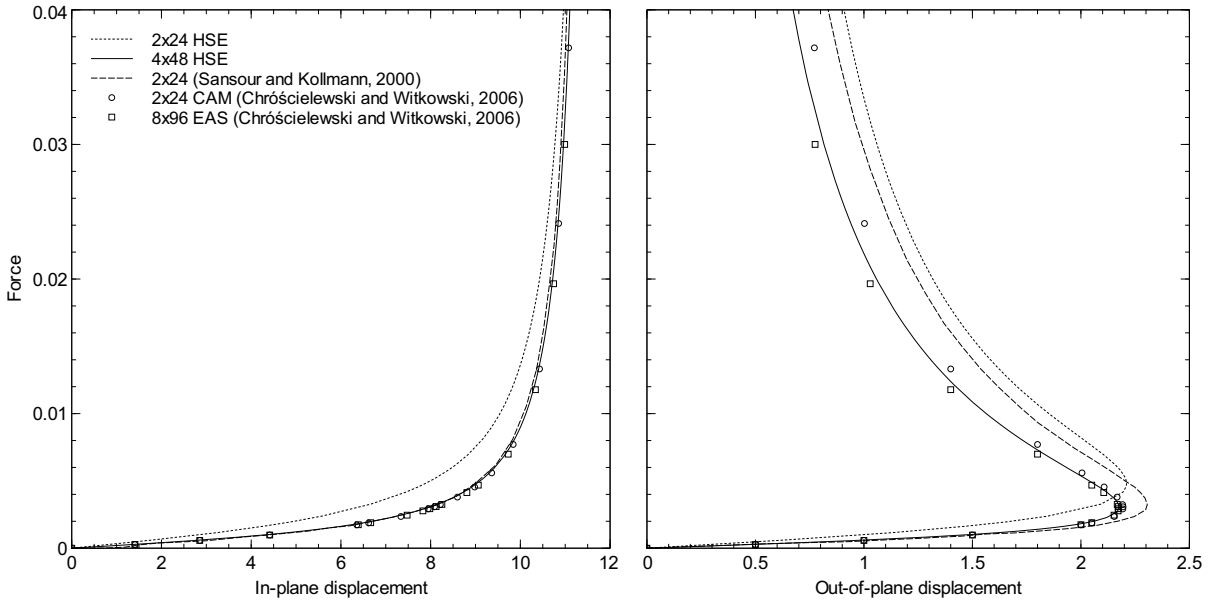

Figure 6. Twisted beam: displacements of tip A.

in Figure 6 and compared with results in the literature. This problem is a good benchmark to test the performance of elements with nonplanar geometry, and the behavior of the HSE seems satisfactory. Some representative displacements are listed in Table 2. The computation is very demanding in this case: with the 2×24 mesh the final load of 0.04 is reached in 194 load steps with an average of 6 iterations per step.

This example is also used to report the computed values of the Biot-axial variables in a shell analysis. The symmetric and skew-symmetric parts of the Biot stress within the three-dimensional domain across

	2×24			4×48	
Force $\times 10^2$	In-plane	Out-of-plane	Force $\times 10^2$	In-plane	Out-of-plane
0.059	1.754	0.620	0.056	2.675	0.939
0.163	4.264	1.466	0.163	6.010	1.924
0.238	5.568	1.846	0.228	7.121	2.119
0.327	6.665	2.092	0.324	8.131	2.173
0.416	7.447	2.194	0.414	8.717	2.121
0.457	7.730	2.208	0.456	8.922	2.083
0.578	8.386	2.182	0.597	9.421	1.937
0.814	9.169	2.006	0.821	9.888	1.714
0.987	9.523	1.863	1.000	10.123	1.564
2.003	10.430	1.316	2.000	10.721	1.058
2.967	10.761	1.067	3.000	10.963	0.816
4.000	10.960	0.909	4.000	11.102	0.674

Table 2. Twisted beam: displacements of tip A up to load of 0.04 with two different meshes.

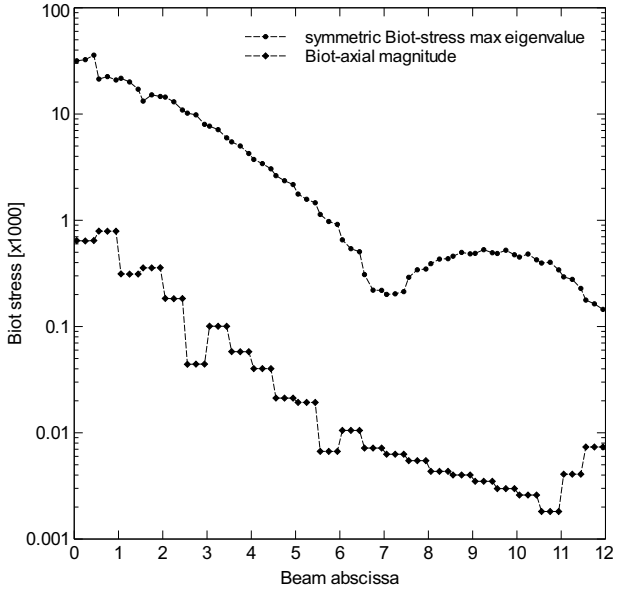

Figure 7. Twisted beam: max(abs(eigenvalue($\hat{\boldsymbol{T}}^{*\mathrm{S}}$))) and $\|\hat{\boldsymbol{\tau}}^*\|$ as representative values of the elastically defined and the workless parts of the Biot stress within the thickness with a 2×24 mesh at the final load of 0.04; plot of the highest values among the twelve Gauss points at each beam abscissa.

the thickness can be compared on a logarithmic scale in Figure 7. The Biot-axial keeps lower than the elastically defined stress by at least one order of magnitude, and features an alternate course as already noticed in full three-dimensional analyses [Merlini and Morandini 2005]. Note that the perfect symmetry of the Biot stress within an isotropic material (see [Bufler 1985]) is lost in the present approximate analysis where the field equations are satisfied in a weak sense — a fact that confirms the computational role of the Biot-axial in a discrete model. The material surface Biot-axial parameter $\hat{\boldsymbol{\tau}}$ is modeled as a vector field uniform over the shell element. In the present computation, it is almost normal to the element surface and is distributed along the strip as the bar graph of Figure 8. The highest values of the Biot-axial are observed near the clamped side.

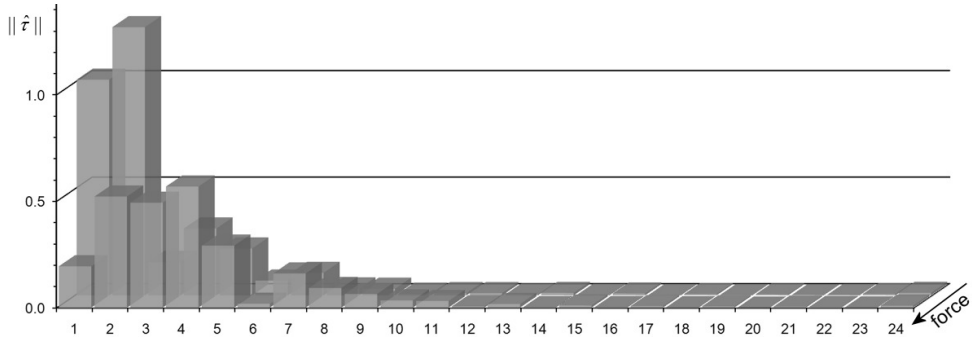

Figure 8. Twisted beam: magnitude of the surface Biot-axial parameter on the elements of a 2×24 mesh at the final load of 0.04.

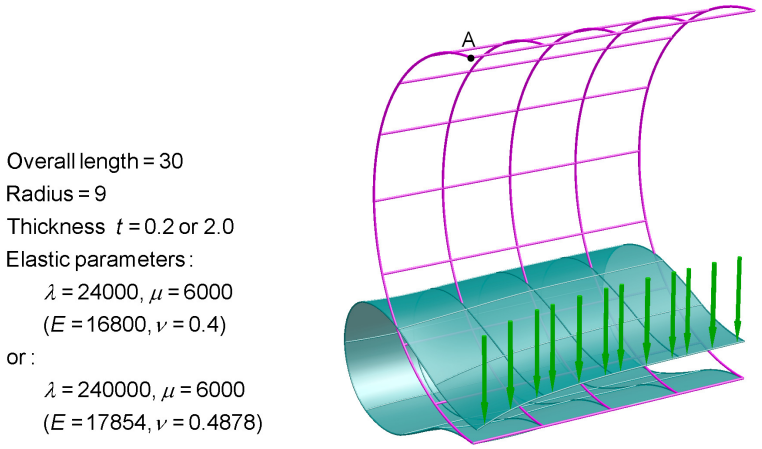

Figure 9. Cylindrical shell under line load: 8×4 mesh of a quarter cylinder and deformed model of case $t = 2.0$ and $\nu = 0.4$ at load of 36000 (displacement of vertex A = 17.388).

4.3. ***Cylindrical shell under line load.*** The cylindrical shell pinched by a line load along a generatrix and simply supported at the opposite generatrix was studied in [Büchter et al. 1994] as a test case for shell elements with nonlinear hyperelastic material. The same compressible neo-Hookean constitutive law, derived from the strain-energy function (22), is used here. The cylinder geometry and properties are given in Figure 9: a thin shell ($t = 0.2$) and a thick shell ($t = 2.0$), with both a compressible ($\nu = 0.4$) and a nearly incompressible ($\nu = 0.4878$) material, are considered. Due to symmetry, one quarter of the cylinder is modeled; three different meshes of increasing refinement along the circumference are analyzed, 8×4, 12×4, and 16×4 curved HSEs; the line load is introduced by four border load elements. A deformed model is also shown in Figure 9.

Portions of the load-displacement plots are shown in Figure 10. For the compressible material (Figures 10a and 10c), a comparison can be made with several shell elements based on 5, 6, and 7-parameter models and exploiting incompatible modes and EAS concepts, as proposed in [Büchter et al. 1994; Brank et al. 2002; Brank 2005] (in the last two of these papers, a slightly different constitutive law is used). The formulation of the HSE does not involve incompatible modes nor assumed strains, and the behavior of the HSE is apparently stiffer than the elements in the literature, in particular for the thick shell. It can be noted that the adaptation of the local constitutive law for the helicoidal shell model, as discussed in Part I, enables us to analyze nearly incompressible thin shells without resorting to any numerical expedient such as reduced integration. The effectiveness of this feature, however, seems to weaken as the shell thickness increases. For the nearly incompressible material (Figures 10b and 10d), no tests with shell elements have been found in the literature and a comparison could only be made with solid elements; published results with solid elements are not included in Figure 10 but can be found in [Reese et al. 2000; Merlini and Morandini 2005] and, with a different constitutive law, in [Chavan et al. 2007]. The computational burden of this test case is much less demanding: 25–35 load steps with about 6 iterations per step for the thin models and 8–12 steps with 9–10 iterations per step for the thick models.

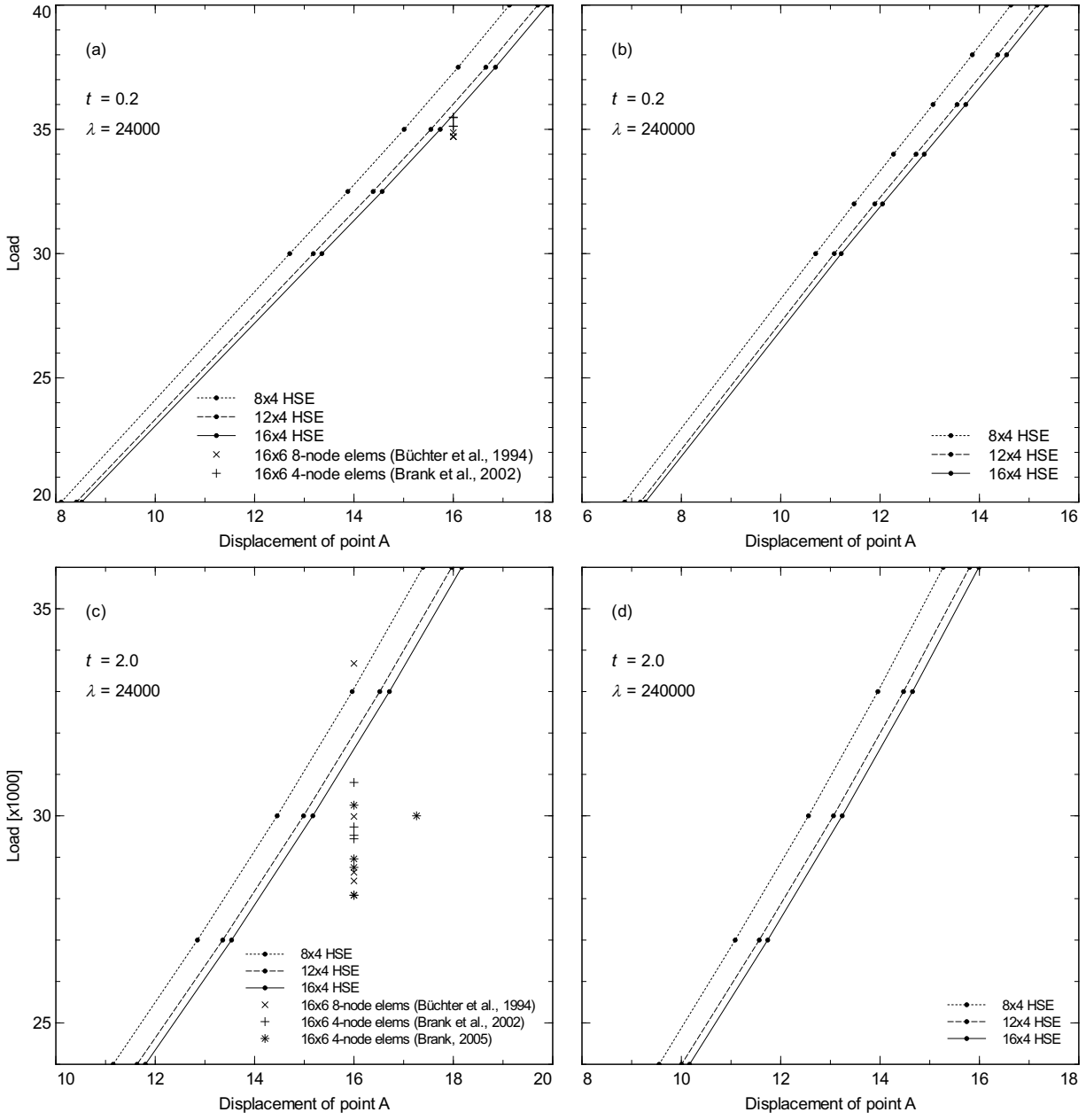

Figure 10. Cylindrical shell under line load: total load versus displacement of point A and some sparse values from literature.

4.4. ***Cylindrical shell pullout.*** The cylinder stretched by two opposite forces is a very popular benchmark test in the shell element literature, for example, in [Sansour and Bufler 1992; Sansour and Bednarczyk 1995; Sansour and Kollmann 2000; Sze et al. 2002; Campello et al. 2003; Fontes Valente et al. 2003; Pimenta et al. 2004; Areias et al. 2005; Brank 2008], among others. The specimen is a cylindrical surface with open ends, pinched by two pulling forces along the mid diameter, see Figure 11. Due to

Node	1	2	3	4	5	6	7	8	9
y	0.00000	0.10506	0.26265	0.49903	0.85361	1.38547	2.18327	3.37996	5.17500

Table 3. Cylindrical shell pullout: node coordinates along the cylinder axis from point A (regular mesh).

symmetry, one octant of the cylinder is modeled using a mesh of 9×8 curved HSEs, with either a regular (rectangular) or an irregular pattern. The regular mesh has 9 elements in the circumferential direction and 8 elements in the axial direction. The coordinates of the first nine nodes from the load-point A in both directions are set by a geometric progression of common ratio 1.5 (see Table 3); the aspect ratio of the narrowest element is higher than 24. The irregular mesh is derived from the regular one by moving randomly the nodes in both directions within the range of half an element size: the quadrilaterals become very irregular, as evidenced in Figure 11.

Using the arc-length procedure, the target load of 40000 is exceeded in 23 steps with the regular mesh (6 iterations per step on average), and in 20 steps with the irregular one. In agreement with published results, a slight snap-through is observed at a load of about 20500. Plots of representative radial displacements at increasing load are shown in Figure 12: the reasonably similar results obtained with the two meshes are a clear evidence of the low sensitivity to irregular geometries of the proposed shell element. In Figure 12, the results from the present coarse regular mesh are successfully compared

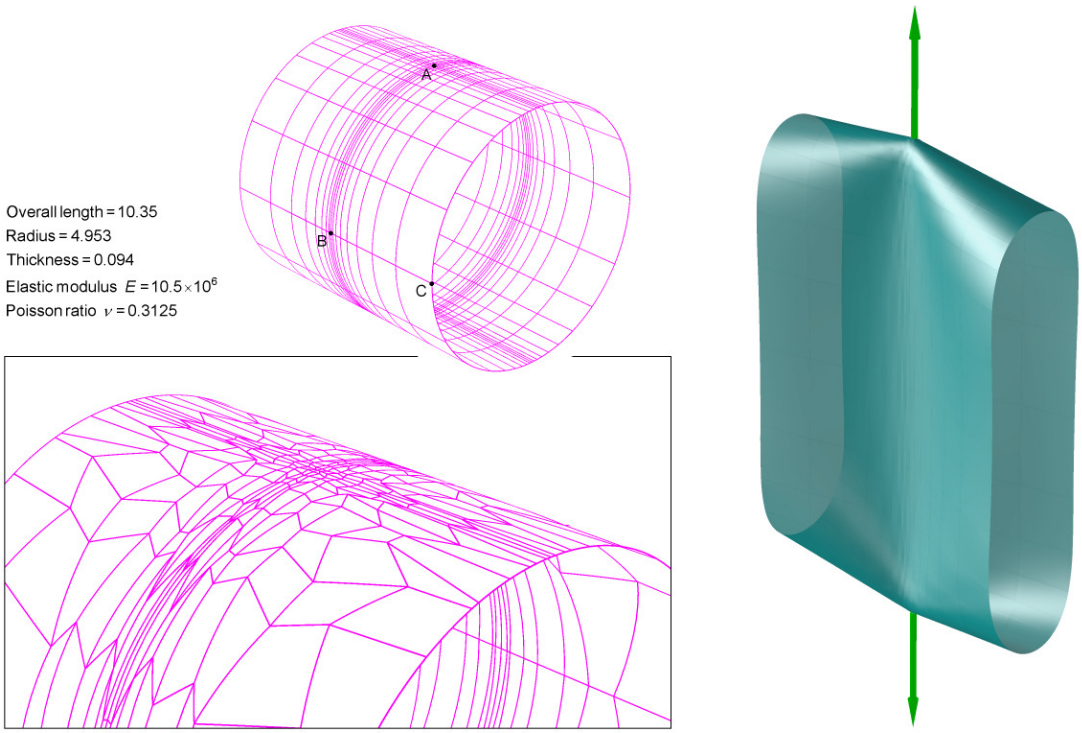

Figure 11. Cylindrical shell pullout: regular mesh in the reference configuration and at the final load of 40000; detail of the undeformed irregular mesh.

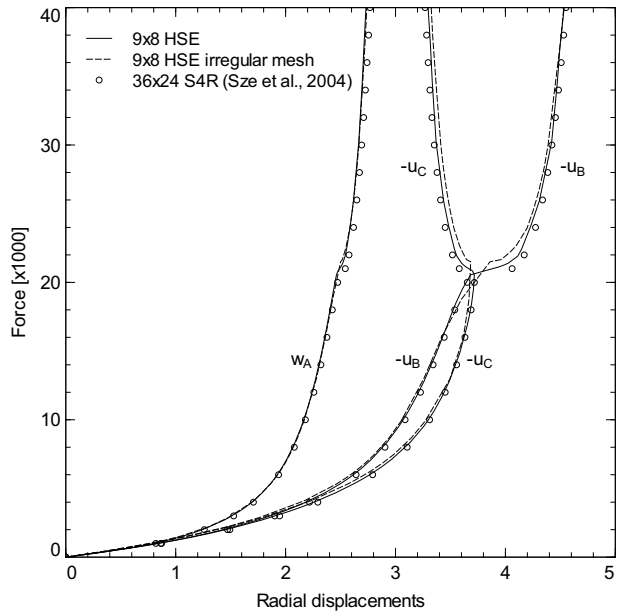

Figure 12. Cylindrical shell pullout: load-displacement curves.

with those obtained with a refined mesh in [Sze et al. 2004]. Loads and displacements at every history step are listed in Table 4.

4.5. ***Pinched cylindrical shell with end diaphragms.*** The cylinder pinched by two opposite point loads is another popular benchmark test; see for example, [Sansour and Bednarczyk 1995; Sansour and Kollmann 2000; Sze et al. 2002; Campello et al. 2003; Pimenta et al. 2004; Brank 2008]. The cylindrical shell is mounted over rigid end diaphragms that lock the in-plane displacements. Thus, the shell folds

Force	w_{A}	$-u_{\mathrm{B}}$	$-u_{\mathrm{C}}$	Force	w_{A}	$-u_{\mathrm{B}}$	$-u_{\mathrm{C}}$
625	0.561	0.551	0.556	10696	2.194	3.122	3.355
781	0.669	0.673	0.680	12806	2.268	3.260	3.490
952	0.776	0.800	0.808	16822	2.376	3.468	3.651
1140	0.881	0.931	0.941	18478	2.414	3.548	3.692
1460	1.036	1.136	1.150	20547	2.462	3.683	3.717
2055	1.262	1.461	1.485	21117	2.502	3.938	3.642
3345	1.583	1.985	2.039	21400	2.520	4.026	3.601
4018	1.696	2.189	2.263	22416	2.555	4.147	3.536
5341	1.861	2.498	2.621	25919	2.617	4.308	3.438
5974	1.921	2.612	2.759	34489	2.697	4.472	3.335
7129	2.011	2.782	2.966	42141	2.743	4.556	3.284
9524	2.144	3.031	3.257	40000	2.731	4.535	3.297

Table 4. Cylindrical shell pullout: radial displacements of points A, B, and C (regular mesh).

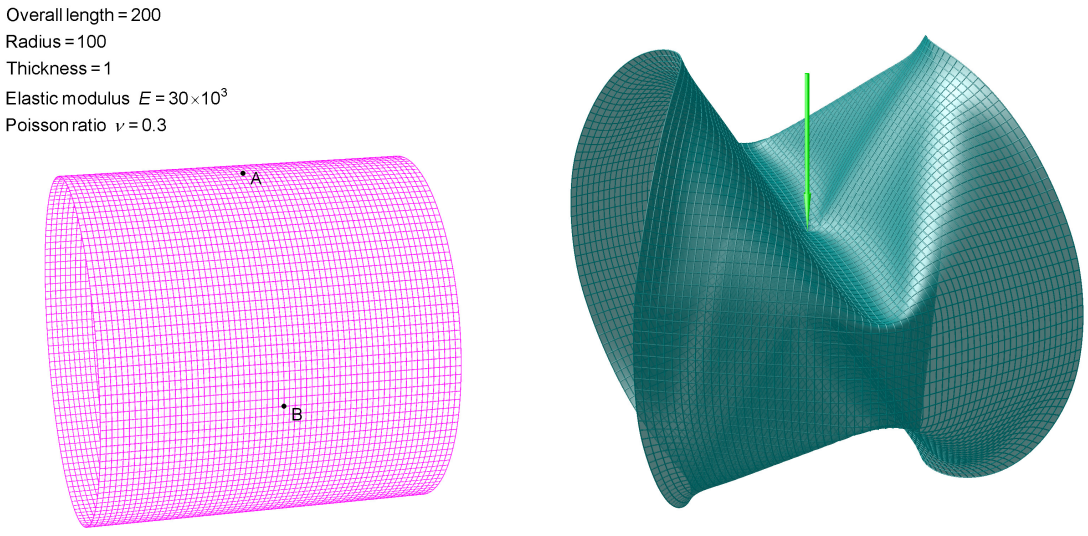

Figure 13. Pinched cylindrical shell with end diaphragms: deformed configuration at the final load of 12000.

notably under the two pushing forces directed as the mid diameter; see Figure 13. A refined, uniform mesh is appropriate to solve this problem: exploiting the problem symmetries, one octant of the cylinder is modeled by 32×32 curved HSEs. The analysis up to the final load of 12000 is performed by the arc-length procedure in 74 steps, with an average of 7 iterations per step. The load history exhibits several slight snap-throughs, as evidenced by the load-displacement plots of Figure 14. However, a

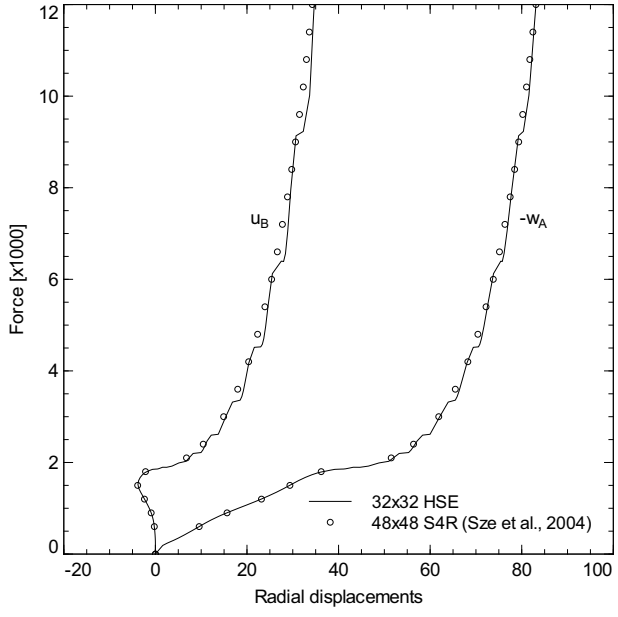

Figure 14. Pinched cylindrical shell with end diaphragms: load-displacement curves.

Force	$-w_A$	u_B
1003	18.171	−1.349
2026	50.980	6.683
4174	68.041	20.399
6125	73.842	25.550
7963	77.841	29.570
10017	81.570	33.686
12000	83.102	34.673

Table 5. Pinched cylindrical shell with end diaphragms: radial displacements of points A and B.

good agreement with the best results reported in [Sze et al. 2004] is observed. Some representative load-displacement pairs are listed in Table 5.

4.6. ***Cylindrical roof under point load.*** The buckling problem of the shallow cylindrical panel hinged along two generatrices and subjected to a central point load has been considered by several authors; refer to [Simo et al. 1990; Chróścielewski et al. 1992; Gruttmann et al. 1992; Sansour and Bufler 1992], and to most of the more recent works cited so far. The problem data and the undeformed configuration with a 4×4 mesh are shown in Figure 15 (owing to symmetry, one quarter of the panel is modeled). Two different thicknesses are examined, with either a coarse mesh of 4×4 curved HSEs or a refined one of 8×8.

The snapping behavior is easily captured by the arc-length procedure. The load-displacement curves, in Figure 16, at the central point A with the 4×4 mesh are plotted and compared with the best results reported in [Sze et al. 2004]; the results with the 8×8 mesh are not included in Figure 16 as they are indistinguishable from those of [Sze et al. 2004]. The thin panel curve (Figure 16a) is traced in 24 steps up to exceed the final load of 3000, with an average of 6.3 iterations per step; the thick panel curve (Figure 16b) is traced in 17 steps, with an average of 5.6 iterations per step. The deformed models

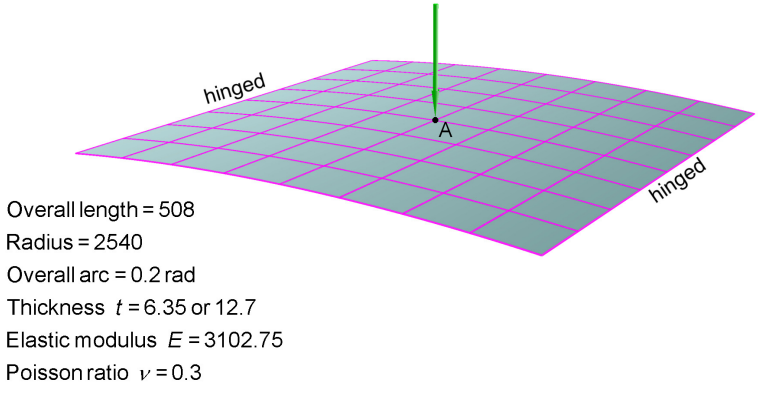

Figure 15. Cylindrical roof under point load: 4×4 mesh in the reference configuration and the applied load.

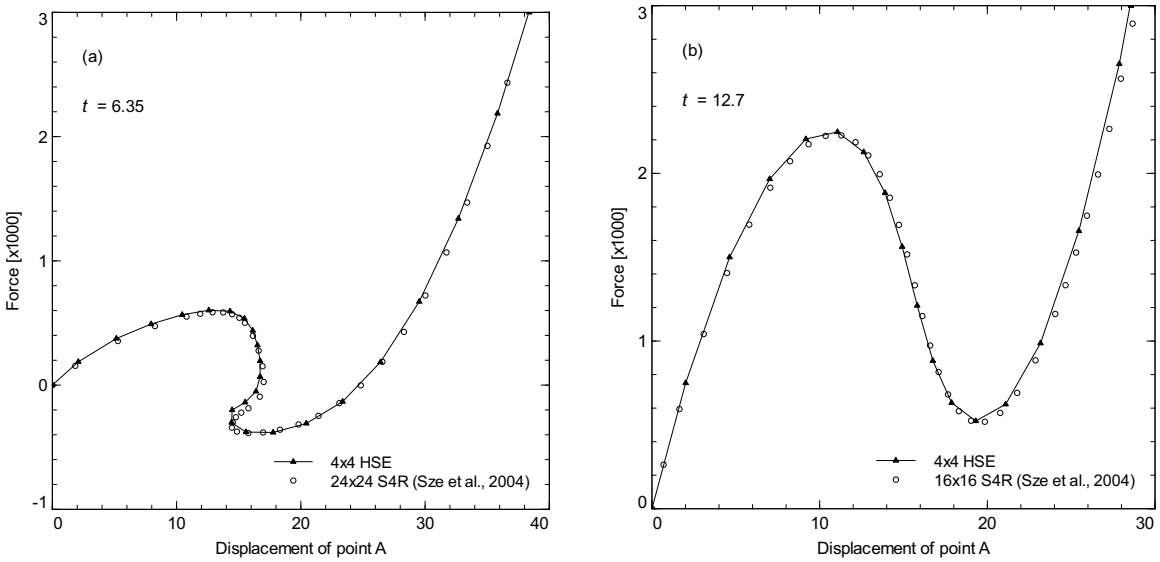

Figure 16. Cylindrical roof under point load: load-displacement curves.

$t = 6.35$		$t = 12.7$	
Force	$-w_A$	Force	$-w_A$
188	2.24	750	2.07
375	5.56	1500	4.78
490	8.50	1960	7.22
562	11.02	2191	9.41
586	13.97	2177	12.13
401	16.13	1589	14.91
-65	16.73	566	18.36
-387	16.36	3674	29.97
270	27.15	3000	28.72
3164	38.52		
3000	38.09		

Table 6. Cylindrical roof under point load: displacement of point A with the 8×8 mesh.

are not shown for this test case, as the maximum displacement, despite the strong effect of geometrical nonlinearity, is small and of the order of the panel camber. In Table 6, all the load-displacement pairs from the computations with the 8×8 mesh are listed; during these computations, the arc-length step was allowed to increase, whence the low number of total steps.

4.7. ***Cylindrical shell pinched by four radial forces.*** The buckling of a cylindrical shell pinched by four radial forces was recently studied [Kuznetsov and Levyakov 2007] to successfully test an unconventional and interesting formulation for a simple curved shell triangle. A short cylindrical shell with free ends is simply supported at four points A on two right-angled diameters, at half the cylinder length. At the

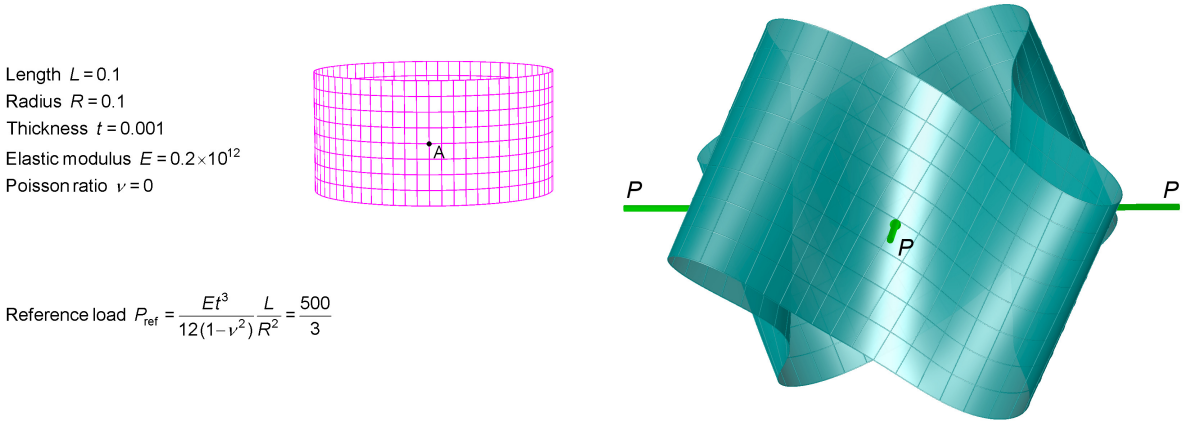

Figure 17. Cylindrical shell pinched by four radial forces: deformed configuration at $P/P_{\text{ref}} = 19.6$ (displacement of point A: $w/R = 0.58$).

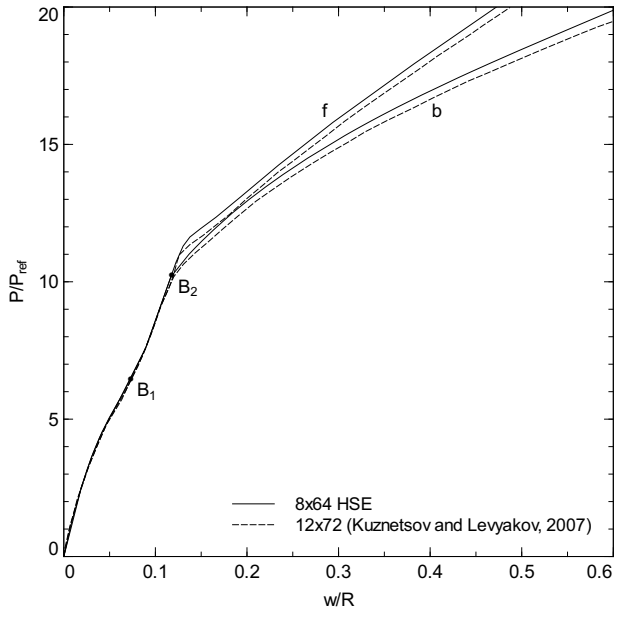

Figure 18. Cylindrical shell pinched by four radial forces: load-displacement curves at points A; fundamental path (f) and branch (b) from the bifurcation point B_2 ($P/P_{\text{ref}} = 10.2$, $w/R = 0.1172$).

constraint points, the shell surface is free to move in the radial direction and to rotate; at the points A themselves, the shell is under the load of four radial forces that push it inward. The problem data and a deformed configuration are shown in Figure 17; the whole shell is modeled with 8×64 curved HSEs.

The problem is solved by the arc-length procedure and yields the load-displacement curves plotted in Figure 18. Along the fundamental path (traced in 17 steps to exceed the target load of $P/P_{\text{ref}} = 20$) the shell deforms with a doubly symmetric four-lobe configuration. As found in [Kuznetsov and Levyakov 2007], buckling occurs at point B_1 on the load-displacement graph, however the deformation keeps the

Fundamental path								
P/P_{ref}	5.705	7.581	10.716	11.301	11.921	13.102	17.941	21.611
w/R	0.0607	0.0893	0.1226	0.1303	0.1488	0.1935	0.3828	0.5422
Bifurcation from B_2								
P/P_{ref}	10.200	11.000	12.000	13.000	13.899	16.045	17.951	20.257
w/R	0.1174	0.1367	0.1672	0.2024	0.2392	0.3463	0.4654	0.6263

Table 7. Cylindrical shell pinched by four radial forces: radial displacements of points A.

four-lobe doubly symmetric. At point B_2, a branch departs from the fundamental path. Along this branch (traced in 33 steps from B_2 to exceed the target load of $P/P_{\text{ref}} = 20$, with 5–6 iterations per step) the shell deforms with a strongly warped configuration, see Figure 17. A fairly good agreement with the published results is observed in Figure 18. Some representative load-displacement pairs are listed in Table 7.

4.8. ***Channel-section cantilever.*** The buckling of the channel-section cantilever, with the data introduced by [Chróścielewski et al. 1992], has been considered by several authors to test shell elements in folded or intersecting structures, with either elastic or elastoplastic materials, for example, [Ibrahimbegović and Frey 1994; Eberlein and Wriggers 1999; Fontes Valente et al. 2005; Chróścielewski and Witkowski 2006; Klinkel et al. 2008]. In the present test, only the elastic case is considered; the problem data and a postbuckling configuration of the model, made of a regular mesh of $(4+12+4)\times 36$ HSEs, are shown in Figure 19. Under the transverse force, which is eccentric with respect to the beam elastic axis, the channel twists and at the limit load (116.77 for the present model) the upper flange buckles into longitudinal waves.

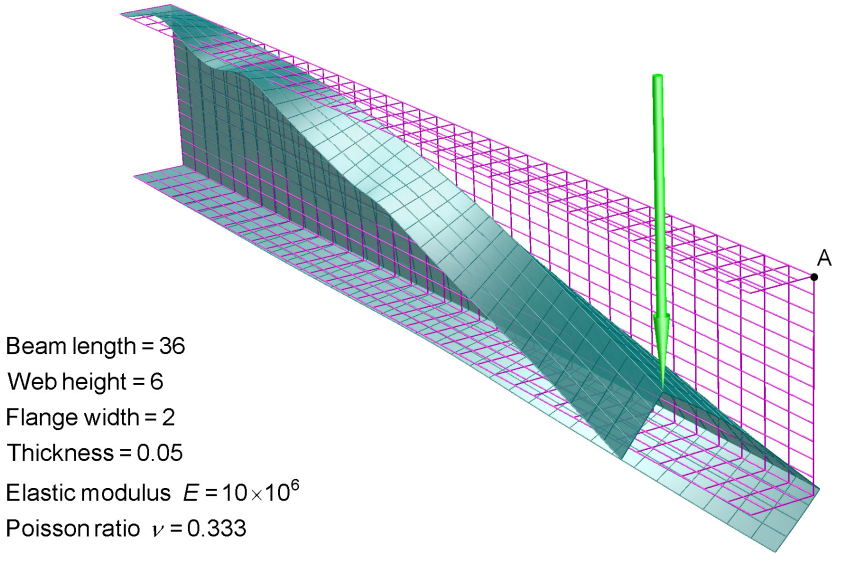

Figure 19. Channel-section cantilever: beam model in the reference configuration and in postbuckling at load of 100.97 (lateral displacement of point A = 4.4524).

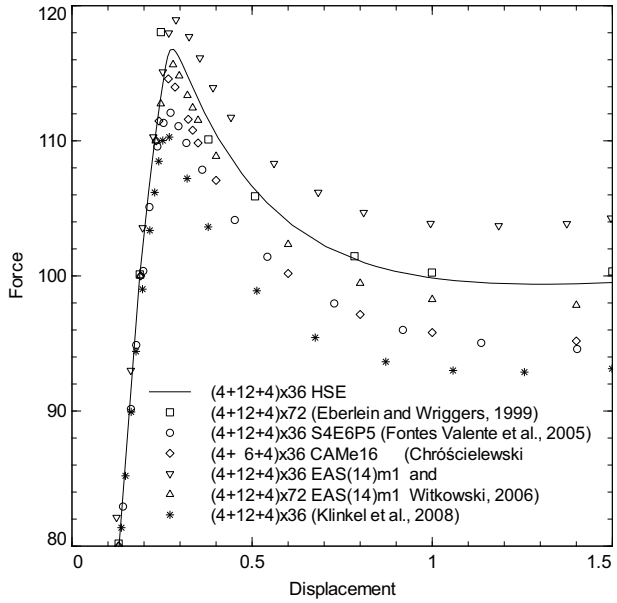

Figure 20. Channel-section cantilever: vertical displacement of point A.

The computation is driven by the monotone Newton–Raphson procedure until a load of 100, then is switched to the arc-length procedure. It takes 36 steps and a total of 190 iterations for the vertical displacement of point A to reach the value 1.5. In Figure 20, a portion of the load-displacement curve is plotted and compared with other curves reported in the literature; the graph is restricted to the load range 80–120 to allow us to distinguish between the curves. Representative displacements are given in Table 8.

Force	Longitudinal	Lateral	Vertical
50.00	0.0077	0.1543	0.0680
100.00	0.0170	0.4411	0.1880
110.78	0.0192	0.5442	0.2336
115.53	0.0201	0.6045	0.2600
116.73	0.0201	0.6427	0.2726
116.70	0.0198	0.6923	0.2847
116.23	0.0192	0.7438	0.2962
114.74	0.0173	0.8606	0.3221
110.18	0.0087	1.2085	0.4063
103.76	−0.0209	1.8799	0.6113
100.96	−0.0561	2.3943	0.8129
99.79	−0.0952	2.8289	1.0173
99.39	−0.1582	3.3735	1.3234
99.83	−0.2408	3.9265	1.6999
100.97	−0.3405	4.4524	2.1295

Table 8. Channel-section cantilever: displacements of point A.

4.9. ***Hemispherical shell with a hole.*** The hemispherical shell with a polar hole, pinched by four alternating radial forces at the sphere equator, is a very popular benchmark example to test finite element models of doubly curved shells and is included in almost all the papers on nonlinear shell elements. The problem data and a deformed configuration with a rather coarse mesh are shown in Figure 21. Due to symmetry, one quarter of the dome is modeled; several meshes of increasing refinement, from 2×2 to 128×128 doubly curved HSEs, are analyzed.

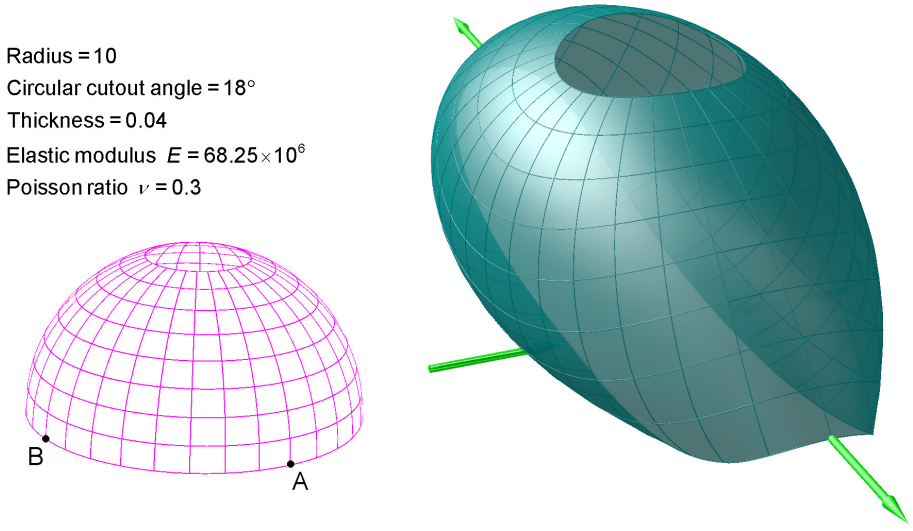

Figure 21. Hemispherical shell with a hole: 8×8 mesh at the final load of 400.

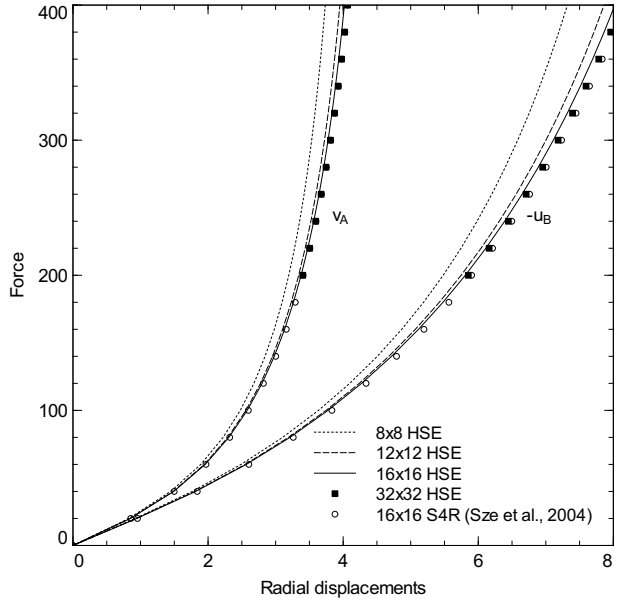

Figure 22. Hemispherical shell with a hole: load-displacement curves.

	v_A				$-u_B$			
Force	8×8	12×12	16×16	32×32	8×8	12×12	16×16	32×32
40	1.447	1.483	1.492	1.498	1.766	1.804	1.816	1.825
80	2.223	2.291	2.308	2.319	3.104	3.190	3.213	3.231
120	2.679	2.776	2.799	2.815	4.098	4.239	4.273	4.299
160	2.980	3.104	3.133	3.154	4.867	5.068	5.116	5.150
200	3.195	3.341	3.377	3.402	5.481	5.746	5.809	5.853
240	3.356	3.522	3.565	3.594	5.983	6.311	6.391	6.445
280	3.481	3.664	3.713	3.747	6.400	6.790	6.888	6.954
320	3.582	3.778	3.834	3.872	6.754	7.199	7.318	7.396
360	3.665	3.873	3.934	3.976	7.057	7.554	7.693	7.784
400	3.735	3.951	4.019	4.065	7.320	7.863	8.023	8.128

Table 9. Hemispherical shell with a hole: radial displacements of points A and B with four different meshes.

The response of the model is measured by the radial displacements of the load-points A and B. The load-displacement curves for four meshes are plotted in Figure 22 and compared with the results published in [Sze et al. 2004]: a good agreement with the reference results is observed. Displacements every 10% of the final force are listed in Table 9. The convergence of the HSE is evident from Figure 23, where the computation with a refined mesh of 128×128 S4R elements by the commercial code ABAQUS is assumed as reference solution.

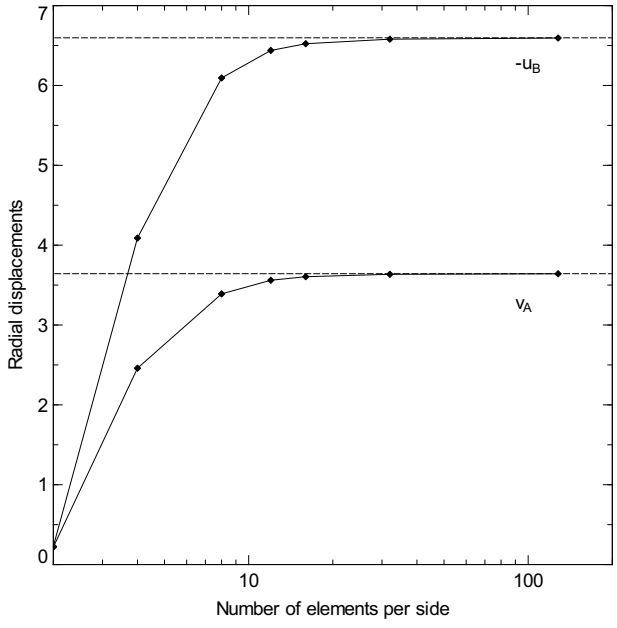

Figure 23. Hemispherical shell with a hole: convergence study at load of 250 (reference values at the dotted lines: $v_A = 3.6426$, $-u_B = 6.5967$).

Mesh	Steps	Iterations
8×8	52	325
12×12	57	361
16×16	52	343

Table 10. Hemispherical shell with a hole: number of steps and iterations up to the final load.

The problem is solved by the monotone Newton–Raphson procedure with the automatic step control enabled. To trace the results, load steps of 5% are set by default. Moreover, some computations are repeated by setting a single initial step of 100% to record the number of iterations actually needed to reach the final load (see Table 10); an average of 6–7 iterations per step is observed.

The example of the hemispherical shell is also used to check the significance of the resolution of the nodal mixed variation variables $\boldsymbol{\eta}_{\partial\delta J}$ by (20) and the effectiveness of the contribution to the diagonal term of the tangent matrix from (21). The computation with the 8×8 mesh is repeated after disabling the correction (21). The iterations performed during the loading history are plotted in Figure 24 and compared with the ones of the original computation. When the geometrical nonlinearity becomes important, a remarkable increase in iterations is observed, and a sharp growth is noted when approaching and exceeding the load of 280. After restarting from 280 with the correction enabled again, the final load is reached in a few more steps, yielding exactly the original final displacements, as expected. This test proves the importance of the resolution formulated in (20) in order to provide the correct tangent matrix, capable of following the nonlinear solution process.

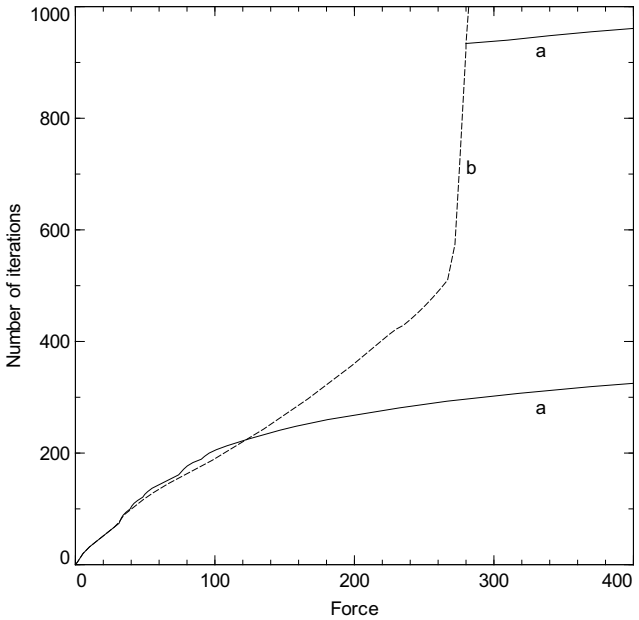

Figure 24. Hemispherical shell with a hole: loading history with 8×8 mesh; comparison between (a) computations with the resolution of the nodal mixed variation variables $\boldsymbol{\eta}_{\partial\delta J}$ and (b) computations without such a resolution.

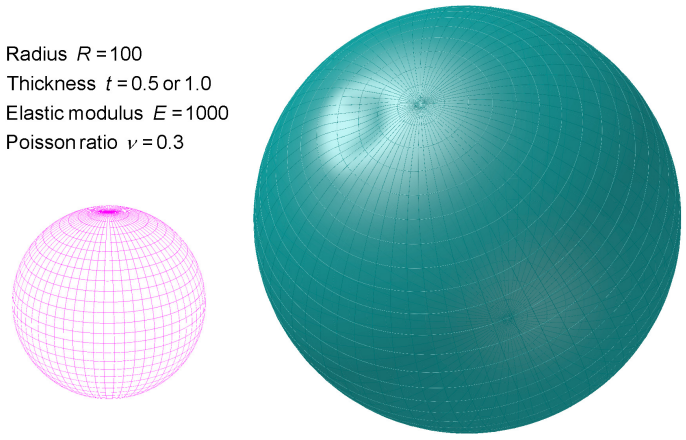

Figure 25. Spherical shell under external pressure: model of case $t = 0.5$ at arc-abscissa 10.594.

4.10. ***Spherical shell under external pressure.*** The numerical study of the postbuckling behavior of spherical shells under external pressure is one of the most despair-inducing problems in structural mechanics. With no claim made of solving this difficult problem, a sample investigation is presented in this section. The problem data and a postbuckling deformation of the model are shown in Figure 25. The geometric and material properties are taken from [Ricci Maccarini et al. 2001], which modeled only one octant of the sphere, and hence could capture just a limited class of buckling modes. The mesh matches a net of meridians and parallels 6 degrees apart, and consists of 60×30 doubly curved HSEs over the whole sphere. At each pole, the last parallel degenerates into a single point and the relevant nodes to which the quadrilaterals are connected share the same coordinates; the quadrilateral shell elements degenerate into triangles. The pressure is applied as a follower normal-load uniform density at the shell element quadrature points.

Despite the strong deviation of the element geometry from a regular quadrilateral at the poles, the model behaves perfectly. A value of external pressure twice the approximate theoretical critical pressure $p_{\text{ref}} = 2E(t/R)^2/\sqrt{3(1-\nu^2)}$, predicted by the shallow shell theory, can be reached with the monotone Newton–Raphson procedure in a single step with 4 iterations. This almost linear computation yields a final radial displacement, uniform over the whole shell surface, of 0.4237 with $t = 0.5$ and 0.8473 with $t = 1.0$. To force the shell to buckle, a very small initial imperfection has been assigned by moving randomly the nodes in the radial direction within the range ± 0.001 (that is, $\pm 10^{-5} R$ or $\pm(0.1\text{–}0.2)\%\ t$).

The imperfect spherical shell is analyzed by the arc-length procedure. The solution of case $t = 0.5$ follows the fundamental path till load fraction 1.082 (arc-abscissa = 3.693). Then a sudden buckling occurs: the load decreases while a shallow buckle appears. In Figure 26a, the radial displacements of four nodes at latitude 72° are plotted against the arc-abscissa. When the arc-abscissa exceeds 7, the pressure stabilizes at a value of about 0.22–0.25 p_{ref} and the role of maximum-displacement holder begins to move from node to node. At the arc-abscissa 10.594 (after 34 steps and 201 total iterations), the node at longitude 126° reaches 3.6666, the deepest displacement of the whole analysis; the corresponding buckle is depicted in Figure 25 and its bottom is very close to the observed node. In Figure 26b, the load-displacement curves of the four nodes are plotted. The analysis was pursued further and another peak of load fraction 1.082 was reached; then the load was found to decrease till negative values.

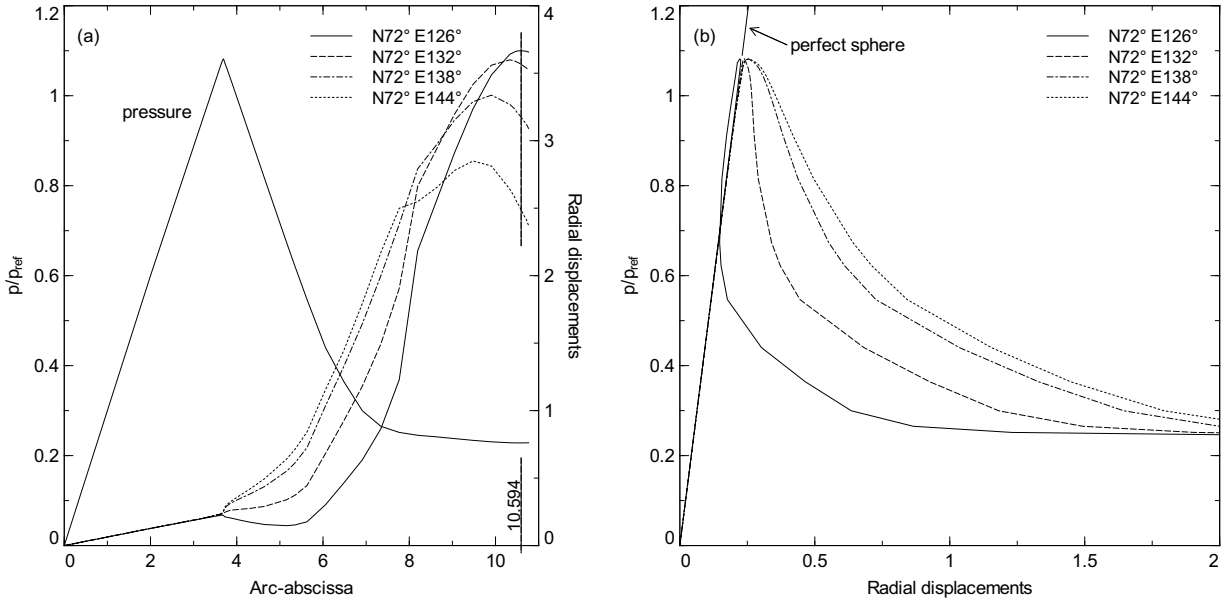

Figure 26. Spherical shell under external pressure (case $t = 0.5$): (a) pressure and four radial displacements against the loading history; (b) load-displacement curves.

With the algorithm of process control at hand, the achievement of a wholly buckled surface as obtained in real experiments is hopeless. In several numerical tests, the occurrence of two or three buckles, either close to each other or far away from each other, was observed. In any case, the buckles manifest a pronounced tendency to migrate, in either a slow or fast manner. As an example, Figure 27 collects five images of the case $t = 1.0$ recorded every 12 load steps: the two buckles keep close to each other and move together on the sphere surface. Also, the repeatability of such computations is questionable: for instance, it is interesting to notice that when assembling the elements concurrently by exploiting the processor multithreading option, analyses starting from identical data never follow exactly the same path when in the postbuckling regime.

5. Conclusion

This paper is focused on computational modeling for nonlinear shell mechanics and is restricted to the simplest case of static boundary value problems involving elastic homogeneous media. Considerations of dynamic problems and anelastic or composite materials are absent and are left as extensions for future work. Nevertheless, the examples and comparisons discussed so far evidence a good performance of the helicoidal shell element (HSE) in several respects. The HSE appears suitable to model in-plane curved and warped shells, thin/thick simply or doubly curved shells with t/R ratios ranging from 2×10^{-3} to 2×10^{-1}, and folded/intersecting shells. It allows a perfect representation of constant-curvature shells, as in the case of the sphere. This quadrilateral shell element is practically insensitive to highly irregular meshes and can easily degenerate into triangles. The HSE has been tested with nonlinear elastic and nearly incompressible materials. In the postbuckling regime, this curving element performs well at the occurrence of snap-through and snap-back conditions. A drawback of the present formulation, already

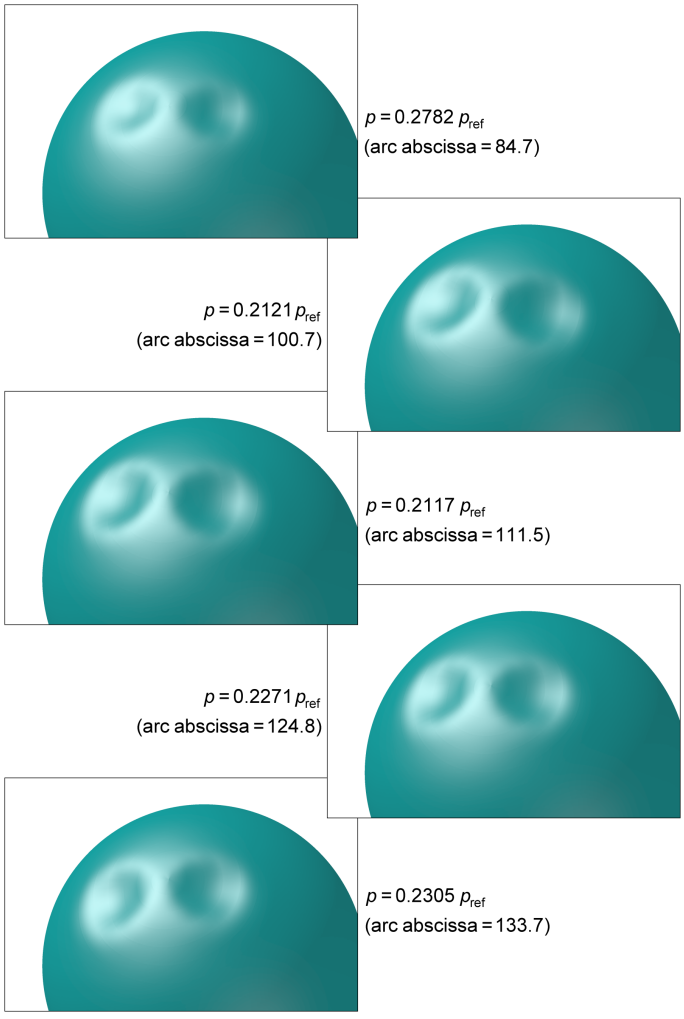

Figure 27. Spherical shell under external pressure (case $t = 1.0$): sequence of five postbuckling deformations.

pointed out with the solid element [Merlini and Morandini 2005], remains the low step size required to solve certain problems, which is sometimes smaller than the values published in the literature. This undesirable feature of the proposed formulation is of course worthy of further investigation.

It is stressed that the present version of the HSE is essentially a low-order element. For the reader's convenience, a short summary of the element formulation is given here. The integral kinematic field across the thickness is assumed helicoidal and is controlled by the six-parameter dual director $\boldsymbol{\theta}$; the local Biot-axial vector field is assumed linear and is controlled by two stress vectors $\hat{\boldsymbol{\tau}}$ and $\hat{\boldsymbol{\mu}}$ (the constant and linear parts, respectively). From through-the-thickness integration of the linearized internally constrained virtual work functional, and after local condensation of the variables $\boldsymbol{\theta}$ and $\hat{\boldsymbol{\mu}}$, the shell constitutive equations are obtained in incremental form. They are written as functions of twelve components of the material surface dual strains $\boldsymbol{\omega}_\alpha$ and three components of the Biot-axial parameter $\hat{\boldsymbol{\tau}}$. The integration

across the thickness is performed numerically at each surface quadrature point of the shell element domain. The integral kinematic field on the quadrilateral surface is interpolated helicoidally between the orientopositions of four corner-nodes, whereas the Biot-axial parameter is assumed uniform. Integration over the element domain gives the element contributions to the problem residual and tangent matrix. The contributions from external loads and boundary constraints are added directly to the shell surface linearized variational principle.

The numerical tests show that this low-order element is essentially free from locking. A clear description of commonly occurring locking phenomena, such as shear and membrane locking, is given, for example, in [Belytschko et al. 2000], and a careful analysis can be found in [Koschnick et al. 2005]. According to [Bischoff et al. 2004] such phenomena originate from "the inability of a finite element formulation to represent certain deformation modes without unwanted, parasitic strains and/or stresses". In such phenomena, the locking mechanism develops from an improper energy exchange between the involved deformation modes that are badly represented by a poor kinematical approximation. The problem becomes more pronounced when the ratio between the stiffnesses of the flexural deformation modes and the parasitic ones (either transverse shear or membrane modes) decreases — that is, when the thickness diminishes. It can be argued that with classical Euclidean modeling of the continuum, when positions and orientations are uncoupled fields, such improper energy exchanges are more likely to happen than with the proposed helicoidal modeling, where the kinematical representation is consistently built through a unique integral field. It is also general belief that this improper energy exchange is more pronounced the lower the order of the representation is. The helicoidal approximation, both on the through-the-thickness domain with the proposed geometric-invariant model (Part I, Section 4.5) and on the element surface domain with the adopted frame-invariant interpolation (Section 3.2), yields a discrete representation of the kinematic field that proves natural and is able to withstand locking even with low-order interpolants. This is clear from the outstanding representation attainable for thin curved elements with the proposed material surface kinematics; see Figure 1. (Remember that linear interpolants on helicoidal modeling do not mean linear displacement fields, due to the interaction with the nodal rotations.)

References

[Arciniega and Reddy 2007] R. A. Arciniega and J. N. Reddy, "Tensor-based finite element formulation for geometrically nonlinear analysis of shell structures", *Comput. Methods Appl. Mech. Eng.* **196**:4–6 (2007), 1048–1073.

[Areias et al. 2005] P. M. A. Areias, J.-H. Song, and T. Belytschko, "A finite-strain quadrilateral shell element based on discrete Kirchhoff–Love constraints", *Int. J. Numer. Methods Eng.* **64**:9 (2005), 1166–1206.

[Başar et al. 1992] Y. Başar, Y. Ding, and W. B. Krätzig, "Finite-rotation shell elements via mixed formulation", *Comput. Mech.* **10**:3–4 (1992), 289–306.

[Belytschko et al. 2000] T. Belytschko, W. K. Liu, and B. Moran, *Nonlinear finite elements for continua and structures*, Wiley, Chichester, 2000.

[Bischoff and Ramm 1997] M. Bischoff and E. Ramm, "Shear deformable shell elements for large strains and rotations", *Int. J. Numer. Methods Eng.* **40**:23 (1997), 4427–4449.

[Bischoff et al. 2004] M. Bischoff, W. A. Wall, K.-U. Bletzinger, and E. Ramm, "Models and finite elements for thin-walled structures", Chapter 3, pp. 59–137 in *Encyclopedia of computational mechanics, 2: Solids and structures*, edited by E. Stein et al., Wiley, Chichester, 2004.

[Brank 2005] B. Brank, "Nonlinear shell models with seven kinematic parameters", *Comput. Methods Appl. Mech. Eng.* **194**:21–24 (2005), 2336–2362.

[Brank 2008] B. Brank, "Assessment of 4-node EAS-ANS shell elements for large deformation analysis", *Comput. Mech.* **42**:1 (2008), 39–51.

[Brank et al. 2002] B. Brank, J. Korelc, and A. Ibrahimbegović, "Nonlinear shell problem formulation accounting for through-the-thickness stretching and its finite element implementation", *Comput. Struct.* **80**:9–10 (2002), 699–717.

[Büchter et al. 1994] N. Büchter, E. Ramm, and D. Roehl, "Three-dimensional extension of non-linear shell formulation based on the enhanced assumed strain concept", *Int. J. Numer. Methods Eng.* **37**:15 (1994), 2551–2568.

[Bufler 1985] H. Bufler, "The Biot stresses in nonlinear elasticity and the associated generalized variational principles", *Arch. Appl. Mech.* **55**:6 (1985), 450–462.

[Campello et al. 2003] E. M. B. Campello, P. M. Pimenta, and P. Wriggers, "A triangular finite shell element based on a fully nonlinear shell formulation", *Comput. Mech.* **31**:6 (2003), 505–518.

[Cardoso and Yoon 2005] R. P. R. Cardoso and J. W. Yoon, "One point quadrature shell element with through-thickness stretch", *Comput. Methods Appl. Mech. Eng.* **194**:9–11 (2005), 1161–1199.

[Chavan et al. 2007] K. S. Chavan, B. P. Lamichhane, and B. I. Wohlmuth, "Locking-free finite element methods for linear and nonlinear elasticity in 2D and 3D", *Comput. Methods Appl. Mech. Eng.* **196**:41–44 (2007), 4075–4086.

[Chróścielewski and Witkowski 2006] J. Chróścielewski and W. Witkowski, "Four-node semi-EAS element in six-field nonlinear theory of shells", *Int. J. Numer. Methods Eng.* **68**:11 (2006), 1137–1179.

[Chróścielewski et al. 1992] J. Chróścielewski, J. Makowski, and H. Stumpf, "Genuinely resultant shell finite elements accounting for geometric and material non-linearity", *Int. J. Numer. Methods Eng.* **35**:1 (1992), 63–94.

[Eberlein and Wriggers 1999] R. Eberlein and P. Wriggers, "Finite element concepts for finite elastoplastic strains and isotropic stress response in shells: theoretical and computational analysis", *Comput. Methods Appl. Mech. Eng.* **171**:3–4 (1999), 243–279.

[Fontes Valente et al. 2003] R. A. Fontes Valente, R. M. Natal Jorge, R. P. R. Cardoso, J. M. A. César de Sá, and J. J. A. Grácio, "On the use of an enhanced *transverse* shear strain shell element for problems involving large rotations", *Comput. Mech.* **30**:4 (2003), 286–296.

[Fontes Valente et al. 2005] R. A. Fontes Valente, M. P. L. Parente, R. M. Natal Jorge, J. M. A. César de Sá, and J. J. A. Grácio, "Enhanced *transverse* shear strain shell formulation applied to large elasto-plastic deformation problems", *Int. J. Numer. Methods Eng.* **62**:10 (2005), 1360–1398.

[Gruttmann et al. 1992] F. Gruttmann, W. Wagner, and P. Wriggers, "A nonlinear quadrilateral shell element with drilling degrees of freedom", *Arch. Appl. Mech.* **62**:7 (1992), 474–486.

[Hauptmann et al. 2000] R. Hauptmann, K. Schweizerhof, and S. Doll, "Extension of the 'solid-shell' concept for application to large elastic and large elastoplastic deformations", *Int. J. Numer. Methods Eng.* **49**:9 (2000), 1121–1141.

[Ibrahimbegović and Frey 1994] A. Ibrahimbegović and F. Frey, "Stress resultant geometrically nonlinear shell theory with drilling rotations, II: Computational aspects", *Comput. Methods Appl. Mech. Eng.* **118**:3-4 (1994), 285–308.

[Klinkel et al. 2008] S. Klinkel, F. Gruttmann, and W. Wagner, "A mixed shell formulation accounting for thickness strains and finite strain 3D material models", *Int. J. Numer. Methods Eng.* **74**:6 (2008), 945–970.

[Koschnick et al. 2005] F. Koschnick, M. Bischoff, N. Camprubí, and K.-U. Bletzinger, "The discrete strain gap method and membrane locking", *Comput. Methods Appl. Mech. Eng.* **194**:21–24 (2005), 2444–2463.

[Kuznetsov and Levyakov 2007] V. V. Kuznetsov and S. V. Levyakov, "Phenomenological invariant-based finite-element model for geometrically nonlinear analysis of thin shells", *Comput. Methods Appl. Mech. Eng.* **196**:49-52 (2007), 4952–4964.

[Li and Zhan 2000] M. Li and F. Zhan, "The finite deformation theory for beam, plate and shell, V: The shell element with drilling degree of freedom based on Biot strain", *Comput. Methods Appl. Mech. Eng.* **189**:3 (2000), 743–759.

[Merlini 2002] T. Merlini, "Differentiation of rotation and rototranslation", scientific report DIA-SR 02-16, Dipartimento di Ingegneria Aerospaziale, Politecnico di Milano, 2002, Available at http://www.aero.polimi.it/diasr/02-16.pdf.

[Merlini 2003] T. Merlini, "Recursive representation of orthonormal tensors", scientific report DIA-SR 03-02, Dipartimento di Ingegneria Aerospaziale, Politecnico di Milano, 2003, Available at http://www.aero.polimi.it/diasr/03-02.pdf.

[Merlini 2008a] T. Merlini, *Boundary constraint variational formulation for helicoidal modeling*, Aracne, Rome, 2008. Scientific report DIA-SR 08-05.

[Merlini 2008b] T. Merlini, *Variational formulations for the helicoidal modeling of the shell material surface*, Aracne, Rome, 2008. Scientific report DIA-SR 08-06.

[Merlini and Morandini 2004a] T. Merlini and M. Morandini, "The helicoidal modeling in computational finite elasticity, I: Variational formulation", *Int. J. Solids Struct.* **41**:18–19 (2004), 5351–5381.

[Merlini and Morandini 2004b] T. Merlini and M. Morandini, "The helicoidal modeling in computational finite elasticity, II: Multiplicative interpolation", *Int. J. Solids Struct.* **41**:18–19 (2004), 5383–5409. Erratum on *Int. J. Solids Struct.* **42**:3–4 (2005), 1269.

[Merlini and Morandini 2005] T. Merlini and M. Morandini, "The helicoidal modeling in computational finite elasticity, III: Finite element approximation for non-polar media", *Int. J. Solids Struct.* **42**:24–25 (2005), 6475–6513.

[Merlini and Morandini 2008] T. Merlini and M. Morandini, *Material surface elements by the helicoidal shell theory*, Aracne, Rome, 2008. Scientific report DIA-SR 08-08.

[Pimenta et al. 2004] P. M. Pimenta, E. M. B. Campello, and P. Wriggers, "A fully nonlinear multi-parameter shell model with thickness variation and a triangular shell finite element", *Comput. Mech.* **34**:3 (2004), 181–193.

[Reese et al. 2000] S. Reese, P. Wriggers, and B. D. Reddy, "A new locking-free brick element technique for large deformation problems in elasticity", *Comput. Struct.* **75**:3 (2000), 291–304.

[Ricci Maccarini et al. 2001] R. Ricci Maccarini, A. Saetta, and R. Vitaliani, "A non-linear finite element formulation for shells of arbitrary geometry", *Comput. Methods Appl. Mech. Eng.* **190**:37–38 (2001), 4967–4986.

[Sansour and Bednarczyk 1995] C. Sansour and H. Bednarczyk, "The Cosserat surface as a shell model: theory and finite-element formulation", *Comput. Methods Appl. Mech. Eng.* **120**:1–2 (1995), 1–32.

[Sansour and Bufler 1992] C. Sansour and H. Bufler, "An exact finite rotation shell theory, its mixed variational formulation and its finite element implementation", *Int. J. Numer. Methods Eng.* **34**:1 (1992), 73–115.

[Sansour and Kollmann 2000] C. Sansour and F. G. Kollmann, "Families of 4-node and 9-node finite elements for a finite deformation shell theory: an assessment of hybrid stress, hybrid strain and enhanced strain elements", *Comput. Mech.* **24**:6 (2000), 435–447.

[Simo et al. 1990] J. C. Simo, D. D. Fox, and M. S. Rifai, "On a stress resultant geometrically exact shell model, III: Computational aspects of the nonlinear theory", *Comput. Methods Appl. Mech. Eng.* **79**:1 (1990), 21–70.

[Sze et al. 2002] K. Y. Sze, W. K. Chan, and T. H. H. Pian, "An eight-node hybrid-stress solid-shell element for geometric non-linear analysis of elastic shells", *Int. J. Numer. Methods Eng.* **55**:7 (2002), 853–878.

[Sze et al. 2004] K. Y. Sze, X. H. Liu, and S. H. Lo, "Popular benchmark problems for geometric nonlinear analysis of shells", *Finite Elem. Anal. Des.* **40**:11 (2004), 1551–1569.

[Wagner and Gruttmann 2005] W. Wagner and F. Gruttmann, "A robust non-linear mixed hybrid quadrilateral shell element", *Int. J. Numer. Methods Eng.* **64**:5 (2005), 635–666.

[Wriggers and Gruttmann 1993] P. Wriggers and F. Gruttmann, "Thin shells with finite rotations formulated in Biot stresses: theory and finite element formulation", *Int. J. Numer. Methods Eng.* **36**:12 (1993), 2049–2071.

Received 8 Mar 2010. Revised 27 Sep 2010. Accepted 2 Oct 2010.

TEODORO MERLINI: teodoro.merlini@polimi.it
Politecnico di Milano, Dipartimento di Ingegneria Aerospaziale, via La Masa 34, 20156 Milano, Italy
http://www.aero.polimi.it/merlini

MARCO MORANDINI: marco.morandini@polimi.it
Politecnico di Milano, Dipartimento di Ingegneria Aerospaziale, via La Masa 34, 20156 Milano, Italy
http://www.aero.polimi.it/morandini/Home

JOURNAL OF MECHANICS OF MATERIALS AND STRUCTURES
Vol. 6, No. 5, 2011

msp

EFFECTIVE PROPERTY ESTIMATES FOR HETEROGENEOUS MATERIALS WITH COCONTINUOUS PHASES

PATRICK FRANCIOSI, RENALD BRENNER AND ABDERRAHIM EL OMRI

This work concerns heterogeneous multiphase materials which may exhibit omnidirectional full or partial cocontinuity of several or all phases. The estimate of their effective (mechanical or physical) properties is not yet well handled as compared to those for well-defined aggregate or reinforced-matrix structures, especially in the context of homogenization methods. We propose in this framework a modeling scheme which aims at accounting for such phase cocontinuity features. In the mechanical application field, the modeling validity restricts to elastic properties of unloaded materials or in load situations as far as bending and torsion effects of possibly strut-like phase parts are not essential. For other physical properties (dielectric, magnetic, etc.), the modeling applications concern those for which homogenization approaches are relevant. The modeling is based on a material's morphology description in terms of a generalization of so-called "fiber systems" that were introduced in early literature reports. Using parameters that describe the clustering characteristics of the individual phases and of their assemblage, we have considered these fiber systems both within a layer-based approach of the material structure and within an aggregate-like one. By these two routes, we have obtained two estimate forms that differ only slightly in definition. The presentation uses the elasticity formalism, in simple cases of isotropic mixtures of two-phase materials with isotropic phase behavior but the modeling extends to n-phase anisotropic materials as established separately. Our estimates are compared with basic variational bounds and homogenization estimates, with some literature data and with homogenization results obtained with the fast Fourier transform approach on numerical structures. All data are matched with different parameter sets corresponding to different types of phase organization. The two estimates remain nearly equal for all of the examined structures regardless of phase contrast and with only slight differences consistent with their definition difference.

1. Introduction

The continuity of a phase in a material here means the existence of an infinite (or sample spanning) cluster of that phase in the material with regard to one, several or all directions of space. Although this phase continuity is sometimes called phase percolation, this latter term is the most often related to the transition threshold between discontinuity and continuity. In that respect, phase cocontinuity is to be understood as the coexistence of multidirectional sample spanning clusters from different phases. Multiphase materials with cocontinuous phases, to be called cocontinuous materials for short, are of many different structure types: sponge-like structures, bones, blends, foams, braided composites, etc. These structures, named from porous examples, can also characterize assemblages of several solid phases. They can be made of ceramics, polymers, metals, biomaterials and composites of these. A wide variety of interesting physical and mechanical properties make the experimental investigations of their effective properties increasing

Keywords: phase cocontinuity, effective properties, heterogeneous materials, clustering.

fast [Nieh et al. 1998; Veenstra et al. 2000; La Vecchia et al. 2003; Morgan et al. 2003; Agrawal et al. 2003; Kinney et al. 2005; Marur 2005]. Yet it is not easy to find data sets that allow the relation of their overall properties with the specific features of their phase arrangements.

On the theoretical ground, insights into aggregates and particle- (or fiber-) reinforced composites have been considerable during the last decades, themselves based on a set of pioneering works [Hill 1952; Hill 1965; Kerner 1956; Boucher 1974; Walpole 1978; 1981; Christensen 1979a; 1979b; Hashin 1979; 1983], in the context of homogenization theory especially. Well defined frameworks have been provided for composite materials that exhibit phase cocontinuity with regard to only one direction (parallel fibers) or two directions (laminate structures) in space and omnidirectional cocontinuity has been explored using some ideal structures such as the overlapping sphere models; see for example [Berryman 1985]. Yet, estimates of effective elastic, electric or other properties for (isotropic or not) materials with multidirectionally cocontinuous phases have not been the matter of many examinations in this homogenization context.

In counterpart, many models derived for cocontinuous materials, are based on rheological descriptions combining series and parallel arrangements of the phases [Ravichandran 1994; Fan 1995; Leßle et al. 1999; Dalmaz et al. 2000]. Also, a lot of works make use of finite element methods or other computational techniques based on meshing or space-partitioning procedures [Feng et al. 2003; Chen et al. 2008]. Numerical homogenization techniques provide as well relevant estimates applicable to various effective properties [Roberts and Garboczi 2002; Delannay et al. 2006; Pavese et al. 2007].

Specific models have been developed for the particular mechanical properties exhibited by some of these cocontinuous materials as the cellular materials or some open cell foams, in order to account for bending and torsion characteristics, due to strut-like elements [Gent and Thomas 1959; Ko 1965; Menges and Knipschild 1975; Warren and Kraynik 1987; 1997]. These effects are partly handled in numerical modeling, they are not in rheological ones and they would not be at all in a homogenization approach. Widely used specific models as the Kelvin cell model [Gong et al. 2005] or also some systematic statistical approaches are also dedicated to these particular mechanical characteristics [Berk 1987; Roberts and Garboczi 2002].

But materials with cocontinuous phases are of very many different types and their mechanical behavior does not necessarily exhibit such particular mechanical characteristics. Furthermore, materials in their unloaded state have intrinsic elastic properties worth to be known if accessible. Experimental information for the unloaded state can be obtained for example from laser ultrasonic probing or from the extrapolation at zero strain of elastic data from the unloading stage of mechanical tests [Lefebvre et al. 2006].

In spite of this quite large variety of proposed models, in proportion to the variety of structures, it is frequently stated in the concerned literature that the obtained fit with measurements remains limited with regard to either mechanical or physical overall properties.

From these considerations, the goal of the present work is to formulate, in the context of homogenization methods, a modeling scheme to estimate the effective properties of multiphase materials which allows to account for a wide diversity of phase cocontinuity situations, partial or total, symmetrically for the concerned phases or not, etc. The proposed modeling is compared with available data and with direct estimates on numerically built structure by using the recent technique of fast Fourier transforms [Moulinec and Suquet 1998; Michel et al. 2001; Lebensohn et al. 2008] which provides an efficient tool for computing the properties of arbitrarily complex periodic structures. Our proposed modeling

scheme is built such as to remain consistent with the possible coexistence of one omnidirectional infinite (sample spanning) cluster of each phase present in the material. It is based on a description of the material structure from a generalization of the fiber systems introduced in [Christensen and Waals 1972] as typical examples of cocontinuous phase arrangements with regard to all directions in space. The generalized fiber systems that can be defined from a set of phases (taking, in turn, each phase as a fiber-reinforced matrix) are in a second step combined within either a layer-based approach or within an aggregate-like one of the material structure, by using parameters which describe the phase clustering characteristics for each phase individually and for their assemblage.

Regarding the employed terminology in this two-scale modeling scheme, we refer to layer-based approaches for the homogenization methods that involve models for laminate structures and to aggregate-like approaches for the methods that make use of a self-consistent modeling. The choice of considering first fiber systems in combination with a layer-based approach has been motivated by the fact that such linear and planar cuts of materials are key elements for the 3D reconstruction methods in tomography analyses [Natterer 1986] as well as for the calculation of the main lower-order "microstructural descriptors"[1] [Torquato 2002]. Secondly, aggregate-like organizations of the same representative domains have also been considered for comparison purposes with the self-consistent property estimates and also because aggregates likely have a concentration range of phase cocontinuity when the phases are in limited number and in comparable concentrations. These two modeling routes that we have explored, without loss of generality, for two-phase materials of isotropic structure and properties and which is presented in the case of the elasticity formalism although they are both holding for many other properties, yield quite similar estimate forms and definitions. They are shown to provide very close moduli estimates in situations of significant phase cocontinuity, while for vanishing cocontinuity a slight estimate difference results from the slight difference in their definitions. It is at last worth to stress that the isotropic platelet and fiber systems here considered for two-phase isotropic materials extend (as aggregate structures) to n-phase materials with possibly anisotropic phase properties and spatial arrangements. Some of their remarkable characteristics here stressed and used extend accordingly, what is presented in [Franciosi and El Omri 2011].

Section 2 introduces the considered structures and the phase continuity characteristics to be accounted for. Section 3 summarizes the fundamentals of the layer-based and aggregate-like approaches of heterogeneous materials properties and presents the estimate forms that we have worked with. Section 4 presents in the fully isotropic case the phase cocontinuity description and the morphology-based phase continuity parameters which have been introduced in the estimate formulation. Section 5 reports the result comparisons with variational bounds and homogenization estimates, with some literature data and with calculations by fast Fourier transform (FFT) numerical scheme on 3D structures with various phase cocontinuity situations.

2. Typical cocontinuous two-phase structures and phase continuity characteristics

Examples of concerned structures by the proposed modeling are collected in Figure 1. The most typical ones are the two-phase blend or sponge-like structure, Figure 1a (aluminum from [Nieh et al. 1998])

[1] N-points and surface correlation functions, lineal path function, chord-length density function, particle pair correlation function, etc. Note that the two-point correlation function also contains the two-point cluster function.

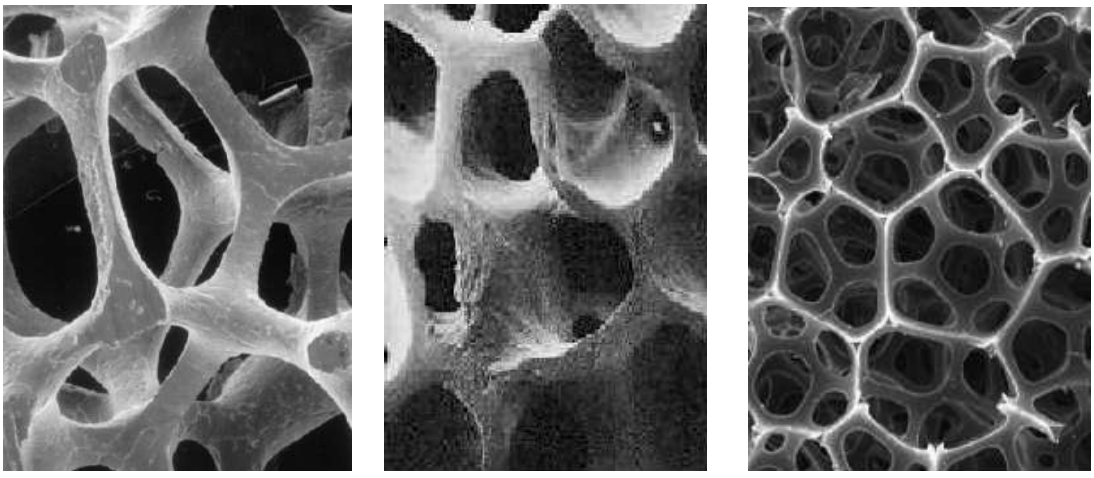

Figure 1. Examples of cocontinuous structures of concern: (a) sponge-like metallic oxide, (b) trabecular bone tissue, (c) cellular foam.

and the structure of trabecular bones, Figure 1b [Mow and Huiskes 2004], where the void volume in the exemplified materials, which can be replaced by a second solid material phase (alumina in aluminum, [La Vecchia et al. 2003], or marrow in bones), is also a continuous phase. The previously pointed importance of bending and torsion effects due to strut elements in open foam structures such as illustrated in Figure 1c [Gong et al. 2005] restricts for these materials the mechanical field of application of the proposed modeling to estimating the elastic properties either in the unloaded state of the material or in the loading situations on it when these effects are not essential.

Now, for these structures the phase cocontinuity is omnidirectional, say multidirectional in a continuous manner, either isotropically or possibly obeying some other global symmetry. There are also cocontinuous materials for which the phase cocontinuity is multidirectional but only concerns a discrete set of directions, as tubular systems and woven or weaved composites. In these architectures the mechanical features as flexibility, bending, torsion, etc can also be important. If they are not of concern here, it is worth to mention that particular arrangements of discrete direction sets for phase cocontinuity can ensure isotropic effective properties, a point to be of use in the discussions to come.

With regard to phase concentrations, many materials as polymer blends or aggregates with a limited phase number are very likely phase cocontinuous in the intermediate phase concentration range, but a dilute phase "naturally" adopts the embedded condition in general[2]. While many composites have no concentration range of phase cocontinuity (as typically glass inclusions in a polymer matrix), real n-phase structures that remain cocontinuous over the whole phase concentration range are quite scarce, if any, even for only two phases. Indeed, this would require for each of the assembled phases the existence of a continuous reinforcement down to an infinitesimal concentration of this phase. It is an advantage of numerical structures to possibly mix two phases in bicontinuous arrangements down to a nearly zero concentration, with the only limit being the chosen voxel density in a unit cell.

[2]Two-phase metals are also multiphase in terms of grain orientation distributions or crystallographic textures [Bretheau et al. 1988; Kocks et al. 1991; Lebensohn et al. 2008].

Now, the structures that would be cocontinuous over the whole phase concentration range or only over a part of it can exhibit a variety of phase cocontinuity characteristics that are specific for each material phase and likely vary with their relative phase concentrations. We have restricted attention to the materials which can be taken as isotropic and statistically homogeneous at the different length scales that we may have to successively consider. The main phase continuity characteristics to which attention is paid are (i) the amount of phase continuity, from null to total, exhibited by each material phase and (ii) the asymmetry of the cocontinuity between the material phases. For structures whose phase concentration can be varied, attention is also paid to the possible concentration dependency of these characteristics.

(1) An isotropic, cocontinuous, two-phase material contains by definition, for each phase and in an intricate manner, one multidirectionally infinite (sample-spanning) cluster possibly having "dead branches" and possibly coexisting with finite clusters that do not contribute to the phase continuity. In that respect the continuity of a phase can be said to be total when no dead branches and no finite clusters remain, and it can be said to be partial otherwise. So it is as well for phase cocontinuity: it can be said total (resp. partial) when all the cocontinuous phases are totally (resp. partially) continuous.

(2) The asymmetry of continuity between the phases can match any intermediate between perfect symmetry and the extreme situations of null cocontinuity when one of the phases totally embeds the other one(s). These latter cases correspond to the widely met and examined reinforced-matrix structures [DeBartolo and Hillberry 1998; Estevez et al. 1999; Martin et al. 2003; Ricotti et al. 2006]. Conversely, perfect phase cocontinuity symmetry even for only two phases is only realizable in a very limited set of manners which are not isotropic [Burt and Korren 1996]. The general status of any partially bicontinuous two-phase structure is consequently an asymmetric bicontinuity.

(3) Both the phase continuity amount and the phase cocontinuity asymmetry are expected to be concentration-dependent for many materials, and this dependency is expected to obey many different law forms. In real materials, changes of phase concentration can be accompanied with changes in phase composition in addition to changes in phase arrangements, such that the phase properties do not remain fixed. In multiscale homogenization schemes, effective properties at inner levels can also change, which also corresponds to changes of the properties of assembled phases at the macroscopic level.

3. Layer-based approach of heterogeneous materials versus the aggregate-like description

Planar and linear cuts are, respectively, at the base of material reconstruction from 2D planar sections of the representative volume element (RVE) and from 1D-rays or lines traversing the RVE [Ramm and Katsevich 1996; Singh et al. 2008]. With regard to each direction $\boldsymbol{\omega}$ in space, any material either is a laminate structure whose layers are its planar heterogeneous sections normal to $\boldsymbol{\omega}$ or is a $\boldsymbol{\omega}$-directional fiber structure with the fibers being the material rays or lines in that $\boldsymbol{\omega}$ direction. While linear cuts necessarily alternate homogeneous subdomains of each phase, in planar sections (Figure 2) one phase can be multidirectionally macrocontinuous while all other ones are not. Sections consequently look like a patchwork of 2D subdomains within which one phase (at the most) is embedding all others in turn. Thus, 2D planar subdomains can be characterized by a continuous phase arranged into one infinite

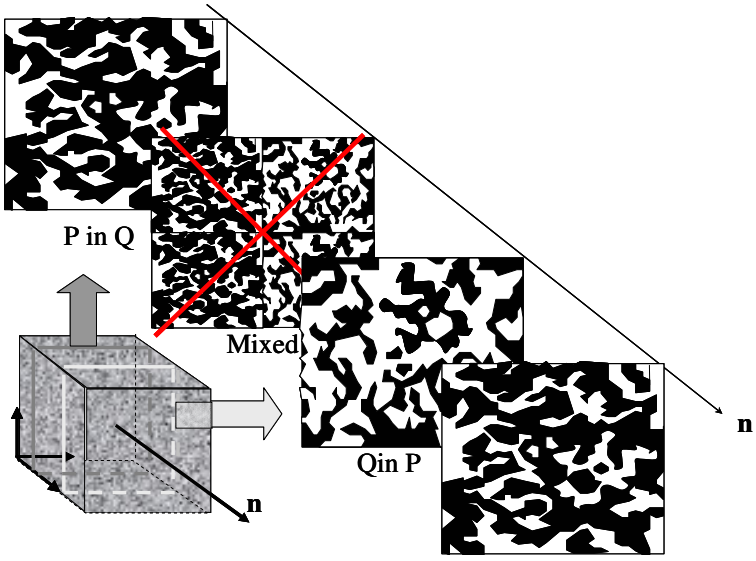

Figure 2. Typical planar sections of general two-phase materials.

cluster possibly having dead branches and being accompanied with finite clusters embedded in the other phase(s).

In planar sections of a two-phase material (p, q), the two phases p and q can only be locally arranged either as $p \subset q$ or as $q \subset p$ (also denoted as $p|q$ and $q|p$, respectively, in the following). For the sake of simplicity, we have ignored intermediate situations that can be resolved as smaller patchworks of these two same subdomains, and we have also disregarded the details of multiple inclusion levels such as $p \subset (q \subset p(\cdots))$, etc. This allows the description of any such macrohomogeneous material, with regard to any direction $\boldsymbol{\omega}$ and at the scale of a representative volume element, as a piling of parallel planes of $p|q$ and $q|p$ structures along $z(\boldsymbol{\omega})$, say as $\boldsymbol{\omega}$-oriented two-phase laminate structures. These planes of identical zero (or infinitesimal) thickness can be arranged into infinitely other sequences than the strictly alternated lamination. Assuming statistical homogeneity, the material phase concentrations are identically f_p and $f_q = 1 - f_p$ in each layer separately, for all directions $\boldsymbol{\omega}$. This is not saying that the material is an aggregate of laminate domains but that each material domain can be viewed from any direction $\boldsymbol{\omega}$ as a laminate structure, provided an appropriate description of the constitutive layers. One first property of importance for the following is that any $\boldsymbol{\omega}$-oriented laminate structure made of n different types of multiphase layers ensures the cocontinuity normally to $\boldsymbol{\omega}$ for all of the phases that are continuous in one layer type. When in a two-phase material (p, q) the $\boldsymbol{\omega}$-oriented layers have either a phase p or a phase q which is continuous, both phases p and q are cocontinuous normally to the direction $\boldsymbol{\omega}$. With regard to all other directions not normal to that $\boldsymbol{\omega}$, the continuity of each phase will depend on its through-section continuity, a crucial point to be closely examined latter on.

3.1. ***Effective elasticity properties of laminate structures in terms of platelet Green operators.*** In order to conveniently treat later on, for each $\boldsymbol{\omega}$ direction in $\mathbb{R}^3$, the two-phase material as such a laminate structure made of two types of sections $p|q$ and $q|p$, useful characteristics of laminate structures and of laminate layers (platelets) deserve to first be recalled.

Effective elasticity of laminates. There are various formulations to represent the effective properties of laminate structures, early calculated for example in [Postma 1955]. One is the hybrid procedure used in [El Omri et al. 2000] for modeling, in a plasticity context, polycrystalline structures as aggregates of laminate domains. Such a procedure is not to be used here, but this aggregate structure type will reappear in the following. The formulation more of concern here is the one which comes from the general homogenization framework for inclusion-reinforced matrices at the limit of infinitely flat and congruent spheroidal inclusions [Hill 1952; Zeller and Dederichs 1973; Walpole 1981]. Take a matrix of phase b, of moduli $\boldsymbol{C}_b$, reinforced with all congruent (shape V) ellipsoidal inclusions of phase ai, of moduli $\boldsymbol{C}_{ai}$, with concentrations c_{ai}, $i \in (1,\ n-1)$ and, according to a spatial distribution symmetry, homothetic to the shape V of all inclusions. The effective moduli read

$$\boldsymbol{C}^{*V}_{(a1,\dots,an-1)\subset b} = \boldsymbol{C}_b - \left(\left(\sum_{i=1}^{n-1} c_{ai}\left((\boldsymbol{C}_b - \boldsymbol{C}_{ai})^{-1} - \boldsymbol{t}^V_{C_b}\right)^{-1}\right)^{-1} + \boldsymbol{t}^V_{C_b}\right)^{-1} \tag{1}$$

Specializing to the case of platelets with $\boldsymbol{\omega}$-oriented normal ($V = P(\omega)$) amounts to substituting, in (1), the operator $\boldsymbol{t}^V_{C_b}$ with the operator $\boldsymbol{t}^{P(\omega)}_{C_b}$ that are respectively the modified strain Green operator integrals (strain Green operators or "GO$_\epsilon$" for short) for the inclusion V and for the platelet $P(\omega)$, in an infinite matrix of moduli $\boldsymbol{C}_b$. It is a key property of laminate structures that any one of the n layer types can be selected as the "matrix" without changing the result. For a two-phase material (a, b) of the laminate type, setting $\boldsymbol{\Delta C}_{b|a} = \boldsymbol{C}_b - \boldsymbol{C}_a = -\boldsymbol{\Delta C}_{a|b}$, the following equation results:

$$\boldsymbol{C}^{*P(\omega)}_{a\subset b} = \boldsymbol{C}_b - c_a\left((\boldsymbol{\Delta C}_{b|a})^{-1} - c_b\boldsymbol{t}^{P(\omega)}_{C_b}\right)^{-1} = \boldsymbol{C}^{*P(\omega)}_{b\subset a} = \boldsymbol{C}_a - c_b\left((\boldsymbol{\Delta C}_{a|b})^{-1} - c_a\boldsymbol{t}^{P(\omega)}_{C_a}\right)^{-1} \tag{2}$$

and the proof of the equality $\boldsymbol{C}^{*P(\omega)}_{a\subset b} = \boldsymbol{C}^{*P(\omega)}_{b\subset a} = \boldsymbol{C}^{*P(\omega)}_{a,b}$ (which only holds for platelet-like inclusions) is recalled in Appendix A. For $\boldsymbol{\omega}$-oriented fibers $F(\omega)$, also a specific case of interest later on, one obtains

$$\boldsymbol{C}^{*F(\omega)}_{a\subset b} = \boldsymbol{C}_b - c_a\left((\boldsymbol{\Delta C}_{b|a})^{-1} - c_b\boldsymbol{t}^{F(\omega)}_{C_b}\right)^{-1} \neq \boldsymbol{C}^{*F(\omega)}_{b\subset a} = \boldsymbol{C}_a - c_b\left((\boldsymbol{\Delta C}_{a|b})^{-1} - c_a\boldsymbol{t}^{F(\omega)}_{C_a}\right)^{-1} \tag{3}$$

In (3), the operator $\boldsymbol{t}^{F(\omega)}_{C_b}$ is the GO$_\epsilon$ for the fiber $F(\omega)$ in an infinite matrix of moduli $\boldsymbol{C}_b$. When $\boldsymbol{t}^V_{C_b}$ is used instead of $\boldsymbol{t}^{F(\omega)}_{C_b}$ (resp. $\boldsymbol{C}_a$), (3) gives the two specializations of (1) for a two-phase material which are the HS (Hashin–Shtrikman) bounds [1963] for all the spatial distributions of the phases a and b characterized by the shape V.

Equations (2)–(3), which hold for moduli tensors $\boldsymbol{C}$, have corresponding forms for the related compliance tensors $\boldsymbol{S} = \boldsymbol{C}^{-1}$, when the appropriate modified stress Green operator integral (stress Green operators or GO$_\sigma$ for short) $\boldsymbol{t}'^V_{S_b}$ is substituted with $\boldsymbol{t}^V_{C_b}$.

Table 1 collects the nonzero terms of these strain Green operators $\boldsymbol{t}^V_{C_b}$ and stress Green operators $\boldsymbol{t}'^V_{S_b}$ for the sphere, the x_3-oriented platelet and the x_3-oriented fiber. They depend on the two constants

$$B = \frac{1}{\mu} \quad \text{and} \quad A = \frac{-B}{2(1-\nu)}$$

for the isotropic elasticity of a matrix phase of shear modulus μ and Poisson coefficient ν.

For isotropic properties that are represented by rank-two tensors, as dielectric ones [Helsing 1993; Fan 1995; Kanaun 2003], there is no term A and the term B acts as the inverse of the dielectric constant. The relationships between these operators, for any ellipsoidal inclusion type V [Zeller and Dederichs 1973]

	t_{iiii}	t_{1122}	t_{ii33}	t_{3333}	t_{i3i3}	t_{1212}
sphere	$\frac{3A+5B}{15}$	$\frac{A}{15}$	$\frac{A}{15}$	$\frac{3A+5B}{15}$	$\frac{2A+5B}{30}$	$\frac{2A+5B}{30}$
x_3-platelet	0	0	0	$A+B=\frac{1}{\lambda+2\mu}$	$\frac{B}{4}=\frac{1}{4\mu}$	0
x_3-cylinder	$\frac{3A+4B}{8}$	$\frac{A}{8}$	0	0	$\frac{B}{8}$	$\frac{A+2B}{8}$
	t'_{iiii}	t'_{1122}	t'_{ii33}	t'_{3333}	t'_{i3i3}	t'_{1212}
sphere	$-\frac{32A}{15B^2}$	$-\frac{2(12A+5B)}{15B^2}$	$-\frac{2(12A+5B)}{15B^2}$	$-\frac{32A}{15B^2}$	$\frac{5B-4A}{15B^2}$	$\frac{5B-4A}{15B^2}$
x_3-platelet	$-\frac{4A}{B^2}=\frac{2\mu}{1-\nu}$	$-\frac{2(2A+B)}{B^2}$	0	0	0	$\frac{1}{B}=\mu$
x_3-cylinder	$-\frac{3A}{2B^2}$	$-\frac{A}{2B^2}$	$-\frac{A}{B^2}$	$-\frac{4A}{B^2}$	$\frac{1}{2B}$	$-\frac{A}{2B^2}$

Table 1. Strain Green operators $\boldsymbol{t}$ (top table) and stress Green operators $\boldsymbol{t}'$ (bottom table) for a sphere, an x_3-platelet and an x_3-cylinder in isotropic media ($i = 1, 2$).

with $\boldsymbol{C}_b = (\boldsymbol{S}_b)^{-1}$, are described by

$$\overline{\boldsymbol{t}'^{V}_{S_b}} = \boldsymbol{C}_b - \boldsymbol{C}_b : \overline{\boldsymbol{t}^{V}_{C_b}} : \boldsymbol{C}_b \quad \text{and} \quad \overline{\boldsymbol{t}^{V}_{C_b}} = \boldsymbol{S}_b - \boldsymbol{S}_b : \overline{\boldsymbol{t}'^{V}_{S_b}} : \boldsymbol{S}_b \tag{4}$$

A well known property of platelet operators that are related to a same normal direction $\boldsymbol{\omega}$ is their direct relation to the stress and strain jumps on both sides of a phase interface with normal $\boldsymbol{\omega}$ [Walpole 1978; 1981]. Less known is that any GO_ϵ (resp. GO_σ) operator related to an ellipsoidal shape of inclusion or distribution can be decomposed into a weighted average of GO_ϵ (resp. GO_σ) platelet operators over all directions $\boldsymbol{\omega}$ in space, according to its polar or spectral decomposition given by the Radon inversion formula [Gel'fand et al. 1966; Ramm and Katsevich 1996], that is,

$$\boldsymbol{t}^{V}_{C} = \int_\Omega \boldsymbol{\psi}^{V}(\omega)\boldsymbol{t}^{P(\omega)}_{C}\,\mathrm{d}\omega \quad ; \quad \boldsymbol{t}'^{V}_{S} = \int_\Omega \boldsymbol{\psi}^{V}(\omega)\boldsymbol{t}'^{P(\omega)}_{S}\,\mathrm{d}\omega \tag{5}$$

In the isotropic (spherical) case, the weight function of this decomposition ($\boldsymbol{\psi}^{V}(\omega) \geq 0$, $\int_\Omega \boldsymbol{\psi}^{V}(\omega)\,\mathrm{d}\omega = 1$) uniformly equals $\boldsymbol{\psi}^{\mathrm{Sph}}(\omega) = (4\pi)^{-1}$, while for a platelet of $\boldsymbol{\omega}_0$ normal it reduces to a Dirac function if $\boldsymbol{\psi}^{P(\omega 0)}(\omega) = \delta(\omega - \omega 0)$. For $\boldsymbol{\omega}_0$ -oriented cylindrical fibers, the weight function $\boldsymbol{\psi}^{F(\omega 0)}(\omega)$ equals $(2\pi)^{-1}$ for all directions normal to the fiber axis $\boldsymbol{\omega}_0$ and is zero otherwise. These Radon forms of Green operators have been discussed in [Franciosi and Lormand 2004; Franciosi 2005; 2010] for inclusions of various shapes and inclusion patterns of various spatial arrangements.

Further properties of platelet Green operators. Simple mathematical manipulations allow the demonstration (Appendix A) that for two-phase laminates in relative phase proportions c_a, c_b, the effective moduli take the symmetric form that appears in [Cherkaev 2000] in a less explicit manner:

$$\boldsymbol{C}^{*P(\omega)}_{a,b} = \langle \boldsymbol{C} \rangle - c_a c_b \boldsymbol{\Delta C}_{b|a} : \boldsymbol{t}^{P(\omega)}_{\{\boldsymbol{C}\}} : \boldsymbol{\Delta C}_{b|a} \tag{6}$$

with $\langle \boldsymbol{C} \rangle = c_a \boldsymbol{C}_a + c_b \boldsymbol{C}_b$ and $\{\boldsymbol{C}\} = c_b \boldsymbol{C}_a + c_a \boldsymbol{C}_b$ being respectively the Voigt (V) moduli tensor for the material $[a, b]$ and the one for its "complementary material" $]a, b[$ defined by an interchange of the phase proportions, say c_a of phase b and c_b of phase a. The dual expressions to (2) and (3) for the effective compliances $\boldsymbol{S}^{*V}_{a,b} = (\boldsymbol{C}^{*V}_{a,b})^{-1}$ read as follows (Appendix B), with $\boldsymbol{\Delta S}_{a|b} = \boldsymbol{S}_a - \boldsymbol{S}_b$ and with the appropriate GO_σ operator $\boldsymbol{t'}^{V}_{Sb} = \boldsymbol{t'}^{P(\omega)}_{Sb}$ for laminates and $\boldsymbol{t'}^{V}_{Sb} = \boldsymbol{t'}^{F(\omega)}_{Sb}$ for fibers:

$$\boldsymbol{S}^{*V}_{a\subset b} = \boldsymbol{S}_b - c_a \big((\boldsymbol{\Delta S}_{b|a})^{-1} - c_b \boldsymbol{t'}^{V}_{s_b} \big)^{-1} \tag{7}$$

Equation (7) also uses the equations (4), which connect $(\boldsymbol{\Delta S}_{b|a})^{-1}$ to $(\boldsymbol{\Delta C}_{b|a})^{-1}$ as they connect $\overline{\boldsymbol{t'}^{V}_{Sb}}$ to $\overline{\boldsymbol{t}^{V}_{Cb}}$, say

$$(\boldsymbol{\Delta S}_{b|a})^{-1} = \boldsymbol{C}_b - \boldsymbol{C}_b : (\boldsymbol{\Delta C}_{b|a})^{-1} : \boldsymbol{C}_b, \quad (\boldsymbol{\Delta C}_{b|a})^{-1} = \boldsymbol{S}_b - \boldsymbol{S}_b : (\boldsymbol{\Delta S}_{b|a})^{-1} : \boldsymbol{S}_b \tag{8}$$

The particular symmetric form reported in (6) for (2) which gives the effective moduli tensor of a two-phase laminate structure has its equivalent form for the dual effective compliance tensor. Noticing that $\langle \boldsymbol{S} \rangle \neq \langle \boldsymbol{C} \rangle^{-1}$ and $\{\boldsymbol{S}\} = c_b \boldsymbol{S}_a + c_a \boldsymbol{S}_b \neq \{\boldsymbol{C}\}^{-1}$, it reads

$$\boldsymbol{S}^{*P(\omega)}_{a,b} = \langle \boldsymbol{S} \rangle - c_a c_b \boldsymbol{\Delta S}_{b|a} : \boldsymbol{t'}^{P(\omega)}_{\{S\}} : \boldsymbol{\Delta S}_{b|a} \tag{9}$$

with the "stress" Green operator referring to the Reuss (R) compliance tensor $\{\boldsymbol{S}\}$ of the complementary composite $]a, b[$, while $\langle \boldsymbol{S} \rangle = c_a \boldsymbol{S}_a + c_b \boldsymbol{S}_b$ is the one of the material $[a, b]$. From the many relations between $\langle \boldsymbol{C} \rangle$, $\langle \boldsymbol{S} \rangle$, $\{\boldsymbol{C}\}$ and $\{\boldsymbol{S}\}$[3], one has in particular the equivalences

$$\boldsymbol{\Delta C}_{b|a} = \frac{\{\boldsymbol{C}\} - \boldsymbol{C}_a}{c_a} = -\frac{\{\boldsymbol{C}\} - \boldsymbol{C}_b}{c_b}; \quad \boldsymbol{\Delta S}_{b|a} = \frac{\{\boldsymbol{S}\} - \boldsymbol{S}_a}{c_a} = -\frac{\{\boldsymbol{S}\} - \boldsymbol{S}_b}{c_b} \tag{10}$$

Using (10) in (6) and (9) yields these remarkable estimate forms for two-phase laminates:

$$\boldsymbol{C}^{*P(\omega)}_{a,b} = \langle \boldsymbol{C} \rangle + (\{\boldsymbol{C}\} - \boldsymbol{C}_a) : \boldsymbol{t}^{P(\omega)}_{\{C\}} : (\{\boldsymbol{C}\} - \boldsymbol{C}_b), \tag{11a}$$

$$\boldsymbol{S}^{*P(\omega)}_{a,b} = \langle \boldsymbol{S} \rangle + (\{\boldsymbol{S}\} - \boldsymbol{S}_a) : \boldsymbol{t'}^{P(\omega)}_{\{S\}} : (\{\boldsymbol{S}\} - \boldsymbol{S}_b). \tag{11b}$$

Not only do Equations (6), (9) and (11a), (11b) incidentally provide new relations between the Green operators of $\boldsymbol{\omega}$-oriented platelets associated with a pair of complementary materials ($[a, b]$, $]a, b[$), but they also essentially reveal the role, to be examined later on, of the two-phase complementary composite $]a, b[$ as a reference medium. The moduli estimates for n types of layers are obtained by recurrence, adding the n-th layer type to the $(n-1)$-laminate previously assembled by adding the $(n-1)$-st layer type to the $(n-2)$ previously assembled ones, and so on. A symmetric form is obtained by averaging over all possible choices for the order or the layered phases. This symmetric form generalizing (11) to n phases is to be presented in a separate work.

3.2. ***Isotropic platelet systems (IPS) for bicontinuous two-phase materials.*** One of the first proposed effective moduli estimates for bicontinuous two-phase materials refers to laminate structures. It is the one which comes from the isotropic platelet system (IPS) introduced in [Christensen 1979a; 1979b]. The IPS estimate is defined as the isotropic averaging of the effective moduli tensor for the $\boldsymbol{\omega}$-oriented

[3]Such as $\langle \boldsymbol{C} \rangle : \boldsymbol{\Delta S}_{b|a} = \boldsymbol{\Delta C}_{a|b} : \{\boldsymbol{S}\}$ or $\langle \boldsymbol{C} \rangle : \langle \boldsymbol{S} \rangle = \{\boldsymbol{C}\} : \{\boldsymbol{S}\} = \boldsymbol{I} - f_a f_b \boldsymbol{\Delta C}_{b|a} : \boldsymbol{\Delta S}_{b|a}$.

	$iiii(0,0)$	$3333(0,0)$	$1122(0,0)$	$ii33(0,0)$	$1212(0,0)$	$i3i3(0,0)$
$\overline{jjjj(\theta,\phi)}$	$\frac{8}{15}$	$\frac{3}{15}$	0	$\frac{4}{15}$	0	$\frac{8}{15}$
$\overline{jjkk(\theta,\phi)}$	$\frac{1}{15}$	$\frac{1}{15}$	$\frac{5}{15}$	$\frac{8}{15}$	0	$-\frac{4}{15}$
$\overline{jkjk(\theta,\phi)}$	$\frac{1}{15}$	$\frac{1}{15}$	0	$-\frac{2}{15}$	$\frac{5}{15}$	$\frac{6}{15}$

Table 2. Coefficients giving the isotropic average of axially symmetric operators ($i = 1, 2$; $j, k = 1, 2, 3$).

laminate systems, from (2), (6) or (11a):

$$\boldsymbol{C}^{*\mathrm{IPS}}_{a,b} = (4\pi)^{-1} \iint_{\theta,\phi} \boldsymbol{C}^{*P(\theta,\phi)}_{a,b}(\theta,\phi)\sin\theta\,\mathrm{d}\theta\,\mathrm{d}\phi \tag{12}$$

where one has, by rotation of matrix $[W]$, the relations $(\boldsymbol{C}^{*P(\theta,\phi)}_{a,b})_{ijkl} = W_{ip}W_{jq}W_{kr}W_{ls}(\boldsymbol{C}^{*P(0,0)}_{a,b})_{pqrs}$. The IPS, as introduced, was said by the author as "implying intersecting platelets of some kind" and "suggestive of morphology known as interpenetrating networks" of (two) phases. This IPS results from performing a geometric averaging process previously applied to isotropic fiber systems (IFSs) in [Christensen and Waals 1972], fiber systems which will be examined later on. With considering layers of the two constitutive phases (p, q) of the material, this IPS estimate is expected to ensure some isotropic phase cocontinuity; because, as underlined previously, for each $\boldsymbol{\omega}$ direction the layered structure ensures the phase cocontinuity normally to $\boldsymbol{\omega}$ and because $\boldsymbol{\omega}$ is taken to span the whole space. However, no material strictly having that type of phase organization is realizable: if it happens that normally to one direction $\boldsymbol{\omega}$ the two phases (p, q) exhibit a laminate-like organization, there is no direction $\boldsymbol{\omega}' \neq \pm\boldsymbol{\omega}$ possibly exhibiting the same organization simultaneously. Aware of this, Christensen imaged the arrangement of this IPS structure as an isotropic aggregate of $\boldsymbol{\omega}$-oriented laminate domains, but this does not satisfactorily depict an interpenetrating network of two phases, and the effective properties of such an aggregate of laminate domains are not properly estimated by (12). An aggregate of laminate domains is more convenient to describe planar slip in grains of polycrystals, as used by [El Omri et al. 2000] for plasticity modeling.[4] Conversely, this slip description illustrates what kind of trans-granular continuity one can expect between the layers of a same phase which are randomly oriented from grain to grain: it is no more than the possible slip continuity between neighboring grains. A better estimate for the elasticity moduli of an aggregate of laminate domains is the one obtained from the SC approximation

$$\boldsymbol{C}^* = \boldsymbol{C}^* - \left(\left(\frac{1}{4\pi}\int_\Omega \left((\boldsymbol{C}^* - \boldsymbol{C}^P\omega)^{-1} - \boldsymbol{t}^{\mathrm{Sph}}_{\boldsymbol{C}^*}\right)^{-1}\mathrm{d}\omega\right)^{-1} + \boldsymbol{t}^{\mathrm{Sph}}_{\boldsymbol{C}^*}\right)^{-1}, \tag{13}$$

where the tensors $\boldsymbol{C}^P\omega$ are the moduli tensors for the ω-oriented laminated grains, given in (6) and (11a). The IPS estimate from (12) is definitely different from the one of (13), to be denoted ISCP in further comparisons. As is easily checked for the shear modulus in the case of two incompressible phases (combine (6) and (13) with using Table 2), when the phase contrast becomes infinite (taking one phase as void-like), this ISCP estimate goes to zero as the Reuss (R) and the HS(−) lower bounds, although in

[4] See also [Franciosi and Berbenni 2007; 2008] for laminate modeling of plastic slip in polycrystals.

a much slower manner. An interpretation is that even if large and intricate clusters of both phases exist, due to trans-granular chord connections between layers of a same phase, the probability of finding an infinite homogeneous path from grain to grain goes to zero with increasing the grain number to cross, and infinite clusters of each phase therefore have vanishingly small contributions. However, the quite high stiffness of the ISCP estimate from (13) makes it probably convenient for intricate mixtures of long tortuous fibers, as in cotton-like tangled or muddled assemblages of two fiber types, for example.

It is clear from all what precedes that the morphology types represented by (12) have to be seen as having the properties of an IPS more in a statistical way than effectively, owing to the impossible IPS topology as strictly defined. It is noteworthy at this stage that (12) has a likely interpretation in terms of a Radon inversion formula, as (5) has for the stress and strain Green operators: (12) can be understood as some spectral decomposition over a set of elementary effective moduli tensors, each representative of a typical planar connectivity property for layers of the materials of concern.

This interpretation would result from particular assumptions on the effective properties at the level of the material sections as exemplified in [Errabii et al. 2007]. Consistently with this view-point, the Christensen interpretation becomes acceptable provided the essential modification we here use that the involved representative "phases" a and b for the layer types are not the constitutive phases (p, q) of the material but are the homogeneous materials "equivalent" to the two types of its $p|q$ and $q|p$ heterogeneous sections, in a way which has to be appropriately defined, as examined in the following.The isotropic arithmetic average from (12) of an operator $\boldsymbol{C}^{*0}$ that corresponds to a structure with an x_3-oriented symmetry yields an isotropic tensor with eigenvalues which can be simply explicated using the relations

$$\begin{aligned} \boldsymbol{C}^{*\mathrm{iso}}_{ijij} &= \tfrac{1}{15}(\boldsymbol{C}^{*0}_{3333} + \boldsymbol{C}^{*0}_{iiii} - 2\boldsymbol{C}^{*0}_{ii33}) + \tfrac{1}{15}(6\boldsymbol{C}^{*0}_{i3i3} + 5\boldsymbol{C}^{*0}_{1212}), \\ \boldsymbol{C}^{*\mathrm{iso}}_{iiii} + 2\boldsymbol{C}^{*\mathrm{iso}}_{iijj} &= \tfrac{5}{15}(\boldsymbol{C}^{*0}_{3333} + 2\boldsymbol{C}^{*0}_{iiii} + 4\boldsymbol{C}^{*0}_{ii33} + 2\boldsymbol{C}^{*0}_{1122}). \end{aligned} \tag{14}$$

In (14) the coefficients are the isotropy coefficients of Table 2, obtained by solving simple trigonometric integrals. The IPS estimate from (12) results from using, as C^{*0} in (14), the laminate effective moduli given by (2) with the GO_ϵ of the x_3-oriented platelet given in Table 1, top. Now, a theoretical form of interest for the effective IPS properties can be obtained from (11a) as

$$\begin{aligned} C^{*\mathrm{IPS}}_{a,b} &= \int_\Omega \frac{C^{*^P}(\omega)}{4\pi}\,\mathrm{d}\omega = \langle \boldsymbol{C}\rangle - c_a c_b \boldsymbol{\Delta C}_{b|a} : \left(\int_\Omega \frac{t^P_{\{\boldsymbol{C}\}}(\omega)}{4\pi}\,\mathrm{d}\omega \right) : \boldsymbol{\Delta C}_{b|a} \\ &= \langle \boldsymbol{C}\rangle - c_a c_b \boldsymbol{\Delta C}_{b|a} : \boldsymbol{t}^{\mathrm{Sph}}_{\{\boldsymbol{C}\}} : \boldsymbol{\Delta C}_{b|a} = \langle \boldsymbol{C}\rangle + (\{\boldsymbol{C}\} - \boldsymbol{C}_a) : \boldsymbol{t}^{\mathrm{Sph}}_{\{\boldsymbol{C}\}} : (\{\boldsymbol{C}\} - \boldsymbol{C}_b). \end{aligned} \tag{15}$$

The important result expressed by (15) is the symmetric dependence of the IPS on a single operator. This point will be of use in the sequel. In (15), the operator $\boldsymbol{t}^{\mathrm{Sph}}_{\{\boldsymbol{C}\}}$ is the GO_ϵ for a spherical inclusion embedded in a matrix of moduli $\{\boldsymbol{C}\}$, given by its polar (Radon) decomposition in (5), where a and b are the effective properties of the representative planar sections which will be estimated in the following. In terms of compliances, although $\boldsymbol{S}^{*P(\omega)}_{a,b} = (\boldsymbol{C}^{*P(\omega)}_{a,b})^{-1}$, one has, in general,

$$\boldsymbol{S}^{*\mathrm{IPS}}_{a,b} = (4\pi)^{-1} \int_\Omega \boldsymbol{S}^{*^P}(\omega)\,\mathrm{d}\omega \neq (\boldsymbol{C}^{*\mathrm{IPS}}_{a,b})^{-1}.$$

This dual average (to be examined in a separate paper) corresponds to dual stress conditions that are not expected to be fulfilled by the phases of cocontinuous structures.

3.3. *Link and differences between the IPS and the isotropic self-consistent (ISC) estimates.*

Compared IPS and ISC estimates in terms of reference medium. The self-consistent (SC) approximation for aggregates of congruent grains is considered to account well for a phase continuity inversion in two-phase materials when the dense/dilute concentrations are inverted and for an intermediate domain of bicontinuity. When the grains are as flat as layers of a laminate structure, the SC approximation is also given by (3) because the HS(+/−) bounds coincide in this case. The calculation of the SC approximation is recalled in Appendix B. As the IPS estimates, various isotropic SC (ISC) approximations can be obtained with considering the various sets of reference phases $(a, b, \dots)$ that result from some preliminary homogenization level(s) on the constitutive phases $(p, q, \dots)$. Remarkably, it is shown in the Appendix C that for two-phase materials and in the isotropic case, the ISC estimate can be also written under a form similar to the IPS estimate in (15), say

$$\boldsymbol{C}^{*\mathrm{ISC}}_{a,b} = \langle \boldsymbol{C} \rangle + (\boldsymbol{C}^{*\mathrm{ISC}}_{a,b} - \boldsymbol{C}_a) : \boldsymbol{t}^{\mathrm{Sph}}_{\boldsymbol{C}^{*\mathrm{ISC}}_{a,b}} : (\boldsymbol{C}^{*\mathrm{ISC}}_{a,b} - \boldsymbol{C}_b) = (\boldsymbol{S}^{*\mathrm{ISC}}_{a,b})^{-1} \tag{16}$$

Equation (16), as a particular form of the ISC approximation for two-phase material not found in the literature to the authors knowledge, provides when comparing with the IPS estimate in (15) new insights of interest with regard to phase cocontinuity representations. For any phase number $n-1$, the generally implicit ISC estimate is fast calculated iteratively from an explicit one such as (1), using an arbitrary initial admissible matrix as the n-th phase. For two phases, one verifies that it can be also fast iterated from the IPS explicit estimate of (15) that converges to the form of (16)[5]. The new insight from comparing (15) and (16) can be put as follows: the SC approximation treats the two-phase material as a three-phase structure where a matrix of infinitesimal volume fraction (the reference medium) embeds the two types of grains. While in the ISC approximation the reference medium (the infinitesimal matrix) is the homogeneous equivalent material itself, in the IPS estimate, (15) identifies the third phase reference matrix to be a Voigt-type (V) structure of the complementary composite $]a, b[$. A comparison of (15) with (16) conversely provides for the IPS estimate the form which enters the general expression reported in (1) as

$$\boldsymbol{C}^{*\mathrm{IPS}}_{(a,b)} = \{\boldsymbol{C}\} - \Big(\Big(c_a \big((\{\boldsymbol{C}\} - \boldsymbol{C}_a)^{-1} - \boldsymbol{t}^{\mathrm{Sph}}_{\{\boldsymbol{C}\}} \big)^{-1} + c_b \big((\{\boldsymbol{C}\} - \boldsymbol{C}_b)^{-1} - \boldsymbol{t}^{\mathrm{Sph}}_{\{\boldsymbol{C}\}} \big)^{-1} \Big)^{-1} + \boldsymbol{t}^{\mathrm{Sph}}_{\{\boldsymbol{C}\}} \Big)^{-1} \tag{15}$$

The similarity established here allows a sound understanding of why the IPS estimate has a strong legitimacy to represent structures having (no matter how) a total cocontinuity of the two phases over the whole range of phase concentration: the reference structure of the IPS is shown to be an aggregate of two phases embedded in an infinitesimal third phase layer of the complementary composite $]a, b[$ arranged into a parallel-like (Voigt-like) mixture of the two phases, where the dilute phase of the bulk is dominant. The consequence is that, considering a highly dilute phase a (resp. b) in the bulk, isolated grains of phase a infinitely far from each other remain connected by the infinitely extended interfacial links in the layer where phase a (resp. b) highly dominates. Conversely, highly concentrated grains of phase b (resp. a) only need a little quantity of phase b (resp. a) in the matrix layer for helping being interconnected.

[5]The same holds for $n > 2$ using the appropriate forms for the IPS- and the ISC-related estimates that we have obtained and are not discussed here

Compared IPS and ISC estimates in terms of phase cocontinuity requests. One second important request for an IPS to be consistent with the cocontinuity of the constitutive phases is for the through-section continuity to be at least partially fulfilled by both phases. For example, planar sections of pure phase p or q are inconsistent with through-section cocontinuity. Planar sections where the phases p and q are arranged in Reuss-type (R) or in HS-type manners are also incompatible with through-section bicontinuity, and so on.

In comparison, making use of an ISC approximation to describe a bicontinuous two-phase medium (p, q) as an aggregate made of grains a and b, requires these grains to be, at least partially, bicontinuous for a possible phase bicontinuity in all proportions though the grain boundaries. Grains of pure phase $(a = p, b = q)$ are consistent with bicontinuity only at comparable proportions of phases (a, b). Grains of Reuss-type effective properties are not relevant at all concentrations because they yield no continuity when the Reuss-type grains dominate. Grain mixtures of HS$(+/-)$ types are consistent with only partial bicontinuity because of the embedded phase part, etc.

In consequence, in order to make the phase cocontinuity possible through material layers in a laminate description or through grain boundaries in an aggregate description, at any phase concentration, we have referred to fiber systems to describe the effective properties of representative layers and grains.

4. The description of the phase cocontinuity from fiber systems

We consider two-phase isotropic materials (p, q) of the reinforced-matrix type, with a part of the p (resp. q) isotropically oriented inclusions being taken as infinite fibers. The presence of such infinite fibers in these "reference reinforced matrices" ensures a cocontinuity of the two (matrix and fiber) phases. Continuous orientation sets of infinite fibers are called fiber systems in general, as illustrated on each side of Figure 3, and isotropic fiber systems (IFSs) in the particular isotropic situations. Assembling

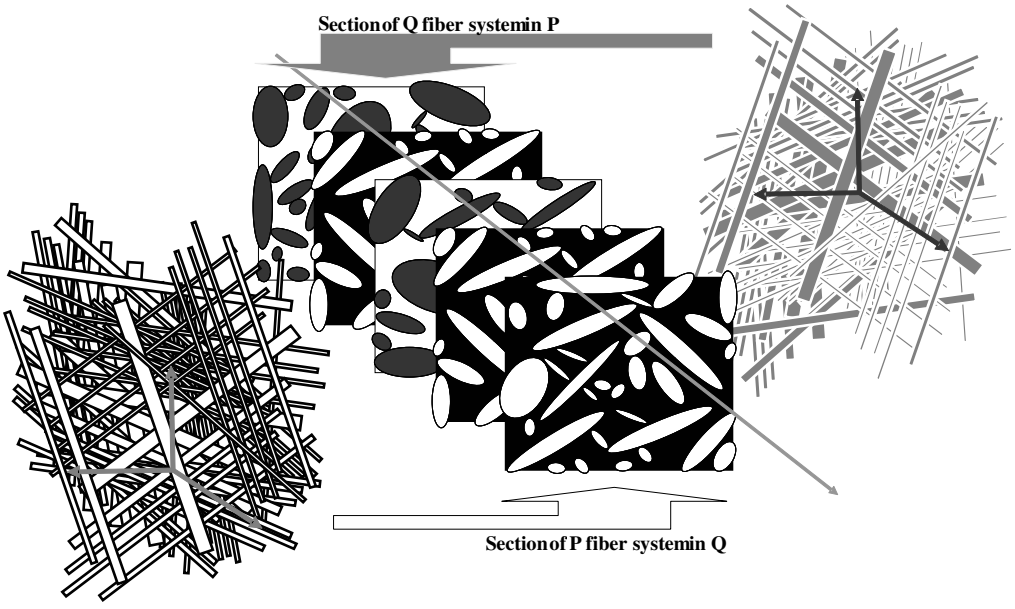

Figure 3. Typical planar sections of isotropic fiber systems.

aggregates of grains of types a and b made of such phase cocontinuous materials ($q \subset p$ for a and $p \subset q$ for b), also ensure long range cocontinuity of the two phases p and q. Now, planar sections of such IFSs are, as drawn in the middle of Figure 3, assemblages of elliptical domains possibly exhibiting all sizes, aspect ratios and orientations. In reconstructed laminations from piling the two types $a(q \subset p)$ and $b(p \subset q)$ of such sections, both phases p and q are possibly continuous between neighboring layers similarly described. Thanks to contacts between surfaces of a same phase p (resp. q), these phase connections across layers a and b allow realizations of continuous arrangements of the phases p and q a priori along all through-layer directions. Consequently, taking sections of IFSs as reference layers in a layer-based homogenization approach of the IPS type or taking grains of IFSs as reference grains in an aggregate approach of ISC type are two descriptions consistent with the possible cocontinuity of the phases throughout the material volume. The so-obtained two estimates from this two-scale procedure will be denoted IPS-IFS and ISC-IFS, respectively.

From their distinct definition or construction, a slight difference distinguishes these two structures and consequently their related estimates. This difference, as made precise later, concerns the limit situations when going either towards null or total phase cocontinuity. Towards null cocontinuity, the difference rests in the amount of residual phase cocontinuity, vanishing to zero in both descriptions but not being rigorously prohibited by construction. A larger residue probably is likely for the layer-based approach. Conversely, towards the total cocontinuity, reintroducing dead branches in the sample spanning clusters of each phase is not rigorously impossible by the structure constructions, either when piling layers of when assembling grains.

Isotropic fiber systems in real materials with two homogeneous phases are realizable in a concentration range that depends on the considered number of fiber directions to realize isotropy. Dendievel et al. [2002] have shown the realizability of fiber arrangements having dodecahedral symmetry (Figure 4a) and it has been established in [Franciosi 2005] how and why finite sets of directions belonging to the dodecahedral-icosahedral symmetry class yield isotropic mean Green operators and consequently isotropic effective properties. Such patterns can be taken as representative of elementary volumes in real fiber systems, as with those exemplified in the middle and right portions of Figure 4. Unavoidable fiber waviness (tortuousness) to reach high fiber concentrations does not much affect the topology of planar sections. The comparison of Figure 3 with Figure 2 shows that the main missing topological properties in our idealized

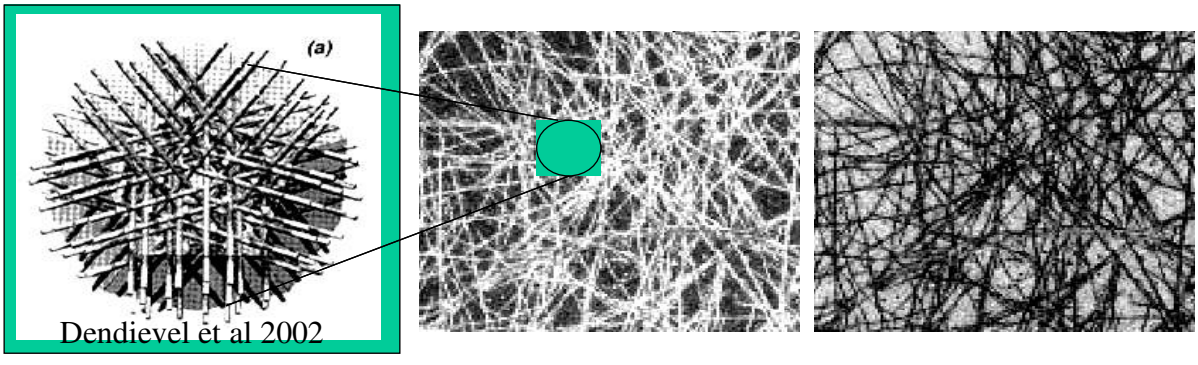

Figure 4. Left: isotropic fiber system built by Dendievel et al. [2002]. Middle and right: real dual 3D isotropic fiber structures.

section description (in addition to the disregarded $p \subset (q \subset p(\cdots))$ multiply embedded patterns) are this nonzero tortuousness of the fibers and the nonconvexity of the 2D bounded domains in the planar sections of real materials. However, we consider that neither one is essential in defining which of the two phases is macrocontinuous in sections. Still, for the sake of simplicity, aside from the infinite cluster of each phase represented by the infinite fibers as assembled, the possibility of finite clusters and of dead branches has been globally accounted for by a volume fraction of spherical (thus embedded) domains, owing to the overall isotropy assumption[6].

4.1. *Effective moduli for generalized IFSs.*

Isotropic fiber systems. The effective moduli for such IFS structures are obtained, following [Christensen 1979a], by "averaging an assigned strain state" over all the positions in space of a directional fiber system, as done for the effective moduli of IPS structures from a laminate. The average over the stresses that results from imposing the same strain in all possible directions with regard to a directional fiber system $\boldsymbol{\omega}$ is taken as equivalent to the stresses obtained when imposing the strain on a material reinforced with an isotropic orientation of fibers. Using (3) with $(a, b) = (p, q)$ and $c_a = f_p$, $c_b = f_q$ as the nominal phase concentrations, the resulting effective moduli for the IFSs upon averaging on $\boldsymbol{\omega} = (\theta, \phi)$ over $\mathbb{R}^3$ read

$$\boldsymbol{C}^{*\mathrm{IFS}}_{p\subset q} = \int_\Omega \frac{\boldsymbol{C}^{*F}_{p\subset q}(\omega)}{4\pi}\,\mathrm{d}\omega, \quad \boldsymbol{C}^{*\mathrm{IFS}}_{q\subset p} = \int_\Omega \frac{\boldsymbol{C}^{*F}_{q\subset p}(\omega)}{4\pi}\,\mathrm{d}\omega. \tag{17}$$

The explicit forms of these IFS moduli result from using the coefficients of Table 2 with the effective moduli of the x_3-oriented fiber systems from (3), for which the GO_ϵ of the x_3-cylinder given in Table 1, top, is introduced. The IFSs are the isotropic superposition of directional $\boldsymbol{\omega}$-oriented fiber systems whose effective moduli $\boldsymbol{C}^{*F(\omega)}_{p\subset q}$ and $\boldsymbol{C}^{*F(\omega)}_{q\subset p}$ are the HS bounds for transversally isotropic material of the ω symmetry axis. As in the platelet case, the average over all $\boldsymbol{\omega}$ directions does not fulfill the inversion property, say

$$\boldsymbol{S}^{*\mathrm{IFS}}_{p\subset q} = \int_\Omega \frac{\boldsymbol{S}*^{F}_{p\subset q}(\omega)}{4\pi}\,\mathrm{d}\omega \neq \big(\boldsymbol{C}^{*\mathrm{IFS}}_{p\subset q}\big)^{-1},$$

although $\boldsymbol{S}^{*F(\omega)}_{p\subset q} = \big(\boldsymbol{C}^{*F(\omega)}_{p\subset q}\big)^{-1}$ (and likewise with $q \subset p$) and the compliance averaging from the request of stress compatibility between the fibers and the entire RVE does not correspond to a characteristic of cocontinuous structures.

Generalized isotropic fiber systems. The generalization of the IFS that is introduced allows the construction of partially (total to null) cocontinuous phase arrangements. We introduce the fraction ϕ_p of the phase p consisting of infinite fibers included in the reference reinforced matrix q, and conversely ϕ_q for fibers q in matrix p. If phase p is included with a nominal concentration f_p, then the fraction of infinite fibers p is $\phi_p f_p$ and it represents the fraction of phase p that belongs to an infinite (sample spanning) cluster; this is the fraction of phase p that carries the applied "loads" and transfers the properties. The complementary fraction of finite (embedded) clusters or dead branches of phase p is $(1-\phi_p) f_p$. These two parts are related to the fraction of clustering and nonclustering (blocking) events, respectively [Torquato 2002]. We call ϕ_p and $1-\phi_p$ the *infinite* and *finite* cluster fractions of phase p, and likewise for phase q; the fractions ϕ_p and ϕ_q are independent and generally different.

[6]The isotropic analysis can be transposed to overall ellipsoidal symmetry for the material.

(i) When all fibers are infinite (total continuity of both phases), one has $\phi_p = \phi_q = 1$ and we denote $\boldsymbol{C}^{*\mathrm{IFS}}_{p|q}$ and $\boldsymbol{C}^{*\mathrm{IFS}}_{q|p}$ as the effective elastic moduli of these maximal IFSs, where the involved two homogeneous phases have moduli C_p and C_q. Taking these "IFS" effective moduli estimates as the effective moduli of the $p|q$ and $q|p$ planar sections of the two-phase material normally to any direction $\boldsymbol{\omega}$ will ensure the through-layers continuity of the p and q phases together with their ensured continuity normal to each $\boldsymbol{\omega}$ by the laminate structure. Any $\boldsymbol{\omega}$-oriented laminate system made of layers of these two phases, say $(a, b) = \begin{pmatrix} \mathrm{IFS} & \mathrm{IFS} \\ q|p & p|q \end{pmatrix}$, has effective moduli given by (2) or by (6) or (11a). The proportion of "phase a" (corresponding to matrix p having a continuous reinforcement of phase q) is $c_a = 1 - c_b$ (resp. b for matrix q continuously reinforced with p). An aggregate made of these two types of grains will also ensure the phase cocontinuity in the whole medium.

(ii) When one of the two phases, p or q, is in the totally embedded situation in the other phase, one has $\phi_p = 0$ or $\phi_q = 0$, respectively, since no infinite fibers exist. The effective properties of the corresponding layers (a) are the isotropic HS (IHS) bounds for the p matrix reinforced with the spherical inclusions taken to globally represent finite isotropic embedded clusters of phase q (resp. b for p in q). The calculation proceeds as in case (i), while taking $(a, b) = \begin{pmatrix} \mathrm{IHS} & \mathrm{IHS} \\ q|p & p|q \end{pmatrix}$ and the appropriate sphere GO_ϵ operator in (3). Effective moduli for laminates made of these two layer types are still given by (2), (6) or (11a). Note that piling sections which have isotropic effective moduli given by $\boldsymbol{C}^{*\mathrm{IHS}}_{p|q}$ and $\boldsymbol{C}^{*\mathrm{IHS}}_{q|p}$ is supposed to account for the limit of no through-section cocontinuity of the phases. However, it does not totally exclude this cocontinuity since in a layer of type (a) considered as embedding isotropic domains, connections with the matrix of phase q in adjacent layers of type (b) can be limit possible situations where single inclusions could link adjacent layers as shown with the small arrows in Figure 5, left. This makes a slight difference between the IPS and the ISC estimates, as defined, since assembling grains with these same $C^{*\mathrm{IHS}}_{p|q}$ and $C^{*\mathrm{IHS}}_{q|p}$ moduli more definitely excludes the cocontinuity of the phases p and q when one of the two phases is in dilute

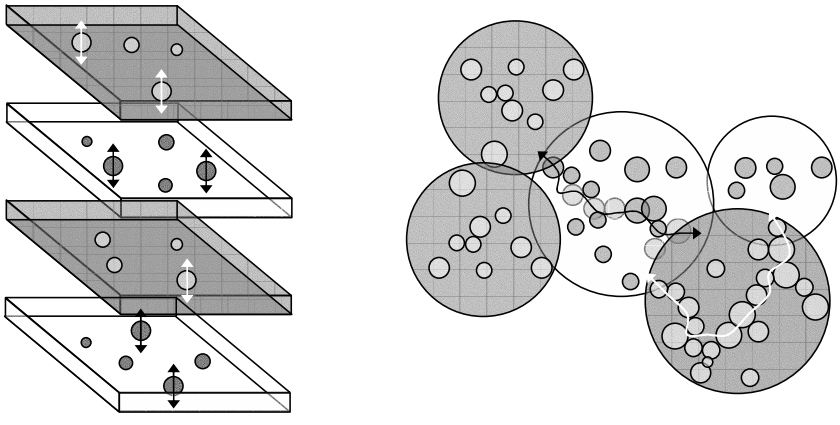

Figure 5. Situations of residual phase cocontinuity in the IPS layered construction (left) and the ISC aggregate construction (right).

concentration: when direct connections between grains of same phase are not enough, cocontinuity through grains of different types a and b would only happen if there exist, as in Figure 5, right, chains of domains q embedded in phase p which are at contact inside grains of type (a) such as to connect, along paths indicated by the arrows, with the matrix q of neighboring grains (b), which has a low probability of happening. This is a similar reasoning which yields to expect more reintroduction of dead branches in piling layers than in assembling grains at the opposite limit of total phase cocontinuity.

(iii) Partial phase cocontinuity possibilities correspond with $0 < \phi_p, \phi_q < 1$. We use a two-step homogenization procedure for successively "embedding" first the finite (spherical) domains that stand for all the finite clusters plus the dead branches and second the infinite fibers. For phase p in q the fraction $\kappa_p = (1-\phi_p) f_p \neq 1 - \kappa_q$ of spheres and the subsequent amount

$$\check{c}_p = \frac{f_p - \kappa_p}{1 - \kappa_p} \neq 1 - \check{c}_q$$

of infinite $\boldsymbol{\omega}$-fibers[7] in the modified matrix $\check{q}$ of moduli $\check{\boldsymbol{C}}_q$ (resp. for phase q in p), one has

$$\check{\boldsymbol{C}}^{*F(\omega)}_{p\subset q} = \check{\boldsymbol{C}}_q - \check{c}_p \big((\check{\boldsymbol{C}}_q - \boldsymbol{C}_p)^{-1} - (1-\check{c}_p) \boldsymbol{t}^{F(\omega)}_{\check{\boldsymbol{C}}_q} \big)^{-1}, \tag{18a}$$

$$\check{\boldsymbol{C}}_q = \boldsymbol{C}_q - \kappa_p \big((\boldsymbol{\Delta C}_{q|p})^{-1} - (1-\kappa_p) \boldsymbol{t}^{\mathrm{Sph}}_{C_q} \big)^{-1}. \tag{18b}$$

The general IFS(ϕ) moduli estimate is then given by

$$\check{\boldsymbol{C}}^{\mathrm{IFS}(\phi p)}_{p\subset q} = \int_\Omega \frac{\check{\boldsymbol{C}}^{*F(\omega)}_{p\subset q}}{4\pi} \, \mathrm{d}\boldsymbol{\omega},$$

as in (17), which corresponds with $\kappa_p = \kappa_q = 0$, say $\check{c}_p = f_p = 1 - \check{c}_q = 1 - f_p$ in (18). The case of null cocontinuity corresponds with $\kappa_p = f_p = 1 - \kappa_q = 1 - f_q$, say $\check{c}_p = \check{c}_q = 0$. The infinite cluster fractions $\phi_i(f_i)$ of each phase (p, q) are similar to the continuous volume fractions of [Lee and Gurland 1978] (see [Ravichandran 1994; Fan 1995]) but are not the same: even when the continuous fractions reach unity, which corresponds with a single (necessarily sample spanning) cluster of each phase, the infinite cluster fraction $\phi_i(f_i)$ may remain smaller than unity because of the possibility of dead branches. But this is a detail.

The parameter $c_a = c^{0<\phi_q<1}_{a\equiv q\subset p}$ is the volume fraction of a phase cocontinuous material where the phase q is more alike a partially continuous reinforcement inside the matrix p than the opposite case (resp. for $c_b = c^{0<\phi_p<1}_{b\equiv p\subset q} = 1 - c_a$ when interchanging p and q). It clearly characterizes the cocontinuity asymmetry for the two phases (p, q) and we here call it the "clustering symmetry factor." In the limit case of no cocontinuity, $\phi_i(f_i) = 0$, it plays the same role of phase continuity inversion (or percolation transition) as the "matricity" parameter introduced by [Leßle et al. 1999], although not defined similarly. From now on, one will mainly examine the IPS-IFS and ISC-IFS estimates with

$$(a, b) = \begin{pmatrix} \mathrm{IFS}\,\phi_q & \mathrm{IFS}\,\phi_p \\ q|p & p|q \end{pmatrix},$$

[7]The second dilution of a volume fraction $\check{c}_p$ of phase p after a first dilution of volume fraction κ_p must match the total value f_p, accounting for the lost part $\check{c}_p \kappa_p$ due to overlapping inclusions (resp. q).

which read, from (15) and (16),

$$\boldsymbol{C}^{*\mathrm{IPSIFS}}_{(a,b,c_a)}(f_p) = \boldsymbol{C}^{\mathrm{IPSIFS}}_{a,b} = \langle \boldsymbol{C} \rangle + (\{\boldsymbol{C}\} - \boldsymbol{C}_a) : \boldsymbol{t}^{\mathrm{Sph}}_{\{\boldsymbol{C}\}} : (\{\boldsymbol{C}\} - \boldsymbol{C}_b), \tag{19a}$$

$$\boldsymbol{C}^{*\mathrm{ISCIFS}}_{(a,b,c_a)}(f_p) = \boldsymbol{C}^{\mathrm{ISCIFS}}_{a,b} = \langle \boldsymbol{C} \rangle + (\boldsymbol{C}^{\mathrm{ISCIFS}}_{a,b} - \boldsymbol{C}_a) : \boldsymbol{t}^{\mathrm{Sph}}_{\boldsymbol{C}^{\mathrm{ISCIFS}}_{a,b}} : (\boldsymbol{C}^{\mathrm{ISCIFS}}_{a,b} - \boldsymbol{C}_b). \tag{19b}$$

The infinite cluster fractions $0 \le \phi_p, \phi_q \le 1$ and the clustering symmetry factor $0 < c_a = 1 - c_b < 1$ may depend on the phase concentrations. The laws $c_a(f_p)$, $c_b(f_q)$ and $\phi_i(f_i)$, $i = p, q$ are expectedly monotonous increasing functions of the phase concentrations, but it is not impossible, as will be seen, to realize structures corresponding with decreasing evolution laws for $c_a(f_p)$, $c_b(f_q)$. The introduced phase continuity parameters are clearly related to phase clustering properties. Their definition is enough to allow measuring them, perhaps with the help of some tools from mathematical morphology and 3D image analysis. The precise relations of these parameters to the microstructural descriptors of systematic theory [Serra 1982; Torquato 2002] call for mathematical developments out of the present scope.

4.2. ***Phase concentration dependency assumptions for the phase continuity parameters.*** Considering phase concentration dependency makes sense in the cases when well-controlled structures can be realized at different phase concentrations without affecting any other property or characteristic. We use empirical forms to identify some general trends from comparisons with various data sets.

(i) For the independent infinite cluster fractions $\phi_p(f_p)$, $\phi_q(f_q)$, we have used

$$\phi_i(f_i) = \frac{\phi_{i0}(\phi_{i1} - \phi_{ik})\left(\dfrac{1-f_i}{1-f_{ik}}\right)^{P_i} + \phi_{i1}(\phi_{ik} - \phi_{i0})\left(\dfrac{f_i}{f_{ik}}\right)^{P_i}}{(\phi_{i1} - \phi_{ik})\left(\dfrac{1-f_i}{1-f_{ik}}\right)^{P_i} + (\phi_{ik} - \phi_{i0})\left(\dfrac{f_i}{f_{ik}}\right)^{P_i}} \quad i = p, q \tag{20a}$$

with, in general, $P_i > 0$ and $0 \le \phi_{i0} \le \phi_{ik} \le \phi_{i1} \le 1$. For all $P_i \ne 0$, the inflexion points have coordinates (f_{ik}, ϕ_{ik}) with $0 \le f_{pk},\ f_{qk} \le 1$. When $P_i = 0$, the partial continuity of the phase is constant at ϕ_{ik}. The $\phi_i(f_i)$ functions are involved as a factor of (f_i). These two parameters should not be phase contrast dependent, which is a characteristic allowing to check the relevancy of their definition.

(ii) For the clustering symmetry factor $c_a(f_p) = 1 - c_b(f_q)$, we have used the similar form

$$c_a(f_p) = \frac{c_{ac}(f_p/f_{pc})^M}{c_{ac}(f_p/f_{pc})^M + c_{bc}(f_q/f_{qc})^M} = 1 - c_b(f_q), \quad f_{pc} + f_{qc} = 1, \quad c_{ac} + c_{bc} = 1 \tag{20b}$$

For all $M \ne 0$, the inflexion point has coordinates $f_{pc} = 1 - f_{qc}$, $c_{ac} = 1 - c_{bc}$. When $M = 0$, the value of c_{ac} fixes the estimate position between the limits IFS(ϕ), for all f_{pc}. When $M > 0$, the transition is from the lower limit to the upper one, and the opposite occurs for $M < 0$. The larger is the value of $|M|$, the sharper the inversion of the cocontinuity symmetry at that point. The variation of this clustering symmetry factor form can be expected to be dependent of the phase contrast because in our two-scale homogenization scheme, it interconnects intermediate IFS(ϕ) phases ($\boldsymbol{C}_a$, $\boldsymbol{C}_b$) which are not of constant microstructures (as they are made from mixing the constitutive ones (p, q) with concentration-dependent $\phi_p(f_p)$ and $\phi_q(f_q)$ continuity characteristics).

5. Result comparisons with numerical and experimental data

The so-defined generalized IFS(ϕ) estimates are taken for the effective properties of the two representative layers in IPS descriptions for two-phase materials from (19a). They are taken as well for the effective properties of the two representative spherical domains in isotropic self-consistent (ISC) descriptions of the same materials from (19b). Note that planar sections of such two-phase aggregates are 2D patchworks of the same two types of domains as those directly introduced in the layer-based approach. The IFS aggregate is expected to be phase cocontinuous at all concentrations provided $\phi_p, \phi_q \neq 0$, as both grain types are phase cocontinuous in that case. The IPS that reassembles sections of IFS aggregates is also expected to be phase cocontinuous at all concentrations when $\phi_p, \phi_q \neq 0$ but possibly with some residual bicontinuity when $\phi_p = \phi_q = 0$ in the layers, as described in Figure 5, and similarly some dead branches are reintroduced when $\phi_p = \phi_q \to 1$. It will be shown, indeed, that the two obtained IPS-IFS and ISC-IFS estimates are identical for the various examined structures when phase bicontinuity in the IFSs is significant and high (no apparent difference towards total bicontinuity), while in situations of vanishing bicontinuity in the IFSs, the ISC estimate involving IHS grains is slightly sharper than the IPS estimate using IHS layers.

Table 3 presents the genealogy of the calculated and compared estimates that are linked in columns from the phase pairs (a, b), the pair Voigt–Reuss(a, b), the pair IHS(+/-)(a, b) and the pair IFS(+/-)(a, b). The estimate from (13) for the aggregate of laminates denoted "ISCP" has been placed in a remaining free cell of the table. The total number of examined estimates is 15, including some cases that have been pointed out as inconsistent with the possible cocontinuity of the phases (namely, the IPS estimates combining either V and R layers or IHS$(+/-)$ layers, and the ISC estimates combining either V and R grains or IHS$(+/-)$ grains). The analytic expressions for the effective shear modulus in the incompressible case (for the two phases a, b) are summarized in Appendix C for the IFS, IPS, IHS and ISC estimates, plus, as a sixteenth estimate, the dual IPS one from the compliance approach of (11b). Typical curves for all of the IPS and ISC estimate types that have been considered are plotted in the left and middle

a/b	VR(a, b)	isotropic HS(a, b)	fiber HS(a, b)
ISC[P$\omega(a, b)$]			isotropic FS[FHS(a, b)]
laminate $[a/b]$	laminate [VR(a, b)]	laminate [IHS(a, b)]	laminate [IFS(FHS(a, b))]
isotropic PS[L(a, b)]	isotropic PS[L(VR(a, b))]	isotropic PS[L(IHS(a, b))]	isotropic PS[L(IFS(FHS(a, b)))]
isotropic SC$[a, b]$	isotropic SC[VR(a, b)]	isotropic SC[IHS(a, b)]	isotropic SC[IFS(FHS(a, b))]

Table 3. Genealogy of the 15 estimates performed. and notations. VR = Voigt–Reuss; HS = Hashin–Shtrikman; FHS = fiber HS = HS bounds for (a,b) 1D-fiber structures; FS = fiber systems; L = laminate structure; PS = platelet Systems; SC = self-consistent estimate; IHS, IFS, IPS, ISC = isotropic HS, FS, PS, SC.

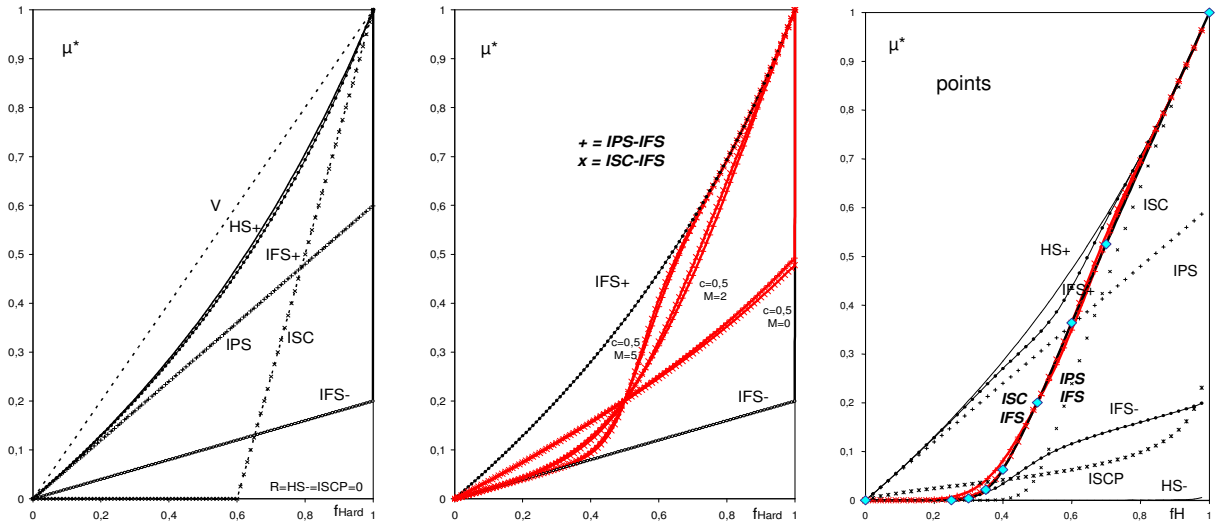

Figure 6. Comparison of moduli estimates for porous materials. Left: estimates not involving (20). Middle: IFS limits and related IPS-IFS and ISC-IFS estimates for $M = 0$, $M = 2$, and $M = 5$. Right: Matching the FFT estimate for a point structure with the IPS-IFS and ISC-IFS estimates.

portions of Figure 6 for an incompressible two-phase material with a void phase, say ($\nu_p = \nu_q = 0.5$), ($\mu_q/\mu_p = 0$). To save space, the rightmost part of Figure 6 reports with some anticipation the match of the IPS-IFS and ISC-IFS estimates with an FFT calculation on a simple point structure in the case of nearly zero contrast: $\mu_q/\mu_p = 5 \times 10^{-5}$ (see Figure 7, left, on page 749, for an illustration).

Figure 6, left, shows plots of the 9 estimates obtained from the pure phases (p, q), namely, the V/R bounds and the two IHS bounds, the IPS, the ISC and the ISCP estimates and the two IFS limits at $\phi_p = \phi_q = 1$. The upper IFS estimate, $\mu_{\mathrm{IFS}(+)} = (1 + \frac{1}{5} f_q) f_p \mu_p/(1 + f_q)$, is closely below the upper IHS bound $\mu_{\mathrm{IHS}(+)} = 3 f_p \mu_p/(3 + 2 f_q)$. The nonzero lower IFS estimate, $\mu_{\mathrm{IFS}(-)} = \frac{1}{5} f_p \mu_p$, is far above the IHS lower bound that is zero when $f_p \neq 1$. The IPS estimate, $\mu_{\mathrm{IPS}} = \frac{3}{5} f_p \mu_p$, is between the two IFS limits in all of the phase concentration range, going from the upper IFS limit to the lower one. From Appendix C, μ_{IPS} and $\mu_{\mathrm{IFS}(-)}$ make a singular jump from respectively $\frac{3}{5}$ and $\frac{1}{5}$ to 1 at $f_p = 1$. When the phase q is a void phase, neither the ISC estimate (which is linear from 0 to μ_p between $f_p = \frac{2}{5}$ and 1) nor the ISCP estimate (which goes to zero at all concentrations $f_p \neq 1$) remain between the IFS limits for all concentrations or for all contrasts.

The dual IPS estimate from the arithmetic mean over compliances, not plotted but given in Appendix C, also remains close to the IHS lower bound and goes to zero in the void phase case. Figure 6, middle, illustrates the flexibility of the two IPS-IFS and ISC-IFS estimates by reporting a typical case of no phase concentration dependency ($M = P_1 = P_2 = 0$, $c_{ac} = c_{bc} = 0.5$, $\phi_{pk} = \phi_{qk} = 1$) and examples of phase concentration dependency for $M = 2$ and $M = 5$. They correspond to the cases denoted by 000 and MPP in Table 4 (page 751), which summarizes all of the parameter values for the performed calculations presented next. The same graph also shows the close proximity of these two estimates arising from two different routes in a few representative cases. The simultaneous match, in Figure 6, right, of the

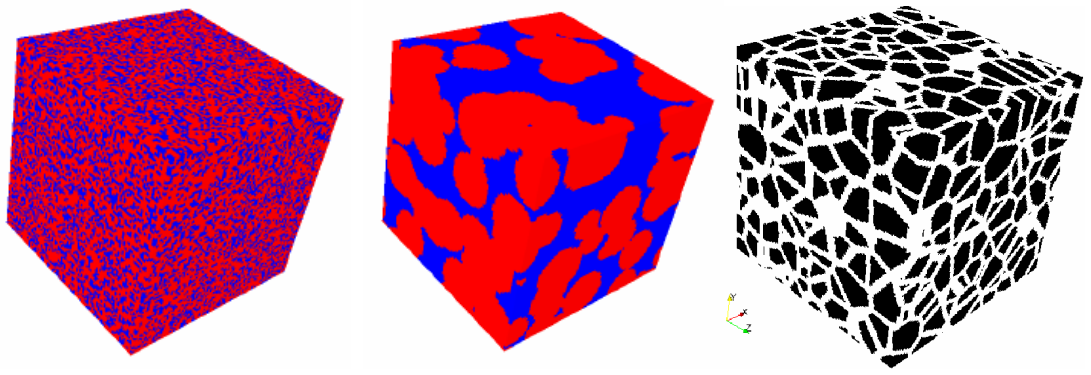

Figure 7. Numerical structures of random points (left), overlapping spheres (middle), and Voronoi cells (right).

IPS-IFS and ISC-IFS estimates with the FFT calculation for the point structure, has needed the use of nonconstant ϕ functions ($P_i = 4$); this is because, as expected, point structures are only bicontinuous in the range of comparable concentrations of the two phases, with the continuity of each phase increasing with its concentration. The already-marked stiffness of the ISCP estimate at this still high contrast, compared to the still nearly zero IHS lower bound, is noteworthy. Figures 7, 8 and 9 illustrate the various numerical or real structures for which available moduli calculations or measurements have been compared to the proposed IPS-IFS and ISC-IFS estimates and to some of the other ones. Figures 10–13 report the performed estimate comparisons of the (shear or Young) effective moduli.

5.1. ***Structure types investigated.*** The three parts of Figure 7 show numerical structures obtained by random point processes. The elementary cube has 128^3 voxels. In the point structure of Figure 7, left, the point number is directly the second phase volume part. In the middle figure, they are the centers of overlapping spheres having all the same radius. In the rightmost figure they are cell centers from which Voronoi structures with different wall thicknesses are built. The overlapping sphere arrangement is known to have a quite large and asymmetric domain of cocontinuity (from 0.30 to 0.95, approximately). The phase contrast inversion matters in this case. This sphere structure is varied in concentration by modifying the sphere radius. The Voronoi cell structure is expected to have, at all phase concentrations, a continuous wall phase separating polyhedral inclusions, without any bicontinuity. The phase concentration is varied by changing the wall thickness and the grain number. If holes happen in walls that are too thin, such Voronoi structures can turn into bicontinuous ones. Piercing or removing walls is a way to create bicontinuous structures.

The parts of Figure 8 present the different phase arrangements obtained from a Poisson–Voronoi tessellation process. Figure 8, left, is obtained by removing the cell faces in a Voronoi structure, just keeping the edges and vertices that remain connected into a continuous second phase reinforcement. This is typically a bicontinuous structure that is expected to be totally bicontinuous (TBi). When the walls are too thin (middle figure), edges can be broken when removing the faces, which yields partial bicontinuity (dead branches in the continuous reinforcement) and possibly a phase continuity inversion with a connected matrix including discontinuous reinforcements (PBi/I). When conversely the walls are too thick (right figure), edges and vertices dominate and there are not enough face points left to connect

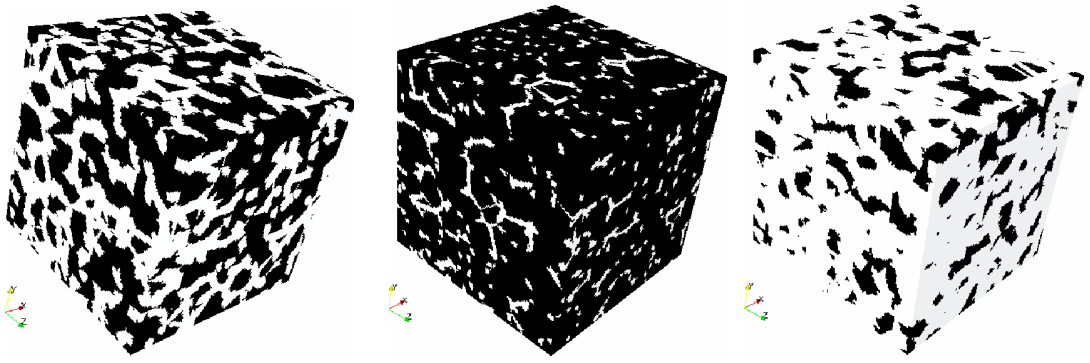

Figure 8. Bicontinuous structures. Left: removing wall faces of Voronoi cells. Middle: partial or inverted phase continuity if thin wall edges have been broken. Right: Voronoi type if walls are too thick.

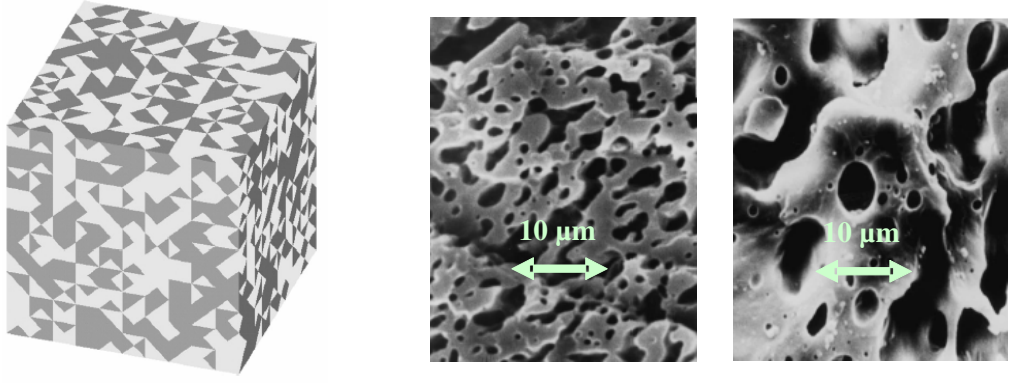

Figure 9. Left: numerical bicontinuous structure of [Chen et al. 2008]. Middle, right: PS and PP bicontinuous polymer blends prepared and examined by Veenstra et al. [2000].

the cell phase by piercing the walls. The structure remains of the Voronoi cell structure type, with only some finite clusters of connected cells and no bicontinuity. Estimates for Voronoi cell structures are not reported.

Figure 9 illustrates some examined structures taken from the literature. The diagram on the left, from [Chen et al. 2008], is a numerical structure of the nonparticulate type created from a random point process that results in an intermediate range of phase bicontinuity. FEM calculations of the effective Young modulus have been reported for moduli values given to the phases that are typically those of an epoxy-glass mixture ($\mu_p = 1,26\,\text{GPa}$, $\nu_p = 0.35$), ($\mu_q = 30\,\text{GPa}$, $\nu_q = 0.22$). The other two parts of Figure 9 are views of two types of polymer blends prepared and investigated by Veenstra et al. [2000]. The two materials (PS and PP for, respectively, blends of polyethylene with poly(ether-ester) and blends of polypropylene with styrene (ethylene-butylene)) exhibit a phase cocontinuity domain of variable extent where their structures are typically sponge-like, as exemplified in the figure. For comparisons with the two PS blends (denoted PSi and PSs), we used $E_p^{\text{PS}} = 2800\,\text{MPa}$, $E_q^{\text{PS}} = 48\,\text{MPa}$, and for the two PP

blends (PPi and PPs), we used $E_p^{\mathrm{PP}} = 1000\,\mathrm{MPa}$, $E_q^{\mathrm{PP}} = 3\,\mathrm{MPa}$. Since the phase Poisson ratios were not given, we used an arbitrary homogeneous value, which does not matter because the Young's and shear moduli are proportional then. However, the assumption of the same Poisson ratio for both phases makes these comparisons more uncertain. The estimates for these structures are reported versus the hard (PS or PP) phase concentration.

5.2. *Main results and discussion.*

Estimated effective moduli and comparisons. According to the case, either the estimated effective shear modulus or the effective Young's modulus (normalized in the case of Chen data) has been reported for the various mentioned models. Most of the calculated moduli estimates for the structures of Figure 7 and 8 assume the same incompressible phases $\nu_p = \nu_q = 0.5$ with a contrast ($\mu_q/\mu_p = 4 \times 10^{-3}$) for the shear moduli. Some calculations with a weaker or a higher contrast for the phase shear moduli (between 0.1 and 0) were also performed for further discussion. For comparisons, the shear effective modulus was calculated by using the FFT method as detailed in [Brenner et al. 2009] for its implementation. For the IPS-IFS and ISC-IFS estimates, we collect in Table 4 the phase continuity parameters involved in (20) that have provided a good match with the compared data sets. No numerical algorithm of fitting parameter identification has been called for because our discussion purpose does not need a perfect matching.

	Figures		M	f_{ac}	c_{ac}	P	$\phi_{\min}$	$\phi_{\max}$	ϕ_k	f_{pk}	f_{qk}
REF 000		6 middle	0		0.5	0	0	1	0.5		
REF MPP		6 middle	2 and 5	0.5	0.5	4	0	1	0.5	0.5	0.5
FFT PTS	7 left	6 right	3	0.45	0.5	4	0	1	0.5	0.45	0.45
Match ISC		10 left	2	0.5	0.5	9	0	1	0.5	0.5	0.5
Match IPS		10 middle	−0.33	0.5	0.8	0	1	1	1	0.5	0.5
Match ISCP		10 right	−0.25	0.5	0.5	1	1	0	0.5	0.5	0.5
FFT h SPH	7 middle	11 right	1.5	0.65	0.5	1.5	0	1	0.5	0.65	0.65
FFT s SPH	7 middle	11 middle	1.5	0.35	0.5	1.5	0	1	0.5	0.35	0.35
FFT vo SPH	7 middle	11 left	2.1	0.35	0.5	1.5	0	1	0.5	0.35	0.35
FEM CHen	9 left	12 left	1.5	0.6	0.7	5	0	1	0.5	0	0
FFT TBi	8 middle	12 middle	0.5	0.7	0.7	1.5	0.25	0.75	0.5	0.5	0.5
FFT PBi/I	8 right	12 right	2	0.5	0.5	3	0.25	0.75	0.5	0.5	0.5
Exp VE PSi	9 middle	13 top left	5	0.45	0.5	3	0	1	0.5	1	1
Exp VE PSs	9 middle	13 top right	4	0.3	0.5	3	0	1	0.5	0.7	0.9
Exp VE PPi	9 right	13 bottom left	0.4	0.97	0.7	10	0	1	0.5	0.5	0.6
Exp VE PPs	9 right	13 bottom right	0.3	0.97	0.7	15	0	1	0.5	0.45	0.55

Table 4. Coefficients for the IPS-IFS and ISC-IFS moduli estimates to match with compared data and notation (the columns P, $\phi_{\min}$, $\phi_{\max}$, ϕ_k refer to both phases). For REF 000 and REF MPP, see page 748. ISCP = ISC estimate on PS systems from (13). TBi/PBi = totally/partially bicontinuous (see page 749). PTS = point structure. EXP VE PS(i/s)/PP(i/s) = experimental data on polymer blends from [Veenstra et al. 2000]. FEM CHen = numerical data from [Chen et al. 2008]. (h/s/vo) SPH = hard/soft/void-like spherical inclusions.

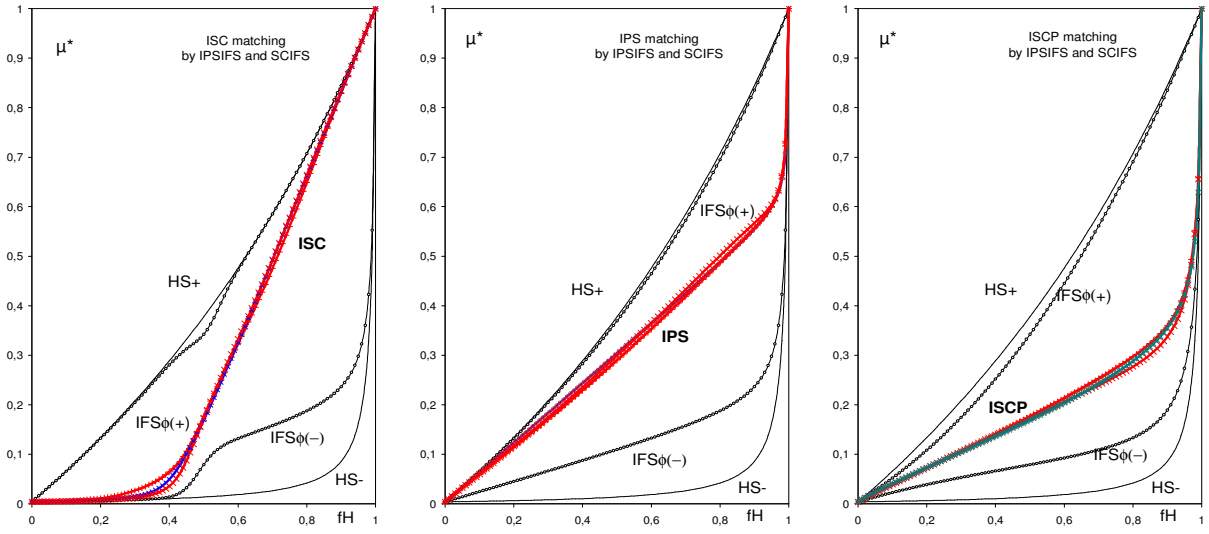

Figure 10. Matching the ISC, ISCP and IPS estimates with the IPS-IFS and ISC-IFS ones.

Figure 10 compares the ISC, IPS and ISCP analytical estimates with the IPS-IFS and ISC-IFS ones adjusted with an appropriate set of parameters. These comparisons provide preliminary information about the ranges of parameter values to be explored according to the case. In particular: the ISC estimate is of the types of reference MPP reported in Figure 6, middle, and it is not much different from the point structure (Figure 6, right) considering statistical fluctuations; the IPS estimate that goes from the upper IFS limit to the lower one is matched by using a negative value for the power M and by keeping the ϕ_i functions constant and equal to unity (total constant cocontinuity); the ISCP estimate is also matched with using a negative M value while furthermore making the ϕ_i functions to decrease from unity to zero, as if corresponding to the dilute phase gaining total continuity when vanishing while the dense one has vanishing continuity when approaching unity. This can be understood as going towards a zero phase concentration under the form of a vanishing but still sample spanning and total cluster.

Figure 11 shows a comparison with the FFT computations on the sphere structures of Figure 7, middle, considering two different phase contrasts for the soft sphere case in a hard matrix (left and middle) and the dual structures with soft and hard spheres (middle and right). Figure 12, left, reports the estimates that match the FEM calculations of [Chen et al. 2008] for the numerical (point-like) structure of Figure 9, left, (normalized Young's moduli), a case of moderate phase contrast ($E_q/E_p \approx 0.045$). The remaining two parts of Figure 12 report the estimate for the structures of the corresponding parts of Figure 8, compared with the FFT calculations. The four parts of Figure 13 match the estimates with the measured values for the PSi, PSs, PPi, and PPs blends from [Veenstra et al. 2000], corresponding to the last two parts of Figure 9. The contrasts, respectively, are $E_q/E_p \approx 0.015$ and $E_q/E_p \approx 0.003$. The concentration ranges of cocontinuity experimentally estimated are respectively 0.5–0.6, 0.3–0.6, 0.5–0.6 and 0.4–0.8, say: larger for the (s) samples than for the (i) ones.

Figure 11 and 12 (parts a and c) show estimates of the reference MPP type, corresponding to a bicontinuity domain between two domains where the dilute phase is expected to be embedded in the concentrate one. Note that the two dual sphere structures (last two parts of Figure 11) are nicely fitted

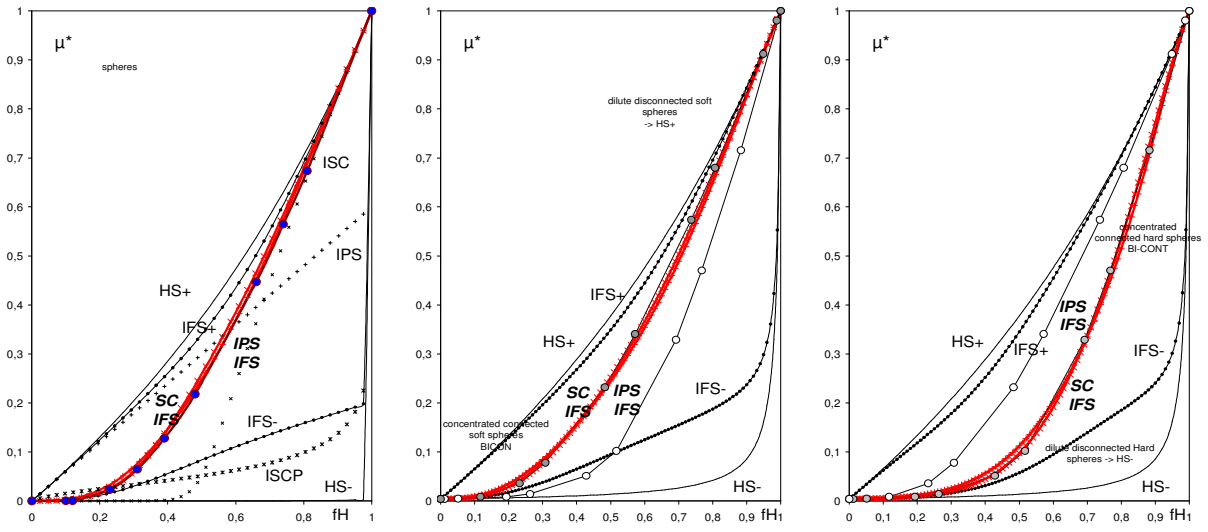

Figure 11. Matching FFT calculations with the IPS-IFS and ISC-IFS estimates for the sphere structure. From left to right: void-like, soft, and hard spheres.

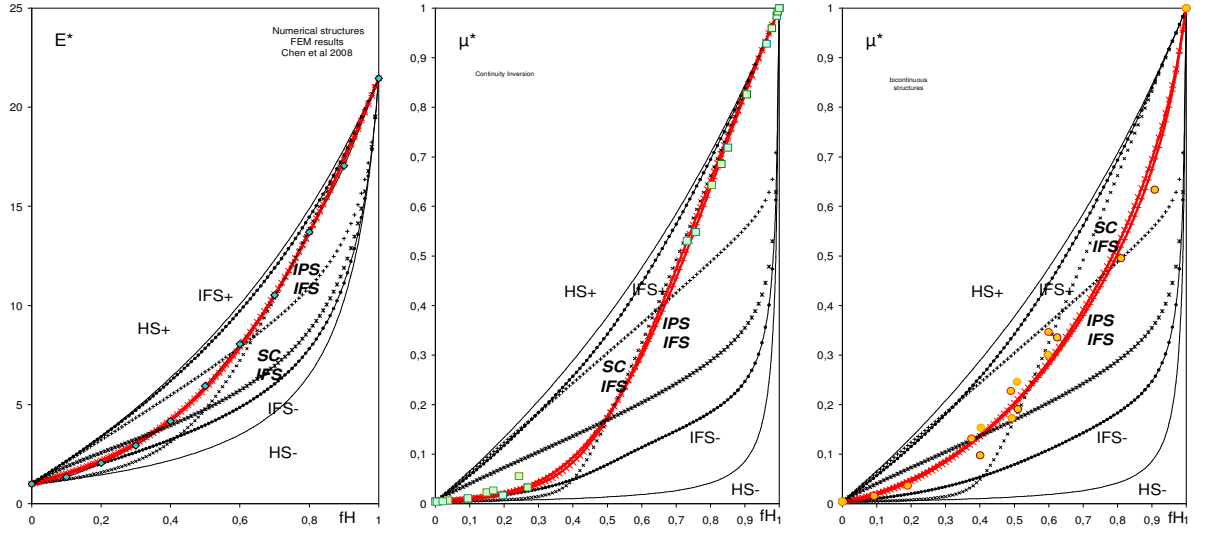

Figure 12. Left: matching the numerical FEM calculations of [Chen et al. 2008, Figure 3] with the IPS-IFS and ISC-IFS estimates. Middle and right: matching the FFT calculations for totally and partially bicontinuous Voronoi-based structures with the IPS-IFS and ISC-IFS estimates.

by the same parameter set, only inverting the value of the critical concentrations (0.35 / 0.65) in (20a) and (20b). The case of Figure 12, middle, although of the same structure type, corresponds to a smaller M value and some other distinct parameter values. In all of these cases, the IFS(ϕ) domain that limits the data set is regular thanks to a low value of P in (20b), as collected in Table 4.

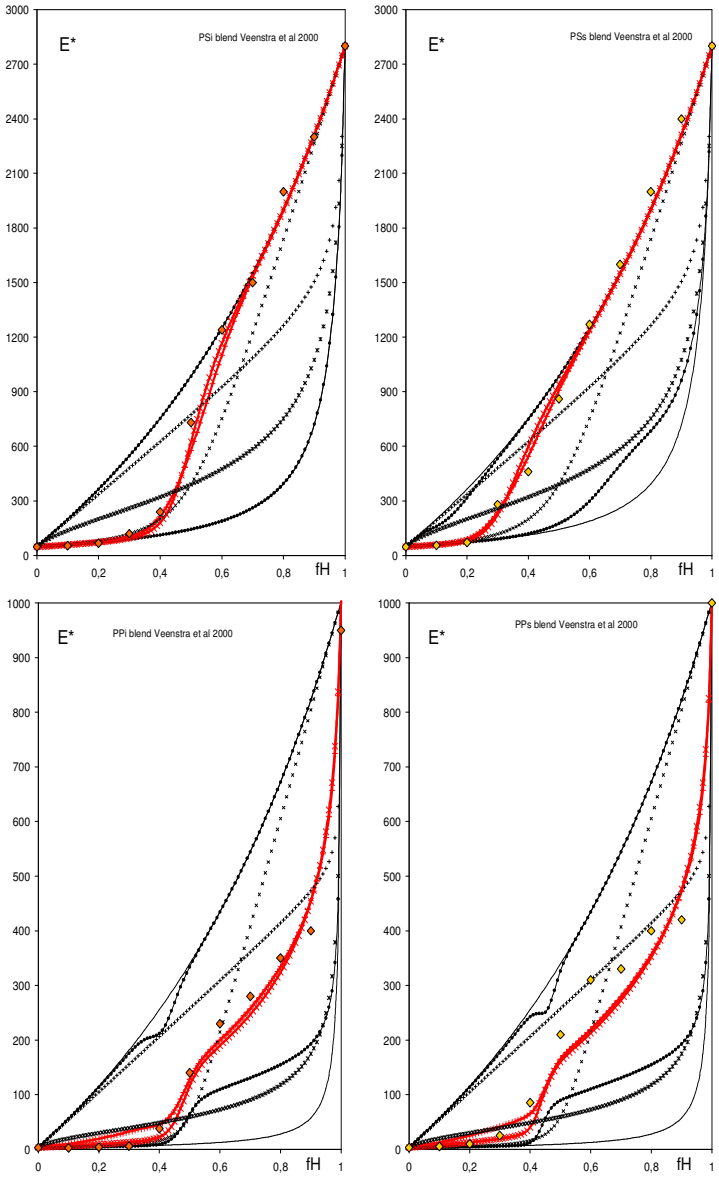

Figure 13. Matching the blend data of [Veenstra et al. 2000, Figure 3] with the IPS-IFS and ISC-IFS estimates. Top row: lower and upper data of Figure 3, left. Bottom row: lower and upper data of Figure 3, right.

The PS and PP polymer blends exhibit two radically different situations compared to the previous ones. For the PS case, the match of the data again corresponds to a typical MPP curve, although with a higher M value (of 5 and 4, respectively, for cases PSi and PSs), in order to give an S shape to the curve corresponding to $M = 5$, as in Figure 6, middle. The PP blends show the particularity of a modulus "jump" when approaching a zero weak-phase concentration, while the PS blends do not. For this PP

case, the "best match" of the data we have obtained with (20), which is not as good as in the other cases, corresponds with a very different set of parameters. In particular, the S shape that has been given to the ϕ curves of (20b) has used high P values and low M values, with inflexion points very far from symmetrical. Although the compared experimental data for PP blends are more uncertain than the other data (at dilute concentrations of the hard phase, some points are not even between the V/R bounds), such a jump to 1 of $\phi_p(f_p)$ when f_p approaches 100% is in agreement with still partial continuity (dead branches) of the hard phase when dense and persisting up to the total vanishing of the soft phase. It is interestingly a case for which the Christensen's IPS estimate appears quite convenient for a dominant volume fraction of the hard phase what means a still significantly continuous soft phase when dilute, especially for the PPs case that exhibits the largest concentration range of phase of bicontinuity. This IPS estimate is thus proved possibly relevant for this type of materials with cocontinuous phases. It is also noteworthy that for these parameter sets in the PP cases, a quite marked difference appears between the IPS-IFS and ISC-IFS estimates in the domain of dilute hard phase, where the estimates remain more of the IPS-IHS and ISC-IHS type ($\phi_p, \phi_q \approx 0$), with nearly no cocontinuity in the representative layers or grains (as described by the high values given to P and to f_{pc}). Accordingly with the difference in their definitions, the IPS-IFS estimate appears smoother than the ISC-IFS, likely in relation to some maintained phase bicontinuity. At the other end, when assuming total continuity by $\phi_p = \phi_q = 1$, one could expect for the same reason of construction difference some more dead branches being reintroduced in piling layers than in assembling grains, but one does not observe a significant difference between the IPS-IFS and the ISC-IFS estimates then. This yields to considering the IPS-IFS estimate as a smoothed version of the ISC-IFS one, especially when the infinite cluster fractions ϕ_p, ϕ_q approach either 0 or 1.

Phase contrast dependency. We end with these comparisons by checking whether the parameters in (20) depend on the phase contrast or not. As far as they represent morphological characteristics, they should be insensitive to the phase contrast in all the cases where the phase composition do not change with the phase concentration and arrangement. In that respect, the phase concentration dependency of the infinite cluster fractions $\phi_p(f_p)$ and $\phi_q(f_q)$ from (20a) that characterizes the morphology of the individual phases is not expected sensitive to phase contrast, oppositely with the variation of the clustering symmetry factor from (20b).

Using the set of parameters given in Table 4, the ISC, IPS and ISCP analytical curves and the FFT results for the soft sphere structure have been matched with the IPS-IFS and the ISC-IFS estimates for different phase contrasts ranging between 0.1 and 0.00005. The net result is that the match remained of similar accuracy, by only modifying the M exponent in (20b) as shown in Figure 14, where the logarithmic plot looks linear, and all other parameters that concern (20a) remaining unchanged[8]. Reporting the miscellaneous data for M corresponding to other calculations with a single available contrast case confirms that the Chen et al. data, the PBi/I data and the ISC plot are similar to the point-structure data type. Going towards an increase of bicontinuity, as the sphere structures and the totally bicontinuous (TBi) structures, seems to correspond with a lower but still positive M value. Negative M values for the IPS and ISCP estimates may also correspond to realizable bicontinuous structures, as with aggregates of laminate domains. In terms of M value, the PP blends are on the side of the bicontinuous structures, while the PS ones are quite far above all estimates.

[8]Also the inflexion point (f_{pc}, c_{ac}) can need a slight adjustment when the phase contrast becomes weak.

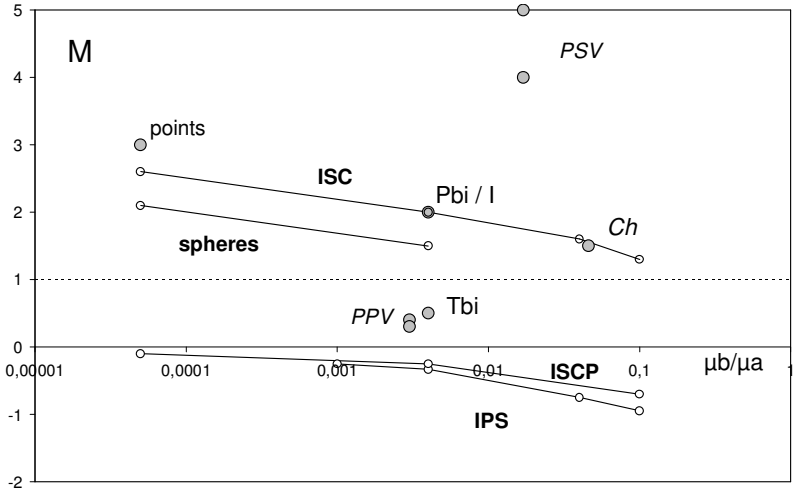

Figure 14. The variation of the M parameter with phase contrast for the different estimates.

The PP and PS blend cases warn that one cannot only compare the M parameter in order to classifying the structure types but this comparison nevertheless provides interesting information on the different possible types of phase cocontinuous structures.

Without going more deeply into the details here, it appears from these elements that some typical trends of phase cocontinuity show up for the different microstructures that have been examined through the presented two not much different modeling schemes. The parameter sets that provide a good match with the available data are related to cluster characteristics and percolation features of the phases, here called the infinite cluster fractions and the clustering symmetry factor. They are measurable quantities but remain to be connected appropriately to the microstructural descriptors. The fact that one nearly obtains by two routes using the same representative domains of IFS estimates, the same estimate for the considered bicontinuous structures can be taken in favor of the relevancy of the given description to the representative, layers or grains, domains. While the ISC-IFS estimate is implicit owing to the SC approximation level in it, the layer-based IPS-IFS estimate remains explicit. Towards null phase bicontinuity, the layer-based approach yields a slightly smoother estimate than the aggregate one, likely related to a residual phase cocontinuity not totally excluded in the layer approach. Conversely, total phase cocontinuity in layers does not either totally exclude the reintroduction of dead branches when assembling the layers, but there is no noticeable difference between the two estimates in that case. These modeling schemes, which have been presented in details in the elasticity formalism in specifying which application restrictions should be kept in mind in the mechanical field, also hold to estimating physical effective properties in all situations for which the homogenization framework holds. The calculation of the IFS estimates is possible for any phase number, and so are the IPS-IFS and ISC-IFS estimates when following the same procedure as for two phases. As will be soon presented elsewhere, (19) can be directly applied to arrangements of isotropic phases in ellipsoidal overall symmetry while using the appropriate operator for the characteristic ellipsoidal shape. They also likely apply as written in the cases of anisotropic structures involving anisotropic phases, as the morphological background to account for phase continuity features remains unchanged.

6. Conclusion

We have proposed, within the homogenization framework, a modeling scheme which aims at estimating the effective properties of heterogeneous materials which exhibit a diversity of phase cocontinuity features for several of their constitutive phases. For mechanical properties, our approach is restricted to the study of elasticity properties in the unloaded limit and to materials whose structural behavior under load is not essentially governed by bending or torsion features. The modeling results from the use of a generalization of the so-called fiber systems combined within either a layer-based or an aggregate-like approach to describe the material structure and on the introduction of phase clustering characteristics as phase continuity and cocontinuity parameters. As shown for two-phase materials in the isotropic elastic formalism, the two obtained estimates are very close to each other for all examined microstructures over the whole phase concentration range where they present significant phase bicontinuity and regardless of the phase contrast. In situations when the phase cocontinuity is weak or null, the layer-based estimate appears to be slightly smoother than the aggregate-based one because of some residual phase cocontinuity not totally excluded by the estimate construction. The various performed comparisons with the experimental and numerical data from the literature and with the FFT calculations performed on different numerical microstructures have shown the high flexibility of the modeling and its ability to consider phase cocontinuity characteristics of a large variety of situations. Since, as stressed from the introduction, platelet (or laminate), aggregate and fiber systems can be defined for multiphase materials whose phases are of general property anisotropy and are assembled according to an ellipsoidal overall symmetry, as being presented in a separate work, the application domain of the two proposed estimate types can be extended accordingly.

Appendix A. Platelet Green operators and moduli and compliance tensors for laminates

The fundamental property of the platelet strain Green operator. From [Walpole 1981], one has

$$\big(\boldsymbol{I} - t^P_{(p)}(\omega) : (\boldsymbol{C}^p - \boldsymbol{C}^q)\big) : \big(\boldsymbol{I} - t^P_{(q)}(\omega) : (\boldsymbol{C}^q - \boldsymbol{C}^p)\big) = \boldsymbol{I} \tag{A.1}$$

for any two phases p, q and any direction $\boldsymbol{\omega}$ in space. This property also corresponds to

$$\boldsymbol{I} = \big(t^P_{(p)}(\omega) : (\boldsymbol{C}^p - \boldsymbol{C}^q)\big)^{-1} + \big(t^P_{(q)}(\omega) : (\boldsymbol{C}^q - \boldsymbol{C}^p)\big)^{-1} \tag{A.2}$$

Thus allows one to write, for all $f_q = 1 - f_p$, the equality $\boldsymbol{C}^{*P\omega}_{q\subset p} = \boldsymbol{C}^{*P\omega}_{p\subset q}$ for a two-phase laminate as

$$\boldsymbol{C}^p - f_q\big((\boldsymbol{C}^p - \boldsymbol{C}^q)^{-1} - f_p t^P_{(p)}(\omega)\big)^{-1} = \boldsymbol{C}^q - f_p\big((\boldsymbol{C}^q - \boldsymbol{C}^p)^{-1} - f_q t^P_{(q)}(\omega)\big)^{-1} \tag{A.3}$$

One backward demonstration results from multiplying (A.3) by $(\boldsymbol{C}^p - \boldsymbol{C}^q)^{-1}$ to obtain

$$\begin{aligned}\boldsymbol{I} &= f_q\big(\boldsymbol{I} - f_p t^P_{(p)}(\omega) : (\boldsymbol{C}^p - \boldsymbol{C}^q)\big)^{-1} + f_p\big(\boldsymbol{I} - f_q t^P_{(q)}(\omega) : (\boldsymbol{C}^q - \boldsymbol{C}^p)\big)^{-1}\\ &= f_q(\boldsymbol{I} - \boldsymbol{X}_p)^{-1} + f_p(\boldsymbol{I} - \boldsymbol{X}_q)^{-1},\end{aligned}$$

which yields $f_q\big(\boldsymbol{I} - (\boldsymbol{X}_q)^{-1}\big) + f_p\big(\boldsymbol{I} - (\boldsymbol{X}_p)^{-1}\big) = 0$ and (A.2).

The symmetric form of the effective properties of two-phase laminates. The tensor $\boldsymbol{C}^{*P\omega}_{q\subset p}$ reads

$$\boldsymbol{C}^p - f_q\big((\boldsymbol{C}^p-\boldsymbol{C}^q)^{-1} - f_p\boldsymbol{t}^P_{(\boldsymbol{C}^p)}(\omega)\big)^{-1} = \boldsymbol{C}^p - f_q(\boldsymbol{C}^p-\boldsymbol{C}^q):\big(\boldsymbol{I} - f_p\boldsymbol{t}^P_{(\boldsymbol{C}^p)}(\omega):(\boldsymbol{C}^p-\boldsymbol{C}^q)\big)^{-1}.$$

Using the homogeneity of rank -1 of $\boldsymbol{t}^V_{(\boldsymbol{C}^p)}$ with respect to the moduli $f_p\boldsymbol{t}^P_{(\boldsymbol{C}^p)}(\omega) = \boldsymbol{t}^P_{(\boldsymbol{C}^p/f_p)}(\omega)$ and setting $\boldsymbol{C}^p-\boldsymbol{C}^q = \boldsymbol{C}'^p - \boldsymbol{C}^{*q}$ with $\boldsymbol{C}'^p = \boldsymbol{C}^p/f_p$, $\boldsymbol{C}^{*q} = \{\boldsymbol{C}\}/f_p$, yields

$$\big(\boldsymbol{I} - f_p\boldsymbol{t}^P_{(\boldsymbol{C}^p)}(\omega):(\boldsymbol{C}^p-\boldsymbol{C}^q)\big)^{-1} = \big(\boldsymbol{I} - \boldsymbol{t}^P_{(\boldsymbol{C}'^p)}(\omega):(\boldsymbol{C}'^p-\boldsymbol{C}^{*q})\big)^{-1} = \boldsymbol{I} - \boldsymbol{t}^P_{(\boldsymbol{C}^{*q})}(\omega):(\boldsymbol{C}^{*q}-\boldsymbol{C}'^p).$$

The last form results from the platelet property. Using $\boldsymbol{t}^P_{(\boldsymbol{C}^{*q})}(\omega) = f_p\boldsymbol{t}^P_{\{\boldsymbol{C}\}}(\omega)$, we arrive at

$$\boldsymbol{C}^p - f_q(\boldsymbol{C}^p-\boldsymbol{C}^q):\big(\boldsymbol{I} - f_p\boldsymbol{t}^P_{(\boldsymbol{C}^p)}(\omega):(\boldsymbol{C}^p-\boldsymbol{C}^q)\big)^{-1} = \boldsymbol{C}^p - f_q(\boldsymbol{C}^p-\boldsymbol{C}^q):\big(\boldsymbol{I} - f_p\boldsymbol{t}^P_{\{\boldsymbol{C}\}}(\omega):(\boldsymbol{C}^q-\boldsymbol{C}^p)\big)$$

and to (6), (11a) as well as to (9), (11b) for $S^{*P}(\omega) = (C^{*P}(\omega))^{-1}$. Note that $\{\boldsymbol{S}\} \neq \{\boldsymbol{C}\}^{-1}$.

Appendix B. Properties of the Hashin–Shtrikman (HS) and self-consistent (SC) estimates

The HS estimates. The general form is given in (2) and (3). In the two-phase case, the proof that $\boldsymbol{C}^{\text{eff HS}}_{p\subset q} = \boldsymbol{C}^q - f_p\big((\boldsymbol{\Delta C}^{q|p})^{-1} - f_q\overline{\boldsymbol{t}^V_{(q)}}\big)^{-1} = (\boldsymbol{S}^{\text{eff HS}}_{p\subset q})^{-1}$ is straightforward:

$$\begin{aligned} f_p\big(\boldsymbol{C}^q - \boldsymbol{C}^{\text{eff HS}}_{p\subset q}\big)^{-1} &= \big(\boldsymbol{\Delta C}^{q|p}\big)^{-1} - f_q\overline{\boldsymbol{t}^V_{(q)}} = \boldsymbol{S}^q - \boldsymbol{S}^q:\big(\boldsymbol{\Delta S}^{q|p}\big)^{-1}:\boldsymbol{S}^q - f_q\big(\boldsymbol{S}^q - \boldsymbol{S}^q:\overline{\boldsymbol{t}'^V_{(q)}}:\boldsymbol{S}^q\big)\\ &= f_p\boldsymbol{S}^q - f_p\boldsymbol{S}^q:\big(\boldsymbol{S}^q - \boldsymbol{S}^{\text{eff HS}}_{p\subset q}\big)^{-1}:\boldsymbol{S}^q\\ &= f_p\boldsymbol{S}^q - \boldsymbol{S}^q:\big((\boldsymbol{\Delta S}^{q|p})^{-1} - f_q\overline{\boldsymbol{t}'^V_{(q)}}\big):\boldsymbol{S}^q. \end{aligned} \tag{B.1}$$

Equation (B.1) gives

$$f_p\big(\boldsymbol{S}^q - \boldsymbol{S}^{\text{eff HS}}_{p\subset q}\big)^{-1} = (\boldsymbol{\Delta S}^{q|p})^{-1} - f_q\overline{\boldsymbol{t}'^V_{(q)}}. \tag{B.2}$$

The SC estimate. For all congruent grains of two constitutive phases, on can write

$$f_p\big((\boldsymbol{C}^{\text{eff}}_{\text{SC}} - \boldsymbol{C}^p)^{-1} - \overline{\boldsymbol{t}^V_{\boldsymbol{C}\text{eff}}}\big)^{-1} + f_q\big((\boldsymbol{C}^{\text{eff}}_{\text{SC}} - \boldsymbol{C}^q)^{-1} - \overline{\boldsymbol{t}^V_{\boldsymbol{C}\text{eff}}}\big)^{-1} = 0, \tag{B.3a}$$

$$f_q\big((\boldsymbol{C}^{\text{eff}}_{\text{SC}} - \boldsymbol{C}^p)^{-1} - \overline{\boldsymbol{t}^V_{\boldsymbol{C}\text{eff}}}\big) + f_p\big((\boldsymbol{C}^{\text{eff}}_{\text{SC}} - \boldsymbol{C}^q)^{-1} - \overline{\boldsymbol{t}^V_{\boldsymbol{C}\text{eff}}}\big) = 0. \tag{B.3b}$$

Equation (B.3b) yields $\overline{\boldsymbol{t}^V_{\boldsymbol{C}\text{eff}}} = f_q\big((\boldsymbol{C}^{\text{eff}}_{\text{SC}} - \boldsymbol{C}^p)^{-1}\big) + f_p\big((\boldsymbol{C}^{\text{eff}}_{\text{SC}} - \boldsymbol{C}^q)^{-1}\big)$. Further simple manipulations yield the SC approximation form of (16) for general (a, b) phases. A similar form is obtained in terms of the corresponding compliances, using the stress Green operators $\boldsymbol{t}'$. One verifies that $\boldsymbol{S}^{\text{eff}}_{\text{SC}} = (\boldsymbol{C}^{\text{eff}}_{\text{SC}})^{-1}$ simply using the platelet decompositions of both operators, which in that case refer to the same reference material, unlike the IPS estimate.

Appendix C. The IFS, IPS and ISC effective shear moduli in isotropic incompressible elasticity

For x_3-oriented fibers, the two shear moduli of the HS bounds read from (3), with $\eta = (1-2\nu_b)/(2-2\nu_b)$:

$$\mu_{1212}{}^{*F(\omega)}_{a\subset b} = \mu_b - c_a\left(\frac{1}{\mu_b-\mu_a} - \frac{c_b}{2\mu_b}(1+\eta)\right)^{-1}, \quad \mu_{i3i3}{}^{*F(\omega)}_{a\subset b} = \mu_b - c_a\left(\frac{1}{\mu_b-\mu_a} - c_b\frac{1}{2\mu_b}\right)^{-1}.$$

The two IFS moduli can be calculated with the coefficients of Table 2 and the moduli of the x_3-oriented fiber system, or at least appropriate partial sums. For the IFS shear modulus, we need the two shear moduli and

$$\Sigma = \tfrac{1}{15}(C_{iiii} + C_{3333} - 2C_{ii33})^{*F(\omega)}_{a\subset b}.$$

In the incompressible case, $\eta = 0$, the two shear moduli are equal and

$$\Sigma = \frac{1}{15}\left(4\mu_b - c_a(\mu_b - \mu_a)\frac{(5\mu_b + 3\{\mu\})}{(\mu_b + \{\mu\})}\right),$$

which gives, from (14),

$$\mu^{\text{eff IFS}}_{a\subset b} = \tfrac{11}{15}\mu^{*F(\omega)}_{a\subset b} + \Sigma = \frac{\mu_b}{15}\left(4 + 11\left(\frac{\mu_a + \langle\mu\rangle}{\mu_a + \{\mu\}}\right)\right) - \frac{c_a(\mu_b - \mu_a)}{15}\frac{(5\mu_b + 3\{\mu\})}{(\mu_b + \{\mu\})}. \tag{C.1}$$

For the IPS estimate in the incompressible case, one has, directly from (15),

$$\mu^{\text{eff IPS}}_{a,b} = \langle\mu\rangle + \frac{4\big(\{\mu\} - \mu^a\big)\big(\{\mu\} - \mu^b\big)}{10\{\mu\}} = \frac{3}{5}\langle\mu\rangle + \frac{2}{5}\frac{\mu^a\mu^b}{\{\mu\}}. \tag{C.2}$$

For comparison, the IHS and the ISC shear moduli estimate read, still with incompressibility,

$$\mu^{\text{eff IHS}}_{a\subset b} = \mu_b - c_a\left(\frac{1}{\mu_b - \mu_a} - \frac{2c_b}{5\mu_b}\right)^{-1} = \mu_b\left(\frac{2\mu_a + 3\langle\mu\rangle}{3\mu_b + 2\{\mu\}}\right), \tag{C.3}$$

$$\mu^{\text{eff ISC}}_{a,b} = \langle\mu\rangle + \frac{4\big(\mu^{\text{eff}}_{S-C} - \mu^a\big)\big(\mu^{\text{eff}}_{S-C} - \mu^b\big)}{10\mu^{\text{eff}}_{S-C}} = \tfrac{1}{6}\big(\sqrt{B^2 + 24\mu^a\mu^b} - B\big), \quad \text{with } B = 2\{\mu\} - 3\langle\mu\rangle. \tag{C.4}$$

For the IFS(ϕ) estimates (18), the first dilution of an embedded phase (a) fraction $\kappa_a = (1-\phi_a)c_a$ in phase (b) (resp. b in a) yields from (C.3) a modified phase $\breve{b}$ of shear modulus $\breve{\mu}_b$ (resp. $\breve{\mu}_a$ for $\breve{a}$). The concentration of phase (b) changes from $c_b = 1 - c_a$ to $1 - \kappa_a \neq \kappa_b$. The second dilution of infinite fibers yields $\mu^{\text{eff IFS}(\phi)}_{a\subset b} = \mu^{\text{eff IFS}}_{a\subset b}$ from (C.1) with $\breve{c}_a = (c_a - \kappa_a)/(1-\kappa_a)$ (resp. $\breve{c}_b$ for $\mu^{\text{eff IFS}(\phi)}_{b\subset a} = \mu^{\text{eff IFS}}_{b\subset a}$). The matrix with $\breve{c}_a$ fiber fraction has concentration $1 - \breve{c}_a \neq \breve{c}_b$. The dual IPS estimate from the compliance integral in (11b) reads, when incompressible,

$$\frac{1}{\mu^*} = \left\langle\frac{1}{\mu}\right\rangle + \left(\left\{\frac{1}{\mu}\right\} - \frac{1}{\mu_a}\right)\frac{5\tilde{B} - 4\tilde{A}}{15\tilde{B}^2}\left(\left\{\frac{1}{\mu}\right\} - \frac{1}{\mu_b}\right) = \left\langle\frac{1}{\mu}\right\rangle + \left(\left\{\frac{1}{\mu}\right\} - \frac{1}{\mu_a}\right)\frac{3}{5\tilde{B}}\left(\left\{\frac{1}{\mu}\right\} - \frac{1}{\mu_b}\right),$$

with $\tilde{B} = \left\{\frac{1}{\mu}\right\} = \frac{\langle\mu\rangle}{\mu_a\mu_b}$ for the reference medium. Hence

$$\mu^{\text{eff IPS(dual)}}_{a,b} = \frac{\langle\mu\rangle}{1 + \dfrac{2c_ac_b(\mu_a - \mu_b)^2}{5\mu_a\mu_b}}$$

This estimate is very close to the lower HS bound and out of the IFS sup limits.

When phase (a) is void, all these estimates equal μ_b at $c_b = 1$ and for $c_b \in [0, 1[$ they become

$$\mu_{0\subset b}^{\text{eff IFS}} = \frac{(5+c_a)c_b\mu_b}{5(1+c_a)}, \quad \mu_{b\subset 0}^{\text{eff IFS}} = \frac{c_b\mu_b}{5}, \quad \mu_{0,b}^{\text{eff IPS}} = \frac{3c_b\mu_b}{5}, \quad \mu_{0\subset b}^{\text{eff IHS}} = \frac{3c_b\mu_b}{3+2c_a},$$
$$\mu_{b\subset 0}^{\text{eff IHS}} = 0, \quad \mu_{0,b}^{\text{eff IPS(dual)}} = 0, \quad \mu_{0,b}^{\text{eff ISC}} = \begin{cases} 0 & \text{for } c_b \in \left[0, \frac{2}{5}\right], \\ \frac{5c_b-2}{3}\mu_b & \text{for } c_b \in \left[\frac{2}{5}, 1\right], \end{cases} \tag{C.5}$$
$$\mu_{0\subset b}^{\text{eff IFS}(\phi)} = \frac{(5+\check{c}_a)(1-\check{c}_a)\check{\mu}_b}{5(1+\check{c}_a)} = \frac{(5+\check{c}_a)(1-\check{c}_a)}{5(1+\check{c}_a)}\frac{3(1-\kappa_a)\mu_b}{3+2\kappa_a}; \quad \mu_{b\subset 0}^{\text{eff IFS}(\phi)} = \frac{\check{c}_b\mu_b}{5}.$$

In the second estimate of (C.5), the lower limit, the first dilution of phase (b) in void phase is lost. The general IPF–IFS(ϕ) and ISC–IFS(ϕ) estimates when one material phase (p or q) is void have analytical forms from using the moduli of (C.5) expressed for the phase pair (p, q) and concentrations f_p, f_q as the moduli of the intermediate homogeneous equivalent media (a) and (b) in (C.2) and (C.4), respectively, making use of (20a) and (20b) for c_a and for the two ϕ_p, ϕ_q functions defining $\check{c}_p$, κ_p and $\check{c}_q$, κ_q in (C.5). For the ISCP estimate when phase (a) is void $\mu_{0,b}^{\text{eff ISCP}}$ must satisfy

$$\frac{4\mu^*}{3} + \frac{2\mu^*(\mu^* - f_b\mu_b)}{3\mu^* + 2f_b\mu_b} = 0,$$

the (not reported) resolution giving $\mu_{0,b}^{\text{eff ISCP}} = \mu^* = 0$ for all f_b.

References

[Agrawal et al. 2003] P. Agrawal, K. Conlon, K. J. Bowman, C. T. Sun, F. R. Cichocki, Jr., and K. P. Trumble, "Thermal residual stresses in co-continuous composites", *Acta Mater.* **51**:4 (2003), 1143–1156.

[Berk 1987] N. F. Berk, "Scattering properties of a model bicontinuous structure with a well defined length scale", *Phys. Rev. Lett.* **58**:25 (1987), 2718–2721.

[Berryman 1985] J. G. Berryman, "Variational bounds on elastic constants for the penetrable sphere model", *J. Phys. D Appl. Phys.* **18**:4 (1985), 585–597.

[Boucher 1974] S. Boucher, "On the effective moduli of isotropic two-phase elastic composites", *J. Compos. Mater.* **8**:1 (1974), 82–89.

[Brenner et al. 2009] R. Brenner, R. A. Lebensohn, and O. Castelnau, "Elastic anisotropy and yield surface estimates of polycrystals", *Int. J. Solids Struct.* **46**:16 (2009), 3018–3026.

[Bretheau et al. 1988] T. Bretheau, D. Caldemaison, A. Feylessoufi, J. P. Fondère, and A. Zaoui, "Plasticity and space distribution of the phases in iron/silver two-phase material", *J. Mater. Sci.* **23**:11 (1988), 4022–4026.

[Burt and Korren 1996] M. Burt and A. Korren, "Periodic hyperbolic surfaces and subdivision of 3-space", pp. 179–183 in *Katachi U symmetry* (Tsukuba, 1994), edited by T. Ogawa et al., Springer, Tokyo, 1996.

[Chen et al. 2008] J. Chen, L. Xu, and H. Li, "Investigation on a direct modeling strategy for the effective elastic moduli prediction of composite material", *Mater. Sci. Eng. A* **491**:1–2 (2008), 385–389.

[Cherkaev 2000] A. Cherkaev, *Variational methods for structural optimization*, Applied Mathematical Sciences **140**, Springer, New York, 2000.

[Christensen 1979a] R. M. Christensen, *Mechanics of composite materials*, Wiley, New York, 1979.

[Christensen 1979b] R. M. Christensen, "Isotropic properties of platelet-reinforced media", *J. Eng. Mater. Technol.* (*ASME*) **101**:3 (1979), 299–303.

[Christensen and Waals 1972] R. M. Christensen and F. M. Waals, "Effective stiffness of randomly oriented fibre composites", *J. Compos. Mater.* **6**:3 (1972), 518–535.

[Dalmaz et al. 2000] A. Dalmaz, D. Ducret, R. El Guerjouma, P. Reynaud, P. Franciosi, D. Rouby, G. Fantozzi, and J. C. Baboux, "Elastic moduli of a 2.5D C/SiC composite: experimental and theoretical estimates", *Compos. Sci. Technol.* **60**:6 (2000), 913–925.

[DeBartolo and Hillberry 1998] E. A. DeBartolo and B. M. Hillberry, "Effects of constituent particle clusters on fatigue behavior of 2024-T3 aluminum alloy", *Int. J. Fatigue* **20**:10 (1998), 727–735.

[Delannay et al. 2006] L. Delannay, F. Lani, T. Pardoen, and F. Delannay, "Mean field modelling of the plastic behaviour of co-continuous dual-phase alloys with strong morphological anisotropy", *Int. J. Plast.* **22**:12 (2006), 2327–2345.

[Dendievel et al. 2002] R. Dendievel, J. J. Blandin, M. Fivel, M. Audier, and M. Duneau, "Mechanical properties of composites with an icosahedral fibre packing reinforcement", *Philos. Mag. A* **82**:14 (2002), 2631–2653.

[El Omri et al. 2000] A. El Omri, A. Fennan, F. Sidoroff, and A. Hihi, "Elastic-plastic homogenization for layered composites", *Eur. J. Mech. A Solids* **19**:4 (2000), 585–601.

[Errabii et al. 2007] A. Errabii, A. El Omri, and P. Franciosi, "Layered-based bounding for effective properties of elastic materials", pp. 293–294 in *8éme Congrès de Mécanique* (El Jadida, 2007), vol. 1, 2007.

[Estevez et al. 1999] R. Estevez, E. Maire, P. Franciosi, and D. S. Wilkinson, "Effect of particle clustering on the strengthening versus damage rivalry in particulate reinforced elastic plastic materials: a 3-D analysis from a self-consistent modelling", *Eur. J. Mech. A Solids* **18**:5 (1999), 785–804.

[Fan 1995] Z. Fan, "A new approach to the electrical resistivity of two-phase composites", *Acta Metall. Mater.* **43**:1 (1995), 43–49.

[Feng et al. 2003] X.-Q. Feng, Y.-W. Mai, and Q.-H. Qin, "A micromechanical model for interpenetrating multiphase composites", *Comput. Mater. Sci.* **28**:3–4 (2003), 486–493.

[Franciosi 2005] P. Franciosi, "On the modified Green operator integral for polygonal, polyhedral and other non-ellipsoidal inclusions", *Int. J. Solids Struct.* **42**:11–12 (2005), 3509–3531.

[Franciosi 2010] P. Franciosi, "The boundary-due terms in the Green operator of inclusion patterns from distant to contact and to connected situations using radon transforms: illustration for spheroid alignments in isotropic media", *Int. J. Solids Struct.* **47**:2 (2010), 304–319.

[Franciosi and Berbenni 2007] P. Franciosi and S. Berbenni, "Heterogeneous crystal and poly-crystal plasticity modeling from a transformation field analysis within a regularized Schmid law", *J. Mech. Phys. Solids* **55**:11 (2007), 2265–2299.

[Franciosi and Berbenni 2008] P. Franciosi and S. Berbenni, "Multi-laminate plastic-strain organization for non-uniform TFA modeling of poly-crystal regularized plastic flow", *Int. J. Plast.* **24**:9 (2008), 1549–1580.

[Franciosi and El Omri 2011] P. Franciosi and A. El Omri, "Effective properties of fiber and platelet systems and related phase arrangements in n-phase heterogeneous media", *Mech. Res. Commun.* **38**:1 (2011), 38–44.

[Franciosi and Lormand 2004] P. Franciosi and G. Lormand, "Using the radon transform to solve inclusion problems in elasticity", *Int. J. Solids Struct.* **41**:3–4 (2004), 585–606.

[Gel'fand et al. 1966] I. M. Gel'fand, M. I. Graev, and N. Y. Vilenkin, *Generalized functions, 5: Integral geometry and representation theory*, Academic Press, New York, 1966.

[Gent and Thomas 1959] A. N. Gent and A. G. Thomas, "The deformation of foamed elastic materials", *J. Appl. Polym. Sci.* **1**:1 (1959), 107–113.

[Gong et al. 2005] L. Gong, S. Kyriakides, and W.-Y. Jang, "Compressive response of open-cell foams, I: Morphology and elastic properties", *Int. J. Solids Struct.* **42**:5–6 (2005), 1355–1379.

[Hashin 1979] Z. Hashin, "Analysis of properties of fiber composites with anisotropic constituents", *J. Appl. Mech.* (*ASME*) **46**:3 (1979), 543–550.

[Hashin 1983] Z. Hashin, "Analysis of composite materials: a survey", *J. Appl. Mech.* (*ASME*) **50**:3 (1983), 481–505.

[Hashin and Shtrikman 1963] Z. Hashin and S. Shtrikman, "A variational approach to the theory of elastic behaviour of multiphase materials", *J. Mech. Phys. Solids* **11**:2 (1963), 127–140.

[Helsing 1993] J. Helsing, "Higher-order bounds on the conductivity of composites from symmetry considerations", *Proc. R. Soc. Lond. A* **443**:1918 (1993), 451–455.

[Hill 1952] R. Hill, "The elastic behaviour of a crystalline aggregate", *Proc. Phys. Soc. A* **65**:5 (1952), 349–354.

[Hill 1965] R. Hill, "Continuum micro-mechanics of elastoplastic polycrystals", *J. Mech. Phys. Solids* **13**:2 (1965), 89–101.

[Kanaun 2003] S. K. Kanaun, "Dielectric properties of matrix composite materials with high volume concentrations of inclusions (effective field approach)", *Int. J. Eng. Sci.* **41**:12 (2003), 1287–1312.

[Kerner 1956] E. H. Kerner, "The elastic and thermo-elastic properties of composite media", *Proc. Phys. Soc. B* **69**:8 (1956), 808–813.

[Kinney et al. 2005] J. H. Kinney, J. S. Stölken, T. S. Smith, J. T. Ryaby, and N. E. Lane, "An orientation distribution function for trabecular bone", *Bone* **36**:2 (2005), 193–201.

[Ko 1965] W. L. Ko, "Deformation of foamed elastomers", *J. Cell. Plast.* **1**:1 (1965), 45–50.

[Kocks et al. 1991] U. F. Kocks, P. Franciosi, and M. Kawai, "A forest model of latent hardening and its application to polycrystal deformations", *Texture. Microstruct.* **14–18** (1991), 1103–1114.

[La Vecchia et al. 2003] G. M. La Vecchia, C. Badini, D. Puppo, and F. D'Errico, "Co-continuous Al/Al_2O_3 composite produced by liquid displacement reaction: relationship between microstructure and mechanical behavior", *J. Mater. Sci.* **38**:17 (2003), 3567–3577.

[Lebensohn et al. 2008] R. A. Lebensohn, R. Brenner, O. Castelnau, and A. D. Rollett, "Orientation image-based micromechanical modelling of subgrain texture evolution in polycrystalline copper", *Acta Mater.* **56**:15 (2008), 3914–3926.

[Lee and Gurland 1978] H. C. Lee and J. Gurland, "Hardness and deformation of cemented tungsten carbide", *Mater. Sci. Eng.* **33**:1 (1978), 125–133.

[Lefebvre et al. 2006] L.-P. Lefebvre, A. Blouin, S.-M. Rochon, and M. N. Bureau, "Elastic response of titanium foams during compression tests and using laser-ultrasonic probing", *Adv. Eng. Mater.* **8**:9 (2006), 841–846.

[Leßle et al. 1999] P. Leßle, M. Dong, and S. Schmauder, "Self-consistent matricity model to simulate the mechanical behaviour of interpenetrating microstructures", *Comput. Mater. Sci.* **15**:4 (1999), 455–465.

[Martin et al. 2003] C. L. Martin, D. Bouvard, and S. Shima, "Study of particle rearrangement during powder compaction by the discrete element method", *J. Mech. Phys. Solids* **51**:4 (2003), 667–693.

[Marur 2005] P. R. Marur, "Effective elastic moduli of syntactic foams", *Mater. Lett.* **59**:14–15 (2005), 1954–1957.

[Menges and Knipschild 1975] G. Menges and F. Knipschild, "Estimation of mechanical properties for rigid polyurethane foams", *Polym. Eng. Sci.* **15**:8 (1975), 623–627.

[Michel et al. 2001] J. C. Michel, H. Moulinec, and P. Suquet, "A computational scheme for linear and non-linear composites with arbitrary phase contrast", *Int. J. Numer. Methods Eng.* **52**:1–2 (2001), 139–160.

[Morgan et al. 2003] E. F. Morgan, H. H. Bayraktar, and T. M. Keaveny, "Trabecular bone modulus-density relationships depend on anatomic site", *J. Biomech.* **36**:7 (2003), 897–904.

[Moulinec and Suquet 1998] H. Moulinec and P. Suquet, "A numerical method for computing the overall response of nonlinear composites with complex microstructure", *Computer Methods in Applied Mechanics and Engineering* **157**:1-2 (1998), 69–94.

[Mow and Huiskes 2004] V. C. Mow and R. Huiskes (editors), *Basic orthopaedic biomechanics & mechano-biology*, 3rd ed., Lippincott Williams & Wilkins, Philadelphia, 2004.

[Natterer 1986] F. Natterer, *The mathematics of computerized tomography*, Teubner, Stuttgart, 1986.

[Nieh et al. 1998] T. G. Nieh, J. H. Kinney, J. Wadsworth, and A. J. C. Ladd, "Morphology and elastic properties of aluminum foams produced by a casting technique", *Scr. Mater.* **38**:10 (1998), 1487–1494.

[Pavese et al. 2007] M. Pavese, M. Valle, and C. Badini, "Effect of porosity of cordierite preforms on microstructure and mechanical strength of co-continuous ceramic composites", *J. Eur. Ceram. Soc.* **27**:1 (2007), 131–141.

[Postma 1955] G. W. Postma, "Wave propagation in a stratified medium", *Geophys.* **20**:4 (1955), 780–806.

[Ramm and Katsevich 1996] A. G. Ramm and A. I. Katsevich, *The radon transform and local tomography*, CRC Press, Boca Raton, FL, 1996.

[Ravichandran 1994] K. S. Ravichandran, "Deformation behavior of interpenetrating-phase composites", *Compos. Sci. Technol.* **52**:4 (1994), 541–549.

[Ricotti et al. 2006] Y. Ricotti, D. Ducret, R. El Guerjouma, and P. Franciosi, "Anisotropy of hygrothermal damage in fiber/polymer composites: effective elasticity measures and estimates", *Mech. Mater.* **38**:12 (2006), 1143–1158.

[Roberts and Garboczi 2002] A. P. Roberts and E. J. Garboczi, "Computation of the linear elastic properties of random porous materials with a wide variety of microstructure", *Proc. R. Soc. Lond. A* **458**:2021 (2002), 1033–1054.

[Serra 1982] J. Serra, *Image analysis and mathematical morphology*, Academic Press, London, 1982.

[Singh et al. 2008] H. Singh, A. M. Gokhale, S. I. Lieberman, and S. Tamisirakandala, "Image based computations of lineal path probability distributions for microstructure representation", *Mater. Sci. Eng. A* **474**:1–2 (2008), 104–111.

[Torquato 2002] S. Torquato, *Random heterogeneous materials: microstructure and macroscopic properties*, Interdisciplinary Applied Mathematics **16**, Springer, New York, 2002.

[Veenstra et al. 2000] H. Veenstra, P. C. J. Verkooijen, B. J. J. van Lent, J. van Dam, A. P. de Boer, and A. H. J. Nijhof, "On the mechanical properties of co-continuous polymer blends: experimental and modelling", *Polymer* **41**:5 (2000), 1817–1826.

[Walpole 1978] L. J. Walpole, "A coated inclusion in an elastic medium", *Math. Proc. Cambridge Philos. Soc.* **83**:3 (1978), 495–506.

[Walpole 1981] L. J. Walpole, "Elastic behavior of composite materials: theoretical foundations", *Adv. Appl. Mech.* **21** (1981), 169–242.

[Warren and Kraynik 1987] W. E. Warren and A. M. Kraynik, "Foam mechanics: the linear elastic response of two-dimensional spatially periodic cellular materials", *Mech. Mater.* **6**:1 (1987), 27–37.

[Warren and Kraynik 1997] W. E. Warren and A. M. Kraynik, "Linear elastic behavior of a low-density Kelvin foam with open cells", *J. Appl. Mech.* (*ASME*) **64**:4 (1997), 787–794.

[Zeller and Dederichs 1973] R. Zeller and P. H. Dederichs, "Elastic constants of polycrystals", *Phys. Status Solidi B* **55**:2 (1973), 831–842.

Received 19 Jun 2010. Revised 28 Nov 2010. Accepted 19 Dec 2010.

PATRICK FRANCIOSI: patrick.franciosi@univ-paris13.fr
LPMTM, UPR9001 CNRS, Institut Galilée, Université Paris 13, 93430 Villetaneuse, France

RENALD BRENNER: renald.brenner@univ-paris13.fr
LPMTM, UPR9001 CNRS, Institut Galilée, Université Paris 13, 93430 Villetaneuse, France

ABDERRAHIM EL OMRI: abderrahim_elomri@yahoo.fr
L M M, Faculté des Sciences et Techniques de Tanger, BP 416, Tanger, Morocco

JOURNAL OF MECHANICS OF MATERIALS AND STRUCTURES
Vol. 6, No. 5, 2011

msp

CONSISTENT LOADING FOR THIN PLATES

ISAAC HARARI, IGOR SOKOLOV AND SLAVA KRYLOV

Structural models are well-established for the governing operators in solid mechanics, yet the reduction of loads (data) is often performed in an *ad hoc* manner, which may be inadequate for the complex load distributions that often arise in modern applications. In the present work we consistently convert three-dimensional data to the form required by Kirchhoff thin-plate theory, in a variational framework. We provide formulas for all types of resultant structural loads and boundary conditions in terms of the original three-dimensional data, including proper specification of corner forces, in forms that are readily incorporated into computational tools. In particular, we find that in-plane components of three-dimensional loads engender distributed couples, contributing to an effective distributed transverse force and boundary shear force, the latter generalizing the notion of the celebrated Kirchhoff equivalent force. However, in virtual work we advocate a representation of the twisting moment in a form that involves neither the Kirchhoff equivalent force nor corner forces. An interpretation of the structural deflections as through-the-thickness averages of the continuum displacements, rather than their values on the midplane, yields explicit formulas for the thin-plate essential boundary data. The formulation facilitates the solution of problems that would otherwise pose formidable challenges. Numerical results confirm that appropriate use of the thin-plate model economizes computation and provides insight into the mechanical behavior, while preserving a level of accuracy comparable with the full three-dimensional solution.

1. Introduction

In solid mechanics the common approach to the analysis of bodies with distinctive geometric characteristics is to perform a dimensional reduction to an appropriate structural model. The analytical solution for these bodies is difficult for general geometries and loadings while the computation is often costly. A classical example is a plate-like body which is commonly described by a thin-plate model.[1] The dimensional reduction of the differential operator describing the original elasticity problem is often performed by variational procedures combined with certain kinematic and constitutive assumptions [Alessandrini et al. 1999; Hu 1984; Soedel 1981; Vidoli and Batra 2000]. This technique can be considered as a restriction of an approach applied to shells [DiCarlo et al. 2001]. Alternatively, hierarchies of reduced-order models of elastic bodies with high aspect ratio are built using asymptotic methods [Ciarlet 1990; Dauge and Gruais 1996; Dauge and Gruais 1998].

Since the thin-plate theory (Kirchhoff theory) has been developed [Kirchhoff 1850; Poisson 1829] based on fundamental contributions by Siméon-Denis Poisson (1811) and Gustav Robert Kirchhoff (1850) (see also [Timoshenko 1983; Todhunter and Pearson 1960] for historical treatises) a large variety

Keywords: Kirchhoff thin-plate theory, structural reduction, Kirchhoff equivalent force, distributed couples, corner forces.

[1] We distinguish between a *plate*, which is a flat structure that has thickness much smaller than the other dimensions, and a *plate model* or *theory*, which is the collection of assumptions that is used to dimensionally reduce the three-dimensional formulation and approximate its solution.

of models were built starting from simple plates theories [Reissner 1969; Sayir and Mitropoulos 1980] and up to nonlinear [Antman 1995; Ciarlet 1997; Libai and Simmonds 1998; Rubin 2000] and composite [Bisegna and Sacco 1997; Calcote 1969; Vasil'ev and Lur'e 1992] plates and shells. Extensive research was performed also in connection with numerical methods [Actis et al. 1999; Engel et al. 2002; Hughes and Hinton 1986; O'Leary and Harari 1985; Vogelius and Babuška 1981]. See also the reviews [Podio-Guidugli 2000; Sayir and Mitropoulos 1980].

In the construction of different structural theories, the procedures of reduction of elastic continua by the appropriate structural models are conventionally based on the body geometry determining the order of the small parameter used in the reduction. However, while such procedures are well-established for the differential operators governing problems of solid mechanics in general and plate-like problems in particular, the reduction of the data of the problem — body forces and boundary conditions — is often performed in an *ad hoc* manner. The form of the loading for problems that are governed by reduced structural theories is quite different from that of the original three-dimensional formulation. As a result, the *ad hoc* approach based on engineering intuition can be inadequate for the analysis of bodies subject to complex three-dimensional loading, and more rigorous procedures are required.

As an example of problems where complex three-dimensional loading is abundant one can mention coupled problems distinguished by the distribution of loading arising as a result of interaction. In the intrinsically multiphysics problems arising in micro and nanoelectromechanical systems (MEMS and NEMS) based applications the interaction forces are obtained in terms of electric or magnetic fields. The distribution of electrostatic or magnetic forces could produce very complex three-dimensional patterns which may include, for example, distributed couples (see [Liu and Chang 2005; Moon and Holmes 1979] and references therein). High aspect ratios of microstructures incorporated in MEMS make the use of structural descriptions attractive. However, due to intricate character of the three-dimensional interface forces, *ad hoc* procedures for their reduction are no longer sufficient. Other applications where the structural representation could be effective but *ad hoc* formulation of the reduced loading is not sufficient include aeroelastic and hydroelastic applications where the loading conditions are formulated in terms of interface velocities or contact pressures [Morand and Ohayon 1995]. High aspect ratios of aero/hydroelastic structures make the use of computationally efficient models based on the structural descriptions attractive, especially when incorporated in optimization or control procedures. For example, entire airplane wings or helicopter blades are routinely modeled as one-dimensional (beams) and two-dimensional structural elements (plates) of variable cross-section. On the other hand, the high gradients and intricacy of interface forces arising in these applications may require three-dimensional representation of the data. One can also mention problems involving complex spatially distributed surface forces originating in contact. This kind of force arises, for example, during forming processes of thin (i.e., high aspect ratio) metal sheet. In these processes surface tractions distributed in the direction tangent to the surface originate mainly from friction between the surfaces of the forming tool and the metal sheet.

The implementation of rigorous reduction procedures which use a variational framework and allow systematic reduction of the three-dimensional loading data to their structural counterparts for beam-like solids was analyzed in [Krylov et al. 2006]. In this work, we extend the implementation of these reduction procedures to the thin (Kirchhoff-Love) plate model. Despite its limitations, Kirchhoff-Love theory of thin-plate bending is one of the most widely used by engineers, mainly due to its simplicity. Nowadays, descriptions of thin bending theory can be found in most textbooks on structural mechanics (e.g., see

[Nádai 1925; Sokolnikoff 1983; Timoshenko and Goodier 1951; Timoshenko and Woinowsky-Krieger 1959; Ugural 1981]).

In the present work special attention is paid to the rigorous reduction, by means of a variational procedure, of the original problem data to the form required by the structural representation. The structural counterparts of the loads are expressed in terms of the data of the original three-dimensional problem. Note that in most cases, in considering bending of plates in the framework of the classical thin-plate theory only transverse loads, namely, loads acting in the direction perpendicular to the plate's plane in a three-dimensional domain, are accounted for. We show that consistent consideration of three-dimensional applied in-plane body forces and surface tractions in the classical thin-plate formulation engenders distributed couples, modifying the Kirchhoff equivalent shear force and the transverse distributed force [DiCarlo et al. 2001; Niordson 1985]. In addition, we present a consistent treatment of essential (kinematic) boundary conditions. Structural counterparts of the essential boundary conditions considered here as through-the-thickness averages [Cowper 1966; Prescott 1942] are obtained in terms of three-dimensional displacements (which generally speaking would not conform the structural assumptions) prescribed on an appropriate part of the surface. It should be noted that certain aspects of thin-plate theory, for example, corner forces arising at the points of discontinuity of the plate's outer boundary, are treated differently in the literature by various sources. Using the systematic variational approach, we confirm that corner forces are actually a part of the natural boundary conditions.

The goal of the work is twofold. First, the results of the work provide better insight into the contribution of different components of data into the structural model. In addition, the structural form of the weak formulation derived systematically from the original three-dimensional elasticity expressions along with essential boundary conditions expressed in terms of the original three-dimensional data are useful as a basis for numerical procedures.

In Section 2 the differential equations and the natural boundary conditions for plate-like bodies are derived from the variational principle. We begin with the formulation of the three-dimensional elastic problem, substitute the kinematic and constitutive assumptions into the variational equation and derive the classical Kirchhoff-Love thin-plate equations and boundary conditions. The validation of the models is performed in Section 3 by comparison to analytical solutions of torsionless axisymmetric elasticity problems. The estimation of the structural efficiency from the computational point of view is performed in Section 4, by comparison to a three-dimensional elasticity problem solved by the finite element method.

2. Structural reduction of elastostatics by the thin-plate model

The dimensional reduction of the elasticity operator in thin flat bodies by various plate models, as outlined above, is a well-established procedure. The reduced structural models are expressed in terms of unknown deflections. When these deflections are found, recovery procedures are available to approximate the three-dimensional displacement field.

The goal of the present work is to derive a systematic conversion of general three-dimensional loads to their structural counterparts, in forms that are readily incorporated into computational tools.

2A. ***Assumptions of Kirchhoff plate theory.*** The domain is a three-dimensional thin flat body (Figure 1) defined by

$$\Omega = \{(x_1, x_2, x_3) \in \mathbb{R}^3 \mid (x_1, x_2) \in A,\ -t/2 < x_3 < t/2\}. \tag{2-1}$$

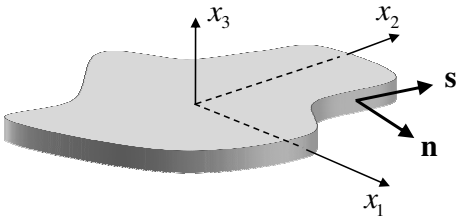

Figure 1. Geometry of a thin flat body.

Here t is the plate thickness, which may vary with x_1 and x_2, and $A \subset \mathbb{R}^2$ is the midplane of the plate.

The kinematic assumptions of the classical Kirchhoff plate theory approximate the displacements u_i by structural counterparts

$$u^s_\alpha(x_1, x_2, x_3) = w_\alpha(x_1, x_2) - x_3 w_{3,\alpha}(x_1, x_2), \tag{2-2}$$

$$u^s_3(x_1, x_2, x_3) = w_3(x_1, x_2). \tag{2-3}$$

The structural displacements are defined in terms of in-plane (stretching) w_α and transverse (bending) w_3 deflections. In the following, the deflections are considered as through-the-thickness averages (although commonly associated with the midplane). Throughout, Latin indices i, j, k, l take on values 1, 2, 3, Greek indices $\alpha, \beta, \gamma, \delta$ take on values 1, 2. The summation convention over repeated indices is applied. In addition, $(\cdot)_{,\alpha} = \partial(\cdot)/\partial x_\alpha$ is used for the partial derivative. From expressions (2-2) and (2-3) the approximate three-dimensional displacements u^s_i can be recovered after determining w_i.

Strains in the x_3-direction are not computed from the displacements but via the constitutive assumption of plane stress

$$\sigma^s_{33} = 0. \tag{2-4}$$

In the homogeneous isotropic case, considered here for simplicity, the strains are

$$\epsilon^s_{\alpha\beta} = u^s_{(\alpha,\beta)} = w_{(\alpha,\beta)} - x_3 w_{3,\alpha\beta}, \qquad \epsilon^s_{\alpha 3} = u^s_{(\alpha,3)} = 0, \qquad \epsilon^s_{33} = \frac{-\nu}{1-\nu}\epsilon^s_{\alpha\alpha}. \tag{2-5}$$

Here, $w_{(\alpha,\beta)}$ are the in-plane strains and $w_{3,\alpha\beta}$ are the curvatures. Parentheses in the subscripts denote the symmetric part of a tensor: $t_{(\alpha\beta)} = \frac{1}{2}(t_{\alpha\beta} + t_{\beta\alpha})$. The resulting two-dimensional constitutive relations are

$$\sigma^s_{\alpha\beta} = \frac{E}{1+\nu}\left(\frac{\nu}{1-\nu}\delta_{\alpha\beta}\epsilon^s_{\gamma\gamma} + \epsilon^s_{\alpha\beta}\right). \tag{2-6}$$

Here, E and ν are Young's modulus and Poisson's ratio respectively. Following convention in Kirchhoff plate theory, $\sigma^s_{\alpha 3}$ are evaluated from equilibrium rather than from the constitutive relations.

The structural reduction is performed in a variational framework, following the description in [Hughes 2000]. Special attention is paid to the reduction of distributed boundary data and body forces to their structural equivalents.

2B. ***Virtual work.*** Consider the standard linear elastostatics boundary-value problem in the bounded domain $\Omega \subset \mathbb{R}^3$, with boundary Γ. The boundary of the domain consists of the top and bottom surfaces ($x_3 = \pm t/2$) and the lateral boundary, assumed to be a cylindrical surface. The boundary Γ has subregions

Γ_g and Γ_h such that $\Gamma = \Gamma_g \cup \Gamma_h$ and $\Gamma_g \cap \Gamma_h = \varnothing$. The data (loads) are prescribed displacements $g_i : \Gamma_g \to \mathbb{R}$ (essential boundary conditions), tractions $h_i : \Gamma_h \to \mathbb{R}$ (natural boundary conditions) and body forces $f_i : \Omega \to \mathbb{R}$. In general, the boundary may admit different decompositions for different components. The procedure is formulated in terms of Γ_g and Γ_h for simplicity of presentation. Extensions to more general cases are straightforward and considered subsequently.

The plate equations, including expressions for structural loads expressed in terms of the original three-dimensional data, are obtained from the standard variational formulation for the elasticity theory. This is the principle of virtual work: find u_i that satisfies $u_i = g_i$ on Γ_g such that

$$\int_\Omega \bar{u}_{(i,j)}\sigma_{ij}\, d\Omega = \int_\Omega \bar{u}_i f_i\, d\Omega + \int_{\Gamma_h} \bar{u}_i h_i\, d\Gamma. \tag{2-7}$$

Here, $\bar{u}_i$ is the weighting function, or variation, satisfying the homogenous counterpart of the essential boundary conditions $\bar{u}_i = 0$ on Γ_g. The stress σ_{ij} is defined in terms of the displacement u_i via strain in the usual way.

To fix ideas, consider applied displacements and tractions on corresponding parts of the lateral boundary, whereas only tractions are specified on the top and bottom surfaces ($x_3 = \pm t/2$). (This configuration is common in practice.) The lateral boundary has a unit outward normal vector $\boldsymbol{n} = n_\alpha \boldsymbol{e}_\alpha$ and a unit tangent vector $\boldsymbol{s} = s_\alpha \boldsymbol{e}_\alpha$, such that $\boldsymbol{n} \times \boldsymbol{s} = \boldsymbol{e}_3$ (Figure 1). Here, the $\boldsymbol{e}_i$ are the Euclidean basis unit vectors. On part of the lateral boundary (Γ_g) we consider essential boundary conditions specified by the transverse displacement g_3 and the normal and tangential in-plane displacements $g_n = g_\alpha n_\alpha$ and $g_s = g_\alpha s_\alpha$. On the remaining part of the lateral boundary we consider natural boundary conditions specified by the transverse traction h_3 and the normal and tangential in-plane tractions $h_n = h_\alpha n_\alpha$ and $h_s = h_\alpha s_\alpha$.

The boundary of the midplane A, denoted S, is subdivided into two non-overlapping regions S_g (such that $S_g \times [-t/2,\ t/2] = \Gamma_g$) and $S_h = S \setminus S_g$. If S is not smooth, the corners, where the normal vector $\boldsymbol{n}$ suffers a discontinuity, are denoted $\partial S = \{\boldsymbol{x}_c\}_{c=1}^{n_{\text{corn}}}$, where $\boldsymbol{x}_c \in S$ is a corner location and n_{corn} is the number of corners.

The boundary Γ_h is partitioned in such a way that

$$\int_{\Gamma_h} \ldots d\Gamma = \int_A \langle \ldots \rangle\, dA + \int_{S_h} \int_{-t/2}^{t/2} \ldots dx_3\, dS. \tag{2-8}$$

Here, dS is the arc length along S, and the $\langle \ldots \rangle$ operator is defined by

$$\langle f(x_1, x_2, x_3) \rangle = f(x_1, x_2, -t/2) + f(x_1, x_2, t/2).$$

Replacing the displacements u_i and stresses σ_{ij} in (2-7) by their structural counterparts u_i^s and $\sigma_{\alpha\beta}^s$ (since $\sigma_{33}^s = 0$ by the constitutive assumption (2-4) and $u_{(\alpha,3)}^s = 0$ by the kinematic assumptions (2-2) and (2-3)) yields

$$\int_\Omega \bar{u}_{(\alpha,\beta)}^s \sigma_{\alpha\beta}^s\, d\Omega = \int_\Omega (\bar{u}_\alpha^s f_\alpha + \bar{u}_3^s f_3)\, d\Omega + \int_A (\langle \bar{u}_\alpha^s h_\alpha \rangle + \langle \bar{u}_3^s h_3 \rangle)\, dA + \int_{S_h} \int_{-t/2}^{t/2} (\bar{u}_n^s h_n + \bar{u}_s^s h_s + \bar{u}_3^s h_3)\, dx_3 dS. \tag{2-9}$$

Here, $\bar{u}_i^s$ are variations of the structural displacements. The explicit dependence of the structural quantities on x_3 (from the kinematic assumptions) simplifies the domain integration

$$\int_\Omega \ldots d\Omega = \int_A \int_{-t/2}^{t/2} \ldots dx_3\, dA. \tag{2-10}$$

This leads to the principle of virtual work for the thin plate. Data for the plate essential boundary conditions, prescribed boundary deflections W_i and rotation Θ defined in Table 1, are obtained by the procedure outlined in Section 2C. The statement of thin-plate virtual work is: find w_i that satisfies $w_i = W_i$ and $w_{3,n} = \Theta$ on S_g such that

$$\int_A (\overline{w}_{\alpha,\beta} n_{\alpha\beta} - \overline{w}_{3,\alpha\beta} m_{\alpha\beta})\, dA = \int_A (\overline{w}_\alpha F_\alpha - \overline{w}_{3,\alpha} C_\alpha + \overline{w}_3 F_3)\, dA + \int_{S_h} (\overline{w}_n N_n + \overline{w}_s N_s - \overline{w}_{3,n} M_n - \overline{w}_{3,s} M_s + \overline{w}_3 Q)\, dS. \tag{2-11}$$

Here, $\overline{w}_i$ is the weighting function, or variation, satisfying the homogenous counterpart of the thin-plate essential boundary conditions $\overline{w}_i = 0$ and $\overline{w}_{3,n} = 0$ on S_g.

The applied structural loads, distributed forces and couples F_i and C_α, along with boundary forces and moments N_n, N_s, Q, M_n and M_s, defined in terms of the underlying three-dimensional data in Table 1, result from integration through the thickness. The thin-plate constitutive relations are obtained by substituting the relations (2-5) and (2-6) into the definitions for the in-plane force tensor $n_{\alpha\beta}$ and the bending moment tensor $m_{\alpha\beta}$ (Table 1). For constant plate thickness we have

$$n_{\alpha\beta} = \frac{Et}{1+\nu}\left(\frac{\nu}{1-\nu}\delta_{\alpha\beta} w_{\gamma,\gamma} + w_{(\alpha,\beta)}\right), \tag{2-12}$$

$$m_{\alpha\beta} = -D\big[\nu\delta_{\alpha\beta} w_{3,\gamma\gamma} + (1-\nu) w_{3,\alpha\beta}\big]. \tag{2-13}$$

Here, $D = \dfrac{Et^3}{12(1-\nu^2)}$ is the isotropic bending stiffness.

Remarks. (1) The principle of virtual work for thin plates, (2-11), incorporates applied distributed couples C_α, engendered by in-plane components of three-dimensional loads. This is rarely done in the context of a Kirchhoff plate model. There are three-dimensional load configurations for which distributed couples constitute a significant portion of the resultant structural load. In such cases, omitting these terms in the structural model will disregard a substantial part of the response.

(2) The virtual work equation (2-11) represents two uncoupled two-dimensional problems, an in-plane problem weighted by $\overline{w}_\alpha$ and a plate bending problem weighted by $\overline{w}_3$.

(3) Assuming sufficient regularity of the prescribed boundary twisting moment M_s along smooth parts of S_h, the term representing the external work it exerts within the virtual work equation (2-11) may be integrated by parts, yielding for the bending terms

$$\int_{S_h} (-\overline{w}_{3,n} M_n - \overline{w}_{3,s} M_s + \overline{w}_3 Q)\, dS = \int_{S_h} \big(-\overline{w}_{3,n} M_n + \overline{w}_3 (M_{s,s} + Q)\big)\, dS - (\overline{w}_3 [\![M_s]\!])|_{\partial S \cap S_h}. \tag{2-14}$$

Here, $[\![M_s]\!] = \lim_{\varepsilon\to 0} M_s(\boldsymbol{x}_c + \varepsilon \boldsymbol{s}) - M_s(\boldsymbol{x}_c - \varepsilon \boldsymbol{s})$ represents a corner force. On the right-hand side of (2-14) are the conventional terms that appear regularly as part of the thin-plate virtual work

Quantity	Description
$n_{\alpha\beta} = \int_{-t/2}^{t/2} \sigma^s_{\alpha\beta} dx_3$	in-plane force tensor
$m_{\alpha\beta} = \int_{-t/2}^{t/2} \sigma^s_{\alpha\beta} x_3\, dx_3$	bending moment tensor
$F_\alpha = \int_{-t/2}^{t/2} f_\alpha\, dx_3 + \langle h_\alpha \rangle$	applied in-plane force
$\hat{F}_3 = F_3 + C_{\alpha,\alpha}$	effective applied transverse force
$F_3 = \int_{-t/2}^{t/2} f_3\, dx_3 + \langle h_3 \rangle$	applied transverse force
$C_\alpha = \int_{-t/2}^{t/2} f_\alpha x_3\, dx_3 + \langle h_\alpha x_3 \rangle$	applied couple
$W_n = \frac{1}{t} \int_{-t/2}^{t/2} g_n\, dx_3$	prescribed normal boundary deflection
$W_s = \frac{1}{t} \int_{-t/2}^{t/2} g_s\, dx_3$	prescribed tangential boundary deflection
$W_3 = \frac{1}{t} \int_{-t/2}^{t/2} g_3\, dx_3$	prescribed transverse boundary deflection
$\Theta = -\frac{12}{t^3} \int_{-t/2}^{t/2} g_n x_3\, dx_3$	prescribed tangential boundary rotation
$N_n = \int_{-t/2}^{t/2} h_n\, dx_3$	prescribed normal boundary in-plane force
$N_s = \int_{-t/2}^{t/2} h_s\, dx_3$	prescribed tangential boundary in-plane force
$M_n = \int_{-t/2}^{t/2} h_n x_3\, dx_3$	prescribed boundary bending moment
$\hat{Q} = Q + M_{s,s} - C_n^-$	effective prescribed boundary shear force
$Q = \int_{-t/2}^{t/2} h_3\, dx_3$	prescribed boundary shear force
$M_s = \int_{-t/2}^{t/2} h_s x_3\, dx_3$	prescribed boundary twisting moment
$C_n^-(\boldsymbol{x}) = \lim_{\boldsymbol{\xi} \to \boldsymbol{x}} C_n(\boldsymbol{\xi}),\ \boldsymbol{x} \in S_h$	the edge trace of applied couple
$R = [\![M_s]\!]$	prescribed boundary shear force at corner $\boldsymbol{x}_c$

Table 1. Structural nomenclature. We have set $[\![M_s]\!] = M_s(\boldsymbol{x}_c^+) - M_s(\boldsymbol{x}_c^-)$, where $M_s(\boldsymbol{x}_c^\pm) = \lim_{\varepsilon \to 0} M_s(\boldsymbol{x}_c \pm \varepsilon \boldsymbol{s})$; $f_n = f_\alpha n_\alpha$, $f_s = f_\alpha s_\alpha$; and $\boldsymbol{x}_c \in S$, for $c = 1, 2, \ldots, n_{\text{corn}}$, is a corner location.

equation in the literature [Bauchau and Craig 2009; Šolín 2006], though both forms are mentioned in [Zienkiewicz and Taylor 2000]. The right-hand side indicates the source of the Kirchhoff equivalent (modified shear) force and the corner forces. Indeed, this form appears in the Euler–Lagrange equations (2-15) below and is essential for the strong form of the boundary-value problem. However, the two forms are equivalent statements of virtual work, subject to the higher regularity requirement on the prescribed boundary twisting moment. We prefer the formulation (2-11) as it is simpler and less constrained, compatible with the variational statement of higher-order plate theories, and obviates the use of the Kirchhoff equivalent force and corner forces (thereby allowing lower regularity of the data and facilitating implementation) in methods based on virtual work such as finite element analysis.

(4) All of the loading terms on the right-hand side of the virtual work equation (2-11) may be incorporated by users into commercial finite element computations without re-programming of the software by using the usual definitions of consistent nodal loads.

Integration by parts yields the Euler–Lagrange equations for the thin plate:

$$\begin{aligned}0=&\int_A \overline{w}_\alpha(-n_{\alpha\beta,\beta}-F_\alpha)dA+\int_A \overline{w}_3(-m_{\alpha\beta,\alpha\beta}-F_3-C_{\alpha,\alpha})dA+\int_{S_h}\overline{w}_n(n_{nn}-N_n)dS+\int_{S_h}\overline{w}_s(n_{ns}-N_s)dS\\&+\int_{S_h}\overline{w}_3(m_{\alpha\beta,\beta}n_\alpha+(m_{ns})_{,s}+C_n^-Q-M_{s,s})dS+(\overline{w}_3[\![-m_{ns}+M_s]\!])|_{\partial S\cap S_h}\\&+\int_{S_h}\overline{w}_{3,n}(-m_{nn}+M_n)dS.\end{aligned}\tag{2-15}$$

Here, $(\cdot)_{nn}=(\cdot)_{\alpha\beta}n_\alpha n_\beta$ and $(\cdot)_{ns}=(\cdot)_{\alpha\beta}n_\alpha s_\beta$ denote the normal and tangential components of the stress resultants. Similarly, $(\cdot)_{,n}=(\cdot)_{,\alpha}n_\alpha$ and $(\cdot)_{,s}=(\cdot)_{,\alpha}s_\alpha$ are used for normal and tangential derivatives, respectively.

The three-dimensional boundary value problem of linear elasticity is reduced to a set of two uncoupled two-dimensional boundary-value problems: an in-plane problem and a plate bending problem. Thin plate equilibrium equations are obtained from the area integrals of (2-15) and the thin-plate natural boundary conditions are obtained from the line integrals of (2-15), along with the discrete corner conditions.

2C. ***Essential boundary conditions.*** Structural essential boundary conditions are imposed on the quantities associated with a variation in the boundary integrals of (2-15). The data are specified by a through-the-thickness averaging procedure [Cowper 1966; Prescott 1942] suggested by the definition of the force resultants. The kinematic assumptions (2-2) and (2-3) yield

$$w_i(x_1,x_2)=\frac{1}{t}\int_{-t/2}^{t/2}u_i^s(x_1,x_2,x_3)\,dx_3,\tag{2-16}$$

$$w_{3,n}(x_1,x_2)=-\frac{12}{t^3}\int_{-t/2}^{t/2}u_n^s(x_1,x_2,x_3)x_3\,dx_3.\tag{2-17}$$

Averaging the prescribed three-dimensional displacements on Γ_g yields the thin-plate essential boundary conditions

$$w_i=W_i,\qquad w_{3,n}=\Theta\qquad\text{on } S_g,\tag{2-18}$$

in terms of the prescribed boundary deflections W_i and rotation Θ (Table 1).

Remark. The common view of deflections as displacements of the midplane

$$w_i(x_1,x_2)=u_i^s(x_1,x_2,0)\tag{2-19}$$

may also be used to specify the plate essential boundary conditions (except for the boundary rotation). If the prescribed displacements g_i conform to the kinematic assumptions, the two approaches are equivalent for the boundary deflections. In general, we prefer to interpret deflections as displacements averaged through the thickness.

2D. ***Strong form of Kirchhoff plate problems.*** As noted, the three-dimensional linear elasticity boundary value problem is reduced to two uncoupled two-dimensional problems:

(1) An in-plane problem for $w_\alpha(x_1, x_2)$;

(2) A plate bending problem for $w_3(x_1, x_2)$.

The differential equations and natural boundary conditions are Euler–Lagrange equations emanating from (2-15). Essential boundary conditions are obtained by the through-the-thickness averaging procedure.

The features of the in-plane problem are conventional, and included here for completeness. The in-plane boundary-value problem is

$$\begin{aligned} -n_{\alpha\beta,\beta} &= F_\alpha \quad \text{in } A, \\ w_n = W_n, \qquad w_s &= W_s \quad \text{on } S_g, \\ n_{nn} = N_n, \qquad n_{ns} &= N_s \quad \text{on } S_h. \end{aligned} \tag{2-20}$$

The structural data are expressed in terms of the original three-dimensional data (Table 1). Boundary conditions are designated in terms that refer to the homogeneous case. For example, a "fixed" boundary condition means that all kinematic quantities are specified (but not necessarily zero). In these terms, (2-20) represents a body fixed on one portion of the boundary and free on the rest. Other possible combinations of normal and tangential boundary conditions are shown in Table 2.

Our formulation of the plate bending problem contains several noteworthy features. The plate bending boundary-value problem is

$$\begin{aligned} -m_{\alpha\beta,\alpha\beta} &= \hat{F}_3 \quad \text{in } A, \\ w_3 = W_3 \qquad w_{3,n} &= \Theta \quad \text{on } S_g, \\ m_{nn} = M_n, \qquad m_{\alpha\beta,\beta} n_\alpha + (m_{ns})_{,s} &= \hat{Q} \quad \text{on } S_h, \\ [\![m_{ns}]\!] &= R \quad \text{on } \partial S \cap S_h. \end{aligned} \tag{2-21}$$

For constant plate thickness, the equilibrium equation reduces to the well-known equilibrium equation of Kirchhoff-Love plate theory in terms of the transverse deflection

$$D\nabla^4 w_3 = \hat{F}_3 \quad \text{in } A. \tag{2-22}$$

Again, the structural data are expressed in terms of the original three-dimensional data (Table 1). The

fixed (*or* clamped)	$w_n = W_n$	$w_s = W_s$
free	$n_{nn} = N_n$	$n_{ns} = N_s$
symmetric	$w_n = W_n$	$n_{ns} = N_s$
skew symmetric	$w_s = W_s$	$n_{nn} = N_n$

Table 2. In-plane problem: common boundary conditions. The designations refer to homogeneous boundary conditions.

distributed loading on the plate is an *effective* transverse force

$$\hat{F}_3 = F_3 + C_{\alpha,\alpha}. \tag{2-23}$$

The standard term is modified by the in-plane divergence of applied couples C_α, engendered by in-plane components of three-dimensional body forces and tangential tractions on the top and bottom surfaces.

Similarly, the shear load is an *effective* boundary shear force

$$\hat{Q} = Q + M_{s,s} - C_n^-. \tag{2-24}$$

The celebrated Kirchhoff equivalent force $Q + M_{s,s}$ [Kirchhoff 1850] is modified by the edge trace of applied couples. It would be difficult to derive these terms intuitively. Such terms are rarely accounted for in the literature [Niordson 1985], and presented in an ad hoc basis [Madureira 2004; Sutyrin and Hodges 1996]. Their origins from in-plane components of three-dimensional loads have not been reported in the literature, to our knowledge. When the boundary is not smooth, shear boundary conditions include discrete corner forces R defined in terms of the prescribed boundary twisting moment, emanating from tangential tractions applied on the lateral boundary (Table 1).

Remarks. (1) The treatment of corner forces in the literature is not uniform. In many instances they are defined as boundary conditions accompanying shear boundary conditions at discrete points, part of the problem statement, as described in (2-21) [Bauchau and Craig 2009; Wells and Nguyen 2007; Grossi and Lebedev 2001; Nayfeh and Pai 2004; Reismann 1988; Tsiatas 2009]. However, corner forces also appear only as reaction forces that are part of the solution [Szilard 2004]. In some descriptions there is no mention of corner forces whatsoever. As outlined above, consistent variational derivation of the plate problem formulation gives rise to the corner forces in the Euler–Lagrange equations, and therefore they should appear explicitly as natural boundary conditions in the problem statement.

(2) Both corner forces and the Kirchhoff equivalent force can be derived from a constrained continuum of grade two material [Forte and Vianello 1988].

In terms that refer to homogeneous boundary conditions, (2-21) represents a body fixed on one portion of the boundary and free on the rest. In general, there should be two boundary conditions at each point: either transverse deflection or shear force, and either tangential rotation or bending moment (Table 3).

Possible combinations of three-dimensional data specified at a lateral boundary point with the corresponding type of structural boundary conditions are listed in Table 4. Due to the presence of the Kirchhoff

fixed (*or* clamped)	$w_3 = W_3$	$w_{3,n} = \Theta$	
free	$m_{nn} = M_n$	$(m_{n\alpha})_{,\alpha} + (m_{ns})_{,s} = \hat{Q}$	$[\![m_{ns}]\!] = R$
simply supported	$w_3 = W_3$	$m_{nn} = M_n$	
symmetric	$w_{3,n} = \Theta$	$(m_{n\alpha})_{,\alpha} + (m_{ns})_{,s} = \hat{Q}$	$[\![m_{ns}]\!] = R$

Table 3. Plate bending problem: common boundary conditions. The designations refer to homogeneous boundary conditions ("simply supported" = "skew symmetric").

Three-dimensional	In-plane	Bending
$g_n\ g_s\ g_3$	Fixed	Fixed
$g_n\ g_s\ h_3$	Fixed	—
$g_n\ h_s\ g_3$	Symmetric	Fixed
$h_n\ g_s\ g_3$	Skew symmetric	Simply supported
$g_n\ h_s\ h_3$	Symmetric	Symmetric
$h_n\ g_s\ h_3$	Skew symmetric	—
$h_n\ h_s\ g_3$	Free	Simply supported
$h_n\ h_s\ h_3$	Free	Free

Table 4. Possible combinations of data on the lateral boundary. The designations refer to homogeneous boundary conditions.

equivalent force in thin-plate bending, tangential tractions h_s must always accompany transverse tractions h_3 on the lateral boundary. The thin-plate flexure does not distinguish between the specification of tangential displacements g_s and tractions h_s along with transverse displacements g_3 on the lateral boundary (for fixed and simply supported boundary conditions).

3. Analytical model validation

The use of structural theories for analysis of bodies subject to intricate loading brings up questions about the validity of reduced models. The validity of different plate theories is usually justified by geometric considerations in terms of relative thickness. Nevertheless the validity of a plate model is affected also by the loading conditions. In this context, we reiterate the importance of the rigorous reduction procedure of the loads on one hand and the importance of the model validity examination on the other hand.

In the following sections we demonstrate the implementation of the structural reduction procedure using examples of torsionless axisymmetric elasticity problems with analytical solutions. In order to focus on the more interesting bending problem, we consider such loading for the elastic body that results in structural, thin-plate, load resultants for which the in-plane problem has a trivial solution. Validation of reduced structural solutions is performed through comparison with the solutions of the elasticity problem. Before proceeding with the comparisons, we discuss different approaches to error evaluation.

3A. ***Error of the model.*** The natural error norm for elasticity is the energy norm

$$\|\boldsymbol{u}\|_E^2 = \int_\Omega \sigma_{ij}(\boldsymbol{u})\epsilon_{ij}(\boldsymbol{u})\, d\Omega. \tag{3-1}$$

The thin-plate energy norm is

$$\|\boldsymbol{w}\|_S^2 = \int_A (n_{\alpha\beta} w_{\alpha,\beta} - m_{\alpha\beta} w_{3,\alpha\beta})\, dA, \tag{3-2}$$

where w_i is the structural deflection.

The elasticity norm (3-1) is inappropriate for measuring the errors of the plate model considered, due to the constitutive assumption, (2-4). A tight bound on the error in stress for Kirchhoff theory is available

[Simmonds 1971]. However, for the purpose of validating the reduction procedure proposed for the loads, we use a simpler error measure, namely, the *relative error in the energy*

$$\frac{\left(\|\boldsymbol{u}\|_E^2 - \|\boldsymbol{w}\|_S^2\right)^{1/2}}{\|\boldsymbol{u}\|_E}. \tag{3-3}$$

In the case of isotropic torsionless axisymmetric elasticity, the elastic strain energy norm (3-1) is expressed in terms of the radial and transverse displacements (u_r and u_z, respectively) as follows:

$$\|\boldsymbol{u}\|_E^2 = \pi \int_{-t/2}^{t/2}\int_0^a \frac{E}{(1+\nu)}\left\{\frac{2\nu}{(1-2\nu)}\left(u_{r,r}+\frac{u_r}{r}+u_{z,z}\right)^2 + 2\left[(u_{r,r})^2+\left(\frac{u_r}{r}\right)^2+(u_{z,z})^2\right]+(u_{r,z}+u_{z,r})^2\right\} r\,dr\,dz. \tag{3-4}$$

The energy norm for the circular thin-plate $\|\boldsymbol{w}\|_S$ is the sum of a membrane part associated with the in-plane forces and of a bending part associated with the transverse forces

$$\|\boldsymbol{w}\|_S^2 = \underbrace{2\pi\int_0^a \frac{Et}{1-\nu^2}\left[(w_{r,r})^2+\left(\frac{w_r}{r}\right)^2+2\nu\frac{w_{r,r}w_r}{r}\right] r\,dr}_{\text{in-plane}} + \underbrace{2\pi\int_0^a D\left[\left(w_{z,rr}+\frac{1}{r}w_{z,r}\right)^2-2(1-\nu)\frac{w_{z,r}w_{z,rr}}{r}\right] r\,dr}_{\text{transverse}}. \tag{3-5}$$

3B. ***Simply supported circular thin plate under uniform normal load.***

3B.1. *Elasticity solution.* Consider a solid of revolution which is free of body forces and is loaded axisymmetrically by uniform normal tractions $h_z = q$ applied at the surface $z = -t/2$, $0 < r < a$ as shown in Figure 2a. The essential and natural boundary conditions corresponding to simple support on the lateral boundary $r = a$, $-t/2 < z < t/2$ are as follows:

$$g_z = -\frac{qt}{160E}\left\{80(1+2\nu+\nu^2)\frac{z^4}{t^4}+\left[120\nu(1-\nu)\frac{a^2}{t^2}-24(5+2\nu+\nu^2)\right]\frac{z^2}{t^2} + 80\frac{z}{t}-10\nu(1-\nu)\frac{a^2}{t^2}+9+2\nu+\nu^2\right\}, \tag{3-6}$$

$$h_n = -q\,(2+\nu)\,\frac{z}{t}\left(\frac{3}{20}-\frac{z^2}{t^2}\right).$$

In addition, axial symmetry conditions are enforced at the center $r = 0$, $-t/2 < z < t/2$:

$$g_n = 0, \qquad h_z = 0. \tag{3-7}$$

Note that in all examples considered hereafter the prescribed body force and boundary loads are consistent with the desired analytical solution obtained by the semi-inverse method.

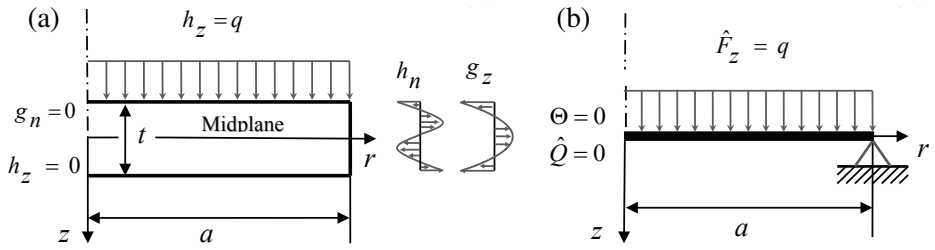

Figure 2. (a) Torsionless axisymmetric thin flat elastic solid under uniform normal tractions. (b) Simply supported circular thin plate under effective uniform transverse force.

The analytical solution, in terms of stress, of the torsionless axisymmetric elasticity problem obtained using Love's stress function is

$$\begin{aligned}
\sigma_{rr} &= q\frac{z}{t}\left[\frac{3\,(3+\nu)}{4}\frac{a^2}{t^2}\left(1-\frac{r^2}{a^2}\right)+(2+\nu)\left(\frac{z^2}{t^2}-\frac{3}{20}\right)\right],\\
\sigma_{\theta\theta} &= q\frac{z}{t}\left\{\frac{3\,(3+\nu)}{4}\frac{a^2}{t^2}\left[1-\frac{(1+\nu)\,r^2}{(3+\nu)\,a^2}\right]+(2+\nu)\left(\frac{z^2}{t^2}-\frac{3}{20}\right)\right\},\\
\sigma_{zz} &= \frac{q}{2}\left(-4\frac{z^3}{t^3}+3\frac{z}{t}-1\right), \qquad \sigma_{rz} = \frac{3q}{4}\frac{r}{t}\left(4\frac{z^2}{t^2}-1\right).
\end{aligned} \tag{3-8}$$

3B.2. *Thin-plate solution.* Using the definitions in Table 1 (with x_3 replaced by z) we obtain the axisymmetric thin-plate load resultants and boundary conditions (thin-plate data) derived from the boundary loads and displacements of the original three-dimensional problem:

$$\begin{aligned}
\hat{F}_z = F_z = q \qquad & (0<r<a),\\
W_z = 0, \qquad M_n = 0 \qquad & (r=a),\\
\Theta = 0, \qquad \hat{Q} = 0 \qquad & (r=0).
\end{aligned} \tag{3-9}$$

Equation (3-9) suggests that the problem corresponds to a thin plate which is simple supported at $r = a$ as shown in Figure 2b. The normal tractions h_3 on the surface $z = -t/2$, $0 < r < a$ of the elastic body contribute to the effective applied transverse force $\hat{F}_z$.

The in-plane reduced problem has a trivial solution. Solving the transverse reduced problem with the data (3-9), we obtain the transverse deflection of the plate

$$w_z = \frac{3qa^4\left(1-\nu^2\right)}{16Et^3}\left(1-\frac{r^2}{a^2}\right)\left(\frac{5+\nu}{1+\nu}-\frac{r^2}{a^2}\right). \tag{3-10}$$

The approximate displacement field $\boldsymbol{u}^s$ is obtained from $\boldsymbol{w}$ using the kinematic assumptions (2-2) and (2-3). Full displacement fields are given in the Appendix. The components of the corresponding thin-plate stress field are as follows — compare (3-8):

$$\sigma^s_{rr} = q\frac{z}{t}\,\frac{3\,(3+\nu)}{4}\frac{a^2}{t^2}\left(1-\frac{r^2}{a^2}\right) \quad \text{and} \quad \sigma^s_{\theta\theta} = q\frac{z}{t}\,\frac{3\,(3+\nu)}{4}\frac{a^2}{t^2}\left[1-\frac{(1+\nu)}{(3+\nu)}\,\frac{r^2}{a^2}\right]. \tag{3-11}$$

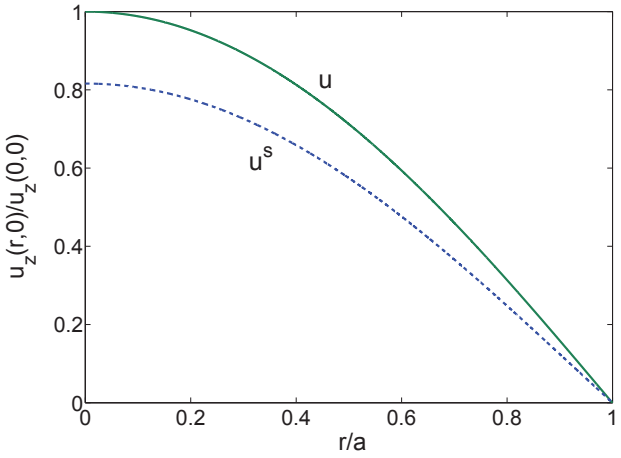

Figure 3. Simply supported circular plate ($t/a = 0.5$, $\nu = 0.3$) under uniform normal load: transverse displacements, $z = 0$.

3B.3. *Error evaluation.*

Relative error of displacement. Figure 3 represents the normalized midplane transverse displacements $u_z/u_z(0,0)$ (solid line) and $u_z^s/u_z(0,0)$ (dashed line) for $t/a = 0.5$ and Poisson's ratio $\nu = 0.3$. Even for this relatively large thickness the error in the structural displacement is relatively small. Recalling that $0 \le z \le t$, $(z/a) \le (t/a)$ and $0 \le r \le a$ one observes that the relative error of the transverse displacement for the circular thin plate in this case tends to zero as $t/a \to 0$ (see also (3-8) and (3-11) for stresses σ_{rr} and $\sigma_{\theta\theta}$ where the first term in the parentheses is dominant for $a/t \gg 1$).

Relative error in energy. The Taylor series expansion of relative error in the energy with respect to the relative thickness t/a up to order five yields

$$\frac{\left(\|\boldsymbol{u}\|_E^2 - \|\boldsymbol{w}\|_S^2\right)^{1/2}}{\|\boldsymbol{u}\|_E} = \frac{2}{5}\sqrt{\frac{30}{(7+\nu)}}\,\frac{t}{a} + \frac{1652 + 2596\nu + 15\nu^2 - 6\nu^3 - \nu^4}{2100\,(1-\nu)\,(7+\nu)}\sqrt{\frac{30}{(7+\nu)}}\,\frac{t^3}{a^3} + \mathcal{O}\left(\frac{t^5}{a^5}\right). \quad (3\text{-}12)$$

One observes that the expression of the relative error in the energy for the simply supported circular thin plate under uniform normal load, (3-12), tends to zero as the ratio of the thickness to the radius of the plate tends to zero (Figure 4).

3C. ***Simply supported circular thin plate under linearly varying tangential load.*** We now consider a different elasticity problem that reduces to the same thin-plate problem as in Section 3B.

3C.1. *Elasticity solution.* A solid of revolution is loaded now by linearly varying tangential tractions $h_r = \pm\frac{q}{2t}r$ (where q is a constant) applied at the surfaces $z = \pm t/2$, $0 < r < a$, as shown in Figure 5a. The essential and natural boundary conditions corresponding to simple support on the lateral boundary

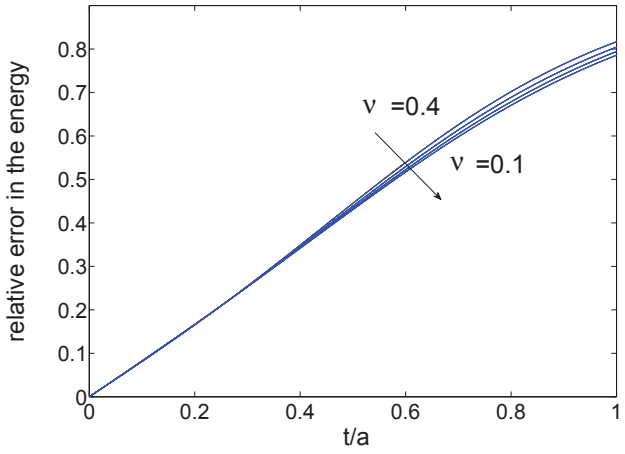

Figure 4. Simply supported circular plate under uniform normal load: relative error in the energy.

$(r = a,\ -t/2 < z < t/2)$ are

$$g_z = -\frac{qt}{160E}\left\{80(1+2\nu+\nu^2)\frac{z^4}{t^4} + \left[120\nu(1-\nu)\frac{a^2}{t^2} - 8(5+6\nu+3\nu^2)\right]\frac{z^2}{t^2} - 10\nu(1-\nu)\frac{a^2}{t^2} + \frac{7}{3} + 2\nu + \nu^2\right\}, \quad (3\text{-}13)$$

$$h_n = -q\,(2+\nu)\,\frac{z}{t}\left(\frac{3}{20} - \frac{z^2}{t^2}\right),$$

while the axial symmetry conditions are satisfied at $r = 0,\ -t/2 < z < t/2$:

$$g_n = 0, \qquad h_z = 0. \quad (3\text{-}14)$$

Note that while here h_n is identical to that given in (3-6), g_z is different.

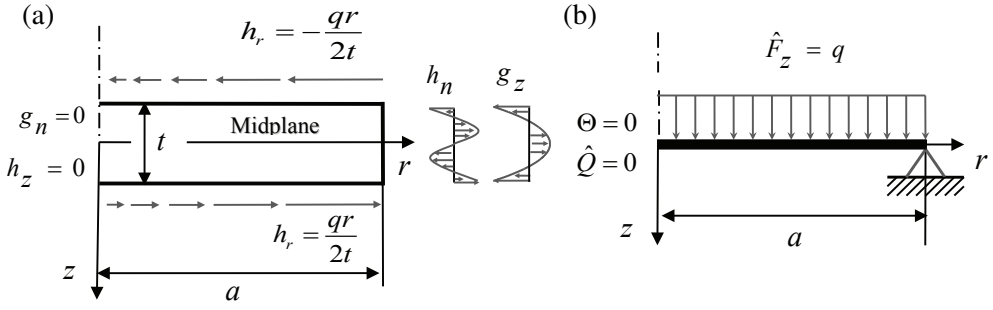

Figure 5. (a) Torsionless axisymmetric thin flat elastic solid under linearly varying tangential tractions. (b) Simply supported circular thin plate under effective uniform transverse force.

The solution of the elasticity problem is as follows:

$$\sigma_{rr} = q\frac{z}{t}\left[\frac{3\,(3+\nu)}{4}\frac{a^2}{t^2}\left(1-\frac{r^2}{a^2}\right)+(2+\nu)\left(\frac{z^2}{t^2}-\frac{3}{20}\right)\right],$$
$$\sigma_{\theta\theta} = q\frac{z}{t}\left\{\frac{3\,(3+\nu)}{4}\frac{a^2}{t^2}\left[1-\frac{(1+\nu)}{(3+\nu)}\frac{r^2}{a^2}\right]+(2+\nu)\left(\frac{z^2}{t^2}-\frac{3}{20}\right)\right\},$$
$$\sigma_{zz} = \frac{q}{2}\left(-4\frac{z^3}{t^3}+\frac{z}{t}\right), \qquad \sigma_{rz} = \frac{3q}{4}\frac{r}{t}\left(4\frac{z^2}{t^2}-\frac{1}{3}\right). \tag{3-15}$$

3C.2. *Thin-plate solution.* The thin-plate data are

$$\hat{F}_z = \frac{1}{r}\frac{\partial}{\partial r}(r\,C_r) = q \qquad (0<r<a), \tag{3-16}$$
$$W_z = 0, \qquad M_n = 0 \qquad (r=a),$$
$$\Theta = 0, \qquad \hat{Q} = 0 \qquad (r=0).$$

The definitions of F_z, W_z, Θ, M_n and $\hat{Q}$ are given in Table 1 (with x_3 replaced by z). Equation (3-16) suggests that the problem corresponds to a thin plate simply supported at $r=a$, as shown in Figure 5b. Only the applied couple C_r that originates in the tractions h_r on the top and bottom surfaces of the elastic body contribute to the effective applied transverse force $\hat{F}_z$.

One observes that the linearly varying tangential tractions are reduced to the same load resultants as for the circular thin plate under uniform normal load derived in Section 3B.2. Thus the transverse deflection of the simply supported circular thin plate is identical to that given by (3-10). The thin-plate stress field is given in (3-11).

3C.3. *Error evaluation.*

Relative error of displacement. Figure 6 represents the normalized midplane transverse displacements

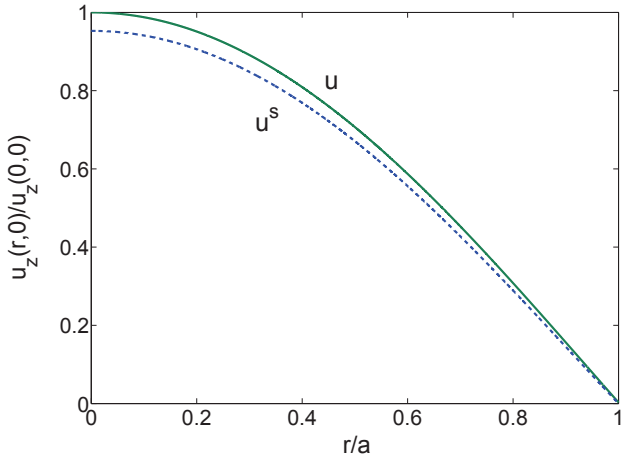

Figure 6. Simply supported circular plate ($t/a = 0.5$, $\nu = 0.3$) under linearly varying tangential load: transverse displacements at $z = 0$.

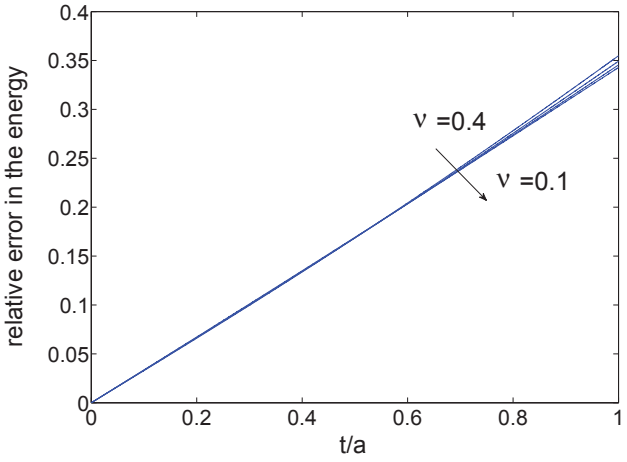

Figure 7. Simply supported circular plate under linearly varying tangential load: relative error in the energy.

$u_z/u_z(0,0)$ (solid line) and $u_z^s/u_z(0,0)$ (dashed line) for $t/a = 0.5$ and Poisson's ratio $\nu = 0.3$. Full displacement fields are given in the Appendix. Once again one observes that the relative error of the transverse displacement for the circular thin plate in this case tends to zero as $t/a \to 0$ (see also (3-15) and (3-11) for stresses).

Relative error in energy. The Taylor series expansion of relative error in the energy with respect to the relative thickness t/a up to order five yields

$$\frac{\left(\|\boldsymbol{u}\|_E^2 - \|\boldsymbol{w}\|_S^2\right)^{1/2}}{\|\boldsymbol{u}\|_E} = \frac{2}{5}\sqrt{\frac{5}{(7+\nu)}}\,\frac{t}{a} + \frac{56+368\nu+45\nu^2-18\nu^3-3\nu^4}{1050\,(1-\nu)\,(7+\nu)}\sqrt{\frac{5}{(7+\nu)}}\,\frac{t^3}{a^3} + \mathcal{O}\left(\frac{t^5}{a^5}\right). \quad (3\text{-}17)$$

We can see that the expression of the relative error in the energy for the simply supported circular thin plate under linearly varying tangential load, (3-17), tends to zero as the ratio of the thickness to the radius of the plate tends to zero (Figure 7). Although the structural reduced problem is identical to the one considered in Section 3B.2, both the relative error in displacements and the relative error in energy are consistently smaller in the case of a plate loaded by a linearly varying tangential tractions (Figures 6 and 7). The reason is the difference in the data of the underlying three-dimensional elasticity problems.

3D. ***Central point supported circular thin plate under linearly varying tangential load.*** We now consider an elasticity problem with the same linearly varying tangential tractions on the top and bottom surfaces of the plate as in Section 3C but different boundary conditions at the center and on the lateral boundary, giving rise to an effective boundary shear force of the thin-plate problem.

3D.1. *Elasticity solution.* The loading applied at the top and bottom surfaces is identical to that considered in Section 3C.1, as shown in Figure 8a. The natural boundary conditions on the lateral boundary

$(r = a,\ -t/2 < z < t/2)$ are

$$h_n = -q\,(2+\nu)\,\frac{z}{t}\left(\frac{3}{20} - \frac{z^2}{t^2}\right), \qquad h_z = \frac{qa}{4t}\left(12\frac{z^2}{t^2} - 1\right). \tag{3-18}$$

The essential boundary conditions at the center $(r = 0,\ -t/2 < z < t/2)$ are

$$g_n = 0,$$
$$g_z = \frac{qt}{160E}\Big\{-80(1+2\nu+\nu^2)\frac{z^4}{t^4} + \Big[-120\nu(3+\nu)\frac{a^2}{t^2} + \big(120+144\nu+72\nu^2\big)\Big]\frac{z^2}{t^2} + 10\nu(3+\nu)\frac{a^2}{t^2} - \frac{7}{3} - 2\nu - \nu^2\Big\}. \tag{3-19}$$

The stress distribution for this elasticity problem is the same as that of the previous problem, (3-15).

3D.2. *Thin-plate solution.* Considering the thin-plate data

$$\begin{aligned} &\hat{F}_z = \frac{1}{r}\frac{\partial}{\partial r}(r\,C_r) = q && && (0 < r < a), \\ &W_z = 0, && \Theta = 0 && (r = 0), \\ &\hat{Q} = -C_r^- = -\tfrac{1}{2}qa, && M_n = 0 && (r = a), \end{aligned} \tag{3-20}$$

one observes that the transverse load $\hat{F}_z$ is identical to the one considered in Section 3C.2 whereas an effective shear force $\hat{Q}$ is applied now at the boundary $r = a$. Equation (3-20) suggests that the problem corresponds to a thin plate which is free at $r = a$ and fixed (central point supported) at $r = 0$, as shown in Figure 8b. Only the applied couple C_r that originates in the tractions h_r on the top and bottom surfaces of the elastic body contributes to the effective applied transverse force $\hat{F}_z$ and effective prescribed boundary shear force $\hat{Q}$ on the edge of the plate.

The transverse deflection of the central point supported circular thin plate is

$$w_z = -\frac{3qa^4\left(1-\nu^2\right)}{16Et^3}\frac{r^2}{a^2}\left(2\,\frac{3+\nu}{1+\nu} - \frac{r^2}{a^2}\right). \tag{3-21}$$

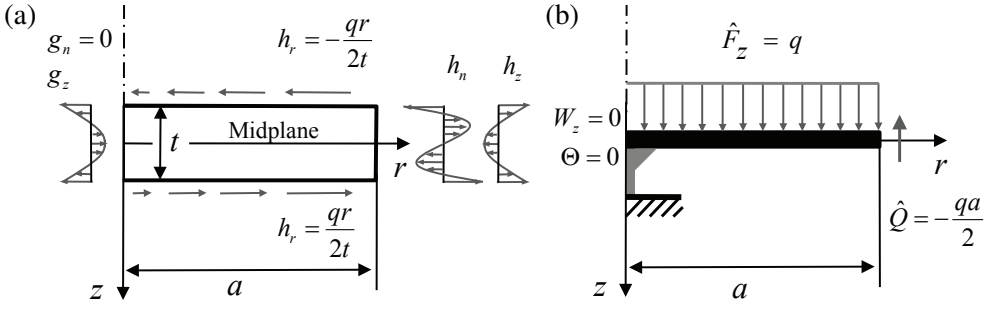

Figure 8. (a) Center-supported torsionless axisymmetric plate-like elastic solid under linearly varying tangential tractions. (b) Central point supported circular thin plate under effective uniform transverse and boundary shear forces.

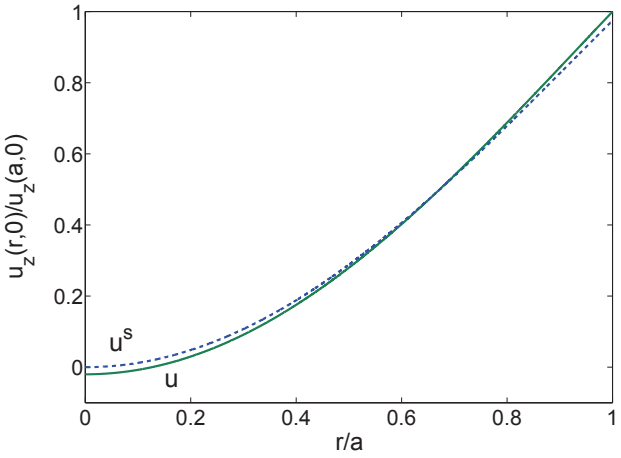

Figure 9. Central point supported circular plate ($t/a = 0.5$, $\nu = 0.3$) under linearly varying tangential load: transverse displacements at $z = 0$.

The approximate three-dimensional structural displacement field $\boldsymbol{u}^s$ is obtained from the kinematic assumptions (2-2) and (2-3). Full displacement fields are given in the Appendix. Note that the thin-plate stress field for the last load case is identical for both previous ones and is given in (3-11). The reason is that the problem considered here is self-equilibrated and the resultant of the distributed transverse load $\hat{F}$ is equal to the resultant of the effective shear force $\hat{Q}$ applied at the boundary $r = a$. As a result, the reaction at the center $r = 0$ of the plate is zero (see Figure 5b) making the stress field of two problems to be identical.

3D.3. *Error evaluation.*

Relative error of displacement. Figure 9 represents the normalized midplane transverse displacements $u_z/u_z(a, 0)$ (solid line) and $u_z^s/u_z(a, 0)$ (dashed line) for $t/a = 0.5$ and Poisson's ratio $\nu = 0.3$. In accordance with Figure 9, the midplane displacement at the center of the plate-like solid (solid line) is not zero whereas the thin plate deflection (the structural problem solution, dashed line) is zero at this point. The reason is in the definition of the structural deflections as displacements averaged through the thickness of the plate-like body rather than the displacements of the midplane (see remark on page 772). The difference between the two solutions corresponds to the rigid body translation and rotation of the plate and does not affect the stress field.

Relative error in energy. Since constants in the relative error in energy corresponding to an axial rigid-body translation may be discarded, the relative error in energy of the central point supported plate is identical to that of the simple supported plate considered in Section 3C.3.

4. Numerical efficiency

Finite element computations illustrate the implementation, as well as the accuracy and efficiency, of the plate formulation proposed for general loading configurations. A comparison of the problem size required to attain a certain level of accuracy by solid elements and thin-plate elements subject to the resultant loads proposed demonstrates the efficiency of the structural model. The load configuration

that is considered would pose a formidable challenge to many conventional approaches to plate loading. Trilinear hexahedral elements with incompatible modes [Taylor et al. 1976] are used for the elasticity solution. Bicubic Hermite Bogner–Fox–Schmit rectangular elements [Bogner et al. 1966; Zienkiewicz and Taylor 2000] are used for the thin-plate problem. This element is restricted to rectangular shapes, limiting the numerical tests to rectangular geometries. It bears emphasis that our structural procedures are subject to no such restriction.

Consider an $a \times a$ plate of aspect ratio $t/a = 0.025$ centered at the origin, undergoing constant rotation ω around the normal axis (Figure 10). The isotropic elastic material has a Poisson ratio $\nu = 0.3$. The density varies linearly through the thickness

$$\rho = \rho_0 \left(1 + \frac{x_3}{2t}\right). \tag{4-1}$$

The three-dimensional loading due to the rotation is represented by an applied body force in the radial direction of magnitude $\rho\omega^2 r$. The transverse structural loading in this problem results solely from distributed couples that arise from the variation of the radial body force. In order to focus on the bending response, we consider only the variable part of the distribution:

$$f_\alpha = \frac{\rho_0 \omega^2}{2t}\, x_\alpha x_3. \tag{4-2}$$

The resultant structural loads are applied couples, computed from the definition in Table 1:

$$C_\alpha = \frac{\rho_0 \omega^2 t^2}{24}\, x_\alpha. \tag{4-3}$$

Clearly, thin-plate formulations that don't account for applied couples are incapable of representing this type of load configuration.

By symmetry, only one quarter of the body is considered in the computation (see Figure 10). We impose free boundary conditions on the outer edges $x_1 = a/2$ and $x_2 = a/2$, and symmetry boundary conditions on the edges $x_1 = 0$ and $x_2 = 0$, and fix the axis of rotation. For the plate problem, consistent nodal loads are computed from the applied couples C_α as indicated by the principle of virtual work (2-11).

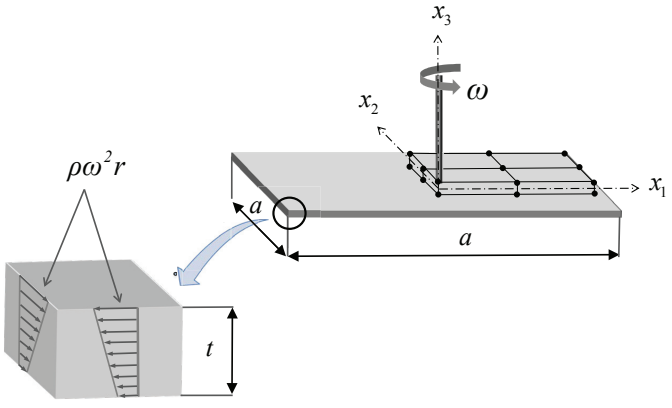

Figure 10. Rotating square plate with varying density: problem statement, the depicted solid mesh is $2 \times 2 \times 1$ (due to symmetry, only one quarter is discretized).

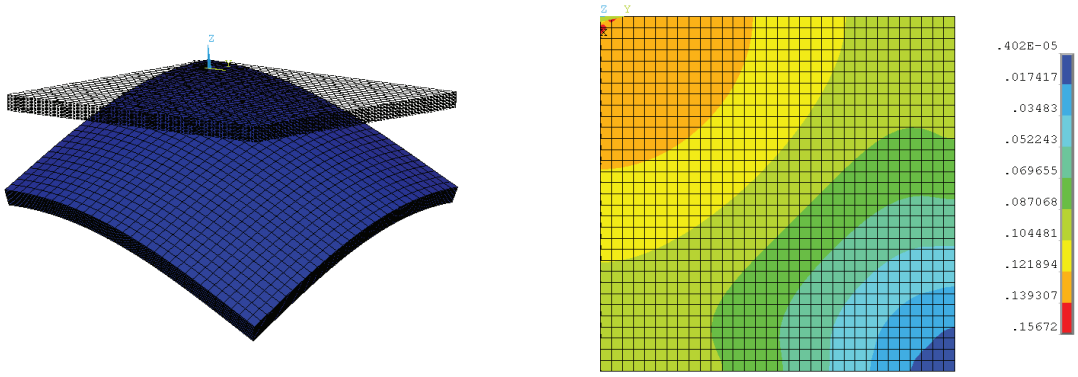

Figure 11. Rotating square plate with varying density: Deformed shape and von Mises stress distribution; 32 × 32 × 16 solid mesh.

Thus, no effective boundary shear force or corner forces are required. Accounting for applied couples is essential for the thin-plate modeling of this problem. Figure 11 shows representative results for the 32 × 32 × 16 solid mesh.

Remark. The applied couples appear explicitly in the variational statement of this problem. In contrast, the loading in the strong form would be expressed in terms of an effective distributed transverse force and effective boundary shear force, both emanating from the applied couples, as well as homogeneous corner force boundary conditions.

A comparison of the number of degrees of freedom in the numerical models of the continuum and structural problems required to attain a certain level of accuracy provides an estimate of the computational efficiency of the structural representation. Let $\boldsymbol{u}^h$ and $\boldsymbol{w}^h$ be the three-dimensional and thin-plate finite element solutions, respectively. The accuracy of both is measured relative to $\boldsymbol{u}^{\text{ref}}$, a converged three-dimensional finite element reference solution obtained on a highly refined mesh (64 × 64 × 32), accounting for the combination of modeling and discretization errors in the thin-plate computations. Since the elastic energy norm (3-1) is inappropriate for measuring errors of the plate models due to the modification of the constitutive law, we use the *relative errors in the energy*

$$\frac{\left(\|\boldsymbol{u}^{\text{ref}}\|_E^2 - \|\boldsymbol{u}^h\|_E^2\right)^{1/2}}{\|\boldsymbol{u}^{\text{ref}}\|_E}, \qquad \frac{\left(\|\boldsymbol{u}^{\text{ref}}\|_E^2 - \|\boldsymbol{w}^h\|_S^2\right)^{1/2}}{\|\boldsymbol{u}^{\text{ref}}\|_E}$$

Results of the comparison are presented in Table 5 and Figure 12. The coarsest plate mesh, 2 × 2 with 24 degrees of freedom, attains a level of accuracy that is comparable with the 16 × 16 × 8 solid model with incompatible modes, that contains 7344 degrees of freedom. The 0.7% error of the converged plate computation is the *modeling error* of the plate theory for this high aspect ratio ($t/a = 0.025$), leading to the high efficiency of the structural representation.

5. Conclusions

The present work describes a systematic conversion of general loads of the classical problem of three-dimensional elastostatics to their thin-plate counterparts. We provide formulas for all types of resultant

	Elasticity					Thin plate			
mesh	2×2×1	4×4×2	8×8×4	16×16×8	32×32×16	2×2	4×4	8×8	16×16
degrees of freedom	36	180	1080	7344	53856	24	80	288	1088
relative error [%]	25.7	14.8	7.6	3.8	1.8	3.2	2.3	0.7	0.7

Table 5. Rotating square plate with varying density: relative error in the energy of the finite element solutions, 3D elasticity with incompatible modes versus thin plate.

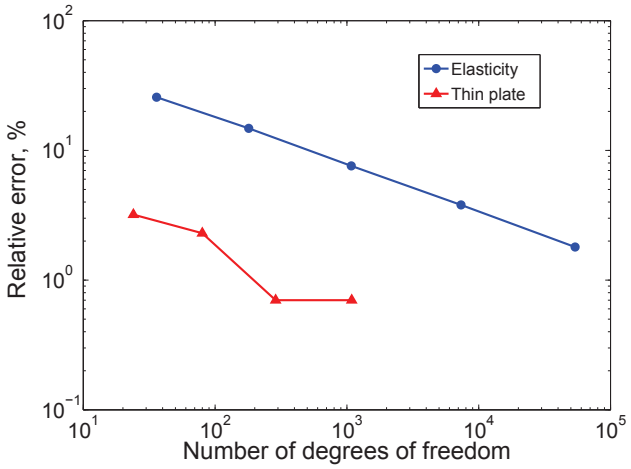

Figure 12. Rotating square plate with varying density: relative error in the energy of the finite element solutions, three-dimensional elasticity with incompatible modes versus thin plate. Reference solution is converged elasticity solution in both cases. The converged plate computation still exhibits a modeling error.

structural loads and boundary conditions in terms of the original three-dimensional data, in forms that are readily incorporated into computational tools, without entailing re-programming of existing software.

The kinematic and constitutive assumptions of Kirchhoff plate theory are substituted into the principle of virtual work for linear elastostatics, leading to a statement of virtual work for the thin plate. This formulation incorporates applied distributed couples engendered by in-plane components of three-dimensional loads, which are rarely accounted for in the context of a thin plate. Disregarding this type of loading may neglect a significant portion of the overall structural response in some cases.

We advocate the treatment of the twisting moment in virtual work in a form that seldom appears in the literature. This simpler form is compatible with the variational statement of higher-order plate theories, and obviates the use of the Kirchhoff equivalent force and corner forces in methods based on virtual work such as finite element analysis, thereby allowing lower regularity of the prescribed boundary twisting moment and facilitating implementation.

Structural essential boundary conditions are imposed on the quantities associated with a variation in the boundary integrals of the Euler–Lagrange equations. The data are specified by a through-the-thickness averaging procedure suggested by the definition of the force resultants. This interpretation of

the structural deflections as through-the-thickness averages of the continuum displacements, rather than their values on the midplane (the more conventional notion), yields explicit formulas for the thin-plate essential boundary data.

In-plane components of three-dimensional body forces and tangential tractions on the top and bottom surfaces engender applied distributed couples, modifying the transverse loading of the plate bending problem. The distributed loading in the equilibrium equation is an effective transverse force. The standard term is modified by the in-plane divergence of the applied couples.

Similarly, the shear loading is an effective boundary shear force. The celebrated Kirchhoff equivalent force is modified by the edge trace of the applied couples. These terms, which are rarely accounted for in the literature, would be difficult to derive intuitively.

When the boundary is not smooth, shear boundary conditions include discrete corner forces defined as jumps of the prescribed boundary twisting moment emanating from tangential tractions applied on the lateral boundary. Corner forces appear in the literature only as reaction forces that are part of the solution in some cases, and in other descriptions there is no mention of corner forces whatsoever. Consistent variational derivation of the plate problem formulation gives rise to the corner forces in the Euler–Lagrange equations, and therefore they should appear explicitly as natural boundary conditions in the problem statement.

Overall, the formulation presented in this work facilitates the solution of problems that would otherwise pose formidable challenges. Numerical results confirm that appropriate use of the thin-plate model economizes computation and provides insight into the mechanical behavior, while preserving a level of accuracy comparable with the full three-dimensional solution.

Appendix: Displacement fields of analytical problems

A. *Simply supported circular thin plate under uniform normal load.*

Elasticity solution.

$$u_r = \frac{qr}{20Et^3}\left\{20(2+\nu-\nu^2)\,z^3+\left[-15(1-\nu^2)\,r^2+15(3-2\nu-\nu^2)\,a^2-(6+27\nu-3\nu^2)\,t^2\right]z+10\nu\,t^3\right\} \tag{A.1}$$

$$\begin{aligned} u_z = \frac{q}{480Et^3}\Big\{&-240(1+2\nu+\nu^2)\,z^4+\left[720\nu(1+\nu)\,r^2-360\nu(3+\nu)\,a^2+(360+144\nu+72\nu^2)\,t^2\right]z^2 \\ &-240\,z\,t^3+90(1-\nu^2)\,r^4-\left[180(3-2\nu-\nu^2)a^2+(288+36\nu+36\nu^2)\,t^2\right]r^2 \\ &+90(5-4\nu-\nu^2)\,a^4+6(48+11\nu+\nu^2)\,a^2\,t^2-(27+6\nu+3\nu^2)\,t^4\Big\} \end{aligned} \tag{A.2}$$

Thin-plate solution.

$$u_r^s = -\frac{3qrz}{4Et^3}\left[(1-\nu^2)\,r^2-(3-2\nu-\nu^2)\,a^2\right] \tag{A.3}$$

$$u_z^s = \frac{3q}{16Et^3}\left[(1-\nu^2)\,r^4-2(3-2\nu-\nu^2)\,r^2\,a^2+(5-4\nu-\nu^2)\,a^4\right] \tag{A.4}$$

B. *Simply supported circular thin plate under linearly varying tangential load.*

Elasticity solution.

$$u_r = \frac{qr}{20Et^3}\left\{20(2+\nu-\nu^2)z^3 + \left[-15(1-\nu^2)r^2 + 15(3-2\nu-\nu^2)a^2 - (6+7\nu-3\nu^2)t^2\right]z\right\} \tag{B.1}$$

$$\begin{aligned} u_z = \frac{q}{480Et^3}\Big\{&-240(1+2\nu+\nu^2)z^4 + \left[720\nu(1+\nu)r^2 - 360\nu(3+\nu)a^2 + (120+144\nu+72\nu^2)t^2\right]z^2 \\ &+ 90(1-\nu^2)r^4 - \left[180(3-2\nu-\nu^2)a^2 + (48+36\nu+36\nu^2)t^2\right]r^2 \\ &+ 90(5-4\nu-\nu^2)a^4 + 6(8+11\nu+\nu^2)a^2t^2 - (7+6\nu+3\nu^2)t^4\Big\} \end{aligned} \tag{B.2}$$

Thin-plate solution. See (A.3) and (A.4).

C. *Central point supported circular thin plate under linearly varying tangential load.*

Elasticity solution.

$$u_r = \frac{qr}{20Et^3}\left\{20(2+\nu-\nu^2)z^3 + \left[-15(1-\nu^2)r^2 + 15(3-2\nu-\nu^2)a^2 - (6+7\nu-3\nu^2)t^2\right]z\right\} \tag{C.1}$$

$$\begin{aligned} u_z = \frac{q}{480Et^3}\Big\{&-240(1+2\nu+\nu^2)z^4 + \left[720\nu(1+\nu)r^2 - 360\nu(\nu+3)a^2 + (120+144\nu+72\nu^2)t^2\right]z^2 \\ &+ 90(1-\nu^2)r^4 - \left[180(3-2\nu-\nu^2)a^2 + (48+36\nu+36\nu^2)t^2\right]r^2 \\ &+ 30\nu(3+\nu)a^2t^2 - (7+6\nu+3\nu^2)t^4\Big\} \end{aligned} \tag{C.2}$$

Thin-plate solution.

$$u_r^s = -\frac{3qrz}{4Et^3}\left[(1-\nu^2)r^2 - (3-2\nu-\nu^2)a^2\right], \quad u_z^s = \frac{3q}{16Et^3}\left[(1-\nu^2)r^4 - 2(3-2\nu-\nu^2)r^2a^2\right] \tag{C.3}$$

References

[Actis et al. 1999] R. L. Actis, B. A. Szabo, and C. Schwab, "Hierarchic models for laminated plates and shells", *Comput. Methods Appl. Mech. Eng.* **172**:1-4 (1999), 79–107.

[Alessandrini et al. 1999] S. M. Alessandrini, D. N. Arnold, R. S. Falk, and A. L. Madureira, "Derivation and justification of plate models by variational methods", pp. 1–20 in *Plates and shells* (Québec, QC, 1996), edited by M. Fortin, CRM Proceedings and Lecture Notes **21**, AMS, Providence, RI, 1999.

[Antman 1995] S. S. Antman, *Nonlinear problems of elasticity*, Applied Mathematical Sciences **107**, Springer, New York, 1995. 2nd ed. published in 2005.

[Bauchau and Craig 2009] O. A. Bauchau and J. I. Craig, *Structural analysis: with applications to aerospace structures*, Solid Mechanics and its Applications **163**, Springer, Dordrecht, 2009.

[Bisegna and Sacco 1997] P. Bisegna and E. Sacco, "A layer-wise laminate theory rationally deduced from the three-dimensional elasticity", *J. Appl. Mech.* (*ASME*) **64**:3 (1997), 538–545.

[Bogner et al. 1966] F. K. Bogner, R. L. Fox, and L. A. Schmit, "The generation of interelement-compatible stiffness and mass matrices by the use of interpolation formulae", pp. 397–443 in *Matrix methods in structural mechanics*, edited by J. S. Przemieniecki et al., Air Force Flight Dynamics Laboratory, Wright-Patterson Air Force Base, OH, 1966. Technical report AFFDL-TR-66-80.

[Calcote 1969] L. R. Calcote, *The analysis of laminated composite structures*, Van Nostrand Reinhold, New York, 1969.

[Ciarlet 1990] P. G. Ciarlet, *Plates and junctions in elastic multi-structures: an asymptotic analysis*, Recherches en Mathématiques Appliquées **14**, Masson, Paris, 1990.

[Ciarlet 1997] P. G. Ciarlet, *Mathematical elasticity, II: Theory of plates*, Studies in Mathematics and its Applications **27**, North-Holland, Amsterdam, 1997.

[Cowper 1966] G. R. Cowper, "The shear coefficient in Timoshenko's beam theory", *J. Appl. Mech.* (*ASME*) **33** (1966), 335–340.

[Dauge and Gruais 1996] M. Dauge and I. Gruais, "Asymptotics of arbitrary order for a thin elastic clamped plate, I: Optimal error estimates", *Asymptot. Anal.* **13**:2 (1996), 167–197.

[Dauge and Gruais 1998] M. Dauge and I. Gruais, "Asymptotics of arbitrary order for a thin elastic clamped plate, II: Analysis of the boundary layer terms", *Asymptot. Anal.* **16**:2 (1998), 99–124.

[DiCarlo et al. 2001] A. DiCarlo, P. Podio-Guidugli, and W. O. Williams, "Shells with thickness distension", *Int. J. Solids Struct.* **38**:6–7 (2001), 1201–1225.

[Engel et al. 2002] G. Engel, K. Garikipati, T. J. R. Hughes, M. G. Larson, L. Mazzei, and R. L. Taylor, "Continuous/discontinuous finite element approximations of fourth-order elliptic problems in structural and continuum mechanics with applications to thin beams and plates, and strain gradient elasticity", *Comput. Methods Appl. Mech. Eng.* **191**:34 (2002), 3669–3750.

[Forte and Vianello 1988] S. Forte and M. Vianello, "On surface stresses and edge forces", *Rend. Accad. Naz. Lincei* **8** (1988), 409–426.

[Grossi and Lebedev 2001] R. O. Grossi and L. Lebedev, "Static and dynamic analyses of anisotropic plates with corner points", *J. Sound Vib.* **243**:5 (2001), 947–958.

[Hu 1984] H.-C. Hu, "Derivation of the classical plate bending theory from elasticity by variational method", *Comput. Struct.* **19**:1–2 (1984), 71–73.

[Hughes 2000] T. J. R. Hughes, *The finite element method: linear static and dynamic finite element analysis*, Dover, Mineola, NY, 2000.

[Hughes and Hinton 1986] T. J. R. Hughes and E. Hinton (editors), *Finite element methods for plate and shell structures*, Pineridge, Swansea, 1986.

[Kirchhoff 1850] G. Kirchhoff, "Über das Gleichgewicht und die Bewegung einer elastischen Scheibe", *J. Reine Angew. Math.* **1850**:40 (1850), 51–88.

[Krylov et al. 2006] S. Krylov, I. Harari, and D. Gadasi, "Consistent loading in structural reduction procedures for beam models", *Int. J. Multiscale Comput. Eng.* **4**:5–6 (2006), 559–584.

[Libai and Simmonds 1998] A. Libai and J. G. Simmonds, *The nonlinear theory of elastic shells*, 2nd ed., Cambridge University Press, Cambridge, 1998.

[Liu and Chang 2005] M.-F. Liu and T.-P. Chang, "Vibration analysis of a magneto-elastic beam with general boundary conditions subjected to axial load and external force", *J. Sound Vib.* **288**:1–2 (2005), 399–411.

[Madureira 2004] A. L. Madureira, "An improved biharmonic model: incorporating higher-order responses of the plate bending phenomena", *Anal. Appl.* **2**:1 (2004), 87–99.

[Moon and Holmes 1979] F. C. Moon and P. J. Holmes, "A magnetoelastic strange attractor", *J. Sound Vib.* **65**:2 (1979), 275–296.

[Morand and Ohayon 1995] H. J.-P. Morand and R. Ohayon, *Fluid structure interaction: applied numerical methods*, Wiley, Chichester, 1995.

[Nádai 1925] A. Nádai, *Die elastischen Platten*, Springer, Berlin, 1925.

[Nayfeh and Pai 2004] A. H. Nayfeh and P. F. Pai, *Linear and nonlinear structural mechanics*, Wiley, Hoboken, NJ, 2004.

[Niordson 1985] F. I. Niordson, *Shell theory*, North-Holland Series in Applied Mathematics and Mechanics **29**, North-Holland, Amsterdam, 1985.

[O'Leary and Harari 1985] J. R. O'Leary and I. Harari, "Finite element analysis of stiffened plates", *Comput. Struct.* **21**:5 (1985), 973–985.

[Podio-Guidugli 2000] P. Podio-Guidugli, "Recent results in the theory of elastic plates", *Transport Theory Stat. Phys.* **29**:1-2 (2000), 217–224.

[Poisson 1829] S. D. Poisson, "Mémoire sur l'équilibre et le mouvement des corps élastiques", *Mém. Acad. Sci. Paris* **8** (1829), 357–570.

[Prescott 1942] J. Prescott, "Elastic waves and vibrations of thin rods", *Philos. Mag. Ser. 7* **33**:225 (1942), 703–754.

[Reismann 1988] H. Reismann, *Elastic plates: theory and application*, Wiley, New York, 1988.

[Reissner 1969] E. Reissner, "On generalized two-dimensional plate theory, II", *Int. J. Solids Struct.* **5**:6 (1969), 629–637.

[Rubin 2000] M. B. Rubin, *Cosserat theories: shells, rods and points*, Solid Mechanics and its Applications **79**, Kluwer Academic, Dordrecht, 2000.

[Sayir and Mitropoulos 1980] M. Sayir and C. Mitropoulos, "On elementary theories of linear elastic beams, plates and shells", *Z. Angew. Math. Phys.* **31**:1 (1980), 1–55.

[Simmonds 1971] J. G. Simmonds, "An improved estimate for the error in the classical, linear theory of plate bending", *Q. Appl. Math.* **29** (1971), 439–447.

[Soedel 1981] W. Soedel, *Vibrations of shells and plates*, Mechanical Engineering **10**, Marcel Dekker, New York, 1981.

[Sokolnikoff 1983] I. S. Sokolnikoff, *Mathematical theory of elasticity*, 2nd ed., Krieger, Malabar, FL, 1983.

[Sutyrin and Hodges 1996] V. G. Sutyrin and D. H. Hodges, "On asymptotically correct linear laminated plate theory", *Int. J. Solids Struct.* **33**:25 (1996), 3649–3671.

[Szilard 2004] R. Szilard, *Theories and applications of plate analysis: classical, numerical and engineering methods*, Wiley, Hoboken, NJ, 2004.

[Taylor et al. 1976] R. L. Taylor, P. J. Beresford, and E. L. Wilson, "A non-conforming element for stress analysis", *Int. J. Numer. Methods Eng.* **10**:6 (1976), 1211–1219.

[Timoshenko 1983] S. P. Timoshenko, *History of strength of materials*, Dover, New York, 1983.

[Timoshenko and Goodier 1951] S. P. Timoshenko and J. N. Goodier, *Theory of elasticity*, 2nd ed., McGraw-Hill, New York, 1951.

[Timoshenko and Woinowsky-Krieger 1959] S. P. Timoshenko and S. Woinowsky-Krieger, *Theory of plates and shells*, 2nd ed., McGraw-Hill, New York, 1959.

[Todhunter and Pearson 1960] I. Todhunter and K. Pearson, *A history of the theory of elasticity and of the strength of materials, vol. I, II*, Dover, New York, 1960.

[Tsiatas 2009] G. C. Tsiatas, "A new Kirchhoff plate model based on a modified couple stress theory", *Int. J. Solids Struct.* **46**:13 (2009), 2757–2764.

[Ugural 1981] A. C. Ugural, *Stresses in plates and shells*, McGraw-Hill, New York, 1981.

[Vasil'ev and Lur'e 1992] V. V. Vasil'ev and S. A. Lur'e, "On refined theories of beams, plates, and shells", *J. Compos. Mater.* **26**:4 (1992), 546–557.

[Vidoli and Batra 2000] S. Vidoli and R. C. Batra, "Derivation of plate and rod equations for a piezoelectric body from a mixed three-dimensional variational principle", *J. Elasticity* **59**:1–3 (2000), 23–50.

[Vogelius and Babuška 1981] M. Vogelius and I. Babuška, "On a dimensional reduction method, I: The optimal selection of basis functions", *Math. Comput.* **37**:155 (1981), 31–46.

[Šolín 2006] P. Šolín, *Partial differential equations and the finite element method*, Wiley, Hoboken, NJ, 2006.

[Wells and Nguyen 2007] G. N. Wells and T. D. Nguyen, "A C^0 discontinuous Galerkin formulation for Kirchhoff plates", *Comput. Methods Appl. Mech. Eng.* **196**:35–36 (2007), 3370–3380.

[Zienkiewicz and Taylor 2000] O. C. Zienkiewicz and R. L. Taylor, *The finite element method, II: Solid mechanics*, 5th ed., Butterworth-Heinemann, Oxford, 2000.

Received 13 Jul 2010. Revised 28 Dec 2010. Accepted 7 Jan 2011.

ISAAC HARARI: harari@eng.tau.ac.il
School of Mechanical Engineering, Tel Aviv University, Ramat-Aviv, 69978 Tel Aviv, Israel
http://www.eng.tau.ac.il/~harari

IGOR SOKOLOV: sokoliv@gmail.com
School of Mechanical Engineering, Tel Aviv University, Ramat-Aviv, 69978 Tel Aviv, Israel

SLAVA KRYLOV: vadis@eng.tau.ac.il
School of Mechanical Engineering, Tel Aviv University, Ramat-Aviv, 69978 Tel Aviv, Israel

SUBMISSION GUIDELINES

ORIGINALITY

Authors may submit manuscripts in PDF format online at the Submissions page. Submission of a manuscript acknowledges that the manuscript is original and has neither previously, nor simultaneously, in whole or in part, been submitted elsewhere. Information regarding the preparation of manuscripts is provided below. Correspondence by email is requested for convenience and speed. For further information, write to one of the Chief Editors:

Davide Bigoni	bigoni@ing.unitn.it
Iwona Jasiuk	ijasiuk@me.concordia.ca
Yasuhide Shindo	shindo@material.tohoku.ac.jp

LANGUAGE

Manuscripts must be in English. A brief abstract of about 150 words or less must be included. The abstract should be self-contained and not make any reference to the bibliography. Also required are keywords and subject classification for the article, and, for each author, postal address, affiliation (if appropriate), and email address if available. A home-page URL is optional.

FORMAT

Authors can use their preferred manuscript-preparation software, including for example Microsoft Word or any variant of TEX. The journal itself is produced in LATEX, so accepted articles prepared using other software will be converted to LATEX at production time. Authors wishing to prepare their document in LATEX can follow the example file at www.jomms.org (but the use of other class files is acceptable). At submission time only a PDF file is required. After acceptance, authors must submit all source material (see especially Figures below).

REFERENCES

Bibliographical references should be complete, including article titles and page ranges. All references in the bibliography should be cited in the text. The use of BibTEX is preferred but not required. Tags will be converted to the house format (see a current issue for examples); however, for submission you may use the format of your choice. Links will be provided to all literature with known web locations; authors can supply their own links in addition to those provided by the editorial process.

FIGURES

Figures must be of publication quality. After acceptance, you will need to submit the original source files in vector format for all diagrams and graphs in your manuscript: vector EPS or vector PDF files are the most useful. (EPS stands for Encapsulated PostScript.)

Most drawing and graphing packages—Mathematica, Adobe Illustrator, Corel Draw, MATLAB, etc.—allow the user to save files in one of these formats. Make sure that what you're saving is vector graphics and not a bitmap. If you need help, please write to graphics@mathscipub.org with as many details as you can about how your graphics were generated.

Please also include the original data for any plots. This is particularly important if you are unable to save Excel-generated plots in vector format. Saving them as bitmaps is not useful; please send the Excel (.xls) spreadsheets instead. Bundle your figure files into a single archive (using zip, tar, rar or other format of your choice) and upload on the link you been given at acceptance time.

Each figure should be captioned and numbered so that it can float. Small figures occupying no more than three lines of vertical space can be kept in the text ("the curve looks like this:"). It is acceptable to submit a manuscript with all figures at the end, if their placement is specified in the text by means of comments such as "Place Figure 1 here". The same considerations apply to tables.

WHITE SPACE

Forced line breaks or page breaks should not be inserted in the document. There is no point in your trying to optimize line and page breaks in the original manuscript. The manuscript will be reformatted to use the journal's preferred fonts and layout.

PROOFS

Page proofs will be made available to authors (or to the designated corresponding author) at a Web site in PDF format. Failure to acknowledge the receipt of proofs or to return corrections within the requested deadline may cause publication to be postponed.

Journal of Mechanics of Materials and Structures

Volume 6, No. 5 May 2011

1559-3959(2011)6:5;1-B